# The changing role of junctional actomyosin in epithelial cell packing during *Drosophila* notum development

**Scott Curran**

A thesis submitted to University College London

for the degree of Doctor of Philosophy

2015

Supervised by Professor Buzz Baum

MRC Laboratory for Molecular Cell Biology

University College London

# DECLARATION

I, Scott Curran, confirm that the work presented in this thesis is my own. Where information has been obtained from other sources, I confirm that this has been indicated in the thesis.

Signed ……

# Abstract

Dramatic changes in tissue architecture can be produced by the cumulative action of individual cell movements within epithelia. During rapid developmental processes polarised recruitment of Myosin-II has previously been shown to drive changes in cell shape and direct neighbour exchange. It is important to ask whether similar mechanisms facilitate junction movement in stable epithelia, that are more prevalent in nature, and whether seemingly noisy fluctuations in junction length contribute to homeostatic tissue packing under ordinary growth conditions.

By using the *Drosophila* notum, I have taken advantage of a model system that remains constant in overall size and shape, whilst it orders, as a result of changes in cells packing. Confocal live imaging enabled quantitative junction fluctuation measurements of control and RNAi expressing nota, before and after periods of cell division, delamination and bristle cell differentiation.

Through a reduction in Myosin II (Myo II) activity, I established that junctional actomyosin was not required to drive neighbour exchange events in this tissue. Conversely, an increase in active Myo II levels was sufficient to inhibit junction fluctuations, cell intercalation and midline live cell delamination events. These results suggest a model in which Myo II independent junction length fluctuations fluidize the tissue, thereby enabling cells to move in order to relieve tissue stresses and crowding.

Furthermore, over the course of pupal development a systematic re-localisation of medioapical actomyosin to the junction correlated with a rise in line tension and an increase in tissue order. Thus, changes to actomyosin levels appear to tune neighbour exchange in a process akin to annealing, as the tissue moves from a state of disorder to hexagonal packing prior to the completion of development.

# Table of Contents

# List of Figures

# List of Tables

# Acronyms

**AJ** - Adherens junction

**A-P** - Anterior-posterior

**BP** - Base pair

**DN** - Dominant negative

**DV**- Dorsal-ventral

**EC** - Extra-cellular

**E-cadherin** - Epithelial cadherin

**F-actin** - Filamentous actin

**Fog** - Folded gastrulation

**GBE** - Germ band elongation / extension

**GFP** - Green fluorescent protein

**h AP** - Hours after puparium formation

**mCh** - monomeric Cherry

**M** - Midline

**MDCK**- Madin- Darby kidney cells

**MIB** - Mediolateral intercalation behaviour

**µm** - micrometre

**MHC** - Myosin heavy chain

**MRLC** - Myosin regulatory light chain

**ns** - Not significant / no significance

**OM** - Outside midline

**PCP** - planar cell polarity

**PFA** - Paraformaldehyde

**PI3K** - Phosphoinositide 3-kinase

**PIP2** - Phosphatidylinositol bisphosphate

**PIP3** - Phosphatidylinositol trisphosphate

***pnr*** - *pannier*

**PTEN** - Phosphatase and tensin homolog on chromosome 10

**RNAi** - Ribonucleic acid interference

**ROI** - Region of interest

**Rok** - Rho kinase

**SD** - Standard deviation

**SJ**- Septate junction

**SOP** - Sensory organ precursor cell

**Spg-Sqh** – Spaghetti Squash

**TEM** - Transmission electron microscopy

**ts** - Temperature sensitive

**UAS** - Upstream activator sequence

# Acknowledgements

I am very thankful to Buzz Baum, who approaches science from a perspective differently to anyone else I know. I made a good choice. It has been a long and valuable lesson in following an idea rather than a plan. Junctions can slide.

The original fly room and reason I joined: Eliana Marinari, André Rosa, & Nélio Rodrigues. Setting impossibly high standards to follow.

My primary collaborator, Charlotte Strandkvist. Who has been brilliant. But after we publish, let's never look at junctions again.

Fellow lab members (2011-2015): Andrea Dimitracopoulos, Helen Matthews, Arturo Araujo, Julien Bellis, Pelin Candarlioglu, Clotilde Cadart, Gautam Dey, Christina Dix, Marina Fedorova, Sushila Ganguli, Juanma Garcia, Nick Heatley, Ginger Hunter, Pato Kunda, Maxine Lam, Oscar Lancaster, Sergey Lekomtsev, Nunu Mchedlishvili, Jigna Patel, Remi Picone, Katarzyna Plak, Nitya Ramkumar, Jenny Rohn, Sacha Sarfati, Mario Ruiz Sorube, Tom Wyatt, Ruta Ziakute.

Collaborators and support: Yanlan Mao (LRI imaging), Jonathan Gale (Laser ablations), Julia Duque Lloredo (MDCK collaboration), Cosetta Bertoli (my 1.24 neighbour), Jean-Paul Vincent (second supervisor), Jemima Burden (EM imaging), Natalia Bulgakova (GBE imaging), Alexandre Kabla, and more recently to Marc de Genne & Guillaume Salbreux for accelerating this work towards a finish.

Rotation Supervisors: Claudio Stern (w/ Angela Anderson) & Roberto Mayor (Graduate tutor) (w/ Manuela Melchondia)

Maria Duda, Rob Tetley, Charlotte & Buzz who I greatly appreciate for reading this thesis and for their comments/ suggesting better words.

I thank the Wellcome Trust for funding and my exceptional 2010 cohort: Elena Scarpa, Miguel Tillo & Kristina Tubby.

Grant, fly enthusiast.

To Sar, who is more important than any other.

# 1. Introduction

## 1.1 Epithelia

First used in 1703 by Frederik Ruysch in his book *Thesaurus Anatomicus*, the word epithelia originates from the Greek words epi-, a prefix for upon, and thēlē, meaning teat – 'on the nipple' (Ruysch, 1703). Epithelia are thin membranous tissues that line a host of structures including blood vessels, organs and surfaces of the body. They act as mechanical and chemical barriers to separate internal contents from the external environment. Their ubiquitous presence across Metazoa reflects the essential requirement of multi-cellular animals to separate physiologically distinct tissue compartments and organelles (Cereijido et al., 2004; Rodriguez-Boulan and Macara, 2014; Tyler, 2003).

Epithelia are constructed from individual cells that are tightly packed together and connected via specialised intercellular junctions (Knust and Bossinger, 2002). Cells are polarised along their apical-basal axis and are organised either as simple monolayers (Fig. 1.1A) or in layered structures. In addition, many epithelia are pseudostratified in that nuclei (and the bulk volume of individual cells) sit at different levels within the monolayer. The apical surface of epithelia faces the external environment whilst basal structures are free to interact with the extra-cellular matrix and inner cavity. Epithelia exist in a variety of forms, as cuboidal, squamous or columnar, each of which performs a host of functions. Cells within cuboidal epithelia are as tall as they are wide and tend to have secretory and absorption roles, such as in kidney tubules and respiratory bronchioles. Squamous cells are thin and flat and tend to mediate efficient filtration and diffusion across surfaces so line lung alveoli and blood capillaries. Columnar epithelia are taller than they are wide and are found in tissues such as the stomach lining and digestive tract to provide barrier protection.

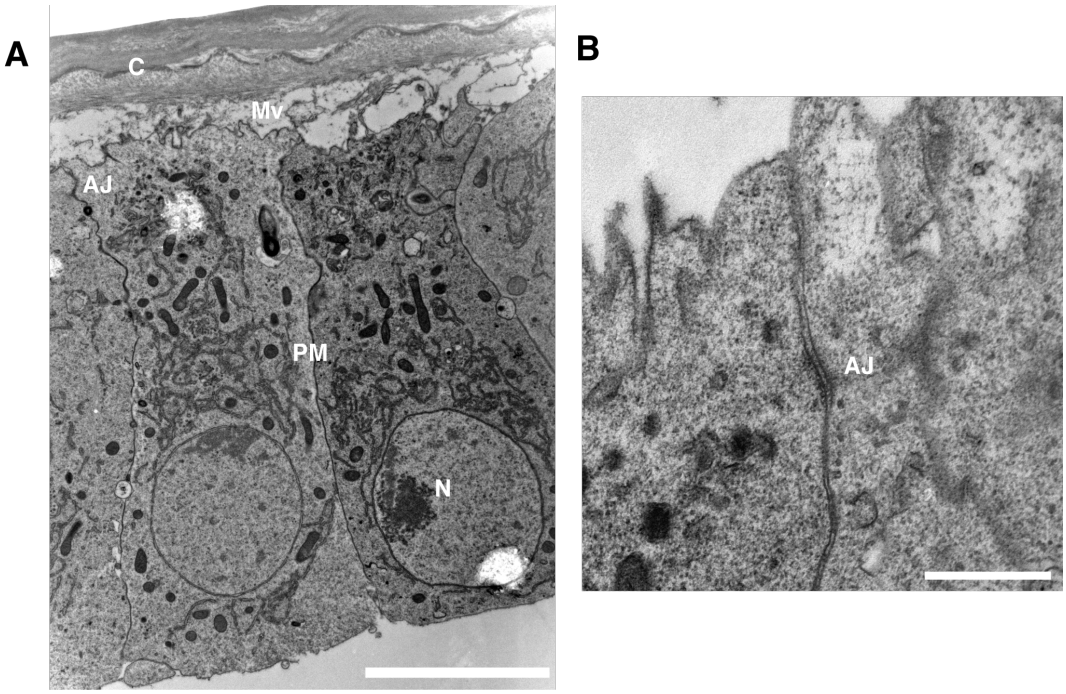


**Figure 1-1: Tight packing of cells within an epithelium.**

(**A**) Transmission electron microscopy (TEM) image of two epithelial cells of the *Drosophila* notum. C, cuticle layer; AJ, adherens junction; PM, plasma membrane; N, nucleus; Mv, microvilli. Scale bar = 5µm. (**B**) Increased magnification of electron dense adherens junction. Scale bar = 500nm

*$w^{1118}$; DE-cad-GFP(KI) ; pnrGAL4 / + ;*

(Larval development at 29°C, Methods: **2.14**)

## 1.2 Junctional differences between vertebrates and invertebrates

Epithelia have a range of specialised cell-cell junctions that hold cells together and maintain tissue integrity (Tepass et al., 2001). Though junctions of invertebrate (e.g. *Drosophila*) and vertebrate epithelia share many similarities there are also significant differences in terms of organisation and structure. *Drosophila* epithelia have an apical zonula adherens (adherens junction - AJ), which I will discuss in more detail in the next section. Above the adherens junction sits a sub-apical domain containing polarity markers, such as Crbs and the Par complex (Knust and Bossinger, 2002). Basal to the AJ is the septate junction (SJ) which functions to seal neighbouring cells. It acts as an effective paracellular barrier preventing the diffusion of solutes across the epithelium. The SJ has a ladder-like structure and is defined by the presence of a number of proteins including homologs of Claudin, Coracle, Neuroglian, Gliotactin and Neurexin-IV (Baumgartner et al., 1996; Lane and Swales, 1982; Oshima and Fehon, 2011; Tepass et al., 2001). The basolateral polarity regulators Lgl, Dlg and Scribbled localise at the level of the SJ and extend more basally (Bilder et al., 2000).

Vertebrate epithelia also have a zonula adherens but lack a septate junction. Instead they have a tight junction (TJ) that sits apical to the zonula adherens and acts as a paracellular barrier. This contains transmembrane proteins including Occludin and members of the Claudin family (Knust and Bossinger, 2002; Schneeberger and Lynch, 2004; Tsukita and Furuse, 2002). Under electron microscopy the outer membranes of neighbouring cells can be seen to be closely opposed to one another (Tsukita et al., 2001). As in *Drosophila*, the apical polarity markers (Crbs and Par) localise sub-apically (Gibson and Perrimon, 2003). Both invertebrates and vertebrates also have various basal cell-cell contacts including hemidesmosomes, gap junctions and desmosomes that attach to intermediate filaments, such as keratin (Schmidt et al., 1994).

## 1.3 Adherens junction function and components

The adherens junction is an adhesive belt that physically couples neighbouring cells. In *Drosophila* the adherens junction localises to a discrete portion of the apical domain (Harris, 2012). This is seen in electron micrographs as an electron-dense cortical plaque that forms close to the plasma membrane (Fig. 1.1B).

The coupling of neighbouring cells is mediated by E-cadherin (Shotgun in *Drosophila*) (Tepass et al., 1996). Cadherins are a superfamily of proteins that facilitate strong cell-cell adhesion in a calcium dependent manner. Classical (type I) cadherins, including E-cadherin, contain three domains: transmembrane, cytoplasmic and extracellular. The extracellular N-terminus contains five repeating extra-cellular (EC)-domains that create four calcium binding pockets (Aberle et al., 1996). In an 'active' calcium-bound conformation, E-cadherin monomers form trans homo-dimers with monomers on adjacent membranes through their membrane-distal EC1 domains (Brasch et al., 2012; Zhang et al., 2009). It has also been suggested that cis interactions are mediated by the binding of EC1 to the EC2 domain in a neighbouring molecule. Together these trans and cis interactions, allow for the formation of a 2D lattice that spans the ~20nm that separates adjacent cells in the epithelium (Brasch et al., 2012).

Different cadherin subtypes share a highly conserved C-terminal cytoplasmic tail that interacts with a set of proteins called catenins (Takeichi, 1995). The p120-catenin is thought to stabilise E-cadherin at the plasma membrane during junction formation (Yap et al., 1998). ß-catenin (Armadillo in *Drosophila*) binds to E-cadherin at its C-terminus (Huber and Weis, 2001; Lickert et al., 2000). It is thought that α-catenin in turn binds to ß-catenin to physically link E-cadherin to the actomyosin cytoskeleton. This is because α-catenin has a binding site for ß-catenin in its N-terminus, an actin-binding site in its C-terminus, and can interact with other actin binding proteins including vinculin, α-actinin and ZO-1 that strengthen this connection (Maiden and Hardin, 2011). Desai et al. demonstrated that α-catenin interactions with E-cadherin were required for its normal function at the adherens junction (Desai et al., 2013). Moreover α-catenin null mutant phenotypes (Sarpal et al., 2012) could be rescued by expression of a fusion of α-catenin to the E-cadherin C-terminus, bypassing the need

for ß-catenin interaction. In addition, F-actin binding was shown to be important, as α-catenin constructs lacking C-terminal F-actin binding sites could not rescue null mutant phenotypes. These results are consistent with the idea that α-catenin acts as a physical bridge between the AJ and cytoskeleton.

### 1.3.1 The actomyosin cytoskeleton

The actomyosin cortex is a meshwork consisting of filamentous actin and Myosin II (Myo II) that localises just beneath the plasma membrane (Salbreux et al., 2012). The bridging of the actomyosin cytoskeleton to the AJ allows forces generated within the cytoskeleton to be transmitted across the bridge and to modulate AJ structure, and vice versa (Heisenberg and Bellaiche, 2013; Takeichi, 2014). Junctional actomyosin therefore maintains cell integrity and controls cell shape. It has a profound impact on epithelial mechanics and adherens junction dynamics.

## 1.4 Actin regulation

Actin exists in a dynamic equilibrium between a monomeric cytosolic pool (43 kd Globular or G-actin) and a polymerised filamentous form (F-actin). Actin monomers bind head-to-tail, with each new actin monomer that binds rotating by $166^{o}$ to give the resulting 7nm diameter filament a double helical appearance. Filaments exhibit bipolarity with a fast growing 'barbed' plus-end and slow growing 'pointed' minus-end.

Actin filaments can be arranged into a variety of higher order structures, whose form is regulated by the Rho family of p21 small GTPases, a subfamily of the Ras superfamily (Hall, 1998; Spiering and Hodgson, 2011). Rho GTPases are G-proteins that act as molecular switches. From an inactive GDP-bound state, GTPases are loaded with GTP via the action of guanine-nucleotide exchange factors (GEFs). The intrinsic phosphatase activity of Rho GTPases hydrolyses GTP to GDP, a process enhanced by interaction with GTPase activating proteins (GAPS) (Etienne-Manneville and Hall, 2002). *Drosophila* has 7 Rho family members (Rubin et al., 2000) of which RhoA (Ras homolog gene family member A), Rac1 (Ras-related C3 botulinum toxin substrate 1), and Cdc42 (Cell division cycle 42) are most commonly

associated with cytoskeletal organisation through interaction with a host of downstream effectors (Ridley, 2001; Tapon and Hall, 1997). Generally, RhoA reorganises pre-existing actin filaments to create contractile stress fibre structures. Rac1 and Cdc42 both promote actin polymerisation, with Rac activation leading to formation of peripheral actin-rich lamellipodia (Nobes and Hall, 1995; Raftopoulou and Hall, 2004).

### 1.4.1 Actin nucleation

The rate-limiting step in actin polymerisation is nucleation. Whilst an actin trimer can elongate, through monomer addition, the formation is exceedingly unfavourable at physiological G-actin concentrations (Sept and McCammon, 2001). Therefore, additional factors are required to facilitate nucleation. Formins mediate nucleation of new unbranched actin filaments, whilst the Arp2/3 complex mediates branching of pre-existing filaments (Goode and Eck, 2007).

Most formins share several conserved domains: formin homology domain 1 (FH1) and 2 (FH2), a diaphanous auto-regulatory domain (DAD), a diaphanous inhibitory domain (DID) and a GTPase binding site. Binding of RhoA to the GTPase binding site relieves the auto-inhibitory interaction of the C-terminal DAD and the N-terminal-DID (Li and Higgs, 2003; Nezami et al., 2006). Activation allows dimerization of the FH2 domain, producing a doughnut shaped structure that attaches to and stabilises the barbed end of actin filaments (Higgs, 2005). Formins act as 'leaky' cappers because they protect the end from inhibitory capping whilst allowing addition of new G-actin monomers (Kovar, 2006; Zigmond et al., 2003). Diaphanous is the primary formin involved in the formation of actin at the AJ (Homem and Peifer, 2008).

Actin branching is mediated by a complex made up of actin-related protein 2 and actin-related protein 3 (Arp2/3) (Mullins et al., 1998). The heptameric Arp2/3 complex initiates the nucleation of a new branch at $70^{o}$ to the mother filament and remains bound to the pointed end (Blanchoin et al., 2000). Arp2/3 activity is regulated by the activity of the Wiskott-Aldrich syndrome protein (WASp) family. This family consists of WASp, N-WASp and SCAR/WAVE (Pollitt and Insall,

2009). Interactions with Rho GTPases promote WASp activity, with Cdc42 activating WASp and N-WASp (Aspenstrom et al., 1996; Mullins, 2000; Rohatgi et al., 2000), whilst SCAR/WAVE is regulated by Rac signalling (Miki et al., 1998). In one model, membrane-bound Cdc42 activates N-WASp that in turn binds profilin-bound GTP-actin monomers and the Arp2/3 complex. The binding of Arp2/3 stimulates ATP hydrolysis. Hydrolysis induces a conformational change to form a stable structure that resembles a trimer of Arp2/Arp3/G-actin (Dayel and Mullins, 2004). This nucleus can then attach to a mother filament and promote branch elongation. Phosphate release from the complex allows the newly forming filament to disassociate from its membrane bound activator (Dayel et al., 2001).

## 1.5 Actin Polymerisation

Once trimers have formed they can rapidly elongate through the addition of ATP-G-actin monomers. Once bound, ATP-actin subunits hydrolyse to ADP, so that the majority of F-actin subunits are ADP-bound. ATP-actin is more stable than ADP-actin so hydrolysis promotes filament disassembly by inducing conformational changes that weaken the association between neighbouring monomers.

Filaments can elongate bi-directionally, but the association of new monomers predominantly occurs at the plus-end (barbed) *in vivo*. This is due to the difference between the critical monomer concentrations required for polymerisation at both ends. This can lead to treadmilling at intermediate soluble monomer concentrations, where the rate of monomer dissociation at the minus-end is equal to the rate of its association at the plus-end (Wegner, 1976). As a result under physiological conditions the kinetics of ATP-G-actin addition at the barbed end are 5-10x faster than compared with the pointed-end (Pollard and Mooseker, 1981).

Actin polymerisation is promoted and inhibited through a host of actin-binding and associating proteins. Cofilin is an inhibitor that catalyses the disassembly and severing of ADP-actin filaments (Andrianantoandro and Pollard, 2006). Upon dissociation, Cofilin-bound G-actin monomers are sequestered in an ADP-bound form preventing them from rebinding. Phosphorylation of Cofilin by LIM kinase proteins 1 and 2 releases the actin monomer for ATP-exchange in the cytoplasm

(Arber et al., 1998). This is reversed by the Slingshot phosphatase (Huang et al., 2006; Niwa et al., 2002; Soosairajah et al., 2005). Cyclase activated protein (CAP) can bind and sequester monomeric actin to prevent polymerisation (Baum et al., 2000). Profilin then stimulates the exchange of ADP for ATP thereby increasing the available pool of ATP-G-actin. Barbed-end loading is aided by formins as the FH1 domain recruits profilin-bound ATP-G-actin monomers (Paul and Pollard, 2008). Profilin is induced to disassociate from filaments by the phosphoinosotide PIP2 (Goldschmidt-Clermont et al., 1990; Lassing and Lindberg, 1985). Therefore, a close association of ATP-G-actin with the FH2-capped barbed-end can ensure steady filament growth.

## 1.6 Myosin II

Cross-linking actin creates bundles and networks that provide resistance to compressive forces of the plasma membrane (Janson et al., 1992). This is achieved through a number of proteins including Fascin, Fimbrin and α-actinin (Matsudaira, 1991). Non-muscle Myosin II is a molecular motor protein that can both cross-link and slide filaments to create tensile stress within an actin gel (Vicente-Manzanares et al., 2009). Myosin II has a hexamer structure consisting of two heavy chains (MHCs) (encoded by *zipper*), two regulatory light chains (MRLCs) (encoded by *spaghetti-squash*) and two essential light chains (Sellers, 2000). The N-terminal globular domains of the MHCs contain actin and ATP binding sites. ATP hydrolysis allows cyclic attachment to actin, movement along the filament (the 'power-stroke') and release. In this way each Myosin head can walk along a filament.

The Myosin C-terminal light chains are α-helical in structure. In its active form the tails mediate coiled-coil dimerization to form homo-dimers. Homo-dimers can then assemble to form bipolar microfilaments (Vicente-Manzanares et al., 2009). Bipolar crosslinking of Myo II microfilaments within parallel actin filaments facilitates bundling and the anti-parallel sliding of actin filaments past each other as Myosin heads walk in opposing directions. Links coupling the cytoskeleton to the cortex and adherens junction converts this sliding motion into cortical contractile force. In a tissue context, this can be used to drive rapid morphogenetic movements (Munjal

and Lecuit, 2014; Roper, 2015) such as germ band extension (GBE) (Bertet et al., 2004) and ventral furrow invagination (Martin et al., 2009).

## 1.7 Myosin II activation

In an inactive state, the individual hexamers fold to auto-inhibit F-actin binding and ATPase activity (Jung et al., 2008). Phosphorylation of serine 19 and threonine 18 on the RLCs is mediated by Rho-associated coiled-coil kinase (Rok) and myosin light-chain kinase (MLCK). This allows hexamers to adopt an open and active conformation to form minifilaments (Craig et al., 1983; Kojima et al., 1996; Matsumura, 2005). Rok is an effector molecule of Rho-GTPase, whereas MLCK is activated by calmodulin in response to increased intracellular calcium (Means et al., 1991; Van Lierop et al., 2002). Whilst MLCK is specific to MLC, Rok is also thought to phosphorylate many other substrates including LIM kinase, Par3 (Bazooka) and Myosin phosphatase (Kimura et al., 1996; Nakamura et al., 1995; Ohashi et al., 2000).

## 1.8 Myosin II inhibition

Non-muscle Myosin II phosphorylation is negatively regulated by Myosin phosphatase. This is made up of a type 1 protein phosphatase (PP1) catalytic subunit (38kD), of which there are four in *Drosophila*, a large ~130kD Myosin binding/targeting subunit (several MYPT isomers) and a smaller subunit of unknown function (M20) (Hartshorne, 1998; Vereshchagina et al., 2004). Sds22 is a non-catalytic subunit that binds all four PP1 subunits to negatively regulate Myo II and Moesin phosphorylation (Grusche et al., 2009). Myosin phosphatase activity is, itself, thought to be negatively regulated by Rok through phosphorylation of the Myosin binding subunit (Kimura et al., 1996).

## 1.9 Adherens junction turnover

In addition to their assembly and disassembly, adherens junctions can also be dynamically turned over. This is key for many morphogenetic processes. AJs are internalised by Clathrin-mediated and dynamin-dependent endocytosis (Baum and Georgiou, 2011). In *Drosophila* epithelia, E-cadherin can be clustered at the junction through the action of Myosin and the actin-nucleator Diaphanous (Levayer et al., 2011). Adaptor proteins, such as AP-2 then bind and target proteins for internalisation (Traub, 2003) with E-cadherin itself containing a binding site for AP-2 in its cytoplasmic tail (Miranda et al., 2001). Clathrin-coated pits bud from the membrane and are pinched off by dynamin-dependent scission to form endocytic vesicles (Cocucci et al., 2014). Pit initiation in the *Drosophila* germ band is driven by SCAR/WAVE regulated Arp2/3 actin branching (Levayer et al., 2011). In later stages of development, during pupal stages in the notum, Cdc42 is thought to act through WASp and Arp2/3 to drive endocytosis (Georgiou et al., 2008).

Internalised vesicles fuse and accumulate in Rab5 positive endosomes. Vesicles are either targeted for lysosomal degradation from the late endosome or are recycled back to the cell surface through Rab11 positive endosomes (Lock and Stow, 2005; Roeth et al., 2009). The fusion of re-trafficked vesicles to the membrane is dependent on the exocyst complex (Whyte and Munro, 2002). In the *Drosophila* notum the loss of the exocyst components *sec5*, *sec6* and *sec15* have been shown to prevent recycling, and cause the accumulation of E-cadherin in recycling endosomes (Langevin et al., 2005).

### 1.9.1 Force sensitivity across junctions

AJs have long been thought to be sites of mechanotransduction (Cavey et al., 2008; Gomez et al., 2011). It has been suggested that E-cadherin acts directly as a force-sensor (le Duc et al., 2010). In addition, evidence from epithelial colon cancer cells strongly supports a role for α-catenin as a mechanotransducer (Yonemura et al., 2010). Under low force, e.g., following addition of the Myo II inhibitor blebbistatin, α-catenin sits in a closed conformation. Applied tension then induces a

conformational change that reveals a vinculin-binding site within the α-catenin N-terminus. Vinculin is an actin-binding scaffold protein that upon recruitment to the adherens junction acts in a positive-feedback loop to bind actin, increase tension and thereby promote adherens junction stability and counterbalance the forces between cells.

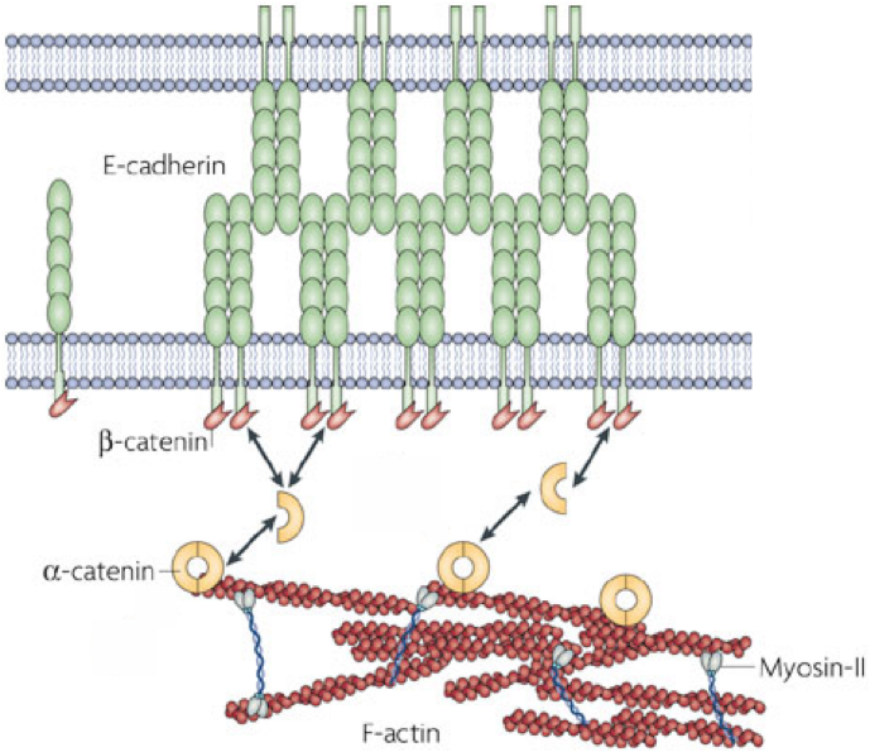


**Figure 1-2: The adherens junction and actomyosin cytoskeleton**

Homophilic extracellular domains of transmembrane E-cadherin (green) adhere neighbouring cells. ß-catenin (pink) binds the intracellular E-cadherin domain thereby linking the adherens junction to the actomyosin cytoskeleton (actin – red, Myosin II – dark blue & grey) via α-catenin (yellow).

Figure adapted from: (Lecuit and Lenne, 2007)

### 1.9.2 The role of Moesin: An alternative mechanism to link the actomyosin cytoskeleton to the apical cortex

As well as transiently linking through the adherens junction, the cortical actomyosin cytoskeleton is also connected to the apical cortex via Moesin, which acts as a bridge to bind actin to Phosphatidylinositol 4,5-biphosphate (PIP2) rich membranes and to transmembrane proteins (Ben-Aissa et al., 2012). *Drosophila* Moesin belongs to the ERM-protein family that has three mammalian members: Ezrin, Radixin and Moesin (Bretscher et al., 2002; Sato et al., 1992), but is the sole member present in *Drosophila melanogaster*.

At its C-terminus Moesin contains an F-actin binding domain. The N-terminus contains a conserved 300 amino acid FERM (4.1-Erzrin-Radixin-Moesin) domain that interacts with transmembrane proteins such as CD43, CD44 and several ICAMs (Niggli and Rossy, 2008). In its inactive state Moesin exists as a dormant auto-inhibited monomer. The C- and N-termini, which are linked through a central alpha-helical-rich region, bind together masking the membrane protein and F-actin binding sites (Gary and Bretscher, 1995). The activation of Moesin is regulated by the Ste20 family kinase Slik that phosphorylates the C-terminal threonine-558 (559 in *Drosophila*), by PIP2 (Ben-Aissa et al., 2012; Hao et al., 2009; Hipfner et al., 2004; Hughes and Fehon, 2006; Nakamura et al., 1995) and negatively, by the serine/threonine phosphatase PP1-87B and its non-catalytic subunit Sds22 (Grusche et al., 2009; Kunda et al., 2012; Roubinet et al., 2011).

## 1.10 Epithelial packing

D'Arcy Wentworth Thompson in the 1917 book 'On Growth and Form' proposed that nature acts in accordance with mechanical force requirements to create minimum energy structures that still result in highly complex biological forms (Thompson, 1917). Having described the junctions that allow individual cells to connect and form tissue structures I now explore how cell packing is regulated. Cell division and death change packing geometries by increasing and decreasing the number of cells within a given area. Intercalation and junction dynamics act to

mediate changes in cell shape in response to internal and external forces. Here I consider minimum energy packing geometries that embody idealised scenarios of tissue packing, before describing *in silico* models that are used to simulate *in vivo* tissue development, based upon a simple set of assumptions. I then discuss how changes in the model parameters can contribute to a range of packing geometries.

### 1.10.1 Hexagonal packing as minimum energy structures

In 2-dimensions, circles are the shape that can enclose the greatest given area for the smallest perimeter (Pearce, 1978). If circles were arranged in rows and columns, where 8 circles surround each individual, this would result in square packing and a packing density of 78.5%. The densest packing of circles within a single plane requires hexagonal packing, so that each circle is surrounded by six others, and covers 90.7% of the area (Chang and Wang, 2010).

This scenario however results in spaces between each circle. Epithelial integrity requires that the whole surface be covered without any holes, whilst also being economic with the partitioning so that cells are a maximum size for a given amount of wall material. Three regular shapes can achieve tessellation: the square, equilateral triangle and the hexagon. Of the three, the regular hexagon has the minimum perimeter for a given area. Many regular hexagonally packed structures exist in nature. Examples include the *Drosophila* epithelial wing disc where regular packing uniformly positions non-sensory hairs that may aid air flow over the wing during flight (Classen et al., 2005; Wootton, 1992); hexagonal packing of fibre cells in the eye lens, that may minimise light scattering (Tardieu, 1988); graphene that is made up of an atomic-scale hexagonal lattice of carbon atoms (Geim and Novoselov, 2007; Novoselov et al., 2004) and honeycombs, which allow bees to store the most amount of honey for the least amount of beeswax (Tóth, 1964).

### 1.10.2 Models of cell movement within an epithelium

However cell packing isn't constant and fixed. The ability to remodel cell-cell contacts allows individual cells to move within the epithelial plane whilst maintaining tissue integrity. For cells to reach regular minimum energy

conformations they must be able to move away from disordered states. Here I describe alternate models for cell intercalation that could facilitate such movement.

In late 1980's the mechanisms by which tightly adhered cells could exchange neighbours was a mystery. The cortical tractor model was first proposed in 1986 by Jacobsen et al. and described in a 1988 review by Dianne Fristrom (Fristrom, 1988; Jacobson et al., 1986). This is a basal-to apical model (Fig. 1.3). Short basal protrusions enable cells to move on a substrate and thereby make contact with non-neighbouring cells. Such basal contacts would then be extended apically leading to a neighbour exchange event.

As an alternate model, the Fristrom review proposed that localised contraction at the adherens junction could also lead to apical neighbour exchange, which is propagated basally. Studies of germ band elongation observed apically driven neighbour exchanges, known as T1 transition events (Irvine and Wieschaus, 1994). This was found to occur in three steps as a cell-cell contact, that connects two cells, shrinks to form a shared vertex between four cells. This vertex is then resolved through the formation of a new junction between the initially non-adjacent cells (Fig. 1.4A).

In a T2 process, cells undergo neighbour exchange events as a single cell is induced to leave the epithelium without compromising tissue integrity (Fig. 1.4B). If all the cell-cell contacts of an individual shrink simultaneously this leads to a loss of apical area until all that remains is a single vertex point at the apical surface (Guillot and Lecuit, 2013b). Alternatively junctions are lost one-by-one as a cell leaves the tissue (Marinari et al., 2012).

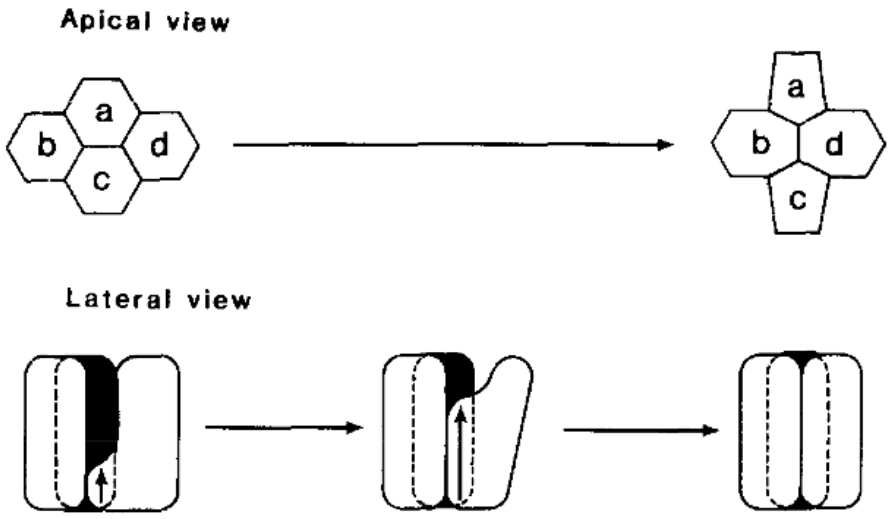


**Figure 1-3: Basal to apical model of neighbour exchange**

**Apical view** of a neighbour exchange event whereby cells **b** and **d** form a new cell-cell contact. **Lateral view** of a basal-to-apical exchange. A basal protrusion from cell **d** makes contact with **b**, prior to apical extension of the contact.

Figure from: (Fristrom, 1988)

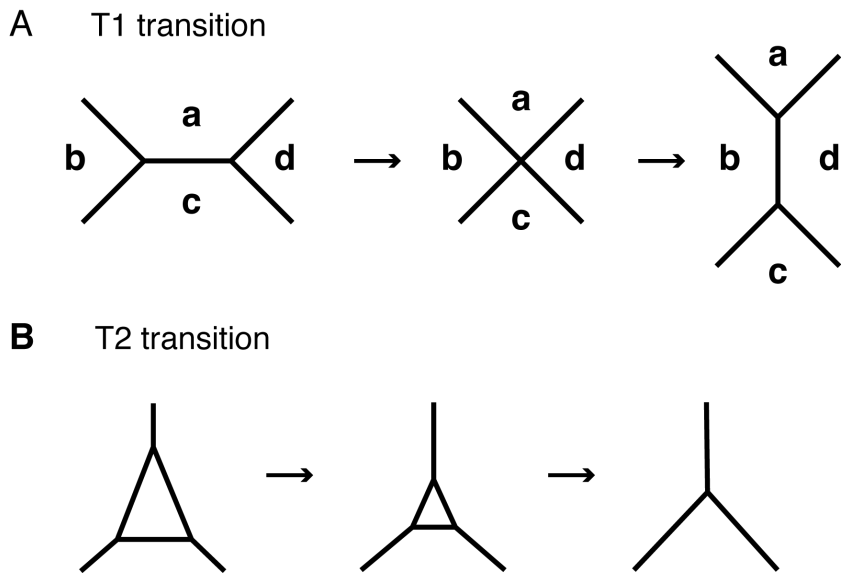


**Figure 1-4: Apical to basal neighbour exchange models**

**A**) Schematic of a neighbour exchange event, a T1 transition, involving four cells. The junction between cells **a** and **c** shrinks to a single vertex, and expands out to form a new cell-cell contact between **b** and **d**. **B**) Schematic of a cell leaving the tissue via a T2 process. All the junctions of a cell shrink simultaneously, causing a loss of apical area and extrusion.

### 1.10.3 Defined polygon distributions of proliferating epithelia

Although tissues can exist in theory as perfectly regular hexagonal minimal energy structures, in reality epithelial tissues often exhibit irregular polygon distributions due to the influence of cell division (Lewis, 1926, 1928). To study the likely input of divisions Gibson et al. identified a simple set of assumptions that could be used to build a discrete-Markov model of division (Gibson et al., 2006). This can be used to study the impact of a stochastic sequence of events, in which the probability for each event only depends on the state immediately preceding it. The assumptions were 1) that cells have a minimum of four sides; 2) cells cannot rearrange their neighbours between waves of division by undergoing cell intercalation events; 3) daughter cells retain a cell-cell contact after division; 4) cells divide asynchronously during each round of division; 5) new junctions form to intersect existing junctions rather than dissecting the mother cell at vertices; 6) junctions are distributed at random around the mitotic cell. Irrespective of the starting polygon distributions, in this model epithelia reach a fixed equilibrium distribution comprising 28.9% pentagons, 46.4% hexagons, 20.9% heptagons, 3.6% octagons and 0.3% nonagons within eight generations. When real tissues were examined the deviation from this distribution was shown to be within a few per cent for each polygon class. This work shows how divisions can lead to a distribution of polygon classes that appear irregular but are not random. While the same result has been achieved using a wide variety of simpler and more realistic assumptions in more recent work, this basic idea stands (Gibson et al., 2011; Patel et al., 2009).

### 1.10.4 2D vertex model of epithelial packing

The proliferating wing epithelium reaches polygon distributions similar to those given by the Gibson Markov-model. However, shortly before hair formation the wing disc cells assume a regularly packed hexagonal configuration through cell intercalation and cell death (Classen et al., 2005). This prompted Farhadifar and colleagues to develop a 2D vertex model to simulate *in vivo* cell packing geometries based upon the dynamic movement of vertices in response to mechanical force (Farhadifar et al., 2007). The cell properties considered were preferred area

elasticity, cortical contractility and differential line tensions that reflect the combined effects of cell-cell adhesion and actomyosin contractility. The resting 2D network will evolve over time through neighbour exchange events and T2 transitions but satisfy mechanical force balances at each step. The simulations converge on two steady states separated by a phase transition. These states depend upon line tension, the forces that result from adhesive cell-cell interactions at specific boundaries and the contractile action of the underlying actomyosin cytoskeleton between vertices; and cortical contractility, which includes the contractile action of actomyosin around the full cell perimeter. With high contractility and high line tension, cells exist as a regularly packed hexagonal array, where work is required to alter cell packing. In a soft network, with low contractility and low line tension, cell geometries are irregular but the system has a large number of states with similar energy. This is a fluid system in which individual cells can move freely through the tissue.

In the 2D vertex model of *Drosophila* notum development (described in this chapter) Mehonic et al. introduced a stochastic noise parameter allowing the model to follow alternative relaxation pathways (Marinari et al., 2012). Increasing noise aided tissue order by facilitating neighbour exchange events enabling the system to reach equilibrium state without cell division.

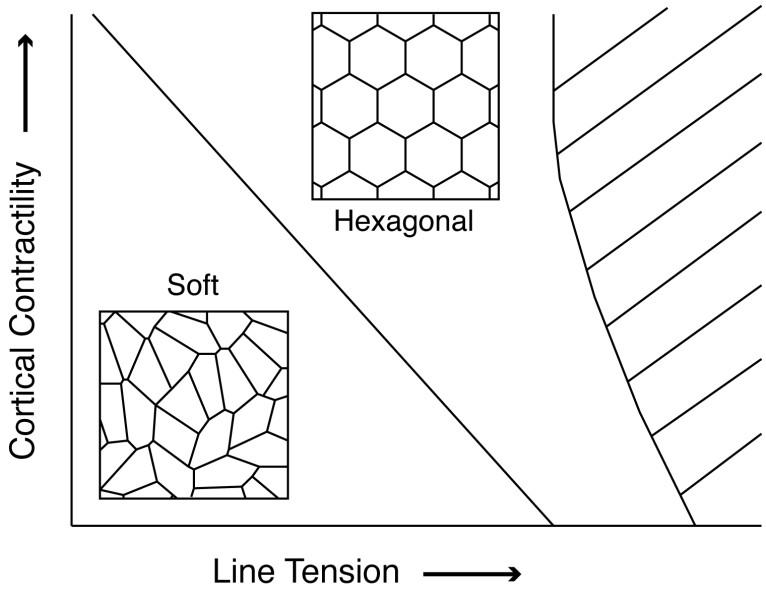


**Figure 1-5: Ground state diagram of the 2D vertex model**

The diagram is a representation of the two main ground states (or relaxed network configurations) when the tissue is stable and stationary under set contractile tensions. The X-axis consists of contractility between vertices and adhesive forces from cell-cell interactions. The Y-axis describes actomyosin action on the whole cell perimeter. The solid regular hexagonal network exists under high contractility and line tension. The soft network is irregular, though cells share the same preferred area, and exists with low contractility.

Simplified diagram adapted from: (Farhadifar et al., 2007).

## 1.11 Medial Myosin II driving tissue morphogenesis

A major focus of this thesis will be to investigate cell intercalation events and the requirement of junctional forces for these processes. Polarised intercalation through junctional actomyosin contractility can drive morphogenetic events including germ band elongation, which I will discuss in detail. However differential subcellular regulation of Myo II localisation can also be utilised to remodel tissues. In the next sections I discuss two examples, ventral furrow invagination and dorsal closure, that show how a cortical Myo-II pool produces contractility that acts on the junctions to change tissue architecture.

### 1.11.1 Ventral furrow invagination

During gastrulation, the formation of a ventral furrow internalises the presumptive mesoderm (Sweeton et al., 1991). Intracellular actomyosin contractile forces are transmitted through apical AJ contacts to drive tissue bending (Martin et al., 2009). In a 'ratchet-model' of apical constriction, Myosin II contracts a medioapical F-actin mesh. In this view of the process, medial constrictions, induced by the transcription factor *snail*, occur asynchronously in neighbouring cells. Actomyosin pulls on the AJ during contraction. The subsequent reduction in apical area is stabilised between pulses through expression of *twist,* allowing for incremental loss of apical area with each pulse and net constriction of the tissue (Martin et al., 2009; Mason et al., 2013).

Apical constriction in the ventral furrow is regulated by the Folded gastrulation (Fog) signalling pathway (Manning and Rogers, 2014). Fog is a large secreted protein that acts as an autocrine factor and is a ligand for the transmembrane GPCR Mesoderm invaginating signal transducer (Mist) (Costa et al., 1994; Manning et al., 2013). In its unbound state, Mist interacts with GDP-bound Concertina (Cta) (Manning et al., 2013; Parks and Wieschaus, 1991). Fog binding to Mist stimulates Cta to exchange GTP for GDP. This causes Cta to dissociate from its binding partners Gβ and Gγ and allows for its binding to RhoGEF2 (Manning and Rogers, 2014). In turn, RhoGEF2 then acts through Rho1, to activate the downstream effector Rok, which phosphorylates Myosin II to drive apical constriction (Dawes-Hoang et al., 2005;

Hacker and Perrimon, 1998). During gastrulation, the transcription factor, Twist, activates the transcription of *fog*, and also *T48*, a transmembrane protein that acts by apically localising RhoGEF2 (Kolsch et al., 2007). Meanwhile, Snail is known to drive expression of *mist* (Manning et al., 2013).

### 1.11.2 Dorsal closure

Dorsal closure is a morphogenetic process that occurs halfway through *Drosophila* embryogenesis. Germ band retraction leaves a discontinuity in the dorsal epidermis, which is covered, continuously with the epidermis, by the extraembryonic amnioscerosa, a squamous epithelium (Martinez-Arias, 1993). Actomyosin contractility acts in two separate ways to pull the lateral epidermal sheets together to form a continuous epidermal sheet and to eliminate the amnioserosa cells. Within the epidermal cells, a supracellular actin cable forms at the dorsal-most leading edge and acts with a 'purse-string' mechanism. This structure is composed of intracellular contractile bars held together by strong intercellular adhesions (Hutson et al., 2003; Kiehart et al., 2000; Young et al., 1993). Filopodia of leading edge cells interact with opposing extensions to actively zipper the sheets together forming a temporary seam along the dorsal midline that matures to produce a continuous epithelium (Jacinto et al., 2000). The supracellular cable also acts to prevent excess formation of filopodia and lamellipodia at the leading edge to maintain a taut contact for efficient zippering (Jacinto et al., 2002). The major force contribution to dorsal closure is provided by intracellular pulsatile actomyosin contractility within the amnioserosa cells. Apicomedial force is supplied in a ratchet-like manner, as seen for ventral furrow invagination, to pull on and displace the lateral epidermis (Solon et al., 2009).

### 1.11.3 Germ band extension

Having discussed how medioapical actomyosin contractility and cables can drive distinct morphogenetic processes, I now move on to junctional forces. When cell rearrangements are oriented in an epithelium they can result in tissue elongation. One good example of this is germ band extension (GBE) (Irvine and Wieschaus, 1994). The *Drosophila* germ band is a monolayer epithelium that gives rise to the

segmented trunk regions (thorax and abdomen) of the adult fly (Campos-Ortega and Hartenstein, 1985). In the early stages of embryogenesis following gastrulation, the epithelium shortens along its dorsal-ventral (DV) axis and more than doubles (2.5x) in length along its anterior-posterior (AP) axis (Irvine and Wieschaus, 1994). Due to external physical constraints, the posterior end of the germ band finishes up on the dorsal side of the embryo as a result of this elongation (Sonnenblick, 1950). The extension of the germ band occurs in two phases. Most of the extension occurs within the first 25 mins. This is followed by a slower phase of extension, driven by cell intercalation, that occurs over 70 mins (Hartenstein and Campos-Ortega, 1985). In addition, cells at the posterior of the tissue, undergo oriented divisions to aid full elongation (da Silva and Vincent, 2007). Cell shape changes contribute to the fast phase, which I will discuss further.

Most of the literature describes tissue movements within the anterior germ band. This is because the cells in this region stay within the same field of view throughout imaging. In this part of the tissue, cell intercalation drives tissue extension (Irvine and Wieschaus, 1994). This process is irreversible (Bertet et al., 2004) and occurs as follows: first, cells shrink their DV oriented junctions (which takes ~7.5 mins for single DV-oriented interfaces and ~10.8 mins for interfaces that form rosettes) (Blankenship et al., 2006), while junctions at $60^{o}$/ $120^{o}$ remain stable in both orientation and length (Bertet et al., 2004). This leads to the formation of 4-way and high-order vertices that result from coordinated junction loss and remain for less than 1 minute (Bertet et al., 2004; Blankenship et al., 2006). Finally, new AP oriented cell-cell contacts are generated leading to the resolution of these vertices, on timescales consistent with junction loss (Blankenship et al., 2006). Importantly, these neighbour exchange events do not order the tissue but create irregular tissue packing.

The planar polarised movements, associated with GBE, are regulated by the prior patterning of the embryo along the AP axis by the three maternally provided patterning systems, anterior, posterior and terminal (Nusslein-Volhard et al., 1987; Schupbach and Wieschaus, 1986). A host of mutations within the pair-rule genes, which are expressed in transverse stripes along the AP-axis, can cause a lack of germ band extension. The greatest reduction in extension was found for mutants of the

transcription factors, Even-skipped (Eve) and Runt, with uniform over-expression of either factor also shown to cause impairment of elongation (Blankenship et al., 2006; Butler et al., 2009; Irvine and Wieschaus, 1994; St Johnston and Nusslein-Volhard, 1992; Zallen and Wieschaus, 2004). Eve/Runt provides positional cues for patterning of downstream effectors, including the Toll family receptors, Toll-2, Toll-6 and Toll-8, which are expressed in overlapping stripes and are required for normal germ band elongation (Pare et al., 2014). However, how transcription factor and Toll receptor signalling is converted to mechanical junction movement is currently unknown (Pare et al., 2014).

### 1.11.4 GBE: Role of non-muscle Myosin II

Polarised GBE is driven by actomyosin-based contractility coupled with turnover of adherens junction material. Localisation of contractile machinery follows the expression pattern of upstream transcription factors and their downstream effectors (Pare et al., 2014; Zallen and Wieschaus, 2004). Non-muscle Myosin II is enriched along DV-oriented disassembling junctions (Bertet et al., 2004; Kasza et al., 2014; Zallen and Wieschaus, 2004). Often actomyosin cables extend across several cells to simultaneously shrink multiple junctions during rosette formation (Blankenship et al., 2006). Myo II is excluded from AJs by the apical polarity marker Bazooka (*Drosophila* homolog of Par3), which localises to AP oriented junctions (Zallen and Wieschaus, 2004). A loss of Baz from these junctions causes the polarised distribution of Myo II to be lost. Polarised distributions of Baz are maintained by Rho kinase (Rok). Rok is the activating kinase of MRLC and localises with Myo II to DV oriented contacts. However Rok also phosphorylates Baz thereby inhibiting the association of Bazooka's C-terminal domain with the cortex (Simoes Sde et al., 2010).

Rok is recruited to the AJ by Rho GTPase (Simoes Sde et al., 2014). Active Rho binds to Rok directly inducing a conformational change that promotes substrate phosphorylation (Riento and Ridley, 2003). Rho also planar polarises the actin-binding protein Shroom, further enhancing the planar-polarised distribution of Rok and Myo II, thereby increasing contractility (Simoes Sde et al., 2014).

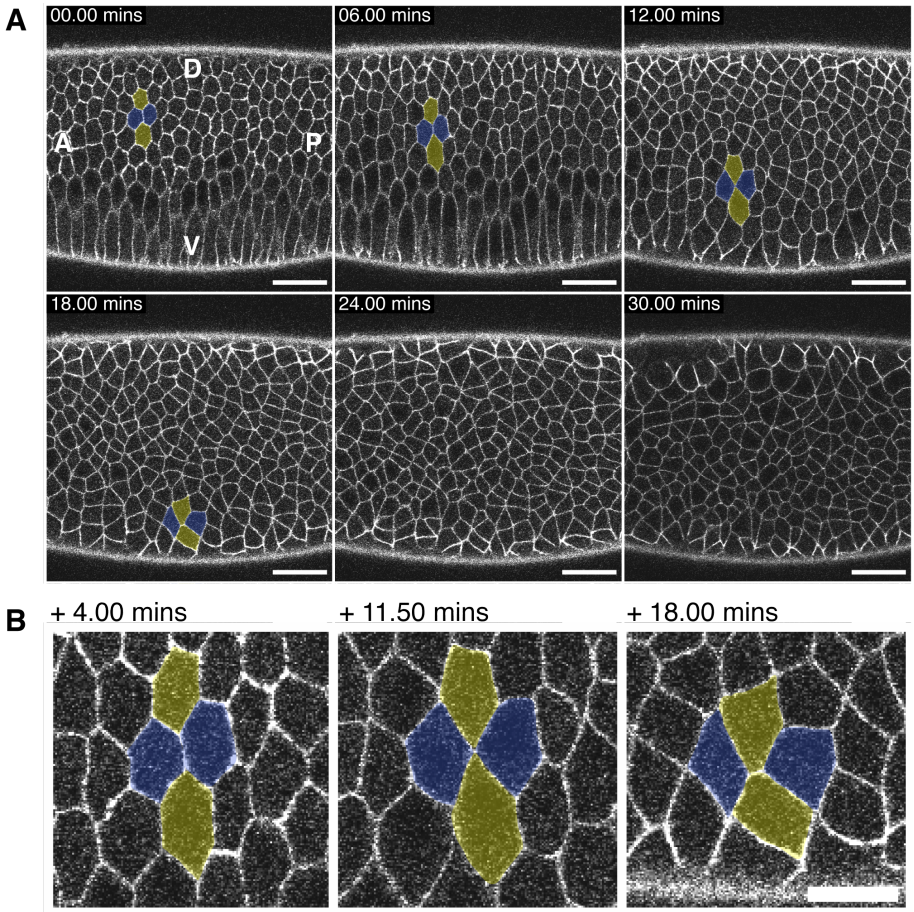


**Figure 1-6: Cell intercalation driving rapid morphogenesis**

(**A**) Lateral view of germ band elongation. An embryo labelled with DE-cadherin-GFP. D, dorsal; V, ventral; A, anterior; P, posterior. Scale bar = 20µm. (**B**) Representative T1 transition, as coloured in A. Scale bar = 10µm.

*; DE-cad-GFP(KI) ;;*

(Imaged with Olympus FV1000 confocal)

### 1.11.5 GBE: Regulation of Myosin II localisation

In 2010 Rauzi *et al.*, proposed that actomyosin does not directly act on junctions to mechanically shrink them (Rauzi et al., 2010). Instead they propose that forces are created through polarised flows of actomyosin to DV oriented junctions. Exhibiting pulsatile behaviour, actomyosin coalesces in medial pools that flow to the junction, consequently increasing junctional Myo II intensity. This contractile flow of medial Myo II causes junctions to shrink, whilst junctional Myo II stabilises the contact length. This is analogous to the phases of contraction and stabilisation seen in ventral furrow formation.

The same group also suggested that actomyosin is prevented from forming medial webs in the ectoderm through JAK/STAT signalling (Bertet et al., 2009). Removal of the JAK/STAT ligand *unpaired* leads to a loss of WASP repression. Constitutive WASP activation, downstream of Cdc42, causes the aberrant formation of an apicomedial branched actin network, apical constriction and impaired cell intercalation. This result mirrors ventral furrow invagination, where apical Myo II is recruited by selective expression of Twist and Snail in the ventral mesoderm. However in this tissue they propose that its medial localisation is actively repressed in the ectoderm by JAK/STAT signalling.

### 1.11.6 GBE: Role of adherens junction turnover

In the developing germ band, anisotropic actomyosin flows are thought to be directed by asymmetries in AJ components, with DE-cadherin levels reduced at shrinking junctions (Rauzi et al., 2010). DE-cadherin is stabilised at the AJ through its association with Armadillo (ß-catenin). Abl tyrosine kinase is expressed in a planar polarised distribution and phosphorylates Armadillo-T667 on DV oriented junctions (Tamada et al., 2012). This promotes turnover of Armadillo and induces junction instability. Furthermore, endocytosis is required to actively remove junctional material (Levayer et al., 2011). DE-cadherin is clustered at the plasma membrane with Clathrin and AP2. Clustering is mediated by F-actin polymerisation through the formin Diaphanous and the action of Myo II, both of which are

downstream of Rho. Branched actin mediates vesicular scission, which they suggest is nucleated by the Arp2/3 complex downstream of the WAVE/Scar complex (Georgiou et al., 2008). Inhibition of Clathrin-mediated endocytosis increases junctional levels of DE-cadherin and blocks cell intercalation (Levayer et al., 2011).

### 1.11.7 GBE: Resolution of vertices and extending junctions

Most studies of GBE focus on the mechanisms that drive convergence rather than the resolution of vertices and the extension of new junctions. Previously I described how junction loss occurs on similar time scales to extension. However the mechanisms guiding the two processes appear to be different. Blankenship et al. described the morphological hallmarks of extension (Blankenship et al., 2006). Actomyosin is enriched at vertices after convergence. During vertex resolution, F-actin is also found enriched at the nascent AP-oriented junction, in this case, in the absence of Myo II. The AJ markers, DE-cadherin and Armadillo are recruited at the onset of extension. Bazooka is initially missing, but is recruited 2-3 mins later, as actin intensity drops to a basal level and junction length is stabilised (Blankenship et al., 2006).

In the fly pupal wing disc, junction extension during cell intercalation is regulated by the tumour suppressor Phosphatase and tensin homolog on chromosome 10 (PTEN) (Bardet et al., 2013). PTEN is a lipid phosphatase that dephosphorylates phosphatidylinositol trisphosphate (PIP3) to phosphatidylinositol bisphosphate (PIP2). Newly formed junctions are enriched with Myo II, Rok and PIP3. The exchange of PIP3 to PIP2 decreases junctional Myo II levels to facilitate junction lengthening. This work showed that, at least in the wing disc, junction extension involves specific regulation and is not a simple process of passive relaxation in response to stretch.

Two roles have been suggested for PTEN in junction expansion. Either phosphoinositide 3-kinase (PI3K) dependent increases in PIP3 activity are antagonised by homogenous PTEN activity, or Rok regulates the localised activity of PTEN (Li et al., 2005; Perez et al., 2008; Rivard, 2009). This could occur as Rok, which is localised on newly formed junctions, phosphorylates PTEN. This initiates a

negative feedback loop, as PIP3 is converted to PIP2, thereby removing Myo II from the junction and facilitating junction expansion.

How differential levels of PIP3 and PIP2 directly regulate Myosin II activity is less clear. PIP3 is the catalytic product of PI3K and is involved in a number of signalling pathways including cell growth, cytoskeletal rearrangements and survival. PIP3 binds the pleckstrin homology (PH) domains of GEFs to relieve inhibitory conformations and allow catalysis. Increased activity of GEFs mediated by PIP3 promotes Rac-induced lamellipodia formation (via Arp2/3) (Dang et al., 2013; Johnson et al., 2015; Qin et al., 2009). In contrast, PIP2 promote formin-based actin filament formation by dissociating G-actin monomers from the sequestering protein Profilin (Goldschmidt-Clermont et al., 1990). Binding of PIP2 to actin cross-linkers such as α-actinin promotes actin bundling (Fukami et al., 1992).

### 1.11.8 GBE: Role of external forces

Cell intercalation and apical actomyosin forces do not drive germ band extension alone (Lye and Sanson, 2011). I have already described the contribution of oriented cell divisions within the posterior half of the germ band. In the anterior half, passive changes in cell shape contribute alongside cell intercalation to full extension (Butler et al., 2009). When AP patterning is perturbed the germ band does not extend fully. However, GBE is biphasic and, during the fast phase, these mutant tissues still extended to normal length. The loss of cell intercalation was countered by increased changes in cell shape. *Twist* mutants caused invagination to fail leading to a decrease in the rate of cell shape change and cell intercalation levels during the GBE fast phase. Therefore, polarised cell intercalation is thought to be acting to relieve externally imposed stress by maintaining more isotropic cell shapes. Thus, external forces may drive elongation of AP oriented junctions in wild-type embryos.

## 1.12 External forces contributing to cell intercalation

Convergent extension in the dorsal mesoderm of chordates is another morphogenetic process where external forces have been shown to contribute to tissue elongation. Explant studies of the dorsal marginal zone of the *Xenopus* gastrula showed that the

mesoderm elongates through a process of cell intercalation termed mediolateral intercalation behaviour (MIB) (Shih and Keller, 1992). Clusters of cells take on a polarised behaviour and project actin-rich protrusions along the axis of convergence. The tissue elongates as traction forces pull cells together along the mediolateral axis and push them apart along the AP axis. This process differs from GBE, as a single force-generator is able to provide simultaneous convergence and extension. *In vivo* live imaging of cell intercalation within the zebrafish dorsal mesoderm revealed that the notochord-forming domain converges and extends at rates consistent with models of MIB. The model predicts that the process would fail in the absence of convergent extension. To test this assumption a *no tail* (*ntl* – ortholog of mouse *Brachyury*) mutant was used to block convergence in the notochord domain. However, in the absence of convergence, efficient extension was observed. This reveals the presence of an unknown external force that acts redundantly to contribute to elongation. This force was hypothesised to come from concurrent blastoderm epiboly.

Another example of external force driving cell intercalation is during *Drosophila* tracheal development where dorsal branches develop from epithelial sacs (Caussinus et al., 2008; Neumann and Affolter, 2006). Branching is initiated by 1-2 tip cells that migrate towards localised sources of the secreted ligand *Branchless* (Sutherland et al., 1996). Tube structures are formed as stalk cells retain contact with and follow the migrating tip cells. This process occurs in the absence of cell proliferation. Intercalation is required to organise cells in tubes, so that cells that lie initially side-by-side stalk take on an end-to-end conformation, thereby elongating the tubes. This process is thought to be actomyosin independent (Samakovlis et al., 1996). It passively relieves the mechanical load and tensile stress placed upon the branches by the pulling force of tip cell migration (Caussinus et al., 2008). This type of intercalation can be recapitulated *in vitro* with ventral ectoderm explants from early gastrula *Xenopus laevis* embryos (Beloussov et al., 2000). By applying artificial stretch to the agarose substrate on which the cells were placed oriented cell intercalation events were observed along the stretch axis. These studies suggest that tissues can respond to an imposed stretch in order to relieve tension and restore resting stress levels.

## 1.13 Notum development

The model system used in this thesis to explore epithelial junction dynamics is the *Drosophila melanonogaster* pupal notum. This goes on to form the adult dorsal thorax. The ease of live imaging, availability of notum specific Gal4 drivers and access to a library of UAS-RNAi knockdowns make the notum ideal for investigating the regulation and mechanics of epithelial junction dynamics. Here I describe the formation of the pre-pupal tissue and the subsequent stages through pupal development.

### 1.13.1 Notum Development: Dorsal thorax closure and pre-pupal stages

The dorsal thorax (the notum) forms as a single continuous epithelium from the fusion of the dorsal sides of the two wing imaginal discs (Martin-Blanco et al., 2000). During metamorphosis this fused tissue covers and takes the place of the larval epidermis that is later histolysed (Zeitlinger and Bohmann, 1999).

Metamorphosis starts at the development of a white prepupa. Staged as 0 h after puparium formation (h AP), the third instar larva stops moving, shortens in length and forms anteriorly located spiracles. The larval cuticle transforms into the pupal case that tans and hardens through time. The larval epidermis remains attached to the larval cuticle / pupal case up to 2-3 h AP (Ashburner, 1989). Its detachment creates space for the expansion and migration of the left and right imaginal discs across the larval epidermal surface before they meet and fuse (Fristrom and Fristrom, 1993). Between 3 and 7 h AP the anterior half of the pupal cuticle is secreted from the imaginal epithelium (Fristrom and Liebrich, 1986). Head eversion at 11-12 h AP signifies the end of the pre-pupal stages and the onset of a true pupal state.

Fusion of the two wing imaginal discs takes place at 7 h AP (Usui and Simpson, 2000). Migration across the larval epidermis is driven by the establishment at the leading edge of long actin-rich filopodia that pull the epithelial sheets towards the midline (Martin-Blanco et al., 2000). Depolymerisation of actin with Cytochalasin B inhibits fusion (Mandaron and Sengel, 1973). Decapentaplegic (Dpp) signalling regulates cytoskeleton dynamics along the leading edge, whilst Jun-N-terminal

kinase (JNK) signalling regulates adhesion between imaginal and larval epidermal cells. A loss of JNK causes the detachment and death of the larval cells leading to a loss of integrity and discontinuities within the imaginal epithelium (Martin-Blanco et al., 2000; Zeitlinger and Bohmann, 1999).

### 1.13.2 Notum Development: Pupal stages, from 12 to 30 h AP

The pupal case can be removed from 11.5 - 12 h AP and the pupa set-up for live imaging (see Methods 2.5). When labelled with DE-cadherin-GFP, maximum projections of the tissue can be made to visualise the morphogenetic landmarks of the notum at set developmental stages (Fig. 1.3). Projections of the notum at 1µm Z-slices can be found in the Appendix (9.1) and show the curvature of the tissue at each time point.

At 12 h AP, two dorsocentral macrochaetes sit symmetrically on either side of the midline (Fig. 1.3A). At this stage the midline region is 2-3 cells in width and runs anterior to posterior (AP) across the centre of the notum. Between 13.5 and 17 h AP is a peak wave of division with all cells across the notum dividing at least once (Fig. 1.3B). Cells within the posteriorly located scutellum will divide twice (Bosveld et al., 2012). Division occurs concurrently with midline basal cell delamination (Marinari et al., 2012) and is mostly finished within the dorsocentral scutellum by 20 h AP (Fig. 1.3C). A subset of cells, within the tissue, differentiate to form sensory organ precursors with their patterned spacing mediated by notch-delta signalling (Cohen et al., 2010; Renaud and Simpson, 2002). Here I explain each of these developmental processes in more detail.

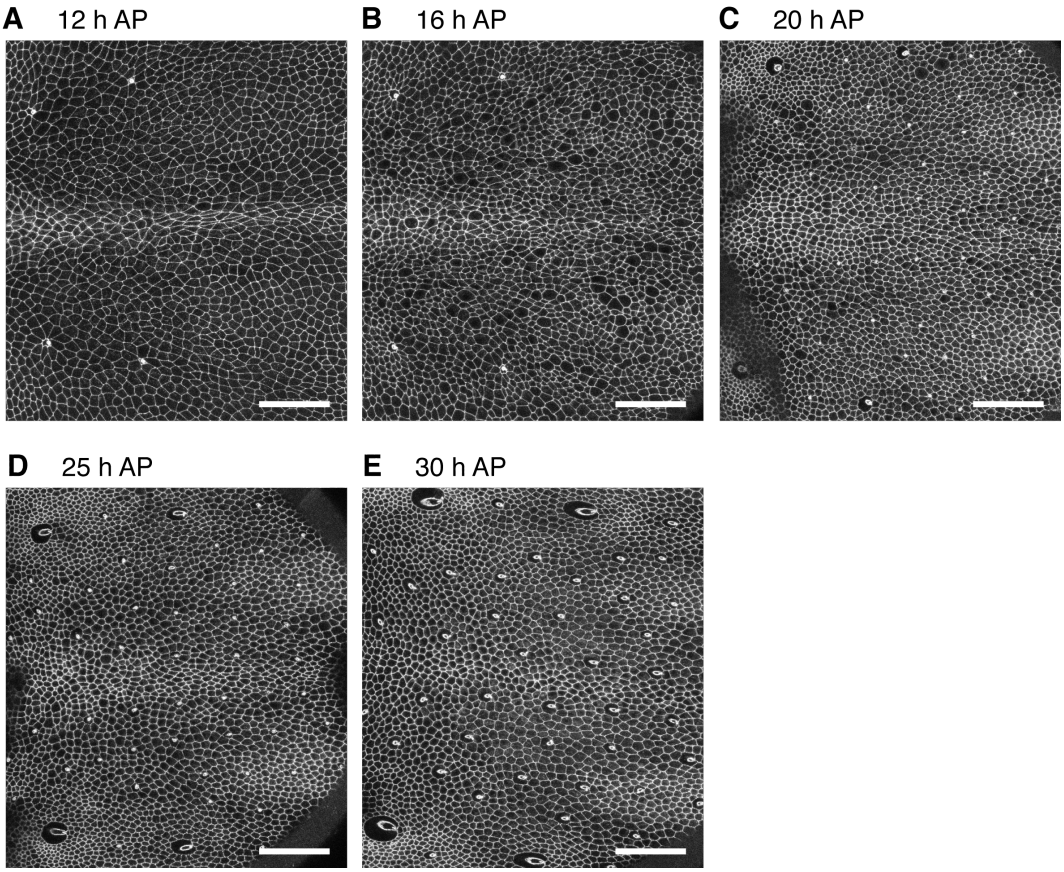


**Figure 1-7: Stages of Notum Development**

Maximum projection images of the notum at 12 (**A**), 16 (**B**), 20 (**C**), 25 (**D**) and 30 h AP (**E**). Posterior (left) to anterior (right), with the midline in the centre of each image. Scale bar = 50µm.

*; DE-cad-GFP(KI) ;;*

(Leica SPE2, Larval development at 25$^{o}$C)

### 1.13.3 Notum development: Bristle development and patterning

The mechanosensory bristles of the adult dorsal thorax develop from single neural precursors (pI) that differentiate within the notum epithelium (Hartenstein and Posakony, 1989). The exact number of microchaetae that form is not pre-determined as any of the epithelial cells can differentiate to a neural fate, and total numbers are not exact between genetically identical animals (Usui and Kimura, 1993; Wigglesworth, 1940). pI cells divide asymmetrically from 16 h AP to produce two secondary precursor cells: pIIa and pIIb. pIIa cells divide further to produce a socket and shaft cell (Gho et al., 1999). In the pI cell, a negative regulator of Notch signalling, Numb, forms an asymmetric cortical crescent, involving the adapter protein Partner of numb (Pon), that is inherited into the pIIb daughter driving neural expression (Gho and Schweisguth, 1998; Guo et al., 1996; Rhyu et al., 1994). The pIIb cell divides to form a glial cell that undergoes apoptosis and a pIIIb cell (Fichelson and Gho, 2003; Gho et al., 1999). Division of the pIIIb gives rise to a neurone and sheath cell (Bellaiche and Schweisguth, 2001).

In the dorsocentral region of the notum, five rows of microchaetae form either side of the midline (Simpson et al., 1999; Usui and Kimura, 1993). Notch-delta signalling controls the spacing of cells (Hartenstein and Posakony, 1990; Heitzler and Simpson, 1991; Parks and Muskavitch, 1993). Expression patterns are set between 8 and 16 h AP, with few cells taking on a neural fate after 18 h and only in larger regions of non-neural tissue (Usui and Kimura, 1993; Wigglesworth, 1940). Patterning does not follow conventional Notch-Delta signalling, as Delta positive neural cells are spaced 4-5 cells apart (Renaud and Simpson, 2002; Simpson et al., 1999). The membrane-tethered ligand Delta interacts with Notch receptors on neighbouring cells, leading to intracellular Notch cleavage in those neighbours inhibiting Delta and pro-neural gene expression. Through lateral inhibition, Notch-positive epithelial cells surround Delta-expressing neural precursors. Dynamic actin-based basal filopodia allow signalling of Delta-positive cells beyond first neighbours (Cohen et al., 2010).

### 1.13.4 Notum Development: Mechanical control of junction movement in the scutellum

Between 17 and 22 h AP polarised morphogenetic movements drive elongation of the medial scutellum, located at the posterior end of the notum (Bosveld et al., 2012). The movement is governed by the Fat/ Dachous (Ds)/ Four-jointed (Fj) planar cell polarity (PCP) pathway. *Fat* and *ds* encode proto-cadherins that can bind as heterodimeric bridges enabling the propagation of polarity information (Clark et al., 1995; Mahoney et al., 1991). Proto-cadherins differ from classical cadherins in that they have longer extra-cellular domains, and lack intracellular cytoskeletal attachments (Frank and Kemler, 2002; Sano et al., 1993). Phosphorylation of Ds by the Fj kinase reduces the affinity of Ds for Fat (Brittle et al., 2010). It should be noted that Fj can also phosphorylate Fat, though can act on both Fat and Ds independently (Brittle et al., 2010; Simon et al., 2010). In the scutellum, Fat and Ds are expressed in opposing gradients to form a V-shaped domain. Fat signalling has previously been described to negatively regulate the junctional localisation of Dachs, an atypical Myosin (Mao et al., 2006). In the scutellum Dachs was shown to planar polarise within the V-shaped domain, where the opposing gradients of Fat and Ds meet. Junctions enriched with Dachs exhibited higher line tension, than those without, thereby promoting local contractions (Bosveld et al., 2012). These data suggest that the anisotropic distributions of junction tension generated by PCP signalling are sufficient to mechanically drive tissue deformation through cell rearrangements in the notum.

### 1.13.5 Notum development: Neighbour exchange contributes to midline cell delamination

Under homeostatic conditions, cell delamination and apoptosis are required to maintain stable cell numbers by counter-balancing growth and proliferation (Eisenhoffer and Rosenblatt, 2013). In the human colon and in the developing zebrafish epidermis, cells extrude from regions of tissue with high cell density. Similarly induced compression of MDCK cells can be relaxed through the elimination of cells from the monolayer by delamination. In these tissues the

inhibition of stretch-activated ion channels, such as *Piezo1* in zebrafish, was shown to block live-cell extrusion demonstrating that epithelial tissues have force-sensitive mechanisms that allow them to detect and respond to changing tissue strains to maintain tissue homeostasis (Eisenhoffer et al., 2012).

Research from our lab on the developing *Drosophila* pupal notum showed that cells are extruded through basal delamination from the midline region (Marinari et al., 2012). The midline is 3-4 cells wide consisting of cells anisotropic in shape, elongated along the AP axis. From 14 h to 26 h AP a third of midline cells are extruded from the tissue, an event that is very rare outside the midline. By 26 h cells are isotropic in size and shape, both inside and outside of the midline region, indicating that midline delamination contributes to tissue refinement (Marinari et al., 2012).

Cells are able to leave the tissue through two distinct processes. During processes we termed 'D2' by analogy with T2, cells extrude by rapidly losing apical area and all DE-cadherin contacts. This process resembles apoptosis but only accounts for the minority of midline delamination events. The majority of cells leave via 'D1' processes (Fig 1.4). These occur like T1 transitions via neighbour exchange. Over variable and extended periods of time, cells undergo neighbour exchange events that allow both gain and loss of junctions. Cells that leave the tissue gradually reach less than 5 neighbours, with an associated loss of apical area (to ~25% their initial size). This is followed by rapid extrusion (~ 10 mins) through the recruitment and action of a contractile Myo II ring in neighbouring cells. Delaminating cells within the midline are randomly positioned, and appear to have no pre-determined fate to die, i.e. cells can remain in the epithelium if tissue growth is reduced.

Cell delamination in the notum acts in accordance with regional differences in tissue tension. When midline junctions are ablated at 14 h AP they exhibit less vertex displacement than those outside suggestive of local crowding. This was confirmed by overexpression of Dp110, the catalytic subunit of *Drosophila* phosphoinosotide 3-kinases (PI3K). This increased cell growth without increasing overall tissue area. The PI3K pathway is activated downstream of insulin binding to receptor tyrosine kinases on the cell surface (Ruderman et al., 1990; Vanhaesebroeck et al., 2012).

RNAi of the pathway member, the lipid phosphatase PTEN, was also used to increase cell growth. Signalling stimulates cell metabolism by increasing protein synthesis, glucose import, glycogen storage and lipid storage (Britton et al., 2002). Increased cell growth increased apical areas, except in regions of buckling, and increased tissue height. This overgrowth led to an increase in delamination rates, particularly in areas of tissue buckling, consistent with observations of extrusion in human colon epithelia (Eisenhoffer et al., 2012). Conversely, overexpression of the tumour suppressor proteins Tsc1 and 2 led to decreased growth, corresponding increases in tissue tension and decreased delamination rates. Knockdown of the 5s Ribosomal subunit (Rbp5s) was also used to decrease growth with similar results. Thus, delamination via T1-like neighbour exchange appears to be triggered by crowding to restore homeostasis (Marinari et al., 2012).

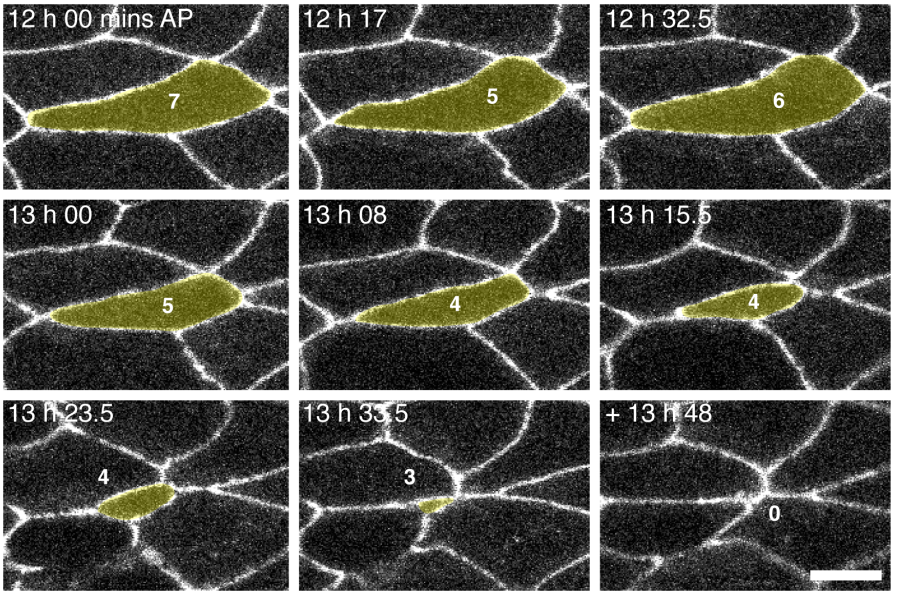


**Figure 1-8: Neighbour exchange events contribute to midline cell delamination**

A time-lapse montage of a characteristic midline delamination (D1-type) event visualised with DE-cadherin-GFP. White number indicates the number of neighbours the delaminating cell has at that time-point. Scale bar = 5µm.

*DE-cad-GFPKI ; pnrGAL4 / +*

(Leica SPE2, Larval development at 25$^{o}$C)

### 1.13.6 Notum Development: Changes in delamination rates are due to changes in cell growth and not changes in developmental timing

One question that arose from the notum delamination study was whether tissue-wide changes in cell growth affected developmental timing and would therefore impact upon delamination rates. I contributed to this work by normalising delamination rates for under- and overgrowth conditions to developmental time.

As no characteristic tissue movements are associated with developmental timing in the dorsocentral scutum, pupal development was normalised to division timing. Nota were visualised with DE-cadherin-GFP and imaged from 13 h AP, with global cell epithelial divisions occurring from ~13.5 h AP. A developmental marker was set at the time it took for 5 asymmetric pI cell divisions to occur for each notum imaged (Fig. 1. 5B). Cell overgrowth, through Dp110 expression, caused pI cells to divide earlier than control, whilst undergrowth, through RNAi-mediated knockdown of Rbp5s caused pI cell divisions to happen later. The number of midline delamination events occurring up to the fifth pI cell division was calculated as a percentage of the midline population at 13 h AP (Fig. 1.5C). A comparison of percentages showed that even when normalising to account for changes in the rate of pupal development, cell overgrowth led to increased delamination levels compared to control. Equally, delamination levels were reduced in conditions of undergrowth even when normalised to a slower rate of development. These results indicate that, rather than the effect of growth-induced changes in developmental timing, it is the effect of local tissue mechanics that influences the tendency of cells to delaminate.

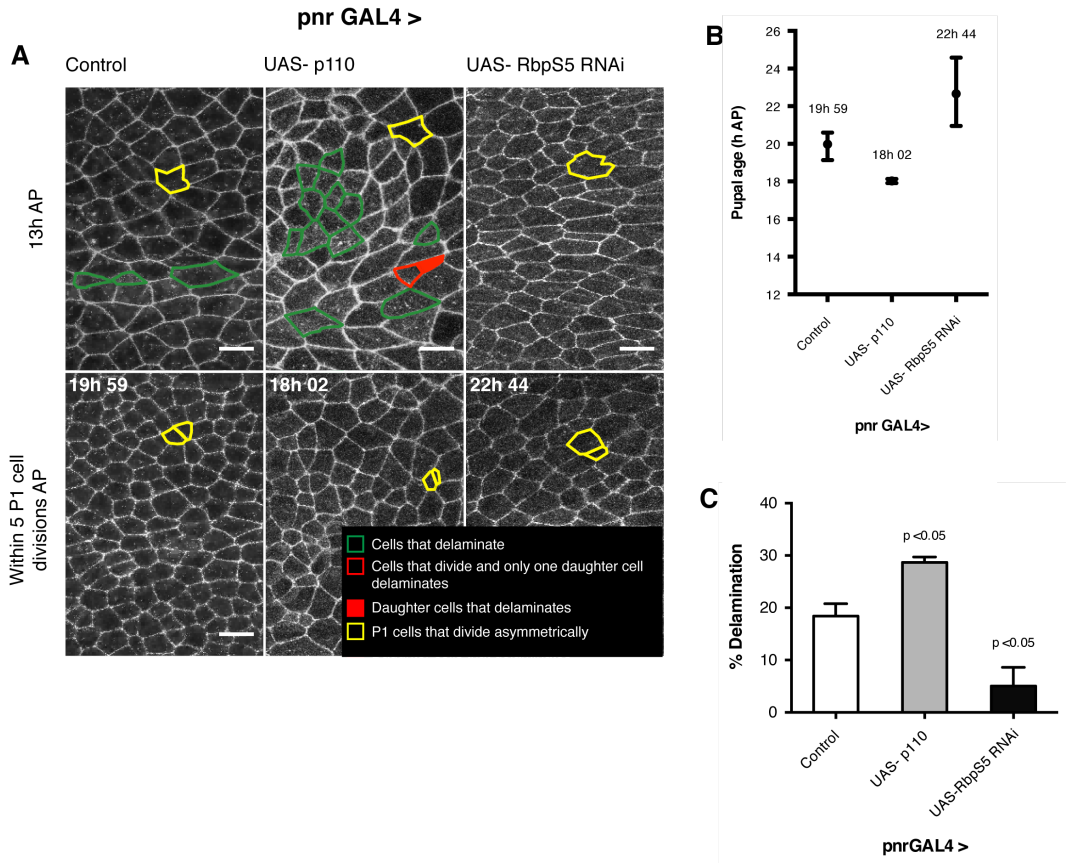


**Figure 1-9: Changes in delamination rates due to differences in cell growth are not due to a consequential change in developmental timing.**

Midline cell delamination percentages were normalised to developmental time for control ($w^{1118}$), overgrowth (*UAS-dp110*) and undergrowth ($UAS\text{-}rbpS5^{RNAi}$) (**A**) Cells that delaminate (green) before 5 P1 cell divisions (yellow) are indicated. Scale bar = 5µm. (**B**) Developmental age at which 5 P1 cells have divided. Dots indicate the mean, tails indicate the data range. For control and $UAS\text{-}rbpS5^{RNAi}$ n = 3, p110 = 2. (**C**) Percentage midline delamination. Bars indicate mean with SEM. p-values (p110 = 0.048; RbpS5 = 0.036) from unpaired t-test versus control.

*ubi-E-cad-GFP / +; pnrGAL4 / +* (Larval development at 29°C)
*ubi-E-cad-GFP / UAS-Myc-dp110; pnrGAL4 / +* (Larval development at 29°C)
$ubi\text{-}E\text{-}cad\text{-}GFP / +; pnrGAL4 / UAS\text{-}rbpS5^{RNAi}$ (Larval development at 18°C)

(All imaged with Leica SPE2)

## 1.14 Thesis aims

The study of basal cell delamination in the notum suggested that neighbour exchange events were contributing to tissue refinement. Midline delamination correlated with a localised decrease in junction tension, whilst delamination rates increased in areas of overcrowding. This indicates that junction dynamics act according to local tissue mechanics.

The aim of the work presented in this thesis is to use stable regions of the notum to describe cell intercalation events in the absence of a clear PCP pathway, see how they compare to transitions that drive rapid morphogenetic processes, and ask how they contribute to local tissue packing.

In this thesis, I describe how I investigated the role of Myo II and the dependence of actomyosin contractility for cell intercalation. I test how modifying the levels of active Myo II correlates with variations in junction dynamics. Furthermore I explore the role of interphase Moesin and the requirement for an adherens junction to facilitate cellular movement.

Finally I aim to explain how developmental changes in Myo II localisation aid regular tissue packing. Together these findings allow me to build a more general model of neighbour exchange under conditions of homeostatic growth, and to show whether packing geometries, induced by changing junction tensions, fit with those predicted by *in silico* models.

# 2. Materials and Methods

## 2.1 Genetic manipulations and the UAS-GAL4 system

dsRNAi and overexpression constructs were expressed in the fly using the UAS/GAL4 system (Brand and Perrimon, 1993; Busson and Pret, 2007). The gene encoding the yeast transcriptional activator GAL4, driven by inducible tissue-specific or gene-specific promoters, was used to allow tight spatial and temporal control of expression. These lines were crossed onto stocks containing constructs fused to upstream activator sequences (UAS) that have binding sites for GAL4. GAL4 binding induces transcriptional expression of these constructs. For gene-knockdown, the UAS/GAL4 system was used to drive expression of 300-400bp inverted repeat sequences that fold to form hairpin RNAs (hpRNAs). These are then processed by Dicer to form siRNAs that guide sequence-specific degradation of target mRNA (Fire et al., 1998). This prevents mRNA translation and protein expression, leading to a hypomorphic phenotype.

The *Drosophila* notum was used as a model system for this study. UAS expression was driven (when stated for each figure) by GAL4 bound to the tissue specific promoter *pannier* (*pnr*) (Gerlitz et al., 2002). *Pannier* expression extends from the head to the end of the abdomen including a broad medial domain of the notum on the dorsal side of the fly (Fig. 2.1) (Calleja et al., 2000).

Additional temporal resolution of UAS-construct expression was provided by utilising temperature sensitive GAL80. At permissive temperatures (18$^{o}$C) GAL80$^{ts}$, expressed under the control of the alpha-Tub84B promoter, binds the transcriptional activation domain of GAL4, blocking its expression (Suster et al., 2004). At restrictive temperatures (30$^{o}$C) GAL80 no longer binds, allowing for GAL4 expression (Matsumoto et al., 1978; McGuire et al., 2003; McGuire et al., 2004).


**Figure 2-1: The expression domain of *pnr*.**

(**A**) Dorsal view of a *pnr*-GAL4 / UAS-lacZ fly stained with X-Gal to show the entire adult *pnr* domain. Darker staining labels *pnr* expression within the notum.

Image from: (Calleja et al., 2000).

## 2.2 Conditions

Adult fly crosses were kept at room temperature (20°C). Fly food recipe: 39 l $dH_2O$, 675 g yeast, 390 g soy flour, 2.85 kg yellow cornmeal, 224g agar, 3 l light corn syrup, 188 ml propionic acid. After two-three days of egg laying stocks were flipped and the tube containing eggs transferred to 18, 25, or 29°C for larval development. The temperature used is stated for each genotype with each figure. AP age develops in real-time at 25 °C, and at half pace at 18 °C. For the majority of imaging, pupae needed to be at 12 h AP (at 25 °C) for dissection so at 0 h were transferred to 18°C overnight for imaging the next day. For later developmental stages pupae were moved between 18 and 25°C accordingly.

For shibire temperature sensitive (ts) experiments room temperature (permissive) flies (and control) were moved to a heated chamber at a 29°C (restrictive) ten mins prior to imaging.

*UAS-zipper-DN* expression was regulated by *tub*-GAL80$^{ts}$ to ameliorate toxicity. Flies were kept at 18°C through larval development, selected at 0 h AP, kept at 18°C overnight and transferred to 29°C for 5-6 h before imaging. Temperature shifts were timed for the pupae to be 12-13h AP at imaging.

## 2.3 Fly Stocks

Stocks were obtained from Vienna Drosophila Resource Center, Austria (Dietzl et al., 2007); Drosophila Genetic Research Center, Kyoto Institute of Technology, Japan; NIG-FLY National Institute of Genetics, Japan; the Bloomington Drosophila Stock Center at Indiana University, USA; or from donations (origins are stated below). Experimental genotypes are written after each figure when necessary.

| Stock | CG Number | Origin | References |
|---|---|---|---|
| *w; P[w[+mC]=tubP-GAL80$^{ts}$]10/ Cyo-GFP; pnrGAL4 / TM6b, tb;;* | | BL7018 | (McGuire et al., 2003) |
| *w; UAS-Myc-dp100;;* | | | (Leevers et al., 1996) |
| *w$^{1118}$;;;* | | BL 3605 | |
| *7016 w*; sco / Cyo; tubGal80$^{ts7}$;;* | | BL7018 | (McGuire et al., 2003) |
| *;; UAS-Moe$^{TD}$-GFP;* | CG10701 | | (Speck et al., 2003) |
| *UAS-Moe$^{RNAi}$;;;* | CG10701 | NIG-FLY: 10701R-3 | |
| *w$^{1118}$; UAS-Moe$^{T559D}$.Myc;;* | CG10701 | BL8630 | |
| *; UAS-armadillo$^{RNAi}$ (ß-cat);;* | CG11579 | VDRC: KK 107344 | |
| *; UAS-zipper-DN-GFP;;* | CG15792 | | (Franke et al., 2005) |
| *; zipper-YFP;;* | CG15792 | CPTI-100036 | (Knowles-Barley et al., 2010) |
| *; viking $^{G454}$;;* | CG16858 | | (Morin et al., 2001) |
| *; UAS- alpha-catenin$^{RNAi}$ ;;* | CG17947 | VDRC: KK107298 | |
| *shibire$^{ts}$ / FM7 Kr-GFP ;;;* | CG18102 | BL2248 | (van der Bliek and Meyerowitz, 1991) |
| *; Basigin-YFP;;* | CG31605 | | (Knowles-Barley et al., 2010) |
| *; UAS- mbs$^{RNAi}$;;* | CG32156 | VDRC: KK105762 | |
| *;; sqh-mCherry;* | CG3595 | | (Martin et al., 2009) |
| *;; UAS-sqh$^{A20A21}$ / TM6b, tb;* | CG3595 | | (Dorsten et al., 2007; Jordan and Karess, 1997) |
| *;; UAS- sqh$^{E20E21}$ / TM6b, tb;* | CG3595 | | (Jordan and Karess, 1997; Winter et al., 2001) |
| *sqh$^{AX3}$ ; sqh-GFP;;* | CG3595 | | (Royou et al., 2004) |
| *; DE-cadherin-GFP;;* | CG3722 | | (Huang et al., 2009) |
| *; UAS-E-cad:: EOSFP ;;* | CG3722 | | (Cavey et al., 2008) |
| *; ubi-DE-cadherin-GFP;;* | CG3722 | | (Oda and Tsukita, 2001) |
| *;; UAS-shotgun$^{RNAi}$ (DE-cadherin);* | CG3722 | NIG: 3722R-1 | |
| *w$^{1118}$;; pnr-GAL4;* | CG3978 | BL 3039 | |
| *; UAS-Slik RNAi;;* | CG4527 | VDRC: GD43783 | |
| *; If / Cyo ; ubi-bazooka-mCh / Tm6b,* | CG5055 | | (Bosveld et al., 2012) |
| *; UAS-sds22$^{RNAi}$;;* | CG5851 | VDRC: GD42051 | |
| *;; UAS-MYPT-75D-d$^{RNAi}$;* | CG6896 | NIG-FLY: 6896R-1 | |
| *;; spider (Gilgamesh)-GFP;* | CG6963 | | (Morin et al., 2001) |
| *;; ribosomal protein S5 (rbp5s)$^{RNAi}$;* | CG7014 | VDRC: 27792 | |
| *; sqh-Rok $^{K116A}$-Venus;;* | CG9774 | | (Simoes Sde et al., 2010; Simoes Sde et al., 2014) |
| *; UAS-Rok$^{RNAi}$;;* | CG9774 | VDRC: KK104675 | |
| *y w*; UAS-Rok.$^{CAT}$;;* | CG9774 | BL 6668 | (Verdier et al., 2006) |

**Table 2-1: Fly stocks**

## 2.4 Germ band elongation (GBE) imaging

The protocol was based upon that given to me by Natalia Bulgakova from Nick Brown's lab Gurdon Institute, University of Cambridge.

- Prepare agar for flies to lay eggs on. Recipe: 25 – 30g agar, 20ml ethanol (95%), 300 ml juice concentrate (Welch's red grape), 0.5 g methyl paraben (p-hydroxymethylbenzoate).
- Autoclave the agar with 700ml $H_2O$ for 40 mins = Solution A.
- Add ethanol to a vial containing methyl paraben. Add the methyl paraben / ethanol mix to the grape juice concentrate = Solution B.
- Add Solution A and B together and pour into plates; do this quickly so that the mixture will not harden in the pouring container.
- Keep flies at 25$^{o}$C on plates within cages for laying.
- Collect embryos so that they are 2-4h when imaging. (GBE is at 3.5 h, and takes 45 mins)
- Prepare a microscope slide with one 18x18mm coverslip stuck with nail varnish to each side.
- Prepare glue for attaching embryos to slide. For glue: dissolve double sided tape (Sellotape) in heptane (Sigma 494526L, 99% biotech grade solvent) overnight (amount of heptane is arbitrary, if the glue is too thick more heptane can be added).
- Add 1µm of glue to the centre of the microscope slide and spread with a coverslip.
- Cut an empty agar slide into small squares and put two pieces on a separate slide.
- Fill the agar dish with embryos with $H_20$.
- Using a brush wash the embryos from the agar surface.
- Add 4-5 ml of bleach (strong economy – sodium hypochlorite solution) for 4 mins (1:1 $H_2O$: bleach).
- Rinse thoroughly with $H_2O$ in a sieve on paper. When fully dechorionated the embryos will float on the water surface.
- Scoop onto one of the agar pieces on the microscope slide.

- Using a needle on a stereomicroscope move the embryos from one agar piece and align them on the other.
- Anterior left, posterior right, dorsal side up, ventral down. Embryos are bean-shaped so ventral side is more curved. For imaging with a lateral view.
- Image Stage 8-9, if the gut autofluoresces under a GFP microscope then they are too old (Stage 11+).
- Cut the agar with the embryos along each side to form thin piece.
- Use the slide with the glue to gently press onto the embryos so that they stick.
- Add 50µl of halocarbon oil (Halocarbon oil 27, Sigma H-8773) to the embryos.
- Place a coverslip on top until it touches the oil and slightly flattens the embryos.
- Leave for 5-10 mins to settle before imaging.
- For imaging: upright confocal FV1000 Olympus using 100x/ 1.40 NA Oil UPlan-SApochromat objective lens.
- Junctions will shrink along dorsal-ventral (DV) axis, and expand along anterior-posterior (AP). Dorsal cells will move into view and divide.

## 2.5 Pupal dissection and Live Imaging

For live imaging, flies were raised to 11.5 to 12 h AP (at 18, 25, or 29 $^{o}$C) and fixed to a microscope slide with double-sided Sellotape. The pupal case was removed to the abdomen to expose the notum. This is achieved by removing the operculum with forceps, cutting down the mediolateral side of the fly with scissors and pealing the case off (Zitserman and Roegiers, 2011). A stack of 18 x 18mm slides was glued to the slide, with clear nail varnish, anteriorly (5 slides) and posteriorly (4 slides). A coverslip was spread with halocarbon oil 700 (Sigma – H8898) and rested onto the stacks so that it is in contact, but not crushing, the notum. The coverslip was glued in place with clear nail varnish at the posterior end. Flies were allowed to settle for 15 mins before imaging.

## 2.6 Microscopes for Live Imaging of Pupae

The microscope usedfor each experiment is stated on each figure whre necessary.

- Leica SPE2 scanning confocal – 40x NA 1.3 Oil objective.

- Leica SP5 inverted confocal – 40x 1.3x Oil objective and 63x 1.3x Oil objective.

- Carl Zeiss Axiovert 200 M with Yokogawa CSU-X confocal spinning disk unit and Andor Zyla cSMOS 5.5 camera – 63 x water objective.

## 2.7 Laser Ablation

Flies were prepared on a microscope slide for live imaging as described in section **2.5**. DE-cadherin-GFP was visualised using 488nm light from an Ar-Kr laser with a Plan-Neofluor 40x/1.3 Oil DIC objective coupled to a Zeiss LSM510 Meta upright confocal microscope. Image acquisition prior to and after ablation was at 1 s intervals.

Junctions were ablated with 720nm multiphoton excitation from a Chameleon-XR Ti-Sapphire laser (AIM, Zeiss). Junctions were ablated by scanning over a 3x3 pixel region of interest (0.009$\mu m^2$) at 25% laser power, 1 iteration with a dwell time of 2.56 µs / pixel.

Kymographs were used in order to calculate vertex displacement velocities. In FIJI straight lines (1 pixel thick, need to remove scale from image stack) were drawn across the pre-ablated junction and the 'Dynamic Reslice' function used to produce a kymograph (X = length, Y = time) of each ablation event. The 'segmented line' tool was used to plot progression of each of the two junction vertices over time. In excel the data is saved as: Column A: Vertex 1 coordinate; Column B: Time Frame of V1; Column C: Vertex 2 coordinate; Column D: Time Frame of V2; Column E: Ablation Frame; Column F: Distance Scale; Column G: Time interval. The distance between the two X,Y vertex coordinates at each time point could then be calculated using MatLab with code written by Andrea Dimitracopoulos.

Matlab code for XY distance at each time point:

```
function magic1

clear all
close all
clc
[filename, url] = uigetfile('*.xlsx', 'select data file');

data = importdata([url, filename]);
vertex1 = data.data(:,1);
vertex2  = data.data(:,3);
time1 = data.data(:,2);
time2 = data.data(:,4);

vertex1(isnan(vertex1)) = [];
vertex2(isnan(vertex2)) = [];
time1(isnan(time1)) = [];
time2(isnan(time2)) = [];

startTime = max(min(time1),min(time2));
endTime = min(max(time1),max(time2));
timeInterval = 1; %seconds
time = (startTime:timeInterval:endTime)';

V1 = interp1(time1,vertex1,time);
V2 = interp1(time2,vertex2,time);

length = abs(V2-V1);
ablationTime = 0; %CHANGE

output = [time-ablationTime,V1,V2,length];
xlswrite('result.xls',output);

end
```

Total distance between vertices was then plotted in Prism at 10 sec after ablation and over a 2 min time course. The first time frame after ablation was not used as the initial vertex displacement measure, because unlike other tissues such as the wing disc, measurable and significant displacement was not observed in the notum in the first frame after ablation (Mao et al., 2013).

## 2.8 Fluorescence Recovery After Photobleaching (FRAP)

Flies were prepared for live imaging as described in section **2.5**. Fluorescence recovery after photobleaching (FRAP) experiments were undertaken on the Leica

SP5 confocal using the Leica Software FRAP wizard. Imaging was undertaken with a 488nm light at 11%, 150 smart gain, no offset and HyD1 detector. Pre (20 frames) and post bleach (120 frames). The nota were imaged at 1.5 s intervals with a 63x objective and 3x zoom. To bleach, ROIs were selected (width 0.5-0.75µm, length depends on distance between vertices, ~ 5-9 µm). The 'zoom in' function was selected and junctions were bleached with 30% 488nm light for 1 iteration. This produces three files per experiment: Pre-bleach, Bleach, and Post-bleach. Pre-bleach and Post-bleach TIFF image sequences were concatenated using FIJI. Intensity measurements of the bleached junction, a non-bleached junction and background region were made by drawing a rectangle and plotting the z-axis profile. The MatLab software EasyFRAP (http://ccl.med.upatras.gr/index.php?id=easyfrap) was used to normalise the data (Rapsomaniki et al., 2012). Data must be saved as a .csv file to insert into EasyFRAP. In Excel column A = time in secs (time of ablation is entered later; Column B = bleached junction intensities; Column C = non-bleached junction intensities; Column D = background intensities. .csv files for each RNAi condition can be saved in an individual folder for import to EasyFRAP. EasyFRAP was used to enable 'Full Scale' normalisation. Normalisation subtracts background values at each time-point to correct for noise. Measurements are divided by non-bleached junction intensities to correct for z-fluctuations as the fly moves and to correct for photo bleaching. Measurements are then divided by the mean pre-bleach intensity to remove systematic error between experiments. Full-scale normalisation is used to account for differences in bleaching depth between experiments. Therefore intensity values range from 1, at pre-bleach, and 0, the intensity after bleaching. Normalised values were exported from EasyFRAP to Prism. Mean (with S.D) two-phase association curves of recovery were then plotted and statistic tests used to determinedifferences in rates of recovery, and plateaus.

**FRAP Equations and Definitions**:

**Fast Phase**=(Plateau-Y0)*PercentFast*.01

**Slow Phase**=(Plateau-Y0)*(100-PercentFast)*.01

**Y**=Y0+ SpanFast*(1-exp(-KFast*X)) + SpanSlow*(1-exp(-KSlow*X))

**Y0** is the Y value when X (time) is zero. It is expressed in the same units as Y. **Plateau** is the Y value at infinite times, expressed in the same units as Y. **Kfast** and **Kslow** are the two rate constant, expressed in reciprocal of the X axis time units. If X is in minutes, then K is expressed in inverse minutes.
**PercentFast** is the fraction of the span (from Y0 to Plateau) accounted for by the faster of the two components.

### 2.9 Notum dissection and Immunohistochemistry

For p-Myosin II staining 12-13 h AP nota were dissected in PBS before fixation in 4% paraformaldehyde in PBS for 20 min at RT. For p-Moesin staining, nota were dissected in PBS and fixed in 10% trichloroacetic acid (TCA) with $H_2O$. Samples were washed and permeabilised for 3x 10 min in PBT (PBS with 0.1% Triton X-100) at room temperature (RT). Nota were incubated with 1:1 PBT: blocking buffer (5% BSA, 3% FBS in PBS). Incubation with primary antibodies was done at $4^oC$ overnight (O/N) prior to 4x PBT 10 min washes. Incubation with secondary antibodies was carried out for 1-2 h at RT in PBT, with gentle shaking. Nota were 3x washed with PBS for 10 mins and kept in 50% glycerol in PBS at $4^oC$ O/N before mounting. TritC-Phalloidin (1:500) and DAPI (1:2000) staining was undertaken during the second wash. Nota were mounted with 50% glycerol in PBS and imaged within days (I found mounting this way preferable to using commercial mounting medias which degraded signal). The following primary and secondary antibodies were used: anti-phospho-Myosin Light Chain Ser19 (rabbit, 1:30 dilution, Cell Signalling 3671), anti-GFP (chicken, 1:500) anti-phospho-Moesin (rabbit, 1:100 dilution, Cell Signalling 3141), goat anti-chicken Alexa 488 (1:250), goat anti-rabbit Alexa 647 (1:250).

## 2.10 Packing Analyzer

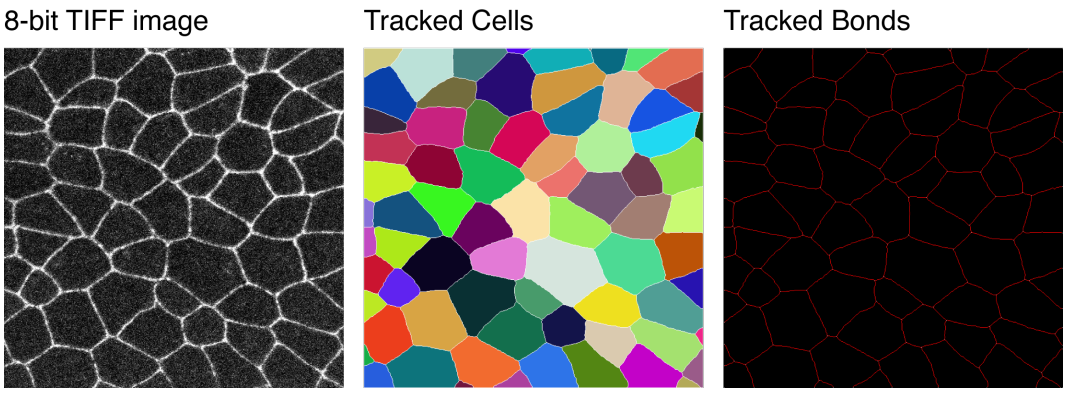


**Figure 2-2: Packing Analyzer segmentation.**

Tutorials for using Packing Analyzer are available at: https://idisk-srv1.mpi-cbg.de/~eaton/ (Aigouy et al., 2010)

- Save movie in FIJI as an **Image Sequence TIFF**. It has to be 8-bit.
- Open Packing Analyzer, drag and drop the Image Sequence into **List**.
- Under **Init**, change the parameters to 3.8 (top) and 1.9 (bottom). This is quite arbitrary, change these parameters as you see fit.
- Click **Detect Bonds**. A notum image with the above parameters is likely to be over-segmented. **Save** (purple floppy disk above tabs).
- Under **Correction**, correct mistakes. Right click to delete junctions. Left click and hold to draw new junctions. Change the pencil size, on the left above the tabs. Use a large pencil size to delete lots of junctions at once. Click second **green tick** to apply changes. **Save**.
- To apply changes to the next image in the sequence click **Seed Next**.
- Correct errors. **Save**. **Seed next**. Continue to end of Image Sequence.
- Once finished, **Post Process**, change **4 way vertices cutoff** to 3. Click **Finish All**. (large datasets will take 10-15 mins).
- **Recenter** tab, click **autocenter based on 2D correlation** (10-15 mins).
- Tracking, click **Track** cells (10 mins).
- **Tracked bonds**, click **track bonds** (10 mins).
- **Plots**, can plot **all bonds** or **plot all cells**. To plot individual cells/junctions draw lines through cells/junction of interest in Current Image then click **plot**

**selected cells** / **plot selected bonds**. Always exclude border bonds or cells.

- **Virtual cloning**, draw a line through cells of interest in Current Image, click **track clones**. Can go back to **Plots** and **plot clone info**.
- Under the **Viewer** tab you can see a range of segmentations for each image.
- In the folder where the original Image Sequence is saved, each image will have a folder containing all the files produced.
- One problem is that files within folders are not numbered/ labelled to that timepoint. They all have the same name. Therefore I manually changed the name of each file eg. bd_fate to bd_fate000 so I could transfer all bd_fate files to a new folder and make a stacked image of them in FIJI.
- Plots will be saved as .csv files in first image folder ….000.
- Open in Excel, highlight first column. Go to **Data**, and click **Text to columns**. Highlight the whole dataset and go to **Data**, **Sort**. Sort by **ID** then **Frame Number**. Sizes (junction lengths and areas) are in pixels. These need scaling.

## 2.11 Image processing and Statistical Analyses

All images presented were processed using FIJI software (http://fiji.sc/Fiji) and Adobe Illustrator CS4. Graphs were produced using GraphPad Prism 6. Statistical analyses were performed in Prism. D'Agostino and Pearson omnibus normality tests were used to determine if data were Gaussian. Nonparametric datasets were compared using a Mann-Whitney test. Data from a Gaussian distribution were compared using an unpaired t-test.

## 2.12 Circularity and Aspect Ratio Quantification

Circularity and aspect ratio measurements were made using FIJI. Shapes were drawn around cells of interest and 'measured'. Circularity is found in the Analyze – Measure tab under 'Shape descriptors'. Circularity = 4π*area/perimeter^2. Values range from 0 to 1. 1 indicates a perfect circle. As values approach zero this indicates an increasingly elongated shape.

Aspect ratios are measured from ellipses that are fit to selections. Fit ellipse is found in FIJI at Analyze – Measure – Fit Ellipse. The macro used to fit an ellipse can be found at: http://imagej.nih.gov/ij/macros/DrawEllipse.txt. The area, centroid and orientation of the original selection are retained. The aspect ratio is calculated by dividing the major axis of the ellipse with the minor axis.

For Fig. 4.5D and 7.3D, ellipse elongation was calculated for large cell numbers from segmented images (PA - bd_fate files) by Tom Wyatt as: (Wyatt et al., 2015).

### 2.13 Junctional Fluorescence Intensity Measurements

To correlate Myosin II intensities with junction length, Bazooka-mCherry (AJ marker) was imaged with Sqh-GFP (MRLC). The scale of the images, 1 pixel = 0.12025μm. Junction intensities were measured without vertices.

- To measure junction intensities Bazooka-mCh imaging was segmented with Packing Analyzer (**2.1**) for single time-points.
- In FIJI, convert the bd_fate image to 8-bit.
- Threshold the images so the junctions are white, background is black.
- Invert the image (Edit – Invert).
- Dilate the image twice (= ~0.5μm) (Process- Binary – Dilate). Save as 'Junctions'.
- To remove the vertices, go to original bd_fate image.
- Convert to 8-bit, and threshold vertices so that the vertices are white, all background is black.
- Invert the image, and dilate vertices 3 times. Save as vertices.
- Process – Image calculator. Take 'Junctions' image and subtract 'Vertices'.
- Delete any pixels where any junctions still touch and save image as 'Junctions without vertices'.
- Analyze - Set measurements – Redirect to – 'Junction without vertices'.
- Then open original junction image (Bazooka mCh) or Myosin II image (Sqh-GFP).
- Analyze – Analyze particles. Tick 'Show: Outlines' and then OK.
- Results are produced as a .txt file.

## 2.14 Transmission Electron Microscopy (TEM)

Nota were then prepared for TEM with the assistance of Jemima Burden, TEM facility, LMCB as: (Georgiou et al., 2008).

TEM was performed on nota dissected at 12-13 h AP. Nota were dissected as for immunohistochemistry (section **2.9**) in disposable PDMS plates. (Recipe for PDMS: 1g curing agent, 20 g Silicone elastomer. Protocol: Mix with a coffee stirrer. Remove any bubbles with a vacuum wine pump. Spin with lid on at 1000rpm for 4 mins. Pour into dishes. Place at 65$^{o}$C for a 2-3 h until set). Fix tissue for 30 mins in 2% PFA / 1.5% glutaraldehyde in 0.1M sodium cacodylate. Wash with 0.1M sodium cacodylate and leave in sodium cacodylate until osmofication. Postfix nota in 1% osmium tetroxide / 1.5% potassium ferricyanide for 1 h at 4$^{o}$C. Wash with sodium cacodylate. All steps are carried out whilst pupa is pinned to PDMS. Nota are then cut away (removed asymmetrically to know apical-basal orientation) for tannic acid treatment.

The tissue is then treated with 0.1% tannic acid in 50 mM sodium cacodylate before dehydration and embedding in a drop of epon sandwiched between a rubber mold and a glass coverslip. Once baked, the glass-epon sandwich containing the tissue is embedded on an epon stub, and the glass was removed with liquid nitrogen. The sample is then trimmed with a razor blade and hacksaw to reorientate the tissue for re-embedding enabling apical-basolateral cross-sectioning. Ultrathin serial sections are prepared with a Leica UCT ultramicrotome (Leica Microsystems, UK), collected on formvar slot grids, and examined, after lead citrate staining, in Tecnai T12 electron microscope (FEI, The Netherlands). In all cases, sections were cut perpendicular to the plane of the epithelium. Images are captured with Morada CCD and iTEM software (Olympus Soft Imaging solutions), which was also used for quantitative analysis. Images from **Fig. 1.1** show junctions oriented in the epithelium such that apical is up and basal down

# 3. Junction rearrangements contribute to a locally dynamic yet globally stable epithelia.

## 3.1 Introduction

The role of cell intercalation and the regulation of adherens junction dynamics have been extensively studied and implicated in the large-scale deformation of morphologically active tissues. The overall goal of this thesis is to understand how fluctuations in the length of cell-to-cell contacts contribute to tissue homeostasis and ordered cell packing under conditions of stable development, in the absence of large-scale changes in tissue size and shape. Mature epithelia are ubiquitously present in nature and must mechanistically respond to changes in force. Internally, local compression forces can be supplied by increased growth rates and cell division, whilst cell loss through delamination and apoptosis creates increased local tensions (Heisenberg and Bellaiche, 2013). Externally applied traumas create force on a macroscopic scale. The ability to dissipate these forces allows epithelia to maintain ordered packing, and to prevent the onset of tumour growth or tissue catastrophe.

Despite not undergoing large-scale morphogenesis during its development, the *Drosophila* notum is a tissue that undergoes a number of dramatic changes that affect cell packing. The aim of this chapter is to describe the notum as a model system in which to investigate the mechanistic properties of neighbour exchange events in a developing but morphologically stable epithelium. Using live imaging, segmentation and analysis I show how junction dynamics, including neighbour exchange events, contribute to tissue shape and order. I then discuss several hypothetical models of T1 transitions that act as a framework to understand the role and regulation of neighbour exchange in developing epithelia.

## 3.2 Neighbour exchange without global changes in tissue shape

The cumulative action of local cell intercalation events can lead to morphogenesis, however this is not always the case. Previously we described a role for neighbour exchange in cell delamination in the midline of the *Drosophila* notum (Marinari et al., 2012). This is a tissue that develops without concomitant changes in global size and shape. Our aim here is to study junction dynamics in the absence of external

forces and morphogenesis and therefore we looked at junctions outside of the midline at stages prior to cell division and delamination.

Adherens junctions in *Drosophila* epithelia form in discrete apical domains (Harris, 2012). Using the endogenous expression of DE-cadherin-GFP, imaging at single time-points and moving apically to basally through the fly at 1µm z-slices it was possible to image the entire tissue (Appendix, Fig. 9.1A). Maximum projections were used to flatten the curvature of the tissue (visible within 2-5µm, ~50 x 100µm in size). This reveals several morphologically distinct features (Fig. 3.1). At 12 h AP the midline region is 3-4 cells in width, where cells are elongated along the anterior posterior axis. Either side of the midline sits a flat region of tissue positioned just behind the two prominent dorsocentral macrochaetes.

With time-lapse microscopy we imaged the region of tissue, outside of the midline, at 30 s intervals between 12 and 13.5 h AP, prior to most cell delamination within the midline and the onset of tissue-wide cell division. Using Packing Analyzer, together with manual corrections (Methods 2.10), each time point was segmented to give cell descriptors such as area, polygon distribution and orientation of the long cell axis, whilst also allowing for the tracking of cells and junctions through time.

First we wanted to assess the changes in tissue size and shape over the course of its development. We identified virtual clones within the tissue, to see how these regions changed in shape over a one and a half hour time period (Fig 3.2A). The area of these clones remained constant (Fig. 3.2B), as did the aspect ratio (Fig. 3.2C), which was calculated by fitting an ellipse to the shape of the clone in FIJI and dividing the length of its major axis by its minor axis. This was true for several nota imaged (Fig. 3.2D). Despite this, individual cell boundaries were not static. Instead junctions were frequently lost and created through neighbour exchange events. Moreover this occurred in a seemingly random spatial and temporal manner (Fig. 3.2A & C). Therefore changes at the cell level don't translate into changes at the tissue scale. All that is changing is cell packing.

When we explored the qualitative nature of these exchanges we observe a range of transition-associated movements. Firstly, characteristic neighbour exchange events

are observed (Fig 3.3A). During these events two initially separate cells, within a cluster of four, will form a new cell-cell contact whilst two initially neighbouring cells will separate over the course of the transition. These transitions have been studied in detail in *Drosophila* germ band elongation (GBE) (Fig. 1.4) and have been shown to be irreversible (Bertet et al., 2004). In the notum, however, junctions frequently shrink to 4-way vertices and expand back out, returning to the initial neighbour configuration (Fig. 3.3B). Moreover, in some cases, multiple neighbour exchange events occur between the same four cells leading to repeated loss and gain of junctions (Fig. 3.3C). Therefore, T1s are reversible and are not associated with morphogenesis in this region of the notum. These data suggest that exchange events could be a consequence of stochastic junction fluctuations.

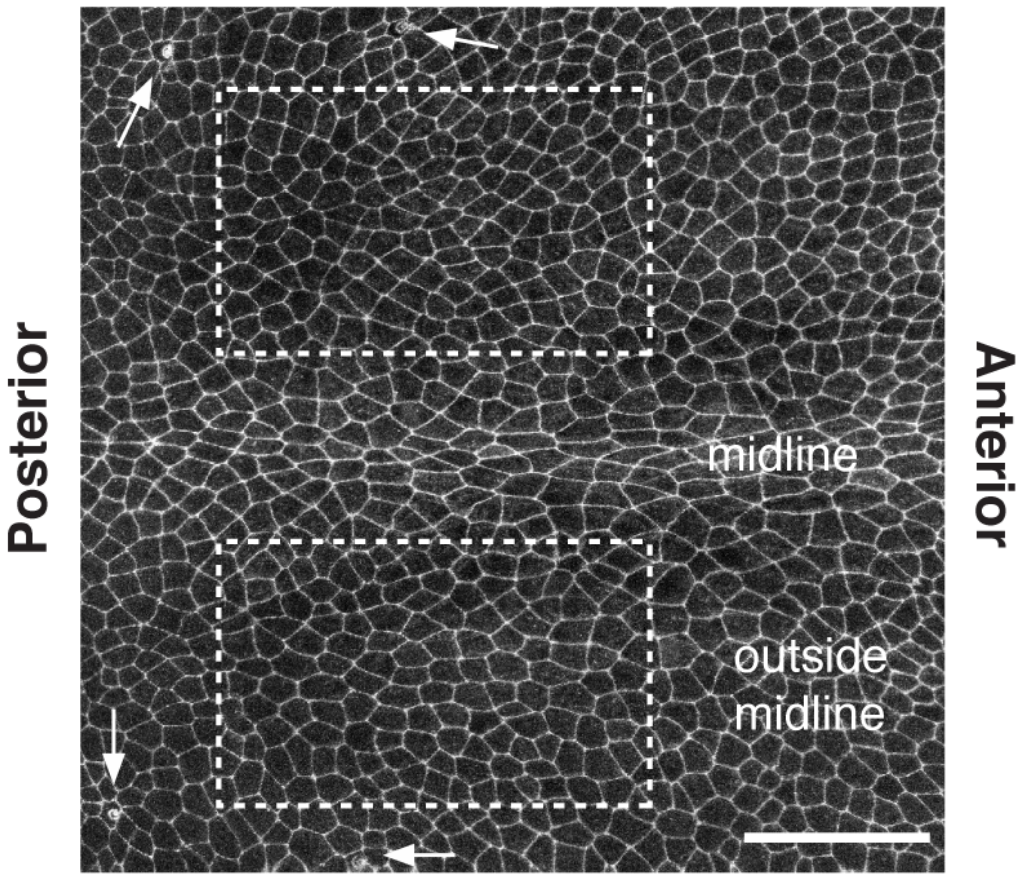


**Figure 3-1: Region of interest for notum imaging.**

A maximum projection of the region of the notum used in these studies labelled with DE-cadherin-GFP at 12 h AP. A region of elongated cells defines the midline, which is where the left and right disks fuse. For junction fluctuation analysis, the notum was imaged within relatively flat regions of tissue outside the midline as indicated by the dotted rectangles. To ensure reproducibility in every case rectangles were positioned anterior of and between the dorsocentral macrochaetes (arrowed) and extend anteriorly. Scale bar = 50µm.

*; DE-cad-GFP(KI) ; pnrGAL4 / + ;*

(Leica SPE2, Larval development at 25$^{o}$C)

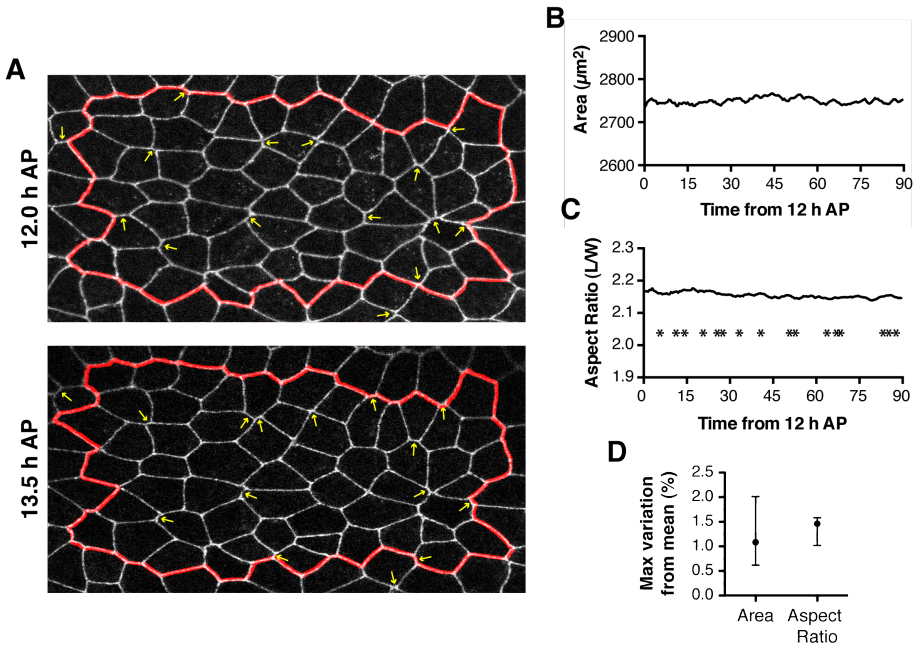


**Figure 3-2: Area and aspect ratio of the tissue remains stable over 90 mins.**

(**A**) Nota were imaged from 12 to 13.5 h AP, prior to the onset of tissue-wide cell division. Yellow arrows indicate junctions that are lost (12 h) during imaging and gained (13.5 h). By tracking large clones of cells (within red line) over 90 mins the change in clone area (**B**) and aspect ratio (**C**) could be measured. The times at which junctions form 4-way vertices, an intermediate in the process of neighbour exchange, are labelled with stars in **C**. (**D**) The maximum variation of the area, and the aspect ratio from the mean are plotted. n = 4 nota. Dots represent median, tails represent the full data range.

*; DE-cad-GFP(KI); pnrGAL4 / + ;*

(Leica SPE2, Larval development at 25$^{o}$C)

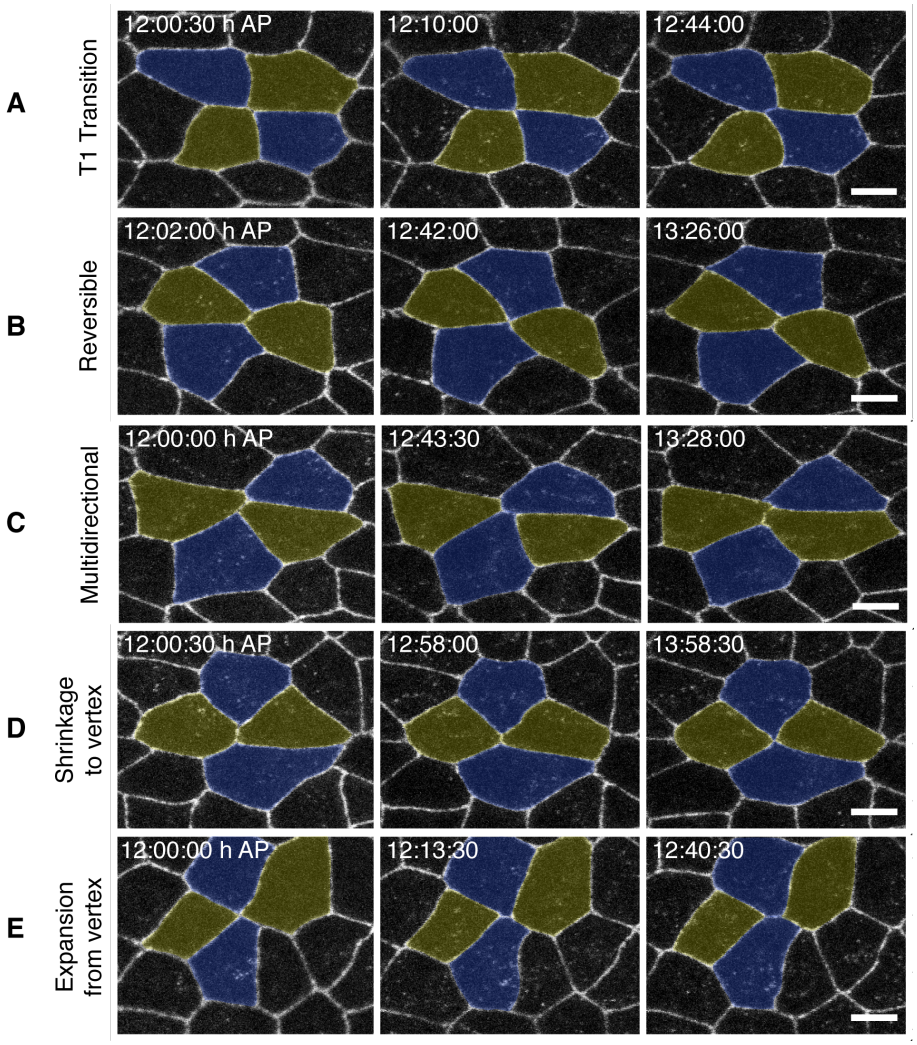


**Figure 3-3: Junction events occurring outside the midline between 12 and 13.5 h AP.**

A range of junction transition-associated events are observed. These can be seen in the notum imaged in **Fig. 3-2**. (**A**) T1 transition (**B**) Reversible T1: junctions can be lost to form 4-way vertices and expand back out again. (**C**) Multidirectional: several exchange events can occur for the same set of cells. (**D**) Shrinkage to vertex: during imaging junctions can be lost to form 4-way vertices and not expand out within the timeframe of the movie. (**E**) Expansion from vertex: new junctions can form as resolution of 4-way vertices present at 12 h AP. Scale bar = 5µm.

*; DE-cad-GFP(KI); pnrGAL4 / + ;*

(Leica SPE2, Larval development at 25$^{o}$C)

### 3.3 Alternative models of Neighbour exchange

It is clear from the previous analysis that the epithelium outside of the midline represents an interesting model, in which T1s occur without global change in tissue shape and size. This may represent a new model of dynamic epithelial homeostasis. To understand how cell intercalation events occur under these conditions, it is useful to compare these events against a set of hypothetical models as detailed below. In future chapters we will explore the molecular role of Myosin-II in the process and the requirement of Dynamin-dependent adherens junction turnover for neighbour exchange in this tissue.

Firstly, we consider a '*Sequential removal & addition*' model. As junctions shrink, their first neighbours ($60^o$ junctions) retain their orientation and junction length (Fig. 3.4A). From the 4-way vertex, junctions expand out to form a new cell-cell contact oriented perpendicular to the starting junction. Rates of contraction and expansion may or may not match. During GBE this type of process, driven by sequential DV shrinkage and AP expansion, causes the embryo to decrease in width by 50% that is matched by corresponding lengthening along its AP axis. This changes the topology of the four-cell cluster so that the long aspect ratio (AR) of the four cells involved shifts by $90^o$. This model also requires a sequential decrease then increase in total junction length, as a single junction is lost and a new junction formed. However, to enable junction loss and gain through this type of process, first neighbour vertices must be free to move, as expected if all junctions in a network are fluctuating in length.

The second model, which we have termed the '*Simultaneous removal & addition'* model, relies on the outer vertices of the first neighbours being fixed (Fig 3.4B). This idealised model would be unlikely to occur *in vivo* as it represents a scenario where junctions are undergoing neighbour exchange, without any other junction movement occurring beyond the first neighbours. In this case, geometric constraints cause the first neighbours to increase in length, as a single junction is lost. Total junction length will increase during junction loss. Conversely total junction length will decrease as a new junction forms as the first neighbours decrease in length creating

space for the new junction to form into. Due to the fixed nature of the vertices, the aspect ratio will remain constant throughout.

Finally, our third model is a '*Fixed total length (sliding)*' model (Fig 3.4C). This model is created from anecdotal events that are seen in the notum and truly look like sliding. Fig. 3.5 represents such an example where 5 junctions are seen undergoing a half T1 event; only the shrinkage to a 4-way vertex is represented. In this example a first neighbour junction moves perpendicular (green arrow) to two parallel junctions: one that is lost (yellow junction) and another that concomitantly expands (blue junction). When we measure the cumulative length of the parallel junctions during junction loss we see that they are strongly anti-correlated; as one junction is lost, its neighbour increases in length (Fig 3.5C). Therefore, we can propose a model in which total junction length is retained. Junction loss and gain is compensated globally by increases and decreases in the length of first neighbours. To prevent over-compensation outer vertices of first neighbours are able to move slightly. This compensation will account for barely detectable changes in aspect ratio during contraction and expansion.

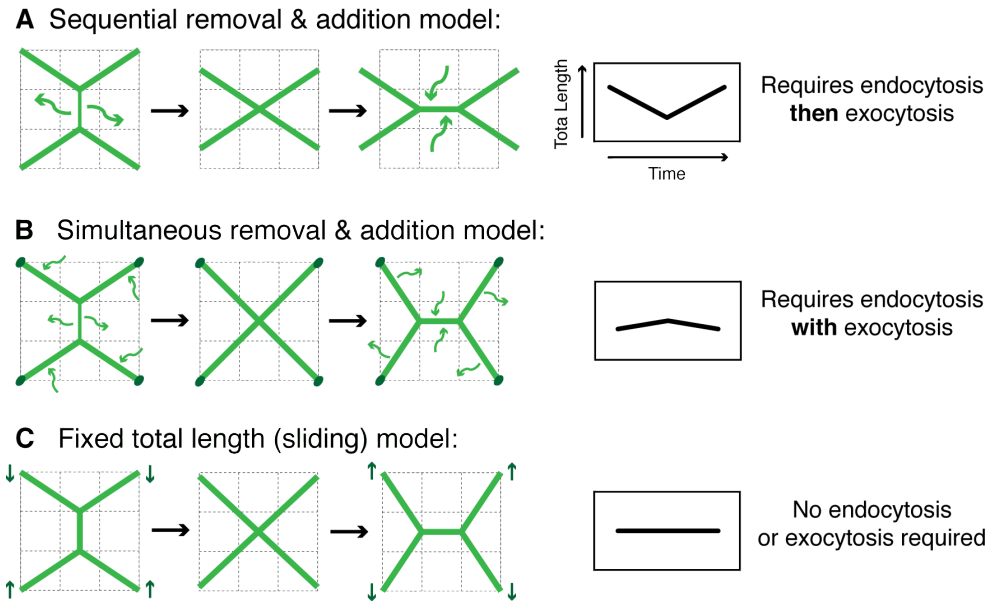


**Figure 3-4: Alternative T1 transition models.**

(**A**) ***Sequential removal & addition*** model: developed from germ band elongation. A junction is actively removed during loss and added during expansion. This causes total junction length to decrease and increase. (**B**) ***Simultaneous removal & addition*** model: first neighbour vertices are fixed during neighbour exchange. This requires addition of junction material to first neighbours to maintain contacts, as a junction is lost, and conversely a loss of first neighbour material to counteract expansion of a new junction. (**C**) ***Fixed total length (sliding)*** model: Junction material and total junction length is maintained throughout transition. Requires movement of first neighbour vertices.

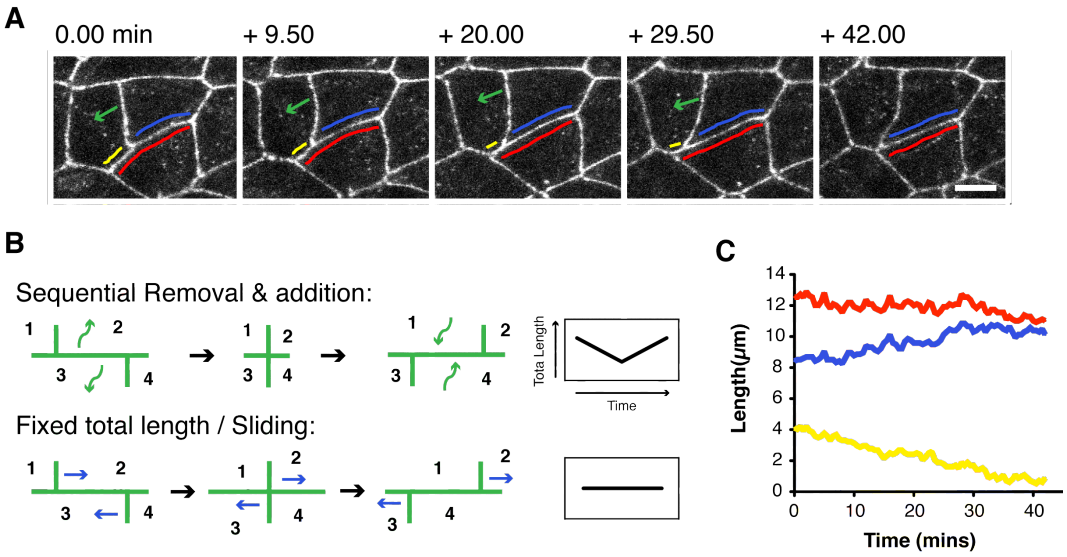


**Figure 3-5: Potential junction sliding**

(**A**) Time-lapse montage of a half- T1 event. Junction that is lost (yellow), parallel first neighbour (blue), cumulative length (red). Green arrow indicates movement of 3-way vertex along parallel junctions. Scale bar = 5µm. (**B**) Comparison of 'Removal and addition' and 'Sliding' models along straight lines. In a '*Sequential Removal and addition'* model total junction length decreases and increases during junction loss and gain, respectively. In a '*Fixed total length / sliding'* model total junction length remains stable. (**C**) Plot of lengths of junctions involved in the T1 event from **A**. Red = cumulative length of neighbouring junctions, Blue and Yellow, which changes little through time.

*; DE-cad-GFP(KI); pnrGAL4 / + ;*

(Leica SPE2, Larval development at 25$^{o}$C)

## 3.4 Neighbouring junctions are anti-correlated during cell intercalation

To look at how neighbour exchange events in the notum compare to the hypothetical models, tetrads of cells undergoing full T1 transition events were cropped and segmented from control DE-cadherin-GFP time-series (Fig. 3.6A). For each transition event, t=0 was defined as the time at which a four-way vertex was reached. For transitions where junctions fluctuated around the vertex, the middle of this period was selected as t0. For each transition I measured the lengths of the 5 junctions at each time interval.

I subtracted the length of junctions at the four-way vertex at t0 from all other time-points in order to plot the change in junction length through time. For plots 3.6B and 3.6C, data was removed for points immediately before and after t=0 as segmentation is poor for small junctions leading to bias.

As expected, when I plotted the total change in junction length for the junction that is lost and the newly formed junction, I observed a steady decrease in length before the four-way vertex and a steady increase in length thereafter (Fig 3.6B). Importantly, comparison of the two slopes shows that there is no significant difference between the rate of junction loss and expansion.

The total length of the four first-neighbours increased as a junction was lost, and decreased as a new junction was formed (Fig 3.6C). Moreover, as seen for the changing interface itself, the rate of length increase was not significantly different from the decrease. This result suggests that the lengths of first neighbours in the notum are anti-correlated with the length of the junction that is lost and formed. Consistent with this, the total change in length for all junctions fluctuated around 0μm throughout the transition (Fig. 3.6D).

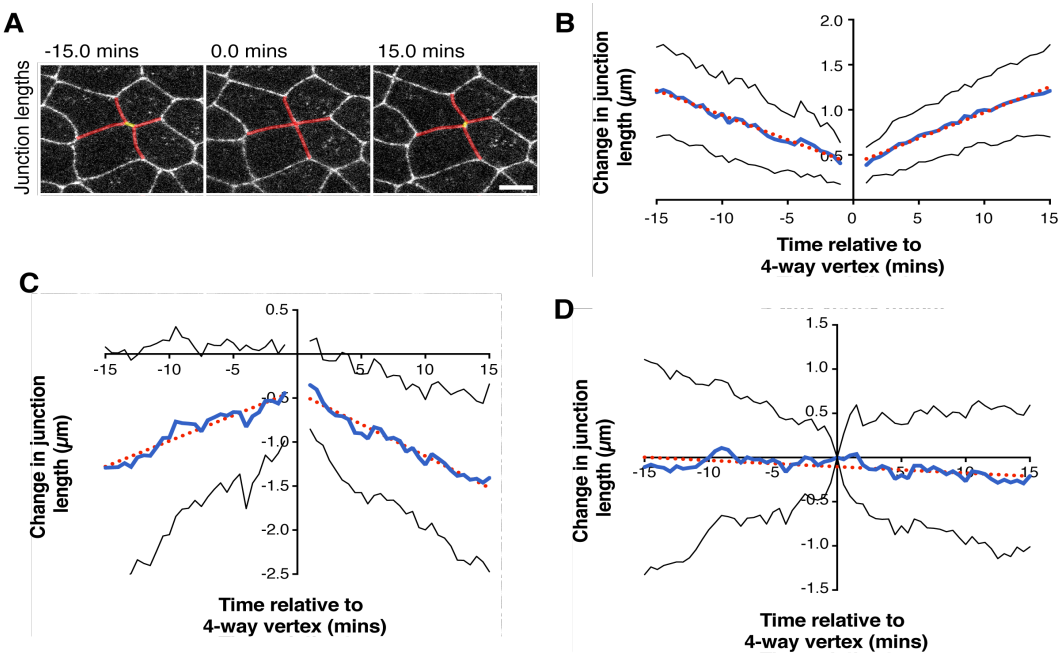


**Figure 3-6: Total junction lengths remain stable during neighbour exchange.**

(**A**) Measuring the change in length of junctions involved in a neighbour exchange event. Yellow labels the junction that is lost and gained. Red labels first neighbours. For all plots, the cumulative length at t0 (4-way vertex) is subtracted from the measured length at each time-point to give the change in junction length. (**B**) Plot of junctions that are lost and reformed during the exchange (yellow junction in the example T1). Slope of junction loss = -0.05463, $R^2$ = 0.24, Slope of expansion = 0.05714, $R^2$ = 0.32. Slopes are not significantly different, F = 0.363, p-value = 0.5468. (**C**) Plot of the cumulative length of the four first neighbours (red junctions). Slope pre- 4-way vertex = -0.0581, R = 0.06, post- 4-way vertex= 0.07215, $R^2$ = 0.13. Slopes are not significantly different, F = 2.125, p-value = 0.145. (**D**) Plot of the sum of all five junctions. Slope = -0.00712, $R^2$ = 0.01. For all plots blue line represents the mean, black lines S.D., red dots = line of best fit. n = 34 transitions / 5 nota. Scale bar = 5μm.

*; DE-cad-GFP(KI); pnrGAL4 / + ;*

(Leica SPE2, Larval development at 25°C)

### 3.5 Neighbour exchange does not contribute to changes in tissue shape

T1 transition events do not appear to be correlated with tissue morphogenesis in this system. However, these transitions are not polarised with respect to the A-P / D-V of the animal (Fig. 3.2), so could still contribute to local changes in tissue architecture that do not cumulatively alter tissue shape. To test whether T1s within tissue alter local cell organisation I measured changes in the shape of the four cells undergoing a neighbour exchange event 15 min before and after t=0. The 4-cell perimeter was used to calculate circularity (Fig. 3.7) and fitting an ellipse to the perimeter was used to measure elongation (Fig. 3.8)

Under a 'removal and addition' model, tetrads would become more isotropic during junction loss and would elongate during junction gain. If the perimeter of the cells were a perfect circle, the circularity value would equal 1, and would move closer to zero as the cell-perimeter became increasingly elongated. In the notum, however, T1 events are not associated with any change in circularity, as shown by comparing t=-15 and t=+15 to t=0 mins (Fig. 3.7B).

As an alternative measure one can fit an ellipse to a group of four cells and calculate its aspect ratio (AR) by measuring the relative length of the major and minor axes (Fig 3.8A). Again, there was no change associated with T1s at either t=-15 or t=+15 mins (Fig 3.8B). Moreover, when we compared the difference in angle orientation of individual tetrads at t=-15 to those at t=+15 there was little change in their orientation (Fig. 3.8C). During a GBE transition, since AP extension occurs perpendicular to DV contraction, one would expect the angle orientation of fitted ellipses to change by $90^{o}$. In the notum 88% of transitions were associated with a change in angle of less than $10^{o}$ as expected from the absence of global changes in tissue shape.

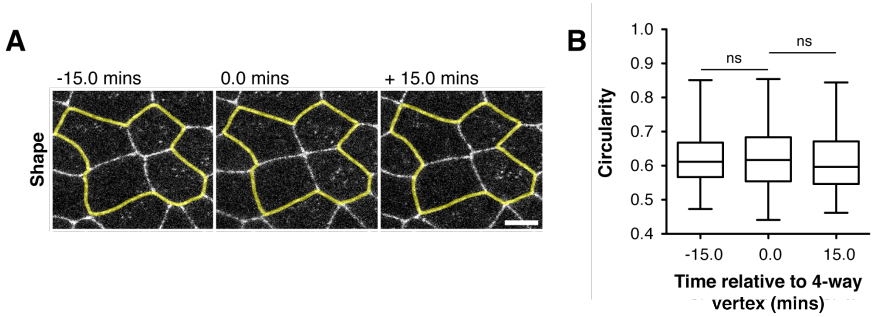


**Figure 3-7: T1 transitions do not lead to a redistribution of apical surface as measured by circularity**

(**A**) Circularity was measured from the perimeter (yellow) shape of the four cells undergoing neighbour exchange (circularity = 4π(area/perimeter^2)). (**B**) Circularity was measured at 15 mins before and after t=0. Line represents median, box represents 25$^{th}$ and 75$^{th}$ percentile, tail represents the full data range. An unpaired t-test was used to compare t=–15 to t=0 (p = 0.7467), and t=0 to t=+15 (p = 0.1490). n = 32 transitions from 5 nota.

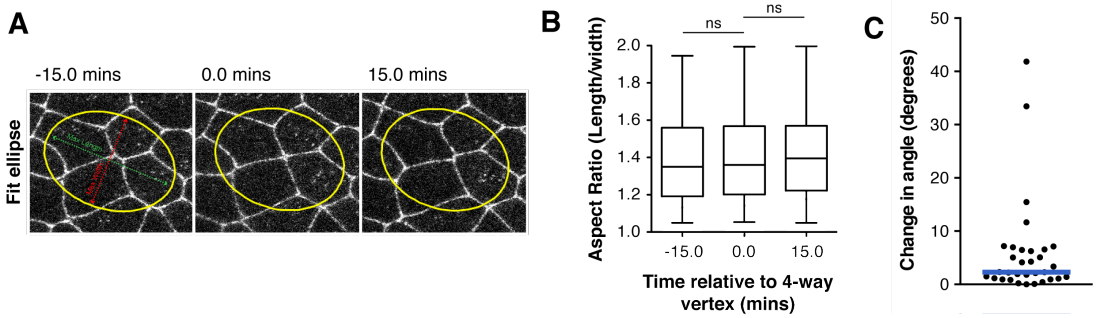


**Figure 3-8: T1 transitions do not affect the aspect ratio of four-cell clusters undergoing neighbour exchange**

(**A**) An ellipse (yellow) was fitted to clusters undergoing a T1 using FIJI, see Methods **2.12**. The max length and width were then used to calculate the aspect ratio (L/W) of the cluster. (**B**) The aspect ratio was measured at t=-15 mins, t=0, and t=+15. Line represents median, box represents 25$^{th}$ and 75$^{th}$ percentile, tail represents the full data range. An unpaired t-test was used to compare t=–15 to t=0 (P = 0.9760), and t=0 to t=+15 (P = 0.9501). (**C**) A dot plot shows the change in orientation of the ellipses during the T1 (from t=-15 to t=+15). Blue line = median. n = 32 transitions from 5 nota.

## 3.6 Junction loss and gain is associated with a respective decrease and increase in cell area

Neighbour exchange events typically change the number of sides and areas of the cells involved. To determine how packing was affected by T1s in this tissue, we measured changes in polygon distributions and cell areas. For each neighbour exchange event, the four cells involved were grouped as pairs depending on whether they lost or gained a junction during the process (Fig. 3.9A). We then plotted the mean number of sides (polygon number) cells have at t=-15 mins and t=+15. As expected, on average, cells that gained a junction increased their mean polygon number (Fig. 3.9B), and cells losing a junction decreased their mean polygon number (Fig. 3.9D). By tracking the change in area during the same period we observed that cells that gained a junction tended to gain apical area (Fig. 3.9C), with the opposite being true for junction loss (Fig. 3.9E). Therefore, although neighbour exchange events do not change the shape of clusters undergoing a T1, they do change the packing of cells within those clusters.

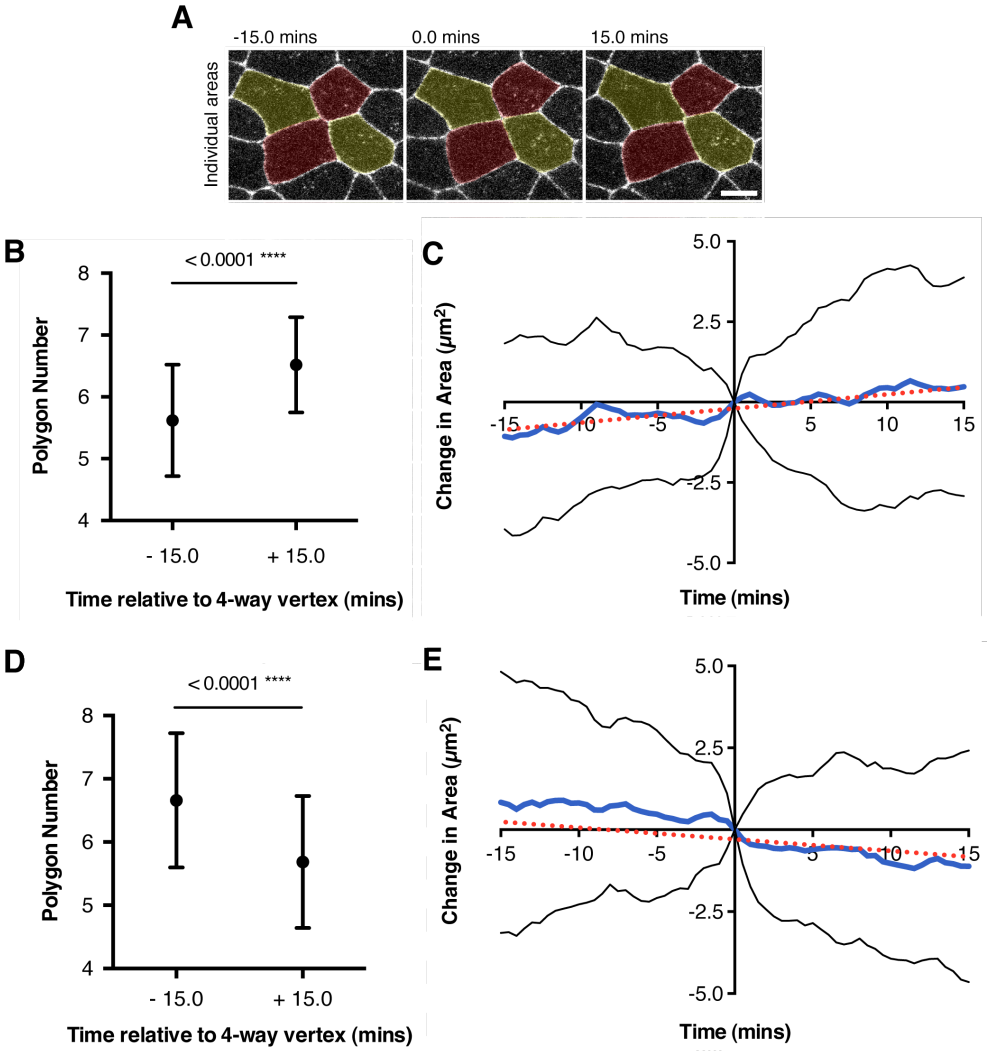


**Figure 3-9: Gain / loss of a junction is associated with a concomitant gain / loss in area**

(**A**) Yellow cells gain a junction through neighbour exchange. Red cells lose a junction. (**B**) Mean polygon number of cells gaining a junction pre- and post transition. Tails indicate SD. n= 50-54 cells. (**C**) Mean change in area (blue line) for cells gaining a junction (minus mean area at t=0) during the transition. Black lines = SD. Slope (red dotted line) = 0.044, $R^2$ = 0.06. n = 60 cells / 30 transitions. (**D**) As in B for cells losing a junction. n = 50-54 cells. (**E**) As in C for cells losing a junction. Slope = -0.0356, $R^2$ = 0.04. n = 60 cells (30 transitions). Unpaired t-test of slopes between C and E, p-value = 0.0058 ***.

### 3.7 Neighbour exchange leads to local and global changes in cell packing

Cells that gain a junction via neighbour exchange usually gain apical area, whilst cells that lose a junction suffer a loss in area. By grouping these data, we can ask how neighbour exchange events contribute to tissue order (Fig 3.10A). The total change in area of the cluster fluctuates around 0 throughout the transition (Fig. 3.10B). As a result, there was no significant change in apical area following a T1 (Fig. 3.10C).

Similarly, the change in mean number of sides before (6.140 sides) and after (6.102) the T1 is not significant (Fig. 3.D). This is to be expected as the mean is calculated from a fixed number of junctions that can only change if T1 events occur on the outside of the tetrad. Standard deviations also became smaller during T1s though the difference was not significant (1.110 to 1.004). However, when polygon distributions are plotted as a histogram we see a sharp increase in the proportion of hexagons from 34.0 to 40.7% (Fig 3.10E). Thus, although the difference is slight, T1s do tend to order the tissue.

To see how this translates into changes in packing at the tissue scale, polygon frequencies, as well as cell areas and junction lengths, were tracked between 12 and 13.5 h AP. In the absence of cell division any changes in frequency distribution are inferred to be a consequence of cell intercalation. By this measure the number of hexagons was found to increase from 37.4 % at 12 h to 43.5% at 13.5 h (Fig 3.11A). Mean polygon number (Fig 3.11B), mean cell area (Fig 3.11C), and mean junction length (Fig 3.11D) however remain stable throughout this period and their variances do not change. These results suggest that cell intercalation has a measureable but small impact on cell packing over this period.

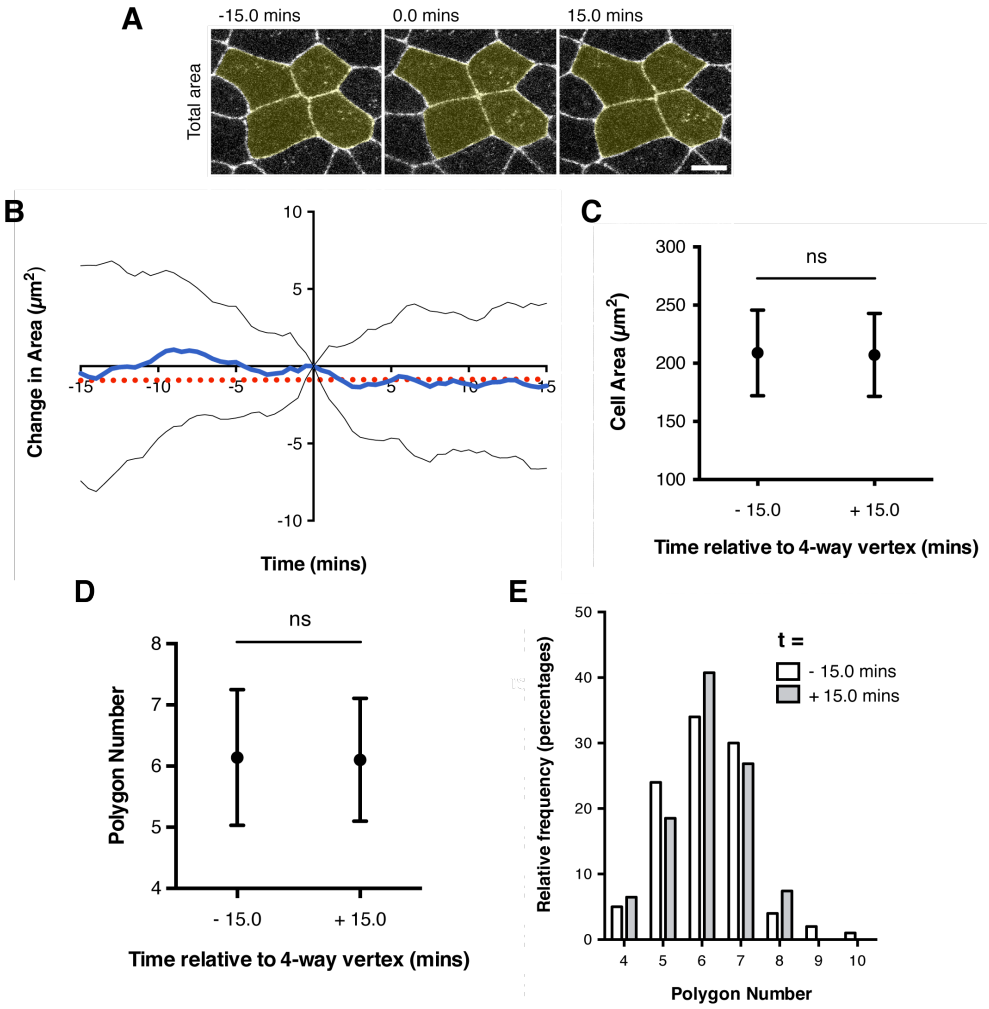


**Figure 3-10: Neighbour exchange leads to a small increase in hexagons for the cells undergoing the transition**

(**A**) The cumulative area of cells (yellow) undergoing a neighbour exchange event was measured. (**B**) The mean area of the cluster was measured (blue line) during a T1. Black line = SD. Slope (red dotted line) = 0.0024, $R^2$ = 0.00007. n = 30 transitions. (**C**) Cell area was measured 15 min before and after transition. -15 min, mean = 208.9µm$^2$, SD 36.9; +15 min, mean = 207.2µm$^2$, SD 35.6. Unpaired t-test p-value = 0.8525, ns; F-test to compare variances = 1.069, p-value = 0.8581, ns. n = 30 transitions. (**D**) Mean polygon number (+ SD) was measured before and after exchange. t=–15, mean = 6.140 sides, SD 1.110; t=+15, mean = 6.102 sides, SD 1.004. Unpaired t-test p-value = 0.795, F-test to compare variances = 1.223, p-value = 0.3077, ns. n = 100-108 cells / 30 transitions. (**E**) The polygon distribution for cells was shown before and after their transition through a neighbour exchange event.

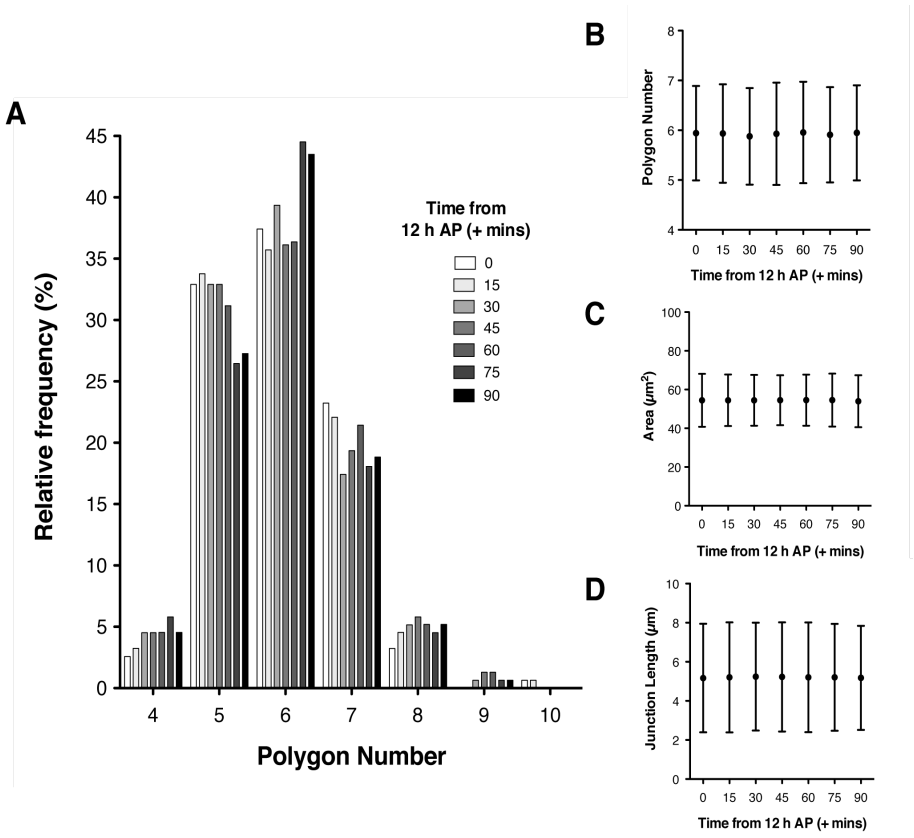


**Figure 3-11: Prior to cell division hexagonal cell packing increases.**

(**A**) Histogram of polygon distributions of cells over a 90' period starting at 12 h AP. We measured mean polygon number (+ SD) (**B**) and mean cell area (+ SD) (**C**) and mean junction length (+SD) (**D**). n = 154-155 cells from 3 flies for polygon and area measurements. Junction lengths were determined from 557-567 junctions from 3 flies.

## 3.8 Discussion

In this chapter I have introduced the *Drosophila* notum as an epithelial system in which to study neighbour exchange. In this tissue, frequent neighbour exchange events occur in the absence of cell division, delamination and overall changes in tissue size and shape. Nevertheless, neighbour exchange events in the scutum region appear randomly positioned in space and time, and are not oriented with respect to the A-P and D-V axes. Moreover, in many instances, T1s transitions were found to be reversible. These behaviours are different to those seen during GBE suggesting a very different model of neighbour exchange.

To explore this idea further we developed three alternate models of neighbour exchange: '*Sequential removal & addition'*, '*Simultaneous removal & addition'* and '*Fixed total length (sliding)*'. By studying individual T1 transition events in isolation we have been able to quantitatively compare *in vivo* neighbour exchange dynamics to each model.

In this tissue, the loss of a single junction was found to be precisely compensated by increases in the length of its first neighbours. As a result, total junction length remained stable throughout the transition. This suggests that neighbours may slide past one another in counter activity with the behaviour described for GBE.

At the same time neighbour exchange events do not change the aspect areas of the cells involved. Cells that gain junctions increase their apical areas, whilst cells that lose junctions decrease in area. However, the total cell area remains constant throughout this exchange. This explains the failure of neighbour exchange to contribute to morphogenesis. Nevertheless, cell intercalation improves tissue packing by leading to a marginal increase in the proportion of hexagonal cells.

In conclusion, neighbour exchange in the notum appears to be profoundly different to that occurring in the developing embryo, where it is driven and associated with morphogenesis. More specifically, cells in the notum appear to slide past one another during neighbour exchange without a loss of junctional material or area. In Chapter 6 we will continue to compare the sliding and geometric models by testing the

contribution of adherens junction turnover. During GBE cell intercalation is driven by actomyosin dependent contractility. Therefore, building on these observations, in the next chapter we will explore the requirement of actomyosin for neighbour exchange in the notum and the impact of altered active Myosin-II levels on junction dynamics.

# 4. A loss of active Myosin II increases tissue fluidity

## 4.1 Introduction

The sliding of actin filaments by the molecular motor, non-muscle Myosin II, produces intercellular contractile force. Transient linkage of the actomyosin cytoskeleton to the adherens junction allows forces to be transmitted from cell to cell via homophilic DE-cadherin interactions between neighbours. Contractile force can also mediate the loss of the discrete cell-cell contact it is acting on by mechanical force and by promoting the loss of junctional material through endocytosis.

For neighbour exchange to induce a change in tissue shape it must be polarised across the tissue. In the germ band, polarised Rho kinase distribution is generated by Rho GTPase and enhanced by the actin-binding protein Shroom (Simoes Sde et al., 2014). In the scutellum, the polarised distribution of the atypical Myosin Dachs is poorly understood but involves Fat signalling and the DHHC palmitoyltransferase protein Approximated (Matakatsu and Blair, 2008). Any obvious PCP pathway appears to be absent from the medial scutum, the region studied here, as neighbour exchange events occur randomly and without orientation, and moreover junction fluctuations are not cumulatively contributing to tissue deformation.

It therefore seems unlikely that Myo II would be polarised or recruited, in a similar way to GBE, to discrete and randomly oriented junctional units. Nevertheless Myo II pulsing could create noisy fluctuations that impose neighbour exchange events on the tissue, though this would not account for the self-organising nature of the transitions. In this chapter, I utilise the UAS-GAL4 system to modulate actomyosin activity across the notum. I confirm the effects of altering Myo II levels through live imaging and immunohistochemistry before quantifying the impact of these perturbations on tissue tensions through laser ablation experimentation. Ultimately I assess the requirement of actomyosin contractility for neighbour exchange.

## 4.2 Junctional Myosin II is not polarised across the tissue

To determine the localisation of Myo II in the tissue, I imaged Sqh-GFP alongside ubi-Bazooka-mCh for single time-points at 12 h AP (Fig 4.1A). Spaghetti-Squash (Sqh) encodes Myosin regulatory light chain (MRLC) and was used to visualise

localisation of total Myo II by expressing Sqh-GFP in a Sqh null ($Sqh^{Ax3}$) background (Royou et al., 2004). Bazooka, the *Drosophila* homolog of Par3, is a scaffold protein that localises to the apical junction as part of the Par complex (Bosveld et al., 2012; Morais-de-Sa et al., 2010). I used this marker to track junction dynamics as its localisation overlaps with DE-cadherin (Appendix Fig. 9.3). I avoided using E-cadherin-mCh as it tends to clump and bleach in the notum (not shown).

First, this revealed that junction lengths have a non-Gaussian distribution. As expected, short junctions are more frequently observed than long junctions (Fig 4.1B). However, the distribution of junction lengths was not polarised, with respect to the A-P axis (Fig 4.1C). As there appear to be no PCP biases in the system, it makes sense that junction lengths do not correlate with angle.

Our goal was to determine whether there were any biases in Myo II (and less-so Baz) localisation. Individual mean intensities for both Sqh-GFP and Baz-mCh were normalised to the global mean intensity and plotted against junction length (Methods 2.13). Bazooka intensity did not correlate with junction length (Fig 4.1D), whilst Myo II levels were very slightly negatively correlated (Fig 4.1E). Thus, short junctions tended to have slightly higher Myo II intensity per μm than longer junctions (~10% difference for 5-fold changes in length). Myo II and Baz intensities were compared for individual junctions in the notum and, somewhat surprisingly (Zallen and Wieschaus, 2004), no correlation was observed (Fig. 4.1F). Importantly though, when normalised Myo II intensities were plotted against junction orientation, the distribution was not found to be polarised (Fig. 4.1G). In this the notum differs from the embryonic germ band, where an anti-correlated distribution of Myosin II and Bazooka correlation is observed, with Myo II enriched along D-V oriented junctions.

To see if the localisation of Rok mirrors that of Myo II, the experiment was repeated using a non-catalytic Venus-tagged Rho-kinase (Fig. 4.2A) (Simoes Sde et al., 2010; Winter et al., 2001). Rok-Venus appeared to predominantly localise to 3-way vertices, but like Myo II, was negatively correlated with junction length. This negative correlation however, was much stronger for Rok-Venus (45% difference in

intensity for a 5-fold change in length) (Fig. 4.2B). This however, could be due to bias generated by increased Rok-Venus intensity at 3-way vertices. Furthermore, no correlation was observed between Rok-Venus and Baz-mCh (Fig. 4.2C), and Rok did not appear to be polarised (Fig. 4.2D). Again this lack of correlation differs from the situation in the germ band where Rok phosphorylates Baz to control its localisation.

In other tissues Myo II has been shown to actively drive junctional shortening and neighbour exchange. Although Myo II was not polarised in the notum it could still play a role in these processes. To test this we investigated how changes in Myo II activity affected junctional dynamics and T1 counts.

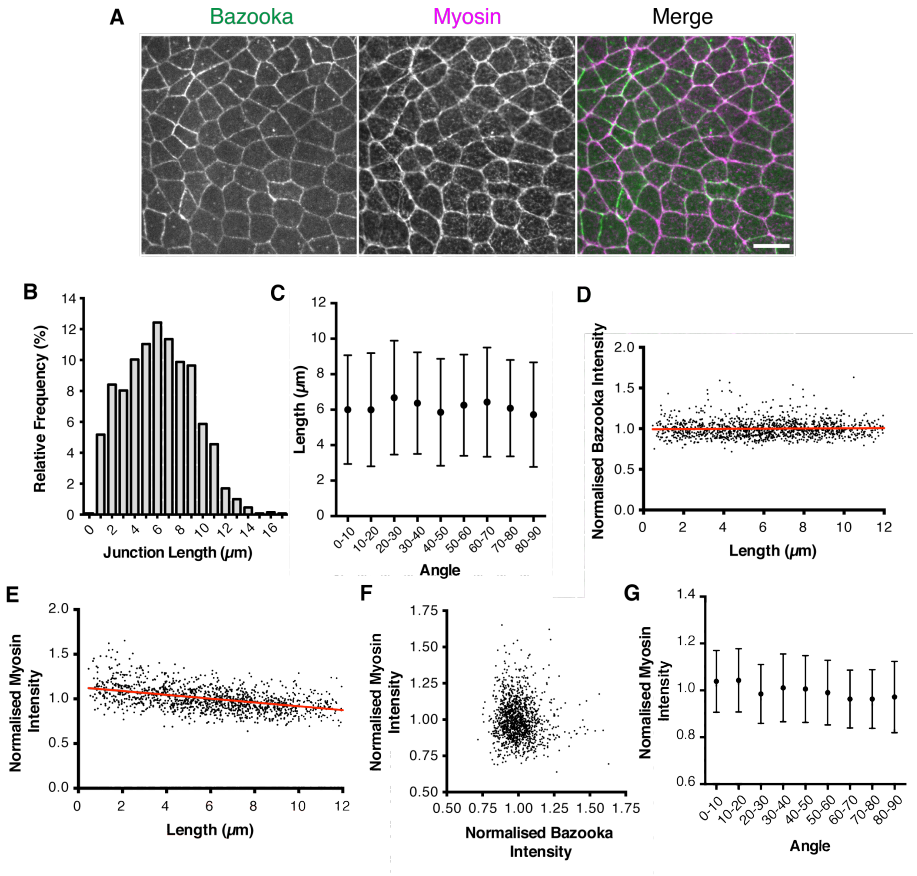


**Figure 4-1: Junctional Myosin II exhibits an unpolarised distribution in the notum.**

(**A**) Nota imaged with Bazooka-mCh and Spaghetti-Squash-GFP (Myosin regulatory light chain). Scale bar = 5µm. (**B**) Histogram plotting distribution of junction lengths. (**C**) Junction lengths plotted against angle. 90 degrees = perpendicular to midline. (**D**) Normalised Bazooka-mCh intensity (Intensity/median intensity) versus junction length. Slope = 0.001, $R^2$ = 0.001. Spearman's Rank = -0.06. (**E**) Normalised Myosin-GFP intensity versus length. Slope = -0.021, $R^2$ = 0.21. Spearman's Rank = -0.47. (**F**) Normalised Bazooka intensity versus normalised Myo II intensity. Spearman's rank = -0.07. (**G**) Normalised Myo II intensity versus angle. N = 1295 junctions / 5 flies.

*$Sqh^{Ax3}$ / + or Y ; Sqh-GFP / If or Cyo ; ubi-Baz-mCh / + ;*

(Carl Zeiss Axiovert, Larval Development at 25°C)

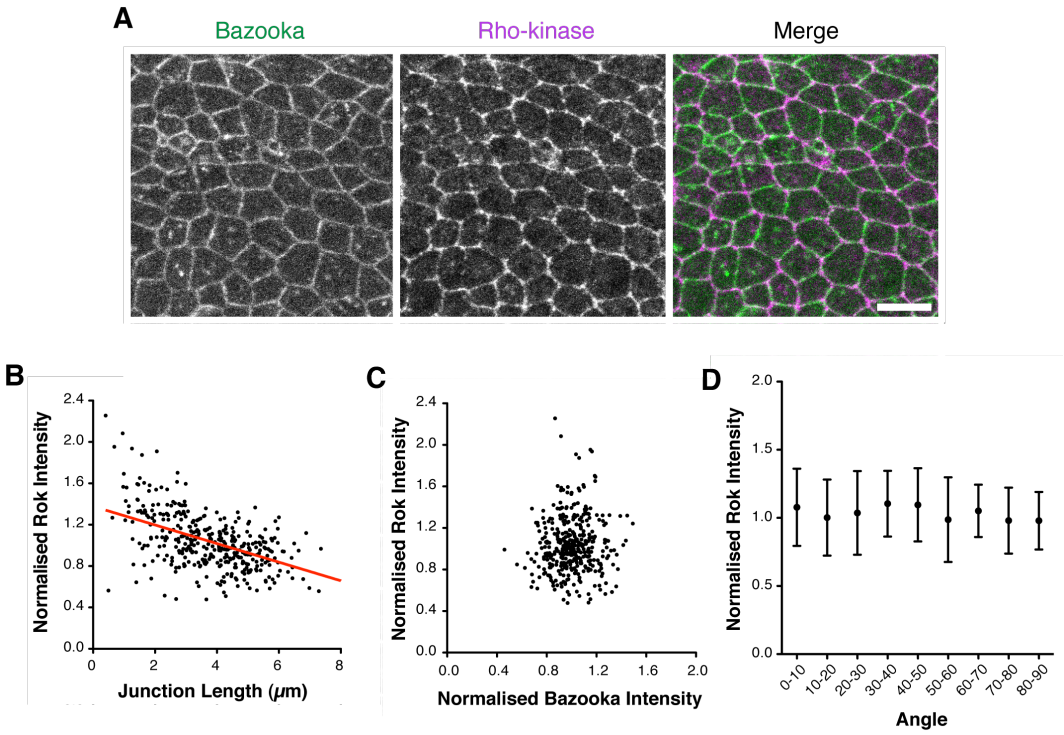


**Figure 4-2: Rho kinase negatively correlates with junction length.**

(**A**) Nota imaged with Bazooka-mCh (AJ) and Rok-Venus. Scale bar = 5µm. (**B**) Normalised Rok intensity (to median intensity) versus junction length. Slope = -0.09, $R^2$ = 0.251. Spearman's R = -0.49. (**C**) Normalised Rok intensity versus normalised Bazooka-mCh intensity. Spearman's rank = 0.06. (**D**) Normalised Rok intensity versus angle. 90°C = perpendicular to midline. N = 384 junctions from one fly.

*; If or Cyo / sqh-Rok-Venus$^{K116A}$ ; ubi-Bazooka-mCh / + ;*

(Leica SPE2, Larval development at 25oC)

## 4.3 Over-active Myosin II induces junction breaks

To determine the effect of altered Myo II levels on the adherens junction, UAS-Myosin II constructs were expressed using the notum specific promoter, *pannier*, and the tissue imaged with DE-cadherin-GFP. To reduce Myo II levels, RNAi was used to silence Rok, a kinase required for minifilament assembly and Myo II activity. In addition, I induced expression of an inactive Sqh variant ($Sqh^{AA}$) in which threonine-20 and serine-21 are replaced with alanines (Dorsten et al., 2007; Jordan and Karess, 1997). For the converse experiment, I increased Myo II activity by expressing a constitutively active version of Rok (Rok CAT), which lacks the regulatory N-terminus (Verdier et al., 2006). In parallel, I expressed an active form of MRLC, $Sqh^{EE}$, in which Threonine-20 and Serine-21 have been replaced with the phosphomimetic glutamic acid (Bertet et al., 2009; Jordan and Karess, 1997; Winter et al., 2001). Finally, RNAi was used to knockdown expression of Sds22, which encodes a PP1 phosphatase regulatory subunit that binds to all four *Drosophila* PP1s to negatively regulate both Myo II and Moesin (Grusche et al., 2009). I shall discuss the effect of *UAS-Sds22*$^{RNAi}$ on Moesin localisation in next chapter.

To test if these perturbations worked, I looked at Myo II in fixed tissue for control, *UAS-Rok*$^{RNAi}$, *UAS-Rok*$^{CAT}$ and *UAS-sds22*$^{RNAi}$ cells at 12 h AP. For these experiments I stained against DE-cadherin-GFP, F-actin and Myo II phosphorylated on Serine 19 of the regulatory light chain (Fig 4.4A). DE-cadherin and F-actin stainings appeared identical in *UAS-Rok*$^{RNAi}$ versus the control. However, p-Myo II was completely lost following Rok silencing. In contrast, medial F-actin structures are observed and the junctional p-Myo II levels were dramatically increased in $Rok^{CAT}$ and Sds22 cells. By focussing on the vertices we observe that increased p-Myo II levels are found with junction breaks and discontinuities, as represented by a loss of DE-cadherin staining (Fig 4.4B). These breaks are absent in the *UAS-Rok*$^{RNAi}$ knockdown. Furthermore, maximum projection images from DE-cadherin-GFP live imaging showed that neither *UAS-Rok*$^{RNAi}$, nor expression of an inactive Myo II (*UAS-sqh*$^{AA}$) altered junctional integrity. In both cases DE-cadherin-GFP intensity was smooth along the junction and present at vertices, as it was in the control (Fig. 4.4A).

However, all three treatments increasing Myo II activity phenocopied one another, inducing adherens junction breaks and discontinuities (Fig 4.4A). Punctate DE-cadherin GFP structures were observed and DE-cadherin was often found missing from vertices (arrows in Fig. 4.4A). Moreover, as cells undergo a neighbour exchange event, DE-cadherin was found to be lost from the four-way vertex. DE-cadherin then remained absent from the initial phase of junctional expansion (Fig. 4.4B). These breaks suggest both that E-cadherin cannot flow in to these junctions, and that the tissue is under high tension

While phosphorylated Myo II can only be observed in fixed stainings, the total pool of Myo II can be used as a proxy for active Myo II in live imaging using mCherry-tagged MRLC. When we combined this with *DE-cadherin-GFP*, we observed that *UAS-sds22*$^{RNAi}$ increased total junctional Myo II levels, as did RNAi knockdown of Mbs, the Myosin-binding subunit of Myosin-phosphatase and MYPT-75D (Fig 4.5A), (Alessi et al., 1992; Hartshorne, 1998; Vereshchagina et al., 2004). Conversely, Myo II was lost from the junction and apical cortex in *UAS-Rok*$^{RNAi}$ tissues.

To determine the impact of constitutively active Rok, total Myo II was imaged using an endogenously tagged Zipper-YFP line (Knowles-Barley et al., 2010) (This line could not be used to image either *UAS-Rok*$^{RNAi}$ or *UAS-sds22*$^{RNAi}$ as it causes lethality). Using this reporter, we could see that *UAS-Rok*$^{CAT}$ expression caused long Myo II cables to extend across the medioapical surface of cells in an A-P orientation, parallel to the midline (Fig. 4.5B), while the control looked much like that as observed with staining and mCherry imaging.

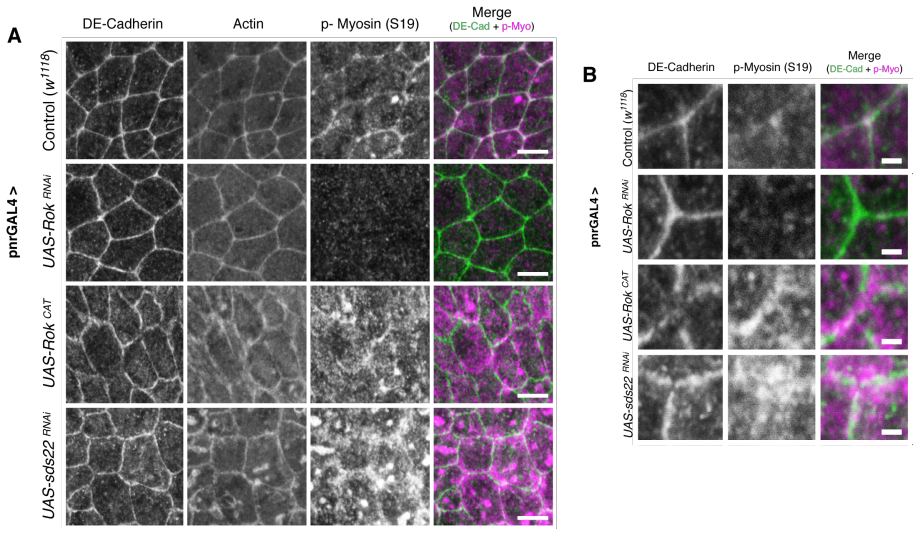


**Figure 4-3: Rok knockdown reduces levels of phosphorylated Myosin II at junctions**

(**A**) Representative tissues of control, *UAS-Rok*$^{RNAi}$, *UAS-Rok*$^{CAT}$ and *UAS-sds22*$^{RNAi}$. Tissues were fixed and stained for E-cadherin (anti-GFP against *DE-cadherin-GFP*), F-actin (Phalloidin) and p-Myo II (S19). Scale bar = 5µm. (**B**) Increased zoom of vertices. Scale bar = 1µm.

*DE-cad-GFP(KI) / + ; pnrGAL4 / +* (Larval development at 29°C)
*DE-cad-GFP(KI)) / UAS-Rok*$^{RNAi}$ *; pnrGAL4 / +* (Larval development at 29°C)
*DE-cad-GFP(KI) / + ; pnrGAL4 / UAS-Rok*$^{CAT}$ (Larval development at 29°C)
*DE-cad-GFP(KI) / UAS-sds22*$^{RNAi}$ *; pnrGAL4 / +* (Larval development at 29°C)

(Imaged on Leica SP5)

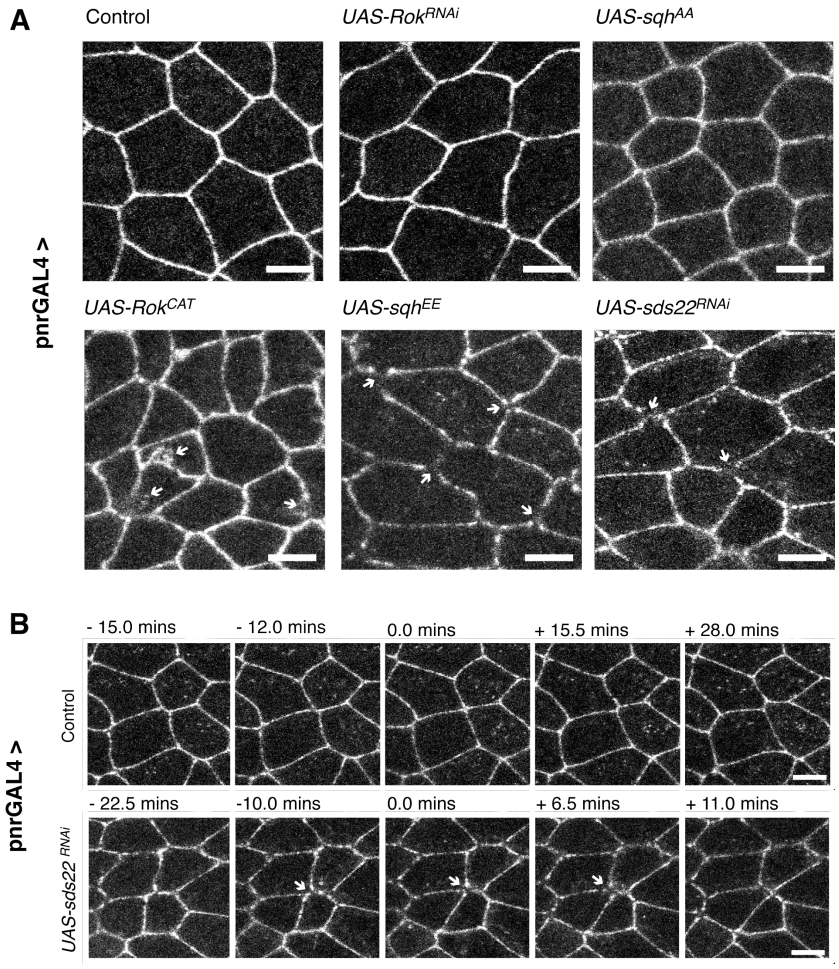


**Figure 4-4: Increasing phospho-Myosin II levels cause junction breaks.**

(**A**) Representative DE-cadherin-GFP images of pnrGAL4 driven UAS constructs decreasing p-Myosin II levels (*UAS-Rok*$^{RNAi}$ and *UAS-sqh*$^{AA}$), increasing p-Myosin II levels (*UAS-Rok*$^{CAT}$ and *UAS-sqh*$^{EE}$) and increasing both p-Myosin II and p-Moesin (*UAS-sds22*$^{RNAi}$). Arrows label junction discontinuities. (**B**) Time-lapse montage of a neighbour exchange event for control and *UAS-sds22*$^{RNAi}$. Arrows label defects. Scale bars = 5µm.

*w*$^{1118}$*; DE-cad-GFP(KI) / +; pnrGAL4 / +* (Larval development at 29°C)
*DE-cad-GFP(KI) / UAS- Rok*$^{RNAi}$*; pnrGAL4 / +* (Larval development at 29°C)
*DE-cad-GFP(KI) / +; pnrGAL4 / UAS-sqh*$^{AA}$ (Larval development at 29°C)
*DE-cad-GFP(KI) / +; pnrGAL4 / UAS- Rok*$^{CAT}$ (Larval development at 29°C)
*DE-cad-GFP(KI) / +; pnrGAL4 / UAS- sqh*$^{EE}$ (Larval development at 29°C)
*DE-cad-GFP(KI) / UAS-sds22*$^{RNAi}$*; pnrGAL4 / +* (Larval development at 29°C)

(Leica SPE2)

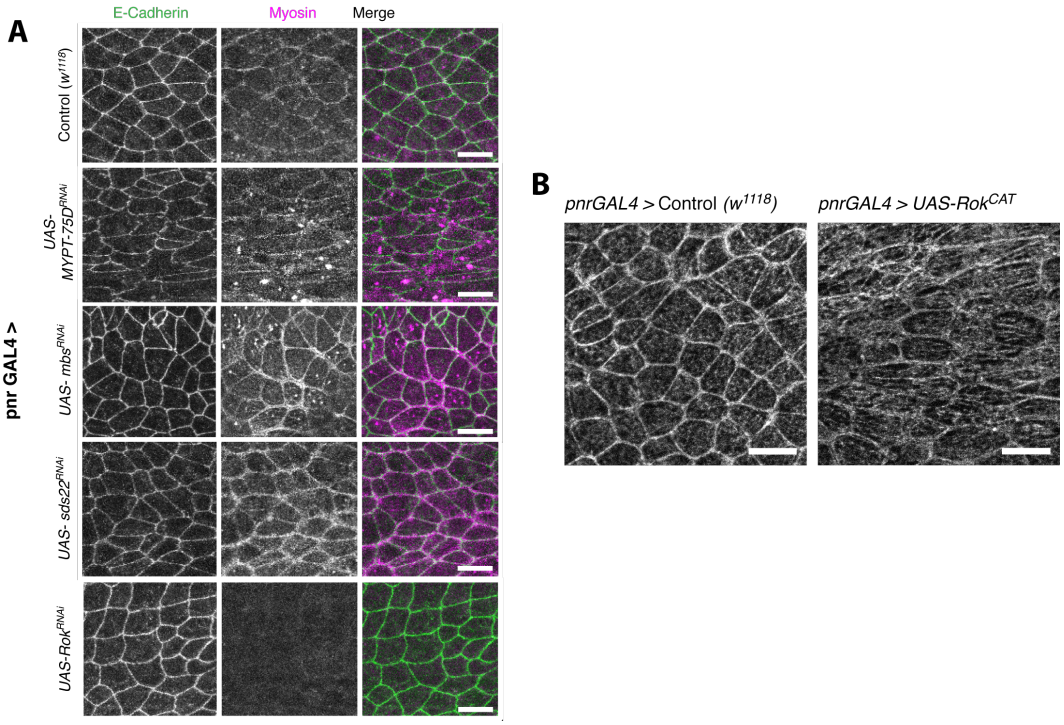


**Figure 4-5: Impact of phosphatases and Rok knockdown on levels of junctional Myosin II**

(**A**) Maximum projection images of representative nota labelled with ubi-E-cadherin-GFP and Spaghetti-Squash-Cherry (MRLC - labelling total Myosin II). Scale bar = 25µm. (**B**) Representative nota imaged with Zipper-YFP (Myosin heavy chain, MHC). Scale bar = 10µm.

*$w^{1118}$ ; ubi-E-cad-GFP / +; pnrGAL4 / +* (Larval development at 29°C)
*ubi-E-cad-GFP / +; pnrGAL4 / UAS-$mbs^{RNAi}$* (Larval development at 18°C)
*ubi-E-cad-GFP / +; pnrGAL4 / UAS-MYPT-$75D^{RNAi}$* (Larval development at 29°C)
*ubi-E-cad-GFP / UAS- $sds22^{RNAi}$; pnrGAL4 / +* (Larval development at 29°C)
*ubi-E-cad-GFP / UAS- $Rok^{RNAi}$; pnrGAL4 / +* (Larval development at 29°C)
*Zip-YFP / +; pnrGAL4 / +* (Larval development at 29°C)
*Zip-YFP / +; pnrGAL4 / UAS-$Rok^{CAT}$* (Larval development at 29°C)

(Leica SPE2)

## 4.4 Increased Myosin II phosphorylation increases the stable pool of DE-cadherin at the adherens junction

The appearance of AJ discontinuities in conditions in which Myo II was hyper-activated suggested the possibility that Myo II could prevent the sliding of AJ contacts. A similar process was suggested to occur in the *Drosophila* embryo, where a contractile actomyosin network has been shown to prevent lateral movement of stable DE-cadherin clusters (Cavey et al., 2008). This tethering is mediated through α-catenin, which transiently links the actomyosin cytoskeleton with ß-catenin, or links more stably through other actin-interacting proteins (Abe and Takeichi, 2008).

To test this and to assess the impact of altered p-Myosin II levels on DE-cadherin movement along a junction, I used fluorescence recovery after photobleaching (FRAP). In flies expressing endogenous levels of DE-cadherin-GFP, individual junctions were bleached between vertices using high 488 nm laser power (Fig. 4.6A). First raw intensity profiles were plotted through time (Fig 4.6B), then the fluorescence recovery was normalised to relative pre-bleach intensities (See Methods 2.8). A curve was fitted to the data representing a 2-phase recovery (Fig. 4.6C) (Appendix: Table 9.1 for statistical comparisons of Fast and Slow phases). From the curves, the maximum recovery or plateau was calculated. The height of the plateau is indicative of the mobile DE-cadherin pool that recovers, whilst the proportion above the plateau represents the immobile pool, which doesn't recover.

For all conditions, fluorescence intensity never returned to pre-bleach levels (Fig. 4.6C). The percentage recovery for control experiments was 44.7% (Fig. 4.6D) and was not affected by Rok knockdown. However the full RNAi curves appears different from control, with a significantly steeper initial fast phase (Fig 4.6C and Appendix Table 9.1). By contrast, increasing p-Myosin II by expression of *UAS-Rok*$^{CAT}$ and *UAS-sds22*$^{RNAi}$ reduced the recovery to 35.5 and 37.2%, respectively, as expected if there were increased levels of relatively immobile cadherin complexes bound more tightly to actin in this context.

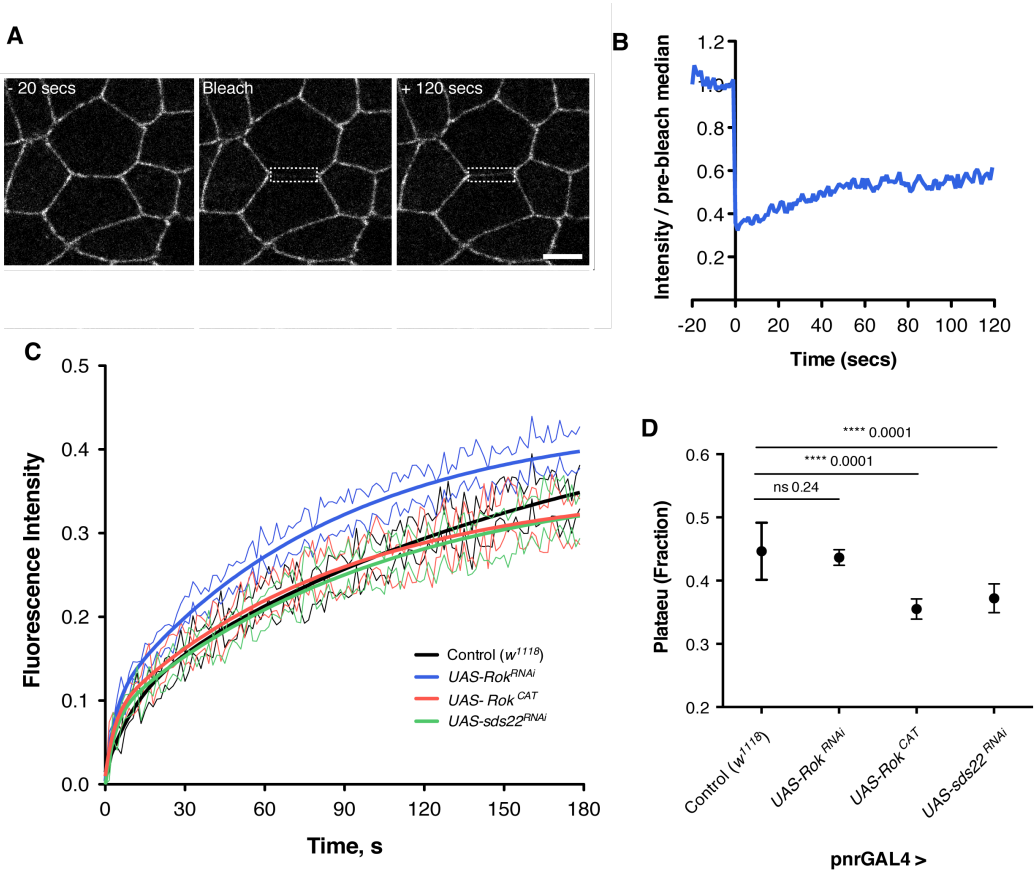


**Figure 4-6: FRAP experiments show changes in DE-Cadherin turnover following changes in Myosin II levels**

(**A**) Example of control FRAP experiment. Junctions labelled with DE-cadherin-GFP-KI. Dotted rectangle indicates bleach region. Scale bar = 2µm. (**B**) Raw intensity recovery of experiment in **A**. (**C**) Two-phase association line fitted to mean fluorescence intensity recovery data, with SEM (thin lines). (**D**) Percentage recovery calculated from two-phase association lines fitted to individual experiments. Line indicates median. n = 30-35 experiments from 3-5 flies per condition.

## 4.5 Increases and decreases in p-Myosin II levels correspond to relative changes in line tension

The previous experiments showed how p-Myosin II levels could be changed through the expression of RNAi and/or overexpression of constitutively active constructs. To enable these results to be related to junctional tension, junctions were cut using two-photon excitation in the plane of the AJ, visualised with DE-cadherin-GFP (Methods 2.7) (Fig. 4.7A). Kymographs were generated to visualise recoil across the two vertices of the cut junction (Fig 4.7B). By following the XY coordinates of the vertices and plotting the distance between them through time, the vertex displacement at differing time intervals could be calculated (Methods 2.7). Comparable junction lengths (ranging from 4 to 10µm) were used for each experiment to avoid problems with length dependent forces (Appendix Fig. 9.4). Total vertex displacement was calculated at 10 s, rather than the very first time point after ablation, as displacement in the notum was more gradual when compared to that seen in other systems, such as the wing disc (Mao et al., 2013).

Using this protocol, junctions in *UAS-Rok*$^{RNAi}$ nota were found to be under less line tension than control (Fig. 4.7C), as expected based upon: (Farhadifar et al., 2007; Fernandez-Gonzalez et al., 2009; Landsberg et al., 2009). Most junctions failed to undergo visible recoil in *UAS-Rok*$^{RNAi}$ flies. Moreover, several cuts had a negative displacement, since the two junction halves moved towards one another after the cut. Overall however, a low residual level of tension was observed in *UAS-Rok*$^{RNAi}$ experiments. In keeping with this result most junctions moved apart from one another over the full 2 mins of imaging in this background (Fig. 4.7D).

For perturbations that increase active levels of junctional Myo II: *UAS-Rok*$^{CAT}$, *UAS-MYPT-75D*$^{RNAi}$ and *sds22*$^{RNAi}$; significant (~30%) increases in vertex displacement at 10 s were observed when compared to control cuts (Fig. 4.6C). These results are in keeping with published data (Fernandez-Gonzalez et al., 2009) and suggest that Myosin II is regulating junction tension in the notum.

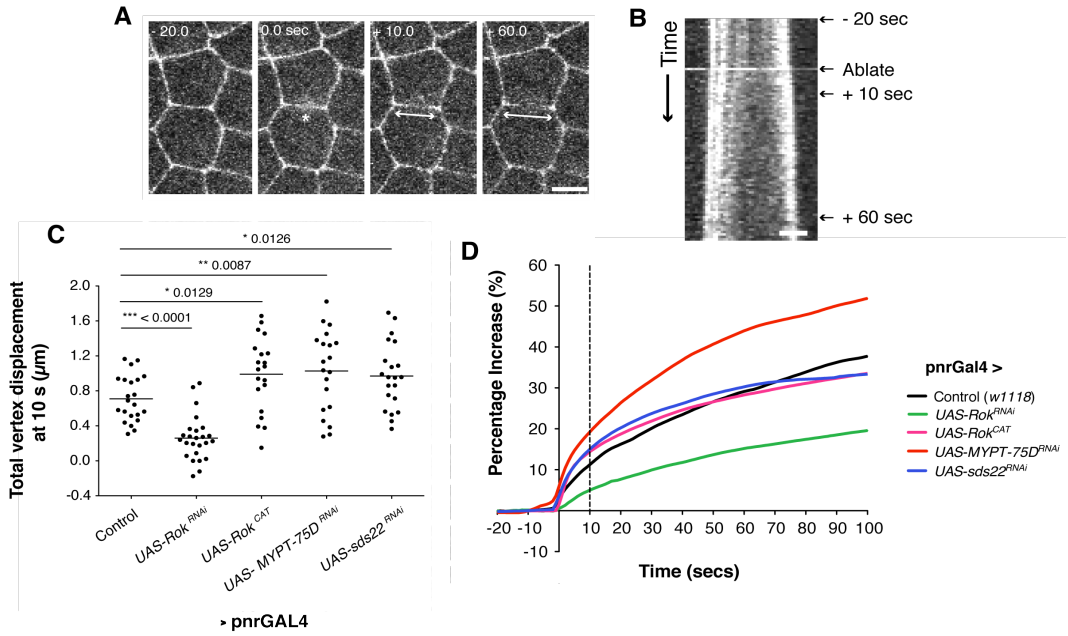


**Figure 4-7: Increased Myosin II phosphorylation increases across junction tension**

(**A**) Time-lapse montage of control laser ablation experiment. Scale bar = 2μm. Star indicates site of ablation; arrows indicate direction of displacement. (**B**) Kymograph of experiment from which XY coordination of the two vertices are measured. (**C**) Total vertex displacement measured at 10 s after ablation. Dots indicate individual experiments. Line indicates median. 4-7 flies per condition. P-values calculated from unpaired t-test. (**D**) Mean displacement measured as a percentage of pre-ablation median length. SEM not shown.

## 4.6 Increasing levels of p-Myosin II cause apical constriction

Having shown how changes in Myosin II activity impacts locally on individual line tensions, we wished to see how increasing or decreasing Myosin II levels affected global cell packing, since our UAS-RNAi / overexpression constructs are expressed across the tissue.

Rok knockdown caused a reduction in the frequency of hexagonal cells (6-sided, not an indication of shape). This occurred as a result of an increase in the frequency of pentagons. Similarly both pentagons and heptagons increased for increased Rok activity, with a reduction in hexagonal packing (Fig 4.8A). Both *UAS-Rok*$^{RNAi}$ and *UAS-Rok*$^{CAT}$ had a similar frequency of outliers to control, suggesting that changes in Myo II levels were not causing dramatic changes in cell morphology (Fig. 4.8A). For all other measures, *UAS-Rok*$^{RNAi}$ nota were indistinguishable from the control. Comparisons of cell areas (Fig. 4.7B), junction lengths (Fig. 4.8C), and ellipse elongation (Fig. 4.8D) all appeared similar.

However, increasing Myo II levels with *UAS-Rok*$^{CAT}$ within the *pannier* region reduced cell areas (Fig. 4.8B) and led to a corresponding loss in junction length (Fig. 4.8C). This may be because increasing intracellular contractile forces are transmitted across the *pnr* domain through adherens contacts. Interestingly for increased Rok activity, cells were more elliptical than they were in control (Fig. 4.8D). This fits with our previous observation that *UAS-Rok*$^{CAT}$ produces intracellular medial Myo II cables that run parallel to the midline and correlates with elongation along this axis (Fig. 4.5B). These results are not unexpected and suggest that Myosin II can generate forces that can be felt tissue-wide, as seen with increasing cortical contractility and line tension in the Farhadifar phase-space diagram (Fig. 1.5).

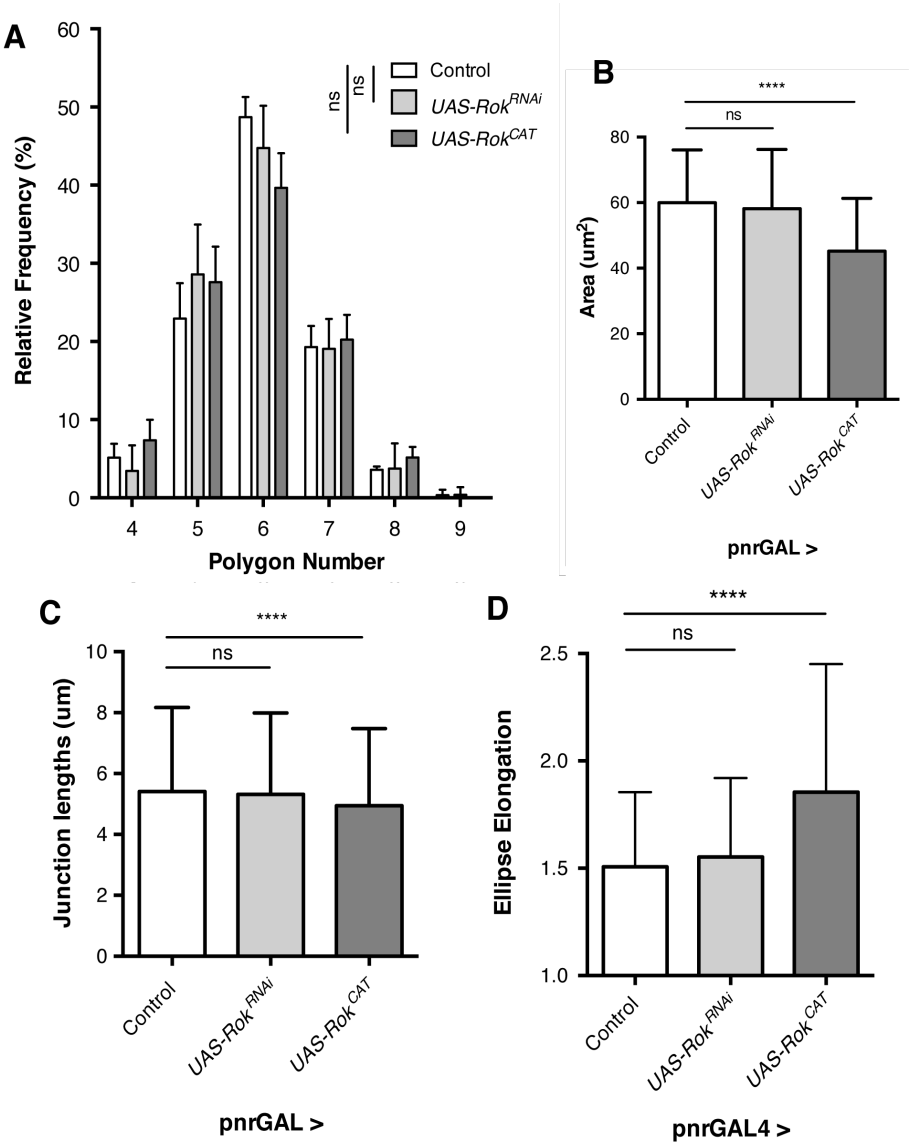


**Figure 4-8 Constitutively active Rok causes smaller and more elongated apical shapes.**

(**A**) Histogram of polygon distribution for Control, *UAS-Rok*$^{RNAi}$ and *UAS-Rok*$^{CAT}$. Error bars indicate standard deviation between individuals. P-values from unpaired t-tests for Control v *UAS-Rok*$^{RNAi}$ = 0.8967 (ns), Control v *UAS-Rok*$^{CAT}$ = 0.5338 (ns). P-values from F-tests to compare variance for Control v *UAS-Rok*$^{RNAi}$ = 0.7373 (ns), Control v *UAS-Rok*$^{CAT}$ = 0.1242 (ns). (**B**) Bar chart of mean cell area with SD. (**C**) Bar chart of mean junction length with SD. N = 1033-1104 junctions from 4-6 flies. (**D**) Bar chart of mean elongation of ellipses fitted to cell shapes. N for **A**, **B** & **D** = 291-305 cells from 4-6 flies. P-value summaries from Mann-Whitney statistical tests due to non-Gaussian distribution of data.

## 4.7 Increasing active junctional Myosin II levels blocks neighbour exchange

Having observed a measurable difference in line tension between altered active Myo II levels, we next wanted to assess the impact of these changes on junction dynamics and neighbour exchange. In the germ band, cell intercalation requires polarised p-Myosin II to drive junction loss. In the notum however, Myo II is not polarised, and T1 transitions are randomly oriented. As a measure of junction dynamics for each condition, the total number of neighbour exchange events were counted, normalised to the number of junctions in the first frame of imaging and normalised to time (Fig. 4.7). This was repeated with 3-4 nota for each condition. If tetrads of cells underwent multiple exchange events, each exchange was counted individually.

We began by examining neighbour exchange following a reduction in Myo II activity. Importantly a loss of p-Myosin II through *UAS-Rok*$^{RNAi}$ or following expression of non-phosphorylatable MRLC (*UAS-sqh*$^{AA}$) did not prevent neighbour exchange, as observed in the germ band. Instead a reduction in active Myo II levels led to an increase in the number of neighbour exchange events observed (Fig. 4.9). Conversely, an increase in p-Myosin II levels by *UAS-Rok*$^{CAT}$ and *UAS-sds22*$^{RNAi}$ decreased the number of neighbour exchange events.

The *UAS-sqh*$^{AA}$ mutant is weak. Therefore I also used a *UAS-zipper-DN* fly that expresses a GFP-tagged MHC fragment that inhibits the function of endogenous Myo II (Franke et al., 2005). This was expressed within a Baz-mCh background to enable junction tracking. Since *UAS-zipper-DN* expression caused lethality at 18$^{o}$C, this was combined with a temperature sensitive *tubulin*-Gal80 to dampen *pnr*-GAL4 activity. Under these conditions *UAS-zipper-DN* was not expressed in all cells at 12.5 h AP, even after moving the pupae to 29$^{o}$C several hours prior to imaging. Rather, *UAS-zipper-DN* was expressed in a mosaic fashion and the number of cells expressing the DN construct increased during imaging (Fig 4.10A). Expression of Zipper-DN caused an increase in apical area, when compared with their non-DN-expressing counterparts, as expected for cells with a reduction in apical junction tension (Fig. 4.10B). In addition the mean number of sides, in cells expressing *UAS-zipper-DN*, was slightly lower than the control. This is indicative of movement away from hexagonal packing (Fig. 4.10C). However, most significantly neighbour

exchange was still observable in tetrads of DN positive cells. This supports the idea that Myo II is not required for intercalation (Fig. 4.10D).

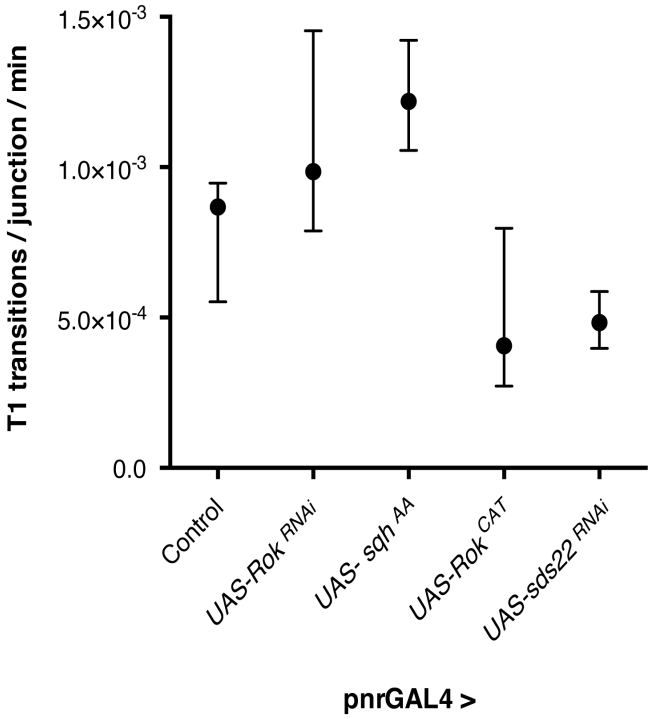


**Figure 4-9: Frequency of neighbour exchange events is inversely correlated with Myosin II activity**

The cumulative number of neighbour exchange events seen for each RNAi condition were counted and normalised to the number of junctions at 12 h AP and normalised to time. Dot indicates median, tails the data range. n = 3-4 flies per condition. Mean of 232 junctions and 111 mins per experiment. Significance not shown due to low n.

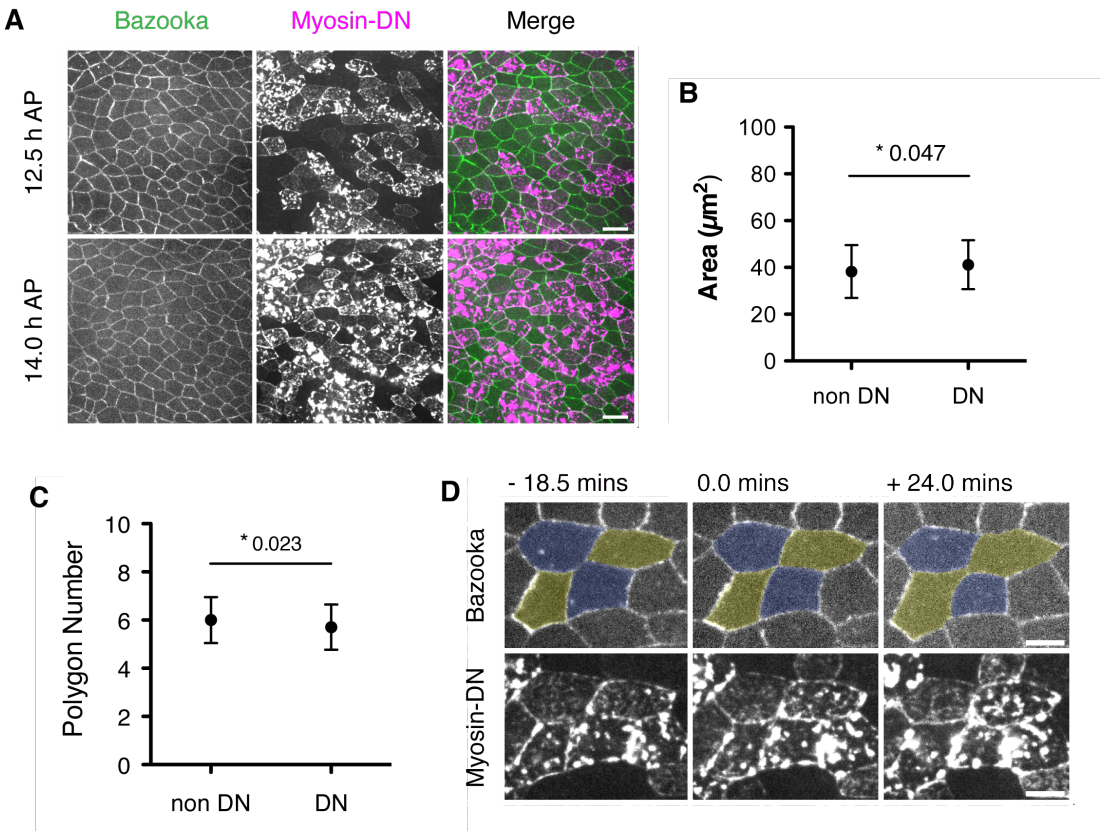


**Figure 4-10: T1 transitions occur with dominant negative Myosin II**

(**A**) Nota imaged with Baz-mCh and Zip-DN-GFP at 12.5 and 14h AP. Scale bar = 10µm. (**B**) Mean area of non-DN (GFP –ve) and DN (GFP +ve) cells at 14.5 h. Tails, S.D. (**C**) Mean polygon number of non-DN (GFP –ve) and DN (GFP +ve) cells at 14.5 h. Tails, S.D. p-values from unpaired t-test. (**D**) Example of Zip-DN (GFP +ve) cells undergoing a neighbour exchange event. Scale bar = 5µm.

*UAS-zipper-DN-GFP / tub-GAL80$^{ts}$ ; ubi-Baz-mCh / pnrGAL4*

(Carl Zeiss Axiovert. Larval development at 18°C, pupae switched to 29°C, 5 h before imaging)

## 4.8 Increasing Myosin II activity causes a reduction in T1 numbers and a decrease in the level of midline cell delamination

Having established a rule for actomyosin in the regulation of neighbour exchange in the tissue, we wanted to test its function. Neighbour exchange contributes to midline cell delamination (Marinari et al., 2012). Cells progressively lose junctions and apical area over 30-90 mins before being rapidly extruded from the tissue. We predicted that blocking neighbour exchange could therefore prevent cells from leaving the tissue.

To test if this is the case, nota were imaged at 5 min intervals from 12 to 20+ h AP with ubi-E-cadherin-GFP for reduced p-Myosin II (*UAS-Rok*$^{RNAi}$) and increased junctional p-Myosin II (*UAS-MYPT-75D*$^{RNAi}$ and *UAS-sds22*$^{RNAi}$). For each fly, the percentage of cells undergoing delamination (yellow cells, Fig. 4.11A) from the midline region (~3-4 cells width, green line) was calculated. This was expressed as a percentage of cells delaminating by 18 h, relative to the cell number at 12 h. Increasing levels of junctional p-Myosin II significantly reduced cell delamination, down from ~20% in control to less than 10% (Fig. 4.11B).

Conversely, the percentage of midline cell delamination in *UAS-Rok*$^{RNAi}$ was slightly (but not significantly) higher than the control. Significantly, in this case, delamination events were also observed outside of the midline (Fig. 4.12A). As seen for midline cells in the control, these *UAS-Rok*$^{RNAi}$ cells outside the midline gradually lost cell-cell contacts through intercalation before extrusion (Fig. 4.12B). Once again, levels of delamination outside the midline were measured by counting cells that delaminate between 12 and 18 h AP and normalising relative to the number of cells present at 12 h. These events represented ~2.5% of cells in Rok knockdown tissues, but were extremely rare in control tissue, with only 1 cell delaminating from 6 nota imaged.

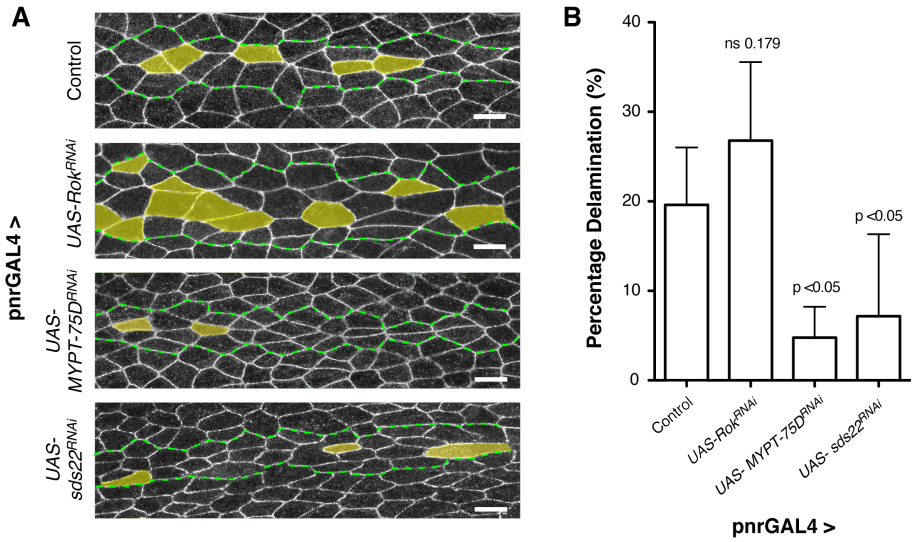


**Figure 4-11: Delamination levels increase with reduced p-Myosin II levels and decrease with increased Myosin II activity.**

(**A**) Representative nota showing midline (dotted green line) with cells that delaminate (yellow) up to 18 h AP. (**B**) Bar chart of percentage midline delamination for decreased (*UAS-Rok*$^{RNAi}$) and increased (*UAS-MYPT75D*$^{RNAi}$ and *UAS-sds22*$^{RNAi}$) activity. Bars indicate mean with S.D. P-values were calculated from unpaired t-tests against control. n = 4-6 nota per condition.

*w*$^{1118}$*; ubi-E-cad-GFP / +; pnrGAL4 / +* (Larval development at 29°C)
*ubi-E-cad-GFP / UAS- Rok*$^{RNAi}$*; pnrGAL4 / +* (Larval development at 29°C)
*ubi-E-cad-GFP / +; pnrGAL4 / UAS- MYPT-75D*$^{RNAi}$ (Larval development at 29°C)
*ubi-E-cad-GFP / UAS- sds22*$^{RNAi}$*; pnrGAL4 / +* (Larval development at 29°C)

(Leica SPE2)

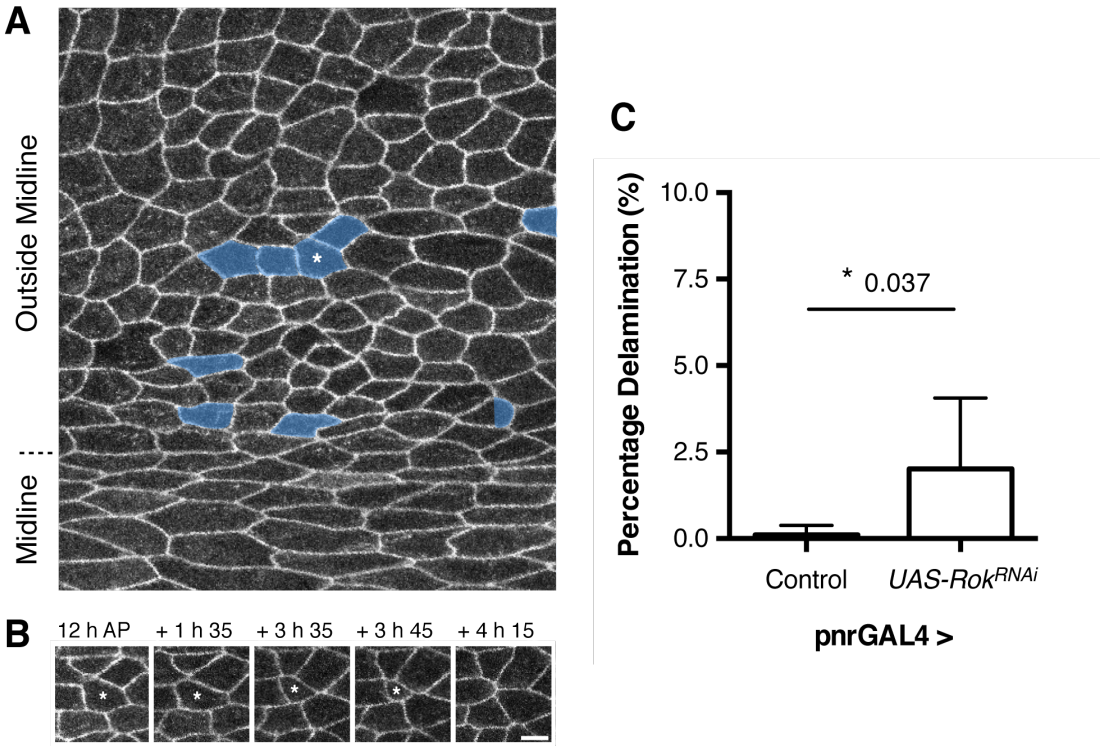


**Figure 4-12: A tissue-wide reduction in active Myosin II allows cells to delaminate from the tissue outside of the midline**

(**A**) Representative example of cells outside the midline (OM) that undergo basal cell delamination (blue) in a nota expressing *UAS-Rok*$^{RNAi}$ up to 18 h AP. (**B**) Time-lapse montage of a cell (labelled with a star in A) that progressively loses junctions, and area, through time before extrusion. (**C**) Delamination levels were measured outside the midline up to 18h AP. Delamination numbers expressed as percentage of the total number of OM cells at 12h AP. N = 6-7 flies with 110-237 (mean = 156) cells at 12h. p-value calculated from Mann-Whitney statistical test.

*w*$^{1118}$*; ubi-E-cad-GFP / +; pnrGAL4 / +* (Larval development at 29°C)
*ubi-E-cad-GFP / UAS-Rok*$^{RNAi}$*; pnrGAL4 / +* (Larval development at 29°C)

(Leica SPE2)

## 4.9 Neighbour exchange events in the absence of p-Myosin II are quantitatively comparable to those in control tissues

Due to the high levels of neighbour exchange observed in the absence of p-Myosin II, we wanted to see how Myo II loss affected rates of neighbour exchange relative to the control. To do so, we used the same measures as we used previously for control intercalation events (Fig. 3.6 – 3.11). T1 transitions events were identified in 30s time-lapse imaging of DE-cadherin-GFP flies with reduced levels of active Myo II (*UAS-Rok*$^{RNAi}$).

To begin, I measured the mean change in length of the five individual junctions undergoing neighbour exchange and plotted this through time (as for control, Fig. 3.6). As in the control, total length of the four first-neighbours tended to be anti-correlated (Fig. 4.13 B) with the length of the junction being lost/gained (Fig. 4.13A). As a result total junction length remained stable throughout (Fig. 4.13C). The rate of junction loss was shown to be slightly faster than the rate of junction gain, however this was not significant (Relevant statistics can be found in Appendix: Table 9.2-9.5). This suggests that the process of junction loss/ gain is mechanistically similar, even in the absence of active Myosin II.

Aspect ratio (Fig. 4.13D) and circularity measures (Fig. 4.13E) also remained stable throughout the transition as measured by comparing t=-15.0 mins and t=+15.0 to t=0. Similarly, ellipse orientations changed by less than 10% over the same period (Fig 4.13F).

These measures are relative to individual junctions. Next we looked to the cellular level to see how neighbour exchange locally affected the packing of the cells involved. As expected, the mean polygon number of cells gaining a junction increased from before and after an exchange (Fig 4.14A) and also gained area (Fig. 4.14B). Cells losing a junction decreased their mean polygon number (Fig 4.14C), and lost area (Fig. 4.14D).

When the entire dataset was grouped together, we could then assess whether these T1 events contribute to cell packing and order. This was not the case. Over 30 mins

there was a small decrease in mean polygon number (Fig. 4.14E), which was not significant (6.044 at t=-15 and 5.906 at t=+15), a slight decrease in the variance of the polygon distribution (Fig. 4.14E & H), and no change in area (Fig. 4.14F-G).

These data suggest that, as in the control, junction lengths are anti-correlated during a T1 and neighbour exchanges are not associated with a change in shape, angle and area of the cluster. As in the control (Fig. 3.10E), the proportion of hexagons increased in *UAS-Rok*$^{RNAi}$, as the variance of polygon distributions decreased, though the effect was less strong, implying that increased levels of junction tension drives the tissue towards order. Thus, the large number of T1s observed, with reduced levels of active Myo II, have little effect on tissue order.

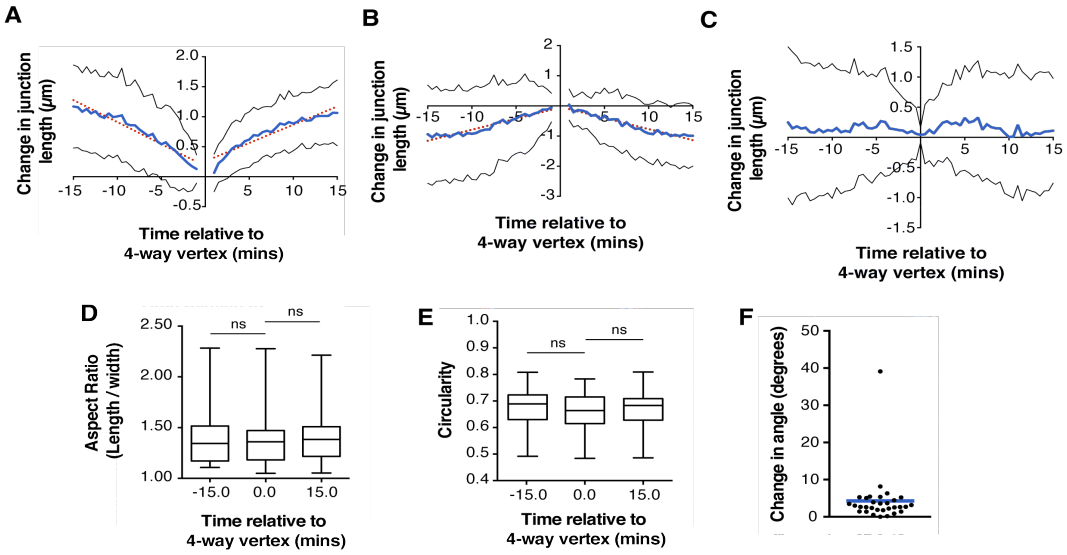


**Figure 4-13: Junction lengths remain anti-correlated during neighbour exchange in the absence of active Myosin II**

Measuring the lengths of junctions involved in *UAS-Rok*$^{RNAi}$ neighbour exchange events, as measured for wild-type neighbour exchange (Fig. 3.6). (**A**) Plot of the change in length (from t0) of the junction that is lost and reformed during the exchange. Slope of junction loss = -0.07338, R = 0.19, Slope of expansion = 0.06086, R = 0.25. Slopes are significantly different, F = 4.519, p-value = 0.0336. (**B**) Plot of the change in cumulative length of the four first neighbours. Slope pre- 4-way vertex = -0.07355, R = 0.107, post- 4-way vertex= 0.0735, R = 0.05. Slopes are not significantly different, F = 0.019, p-value = 0.8906. (**C**) Plot of change in length (from t0) of the sum of all five junctions. Blue line represents mean, black lines, S.D. n = 35 transitions from 4 nota. (**D**) The cell shape perimeter, as shown in **Fig. 3.9** is used to fit an ellipse. Aspect ratio measured as **Fig. 3.6**. Line represents median, box represents 25$^{th}$ and 75$^{th}$ percentile, tail represents the full data range. A Mann Whitney test was used to compare t=-15 to t=0 (P = 0.9027), and t=0 to t=+15 (P = 0.8641). (**E**) Circularity is measured at t=-15 mins, t=0 (4-way vertex)., and t=+15 relative to t=0. An unpaired t-test was used to compare t=–15 to t=0 (p = 0.2632), and t=0 to t=+15 (p = 0.9545). (**G**) Cell area 15 min before and after transition. t=-15min, mean = 252.4μm$^2$, SD 54.09; t=+15, mean = 246.7μm$^2$, SD 55.34. Unpaired t-test p-value = 0.696, ns; F-test to compare variances = 1.047, p-value = 0.901, ns. n = 35 transitions. (**H**) Polygon distribution of cells before and after T1. n = 128-136 cells / 35 transitions.

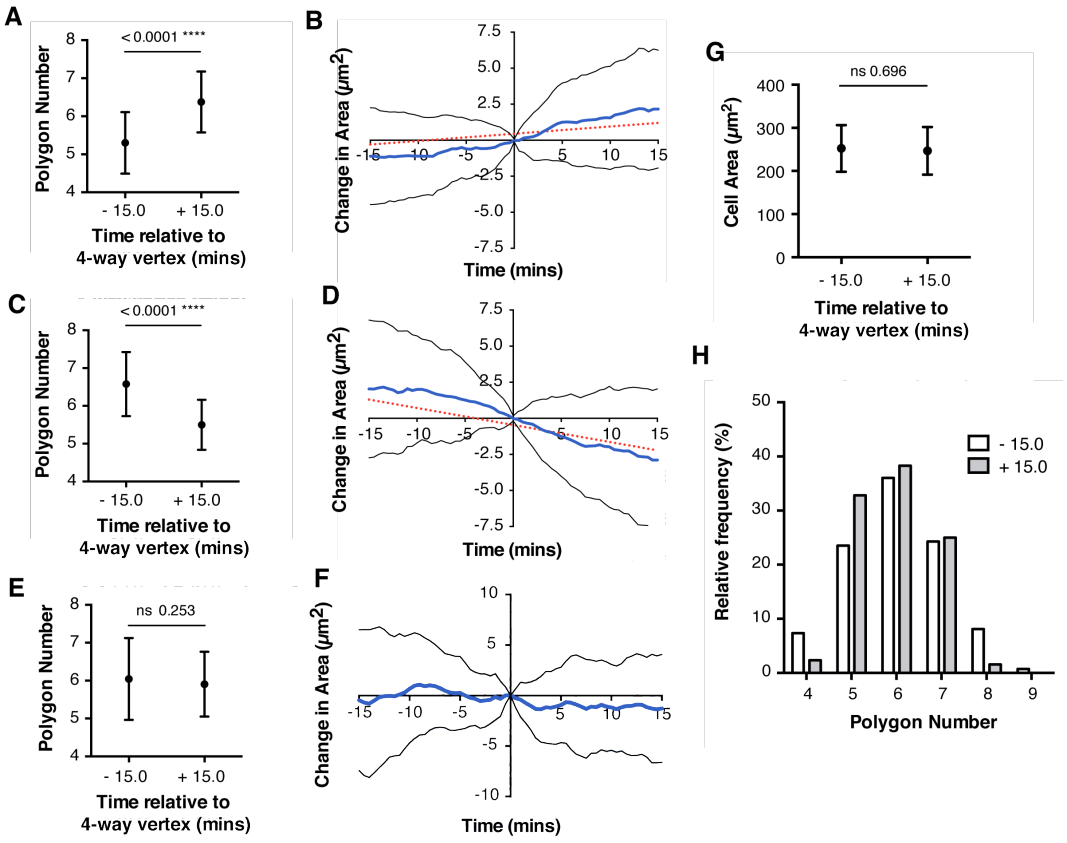


**Figure 4-14: Gain / loss of a junction is associated with a concomitant gain / loss in area during *UAS-Rok*$^{RNAi}$ neighbour exchange**

(**A**) Mean polygon number of cells gaining a junction pre- and post transition. Tails indicate S.D. n = 56-60 cells. (**B**) Mean change in area (blue line) of cells gaining a junction (Minus mean at t=0). Black lines, S.D. Slope (red dotted line) = 0.05, $R^2$= 0.062. n = 62 cells / 35 transitions. (**C**) As **A** for cells losing a junction. n = 52-56 cells. (**D**) As B for cells losing a junction. Slope = -0.1174, $R^2$ = 0.21. n = 62 cells / 31 transitions. Statistical tests are unpaired t-tests. (**E**) Mean polygon number with SD before and after exchange. t=–15, mean = 6.044 sides, SD 1.081; t=+15, mean = 5.906 sides, SD 0.0855. Unpaired t-test p-value = 0.2534, F-test to compare variances = 1.598, p-value = 0.0079, **. n = 128-136 cells / 35 transitions. (**F**) Mean change (blue) in total area from t0 through neighbour exchange. Black line, S.D. n = 35 transitions. (**G**) Cell area 15 min before and after transition. t=-15min, mean = 252.4μm$^2$, SD 54.09; t=+15, mean = 246.7μm$^2$, SD 55.34. Unpaired t-test p-value = 0.696, ns; F-test to compare variances = 1.047, p-value = 0.901, ns. n = 35 transitions. (**H**) Polygon distribution of cells before and after T1. n = 128-136 cells / 35 transitions.

## 4.10 Discussion

The analysis of Myo II, in the control, revealed that the distribution was not polarised. If actomyosin contractility were the driving force of these transitions, the lack of Myo II polarity in the scutum could nevertheless account for the random distribution and orientation of neighbour exchange events observed. However, a loss of p-Myosin II, through RNAi knockdown of its activating kinase Rok resulted in increased levels of neighbours exchange and facilitated basal cell delamination outside of the midline. This implies that alternative mechanisms are driving neighbour exchange in the notum other than actomyosin contractility. Moreover, as in the control, an analysis of *UAS-Rok*$^{RNAi}$ T1 transitions showed them to be mechanistically similar to the control. Thus, neighbour exchange was not associated with changes in total junction length. Also T1s in *UAS-Rok*$^{RNAi}$ tissues did not contribute to a change in the aspect ratio of cell clusters undergoing neighbour exchange and did not create local packing disorder. This suggests that the mechanisms driving T1 transitions in the notum are independent of apical actomyosin contractility and of junction tension, which is Myosin II dependent. Conversely increasing active levels of Myosin II, through tissue-wide expression of constitutively active Rok and RNAi of inhibitory Myosin phosphatase subunits, decreased the number of T1 transition events and blocked midline delamination.

Our FRAP experiments revealed that E-cadherin turnover was lower in the presence of high p-Myosin II. This result fits with published work that showed the actomyosin cytoskeleton stabilises E-cadherin at the AJ and prevents its lateral movement (Cavey et al., 2008). This could prevent neighbour exchange if lateral E-cadherin movement was required for junction sliding. Although, I was not able to observe an increase in E-cadherin mobility in nota with less actomyosin contractility junction fluidity may already be high in the control. Moreover, the initial rate of recovery was increased suggesting complex dynamics.

To conclude, our data suggests an unexpected role for junctional actomyosin in the notum. This is opposite to that described for GBE. In embryo development polarised actomyosin contractility actively drives cell intercalation to contribute to tissue extension. In stable epithelia, without a polarised distribution, Myosin II inhibits

junction dynamics, with increased contractility blocking neighbour exchange events. This could be due to differences in system, or the same underlying behaviour may have different consequences in cases where it is polarised (GBE) versus isotropic (notum).

# 5. The role of Moesin in the regulation of junctional Myosin II

## 5.1 Introduction

In the previous chapter we introduced Sds22 as a negative regulator of Myo II phosphorylation. However Sds22 binds to all four of the *Drosophila* PP1 phosphatases to antagonise both MRLC and Moesin phosphorylation. In the columnar epithelium of the *Drosophila* wing imaginal discs and the follicle cells, Sds22 knockdown has been associated with a loss of cell shape, epithelial polarity and tissue integrity (Grusche et al., 2009). I have shown that in the notum that a loss of inhibitory regulation leads to increased Myo II activity and a decrease in junction dynamics.

However as well as linking to the apical cortex through the adherens junction, the actomyosin network is bridged to apical transmembrane proteins by the ERM-family protein Moesin. Though the phenotypes we saw for *UAS-sds22*$^{RNAi}$ were similar to those specific for Myo II regulation, with high junctional p-Myosin levels and increased junctional tensions as measured by vertex displacement, the contribution from the loss of Moesin regulation to these results remain unclear.

Therefore in this chapter we modulate the levels of specific Moesin regulators to alter Moesin activity. We then examine the effects of altered Moesin activity on the localisation and activity of the apical actomyosin pool and ask how this impacts upon junctional organisation.

## 5.2 Moesin keeps adherens junctions straight

To assess the requirement of Moesin in maintaining AJ structure, Moesin's activating kinase, Slik, was knocked-down through *pnr*-GAL4 driven UAS-RNAi (Fig. 5.1A). By visualising junctions with DE-cadherin-GFP it was obvious that a loss of p-Moesin caused major junction defects. Rather than being smooth and straight between vertices, junctions were wavy and formed medially pointing punctate structures. Overexpression of a phosphomimetic Moesin variant, Moe$^{TD559}$ (Speck et al., 2003), did not lead to the appearance of junction breaks at vertices, as seen for *UAS-sds22*$^{RNAi}$ (but did produce a hazy GFP signal either side of the junction), implying that this effect may be due to Myosin II (Fig. 5.1A).

Next I imaged Moesin loss and overexpression, with Zipper-YFP to see if altered Moesin levels affected the localisation of the total Myo II pool. For constitutively active Moesin, Myo II was less visible in the medial pool, but it is unclear to whether junctional intensity was higher than control (Fig 5.1B). Strikingly though, *UAS-Slik*$^{RNAi}$ and *UAS-Moe*$^{RNAi}$ caused a mass relocalisation of Myo II from the junction to the medioapical cortex. Some Myo II was still observed at the junction (with this particular Zipper-YFP construct) but at a lower level than seen in controls.

Beyond 13.5 h AP, cells in the notum start to divide. For control cells, as they round from prophase to metaphase, Myo II moves from a medioapical mesh to the cortex. For *UAS-Slik*$^{RNAi}$, however, a pool of Myo II remains medioapical throughout division. The medial Myo II does decrease in intensity during rounding of these cells, but the cortical Myo II was less thick than control (Fig 5.1C).

In all of our previous RNAi experiments to decrease Myo II, I had not observed such a striking change in junction morphology as seen for Moesin loss. Also Myo II did not relocalise to a medial pool in these cases. By undertaking time-lapse imaging of Zipper-YFP with *UAS-Slik*$^{RNAi}$ I observed medial Myo II cables that linked the medial pool to the AJ. Ideally, I would have imaged a junctional mCherry marker to independently follow AJs but it was not possible to balance these stocks with *zipper-YFP* flies. Nevertheless. I was able to infer the shape of the AJ from the junctional Myo II localisation. As cells underwent apical constriction junctional actomyosin was connected to the medial pool by Myo II cables (Fig. 5.1D, arrowed at 0.00 min). With time, these connections would break allowing the junction to relax (+ 8.00 mins) before newly formed cables reattached and pulled on the junction (+ 12.5 mins). This lead to area pulsatility, and the previously described wavy junctions, as observed with DE-Cadherin-GFP for Moesin loss-of-function (Fig. 5.1A).

Furthermore, the relocalisation of Myo II, seen following a depletion of active Moesin, was confirmed by immunohistochemistry (Fig. 5.2). Fixed staining against DE-cadherin for *UAS-Slik*$^{RNAi}$ nota (as Fig. 4.4) reproduced the undulating appearance of junctions observed during DE-cadherin-GFP live imaging (Fig. 5.2A). A junctional pool of actin remained. However P-Myo II was completely removed from the junction, as a result of the shift to the medioapical pool. This is clearer in

increased zoom images of the vertices. Distinct patches of p-Myo II visible at vertices in control stainings are absent in *UAS-Slik*$^{RNAi}$ flies (Fig. 5.2B).

The Moesin dependent localisation of Myo II was confirmed with stills from live total Myo II imaging (*MRLC-mCherry*) (Fig. 5.2C). Again, Myo II was completely absent from the junctions of *UAS-Slik*$^{RNAi}$ tissues. Small regions of junctional Myo II were still observed with *UAS-Moe*$^{RNAi}$, which was less effective in depleting p-Moesin pools, though in this case it was clear that the localisation of Myo II shifted medially.

## 5.3 A loss of junctional Myosin II correlates with a loss of line tension

I have shown previously that a loss of junctional Myo II, through *UAS-Rok*$^{RNAi}$, causes a reduction in line tension as measured by laser ablation (Fig. 4.8). Slik knockdown leads to a relocalisation of Myo II from the junction to a medioapical pool. Consistent with this loss of junctional Myosin II, laser cuts of these junctions exhibited a significant decrease in line tension compared to the control, as measured by initial vertex displacement at 10 s (Fig. 5.3A). Vertex displacement for *UAS-Slik*$^{RNAi}$ junctions was also lower than control over 1.5 mins indicative of lower tissue tension (Fig 5.3B). Thus, this loss of junctional myosin leads to an increase in junctional forces.

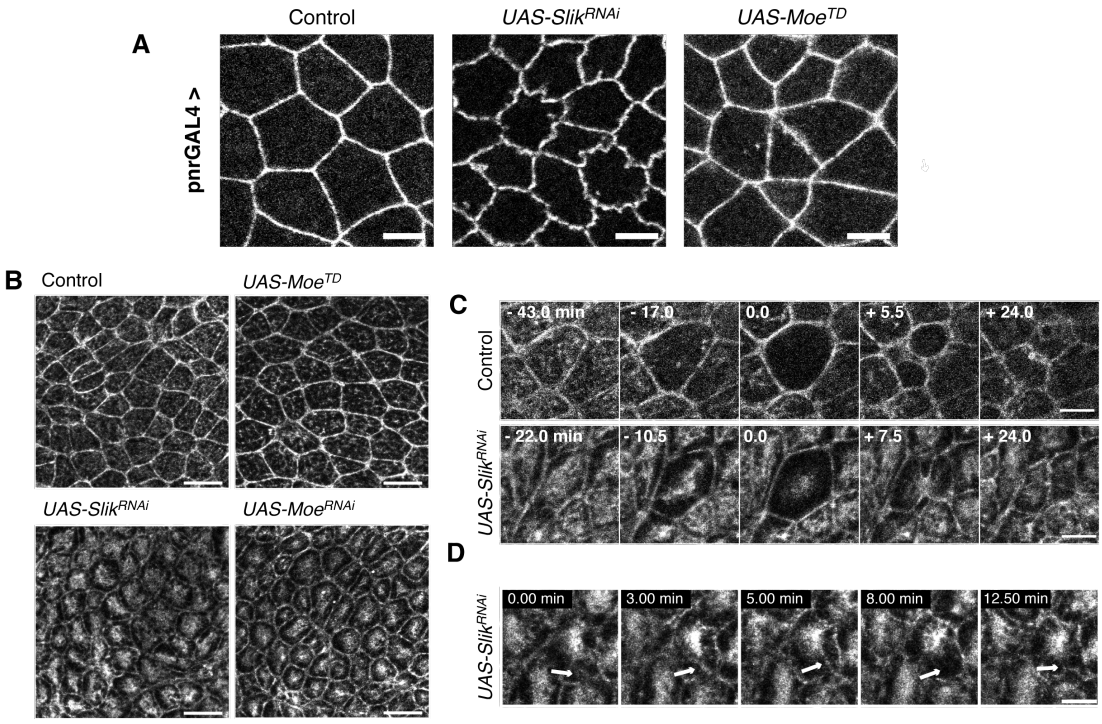


**Figure 5-1: A loss Slik, Moesin's activating kinase, causes a wavy junction phenotype.**

(**A**) DE-cadherin-GFP images of control, decreased active Moesin levels (*UAS-Slik$^{RNAi}$*), increased active Moesin levels (*UAS-Moe$^{TD}$*). (**B**) Nota imaged with Zipper-YFP for increased Moesin activity (*UAS-Moe$^{TD}$*) and reduced activity (*UAS-Slik$^{RNAi}$*and *UAS-Moe$^{RNAi}$*). Scale bar = 10µm. (**B**) Comparison of cell division in control and *UAS-Slik$^{RNAi}$*. (**C**) Myosin II cables (arrowed) forming from the medial pool, pulling on, and detaching from the AJ. Scale bar = 5 µm.

*DE-cad-GFP(KI) / +; pnrGAL4 / +* (Larval development at 29°C)
*DE-cad-GFP(KI) / UAS-Slik$^{RNAi}$; pnrGAL4 / +* (Larval development at 29°C)
*DE-cad-GFP(KI) / UAS-Moe$^{TD559}$-Myc; pnrGAL4 / tubGal80$^{ts}$*
*w$^{1118}$ ; zipper-YFP /; pnrGAL4 / +* (Larval development at 29°C)
*zipper-YFP / UAS-Slik$^{RNAi}$; pnrGAL4 / +* (Larval development at 29°C)
*zipper-YFP / +; pnrGAL4 / UAS-Moe$^{TD559}$-Myc* (Larval development at 29°C)

(Leica SPE2, * *UAS-Moe$^{TD559}$* temperature sensitive pupae transferred to 29°C from 18°C, 6 h prior to imaging)

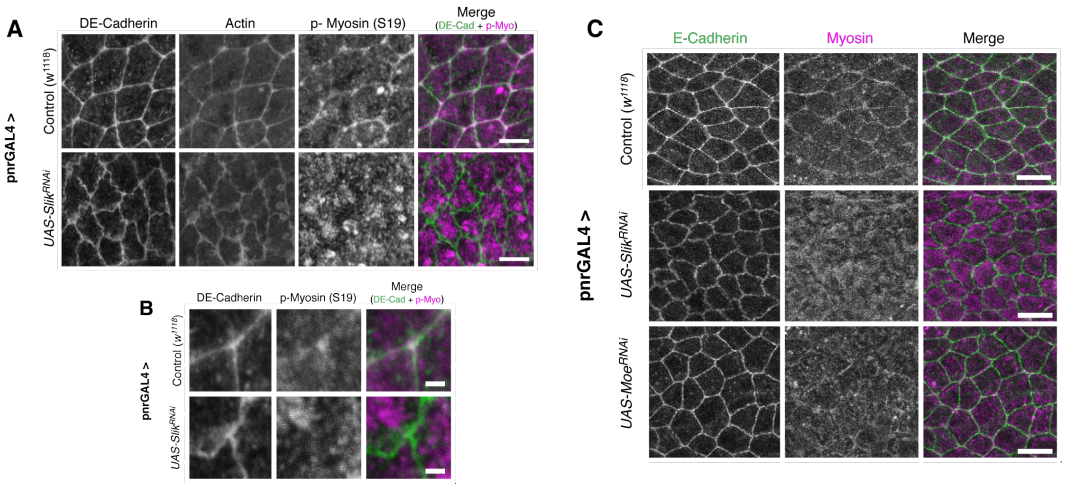


**Figure 5-2: A loss of p-Moesin causes junctional Myosin II to relocalise to the medio-apical cortex**

(**A**) Fixed stain for DE-cadherin (anti-GFP), F-actin (Phalloidin), and p-Myosin II (S19) for control and reduced Moesin activity (*UAS-Slik*$^{RNAi}$). Scale bars = 5µm. (**B**) Increased zoom of vertices. Scale bar = 1µm. (**C**) Maximum projection images of nota imaged with ubi-E-cadherin-GFP and Spaghetti-Squash-Cherry (MRLC) labelling total Myo II levels. RNAis are driven by pnrGAL4 to decrease p-Moe (*UAS-Slik*$^{RNAi}$) and total Moesin (*UAS-Moe*$^{RNAi}$). Scale bar = 25µm.

*DE-cad-GFP(KI) / +; pnrGAL4 / +* (Larval development at 29°C)
*DE-cad-GFP(KI) / UAS- Slik*$^{RNAi}$*; pnrGAL4 / +* (Larval development at 29°C)
*w*$^{1118}$ *; ubi-E-cad-GFP / +; pnrGAL4 / +* (Larval development at 29°C)
*ubi-E-cad-GFP / UAS-sds22*$^{RNAi}$*; pnrGAL4 / +* (Larval development at 29°C)
*ubi-E-cad-GFP / UAS-Slik*$^{RNAi}$*; pnrGAL4 / +* (Larval development at 29°C)
*ubi-E-cad-GFP / UAS-Moe*$^{RNAi}$*; pnrGAL4 / +* (Larval development at 29°C)

(Leica SPE2)

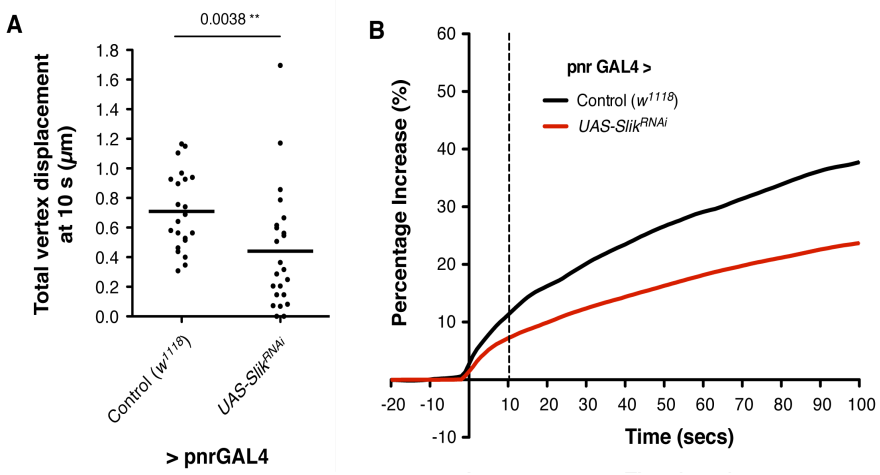


**Figure 5-3: A loss of junctional Myosin II through Slik knockdown decreases junction tension.**

(**A**) Total vertex displacement measured at 10 s after ablation for control (as **Fig. 4.6**), Dots indicate individual experiments. Line indicates median. (**B**) Mean displacement measured as a percentage of pre-ablation median length. SEM not shown. n = 23-25 cuts/ 6 nota per condition. P-values calculated from unpaired t-test.

## 5.4 Active Moesin localises to the medioapical cortex

It has previously been reported in mouse epithelial tissues that Ezrin and Moesin both localise to actin-rich structures including the apical microvilli (Berryman et al., 1993). As the sole ERM family member in *Drosophila*, we wanted to see where Moesin localised within the notum and how this changes with altered activity. Through over-expression of GFP-tagged wild-type Moesin we could use an anti-GFP antibody to follow total Moesin localisation and compare this to active Moesin, imaged with an anti-phospho Thr558 antibody.

Active Moesin localised very apically at the apicomedial surface (Fig. 5.3). Its dotted appearance was indicative of microvilli localisation. The isolated clustering of signal showed the p-Moesin stain to be intra-cellular and absent from the adherens junction. P-Moesin was also absent from the basolateral membrane, but was again present in the basal filopodia (-9.0µm from the AJ) (Fig. 5.3). Total Moesin labelling overlapped with p-Moesin at the apical surface. However at levels - 3.0µm beneath the apex at the level of the septate junction, although P-Moesin was not observed, total Moesin was present at the junction and its expression extended basally along the lateral membrane. Strong total Myo II signal overlapped with p-Moesin staining in the filopodia.

At the apical surface, p-Moesin intensity was reduced through RNAi of its activating kinase Slik. Conversely, the signal increased following RNAi silencing of its negative regulator, Sds22 (Fig 5.4A). Increasing p-Moesin, though a loss of Sds22, did not lead to the appearance of p-Moesin at the AJ. Instead constitutive p-Moesin expression was found along the basaolateral membrane and strongly in basal filopodia (Fig. 5.4B). Full apical to basal expression of p-Moesin was only ever seen during mitosis for control cells (Fig. 5.4C).

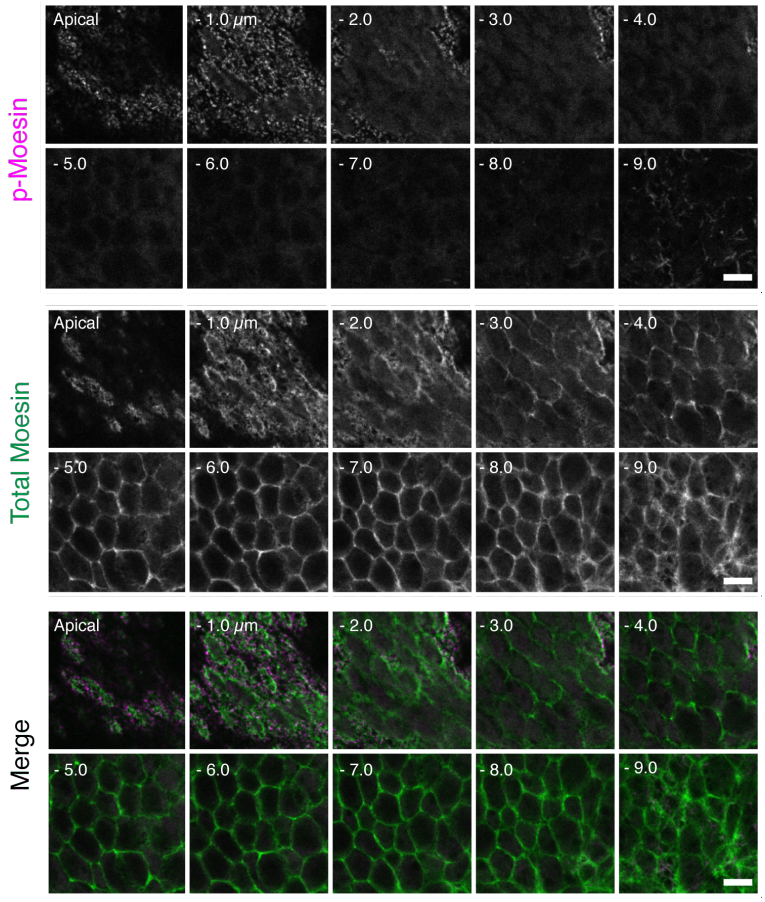


**Figure 5-4: Total Moesin localises to the junction and membrane whereas phospho-Moesin is only seen at the apico-medial cortex.**

Fixed stain for p-Moesin and total Moesin (anti-GFP against *UAS-Moe-GFP*). Scale bars = 5µm.

*If / UAS-Moesin-GFP ; pnrGAL4 / +*

(Leica SP5, Larval development at 25oC)

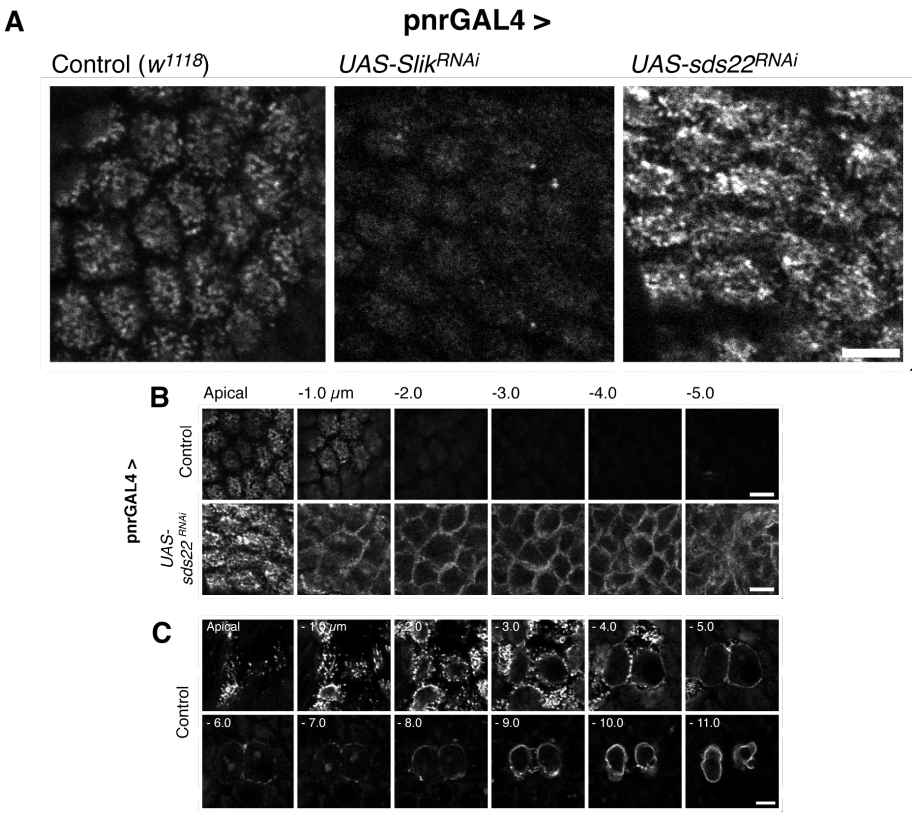


**Figure 5-5: Slik knockdown reduces p-Moesin levels.**

(**A**) Representative tissues of control, *UAS-Slik*$^{RNAi}$ and *UAS-sds22*$^{RNAi}$ fixed and stained for p-Moesin. (**B**) Z-slice montage of control and *UAS-sds22*$^{RNAi}$ nota at 1µm slices stained for p-Moe. (**C**) Representative image of p-Moe localisation during cell division in control. Scale bars = 5µm.

*DE-cad-GFP(KI) / +; pnrGAL4 / +* (Larval development at 29°C)
*DE-cad-GFP(KI) / UAS-Slik*$^{RNAi}$*; pnrGAL4 / +* (Larval development at 29°C)
*DE-cad-GFP(KI) / UAS-sds22*$^{RNAi}$*; pnrGAL4 / +* (Larval development at 29°C)

(Leica SPE2)

## 5.5 Discussion

The aim of this chapter was to investigate the role of Moesin in the regulation of apical actomyosin. I showed that p-Moesin localised to the apical cortex with a punctate expression consistent with its function in forming actin-rich microvilli. Active Moesin was not visible at the adherens junction.

A loss of p-Moesin through RNAi of the protein itself, or its activating kinase Slik, produced a very striking and surprising phenotype. Firstly, Moesin was shown to maintain junctional integrity as its loss led a distinctly wavy AJ structure within the XY plane. Secondly, through *UAS-Slik*$^{RNAi}$ and *UAS-Moe*$^{RNAi}$, Moesin was shown to regulate the localisation of apical Myo II, a previously unreported result. Myo II was lost from the junction and moved to a medioapical localisation. Actin cables protruding from this medial pool were inferred to be pulling on the adherens junction, creating the wavy architecture observed.

The loss of junctional Myo II was associated with a decrease in line tension across the junction. As actomyosin was seen to be pulling on the AJ, it would be interesting to ablate this medial pool to see if it would return the junction to a straight line and how these medial pulling forces compare to control.

A question remains from this work. How does Moesin regulate junctional Myo II? The medial localisation of p-Moesin appears to exclude Myo-II from the medial cortex; keeping it at the junction. It seems unlikely that Moesin is directly tethering Myo II to the junction as their activity levels are anti-correlated. Where there is low p-Moesin at the junction there is high p-Myo and vice verse across the medial cortex. The regulation is therefore likely to be indirect, perhaps as a result of a change in apical actin organisation, creating competition between different structures that recruit Myosin II.

# 6. Adherens junction turnover is not essential for neighbour exchange

## 6.1 Introduction

Returning to our models of neighbour exchange (Fig. 3.4), we have confirmed that cell intercalation in the notum is quantitatively distinct from that predicted by a conventional germ band elongation model. In Chapter 4, we further disproved a GBE-type mechanism by showing that neighbour exchange can occur independently of Myo II recruitment, and that increased p-Myo II levels are actually inhibitive to this process. In this chapter we return to our two remaining models, '*Simultaneous removal and addition*' and '*Fixed total length (sliding)*', to investigate the distinguishing feature between the two: junction turnover.

In a purely sliding model, no junction turnover is required. During expansion and loss, changes in the length of all junctions allow the total junction length to remain stable during the transition. In the *Drosophila* germ band Clathrin-mediated endocytosis is required to facilitate junction loss (Levayer et al., 2011). In the pupal wing disc cadherin turnover is required to mediate junctional remodelling and maintain tissue integrity (Classen et al., 2005). Here I block endocytosis in the notum to test for the same requirement of cadherin turnover for cell intercalation.

In addition, the analysis this far has focussed on movements occurring in the 2D XY plane, at the level of the adherens junction. In reality, movements seen in 2D only represent part of the dynamic interactions between individual 3-dimentional cells that make up the epithelial sheet. As the TEM imaging showed (Fig. 1.1), the notum consists of a row of tightly juxtaposed polarised cells. Thus, movement within the epithelial plane requires the maintenance of cell-cell contacts to ensure the integrity of the tissue during transition, as envisaged by Fristrom.

We therefore test the requirement of apical contacts and the adherens junction itself for maintenance of a stable epithelium. We then ask whether there is a relationship between apical and basal junctional dynamics during a neighbour exchange event. This allows us to ask if a basally driven 'Fristrom' model of neighbour exchange can drive apical movements in the absence of contractile actomyosin force?

## 6.2 Neighbour exchange in the absence of endocytosis

In a purely sliding model, endocytosis of adherens junction material would not be required for neighbour exchange. To test this hypothesis, I took advantage of a temperature sensitive *shibire* mutant line. Shibire is a *Drosophila* ortholog of mammalian Dynamin (Chen et al., 1991; van der Bliek and Meyerowitz, 1991). During Clathrin-mediated endocytosis, Dynamin wraps in a spiral structure around the neck of the vesicles being pinched off from the plasma membrane. Through GTP hydrolysis, Dynamin is thought to extend and contract causing scission of the vesicle. The precise mechanism by which the *shibire* mutation renders the protein inactive is unknown, but the mutation replaces a neutral glycine with a negative aspartate. This is predicted to cause increased flexibility of the link between the GTPase and regulatory C-terminal domains (Damke et al., 1994; van der Bliek and Meyerowitz, 1991). At restrictive temperatures, above 29$^{o}$C, *shibire* mutations block endocytosis (and export from the Golgi) through defective vesicle scission.

*Shibire$^{ts}$* flies were time-lapse imaged with DE-cadherin-GFP from 12 to 13.5 h AP at 30 s intervals. Flies were either imaged at 22$^{o}$C (Permissive - room temperature) as a control, or placed in a 29$^{o}$C (restrictive) heated-box 10 mins prior to and during imaging (Fig 6.1A). At restrictive temperatures, junction defects became progressively worse over time. Junction discontinuities were created through lateral DE-cadherin movement. Punctate structures formed and protruded into the cell from clusters (arrowed in Fig. 6.1B). It can be assumed that these are pits that would have been that otherwise pinched off under normal circumstances. Instead they flow back into the junction and re-spread laterally along the cell-cell contact (Fig. 6.1B). These observations fit with previous findings (Classen et al., 2005; Georgiou et al., 2008) and clearly indicate endocytosis is compromised at restrictive temperatures.

The main motivation of this experiment was to test if neighbour exchange could occur in the absence of junction turnover. Even with the presence of junction discontinuities at restrictive temperatures, neighbour exchange events were seen between tetrads of cells at both permissive and restrictive temperatures (Fig. 6.1C). By counting the number of T1 events, and normalising by the number of junctions in the frame at 12 h, the frequency of T1 events (Fig 6.1D) were found to be similar to

levels measured for non-*shibire*$^{ts}$ flies at 25$^{o}$C (Fig. 4.1). At restrictive temperatures, the frequency of neighbour exchange events decreased marginally nevertheless (Fig. 6.1D).

These results show that junction turnover is dispensable for neighbour exchange. However the reduced frequency of events observed with blocked endocytosis suggests that turnover does play a role in facilitating cell intercalation, as expected. Therefore, notum neighbour exchange appears to be a compromise between our '*Simultaneous removal and addition'* and '*Fixed total length (Sliding)*' models. Interestingly under these conditions there is an increase in variance in the size of apical areas. At permissive temperature the variance is cell areas is the same at 12 h as it is at 13.5 h AP. However at restrictive temperatures the variability of apical areas increases over the same time (Fig. 6.1E). This may or may not be linked to adherens junction turnover.

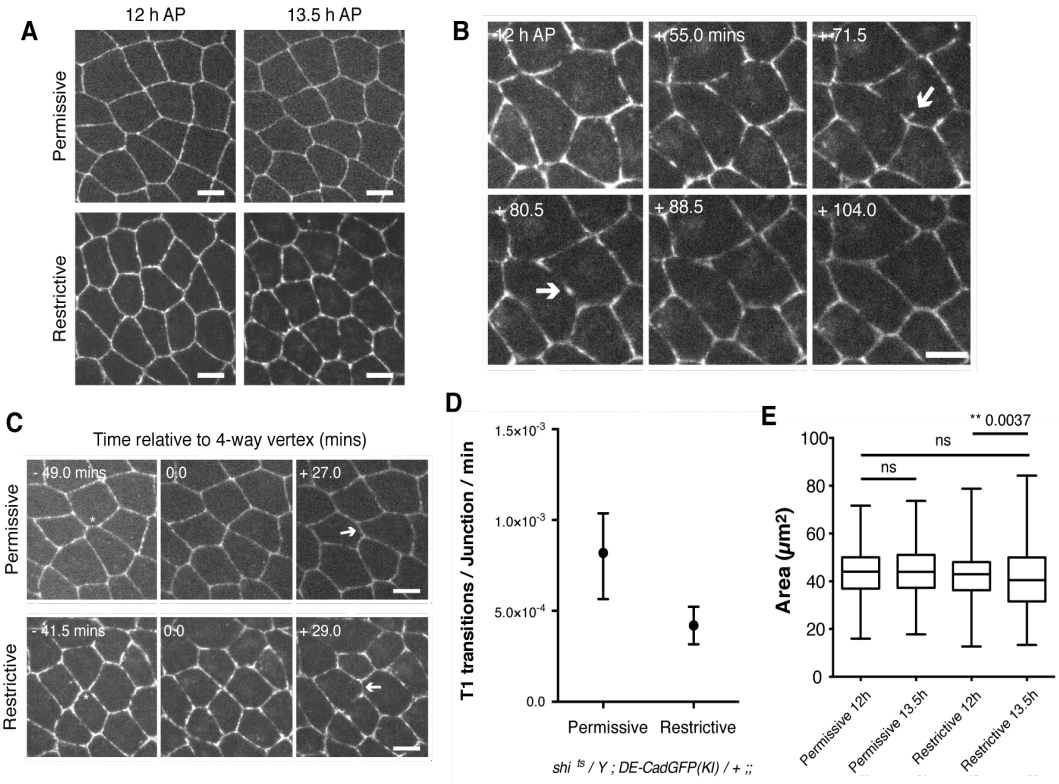


**Figure 6-1: Neighbour exchange events occur with blocked endocytosis**

(**A**) Representative *shibire*$^{ts}$ DE-cad-GFP labelled tissues imaged at 12h and 13.5 h AP at both permissive (22$^{o}$C) and restrictive (29$^{o}$C) temperatures. (**B**) Time-lapse montage of puncta formation, lack of excision and incorporation back into the junction in nota at a restrictive temp. (**C**) Representative T1 transition at permissive and restrictive temperatures. Star labels junction that is lost, arrow indicates newly formed junction. (**D**) T1 transitions per junction per min. Dot indicates median, tails the data range. n = 2-3 flies per condition. Mean of 252 junctions and 122 mins per experiment. (**E**) Box and whisker plot of cell areas at permissive and restrictive temperatures. Line = median, box = 25$^{th}$ and 75$^{th}$ percentile, tails = max and min. Unpaired t-tests indicated ns between means. F-test to compare variances were ns for all, other than Restrictive 12h v Restrictive 13.5 (p-value = ** 0.0037). n = 154-160 cells from 2 flies for each condition.

*shibire*$^{ts}$ */ Y ; DE-cad-GFP(KI) / +*

(Carl Zeiss Axiovert, Larval development at 18$^{o}$C. Permissive temp = 22$^{o}$C (RT), Restrictive = 29$^{o}$C, placed in heated box 10 mins prior to start of imaging)

## 6.3 An epithelium forms in the absence of an adherens junction

As junction turnover was not shown to be essential for neighbour exchange, next I tested the requirement of the adherens junction itself in facilitating cell movement and neighbour exchange. In the embryo, a loss of ß-catenin (Armadillo) prevents the formation of an adherens junction. Cells round up, lose polarity and start to undergo an epithelial-to-mesenchymal transition. The loss of an AJ is catastrophic to the embryo as gastrulation fails (Cox et al., 1996). To test the requirement of the adherens junction in the notum, flies were kept at a non-lethal 18$^{o}$C for expression of dsRNA specific to adherens junction components. This temperature allowed pupal development and for adults to hatch. At early pupal stages (12 h AP) the notum was visualised across the *pannier-ND* boundary with endogenously expressed DE-cadherin-GFP (Fig. 6.2A). For *UAS-shotgun*$^{RNAi}$ (*DE-cadherin*) nota, the GFP signal was largely lost from junctions across the entire the *pannier* region (Fig 6.2A). For *UAS-ß-catenin*$^{RNAi}$, most junctional DE-cadherin was lost, but this did not cause a decrease in total levels, as the GFP signal moved to the cytoplasm. This is as expected if DE-cadherin could not be delivered to, or stabilised, at the junction. For *UAS-α-catenin*$^{RNAi}$, DE-cadherin remained at the junction, but no longer localised to an apical domain. Instead it spread basolaterally. These data confirm the roles of α- and ß-catenin in establishing and maintaining a discrete apical adherens junction.

By increasing the contrast of images taken with *UAS-ß-catenin*$^{RNAi}$, it was possible to distinguish enough GFP- signal for individual cells and junctions to be made out and segmented within the *pannier* region. Cells next to the midline and on the edge of the *pannier* domain were compared with non-RNAi expressing cells from the neighbouring *ND* domain. To measure the loss of DE-cadherin at junctions within the *pannier* region, junction intensities were normalised to mean intensity of control junctions within the *ND* domain (with mean *ND* background intensity subtracted from all measures). With *UAS-ß-catenin*$^{RNAi}$ DE-cadherin-GFP intensities in the *pannier* domain were reduced three-fold (Fig. 6.2B). Junction intensities next to the midline were no different from those on the edge of the pannier domain.

Even though levels of DE-cadherin-GFP were greatly reduced, neighbour exchange events were observed (Fig. 6.2C). Although, due to the poor junction signal it was

impossible to segment large regions of *UAS-ß-catenin*$^{RNAi}$ tissue through time. T1 transitions events within the *pannier* domain (Fig. 6.2D) occurred on timescales consistent with those outside the region (Fig. 6.2E).

To see how the loss of an AJ affected Myo II localisation, *UAS-ß-catenin*$^{RNAi}$ was imaged together with DE-cadherin-GFP and MRLC-mCh. The reduction in the levels of junctional DE-cadherin was accompanied by a relocalisation of Myo II to medioapical ring structures (Fig 6.3A). These ring structures contained active Myo II, as confirmed by fixed staining for p-MRLC S19 (Fig. 6.3B). Myo II ring structures were also observed for *UAS-DE-cadherin*$^{RNAi}$, confirming that the phenotype is a result of adherens junction loss (Fig 6.3B). Under these conditions Myo II is unable to bind cell-cell contacts. Following *UAS-α-catenin*$^{RNAi}$ the junctional Myo II signal was not as distinct as control. Again this leads to more medial Myo II (Fig. 6.3C). These results emphasise the role of the adherens junction in providing an anchor for Myo II.

Fortunately using the MHC-YFP marker, the medial ring structures could be imaged through time. In the absence of an adherens junction cells still divided in the plane of the epithelium (Fig. 6.3D). During rounding Myo II relocalised from the medial cortex to the adherens junction, perhaps mediated through activation of p-Moesin (Carreno et al., 2008; Kunda et al., 2008; Kunda et al., 2012). In the absence of neighbouring cortical tension, the cytokinetic ring contracted to a single point, rather than forming a straight cell-cell contact between the two daughter cells (Founounou et al., 2013; Guillot and Lecuit, 2013a; Herszterg et al., 2013). To conclude, results support a Myo II independent model of neighbour exchange, as cell intercalation within the *pannier* region is not associated with junctional Myo II.

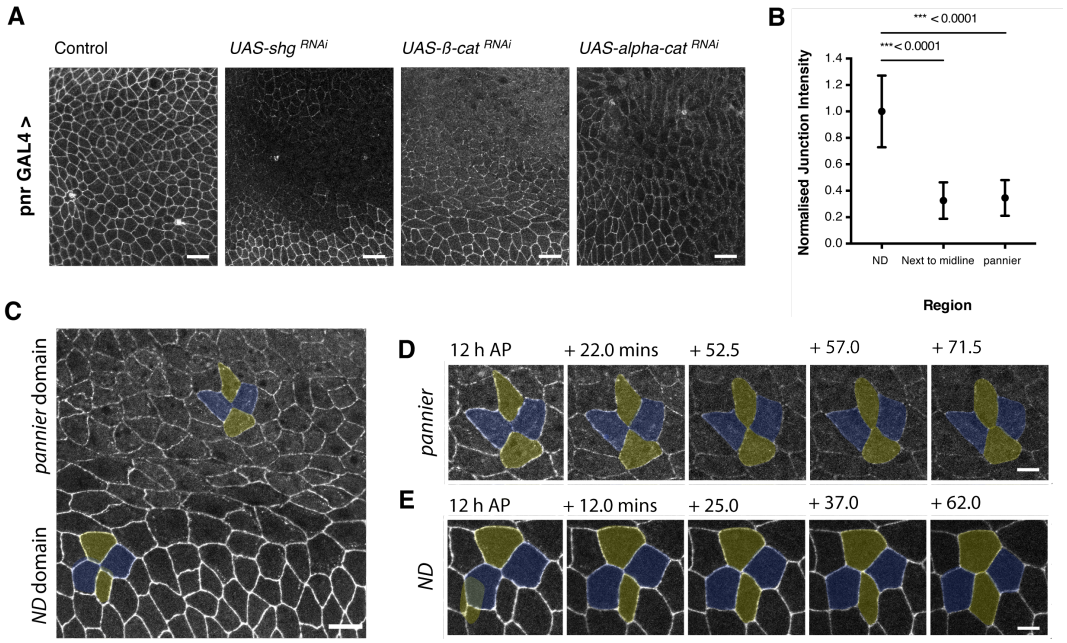


**Figure 6-2: Neighbour exchange occurs in the absence of E-cadherin**

(**A**) Representative nota labelled with DE-cad-GFP for control, *UAS-DE-cadherin*$^{RNAi}$, *UAS- ß-catenin*$^{RNAi}$ and *UAS-α-catenin*$^{RNAi}$. Scale bar = 50µm. (**B**) Plot of mean junction intensities (with S.D.) normalised to ND background intensity. P-values are calculated from unpaired t-tests. n = 132-209 junctions / 1 nota. (**C**) A DE-cad-GFP image of the nota on the edge of the pannier expression domain for *UAS-DE-cadherin*$^{RNAi}$. Time-lapse montages represent T1 transitions occurring within the pannier (**D**) and ND domains (**E**). Scale bar in main image = 10 µm, montages = 5 µm.

*w*$^{1118}$ *; DE-cad-GFP(KI) / +; pnrGAL4 / +* (Larval development at 18$^{o}$C)
*DE-cad-GFP(KI) / UAS-ß-catenin*$^{RNAi}$*; pnrGAL4 / +* (Larval development at 18$^{o}$C)
*DE-cad-GFP(KI) / +; pnrGAL4 / UAS-shotgun*$^{RNAi}$ (Larval development at 18$^{o}$C)
*DE-cad-GFP(KI) / UAS-α-catenin*$^{RNAi}$*; pnrGAL4 / +* (Larval development at 18$^{o}$C)

(Leica SPE2)

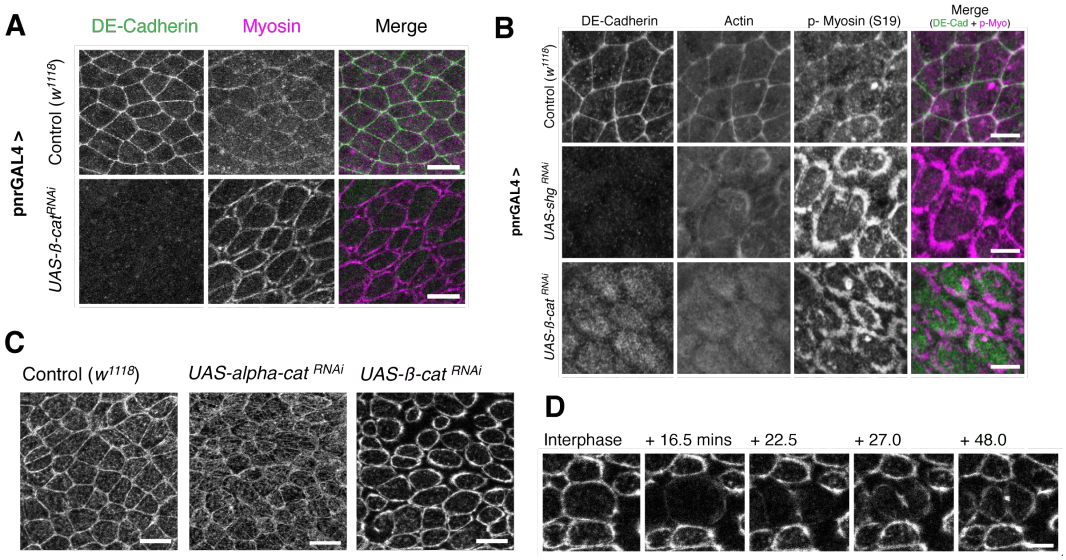


**Figure 6-3: E-cadherin is required to maintain Myosin II at the adherens junction**

(A) Maximum projection images of nota imaged with ubi-E-cadherin-GFP and Spaghetti-Squash-Cherry (MRLC) labelling total Myo II levels for control and *UAS-ß-catenin*$^{RNAi}$. Scale bar = 25µm. (**B**) Representative tissues of control, Shotgun (DE-cadherin) and *UAS-ß-catenin*$^{RNAi}$. Tissues were fixed and stained for E-cadherin (anti-GFP against DE-cad-GFP), F-actin (Phalloidin) and phospho-Myosin II (S19). Scale bar = 5 µm. (**C**) Representative nota imaged with Zipper-YFP (Myosin heavy chain, MHC) for control, *UAS-ß-catenin*$^{RNAi}$ (armadillo) and *UAS-α-catenin*$^{RNAi}$. Scale bar = 10µm. (**D**) Representative cell division in *UAS-ß-catenin*$^{RNAi}$ tissue. Scale bar = 5µm.

*w*$^{1118}$*; DE-cad-GFP(KI) / +; pnrGAL4 / +* (Larval development at 29°C)
*DE-cad-GFP(KI) / +; pnrGAL4 / UAS- shotgun*$^{RNAi}$ (Larval development at 18°C)
*DE-cad-GFP(KI) / UAS-ß-catenin*$^{RNAi}$*; pnrGAL4 / +* (Larval development at 18°C)
*w*$^{1118}$ *; zipper-YFP / +; pnrGAL4 / +* (Larval development at 29°C)
*zipper-YFP / UAS-ß-catenin*$^{RNAi}$*; pnrGAL4 / +* (Larval development at 18°C)
*zipper-YFP / UAS-α-catenin*$^{RNAi}$*; pnrGAL4 / +* (Larval development at 18°C)

(Leica SPE2)

## 6.4 Apical and Basal neighbour exchange events occur independently

To be completed, neighbour exchange must propagate apically to basally. Here I wished to see if this was true for apical neighbour exchange in the notum. Due to the poor basal membrane signal it was not possible to individually segment the basal junctions that are associated with an apical T1 transition at each 1 min time interval. Instead to determine whether apical and basal movements were linked I asked how apical structure matched with basal before and after a T1 and looked to see whether apical exchange occurred concomitantly with basal exchange. Apical T1 transition events were isolated ~ 20 min before and after the formation a 4-way vertex, where clear junction structures could be observed. At ~ -20 (pre-T1), 0, and + 20 mins (post-T1) I segmented basal signal (- 4μm from the AJ) to see how the basal junction structure matched that seen apically. Then, basal neighbour exchange events were isolated, and apical junctions were segmented at corresponding time-points too.

Through this analysis I asked whether apical neighbour exchange events occurred concomitantly with basal neighbour exchange. The vast majority (88%) of apical neighbour exchange events occurred without changes in basal neighbours (Fig 6.4A). 69% of basal T1 transitions occurred in the absence of apical neighbour exchange (Fig. 6.4B). Fewer basal T1 events were observed, so any concomitant apical events would contribute higher to the total proportion. In very rare instances apical neighbour exchange occurred alongside a basal neighbour exchange in the opposite direction (Fig 6.4C). In this example apical neighbours did not match basal either before or after the transition.

As the majority of apical neighbour exchange events occurred independently of basal exchange, we looked to see if apical movement corresponded to basal organization. Essentially, do cells share the same neighbours apically as they do basally post-transition? If yes, then we termed these an '*Apical following basal*' event (Fig. 6.5A) and if not, these were termed an '*Apical opposing basal*' event (Fig. 6.5B). Prior to the T1 the apical junction structure matched the basal junction structure in 40% of cases (Fig. 6.5C). Post-T1 apical and basal junction structures matched in 60% of cases (Fig. 6.5D). For this post-T1 value to have been 100% this would have required the 40% that did have the same apical and basal structure prior to the T1 to

have undergone concomitant apical-basal neighbour exchange, which we have already shown is rare. These results show that apical neighbour exchange occurs without associated changes in basal junction structure, and do not follow basal junction structure.

By undertaking the same study on basal T1 events similar results are observed. Prior to a basal T1 event, 80% of apical and basal junctions do not match (Fig. 6.6C). Therefore we may have expected that this would lead to 80% of junctions matching post-T1, which would suggest that basal neighbour exchange is following apical organisation, such as Fig. 6.6A. However post-T1, only 61.5% of apical and basal junction structures match. This can be explained by a previous result (Fig. 6.4B) that showed a larger proportion of basal transitions are associated with concomitant apical transitions. To conclude, neighbour exchange events are therefore not driven by apical Myo II or adherens junction endocytosis and are not driven apical-first.

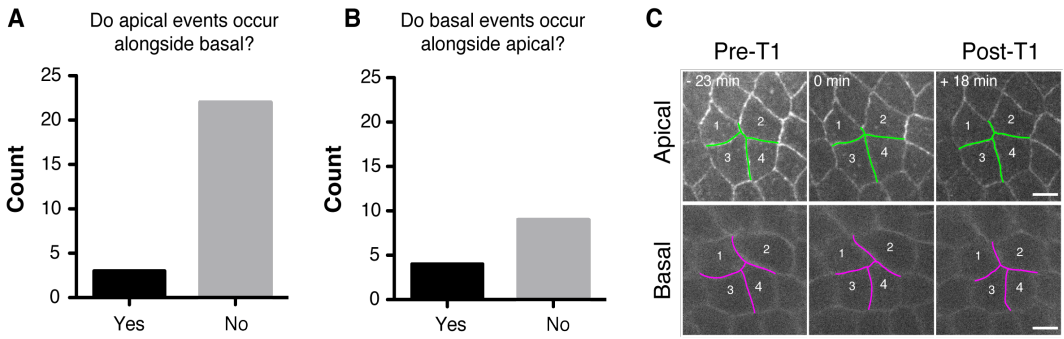


**Figure 6-4: The majority of apical neighbour exchange events occur independently of basal neighbour exchange.**

(**A**) Bar chart showing count of apical neighbour exchange events occurring alongside basal events. (**B**) Conversely, a count of basal transitions that occur concomitantly with an apical transition. (**C**) A rare example of an apical T1 occurring alongside a basal transition. Apical-basal junction structure does not match either before or after each transition. Scale bar = 5 µm.

*If or Cyo / Basigin-YFP; ubi-bazooka-mCh / +*

(Carl Zeiss Axiovert, Larval development at 25$^{o}$C)

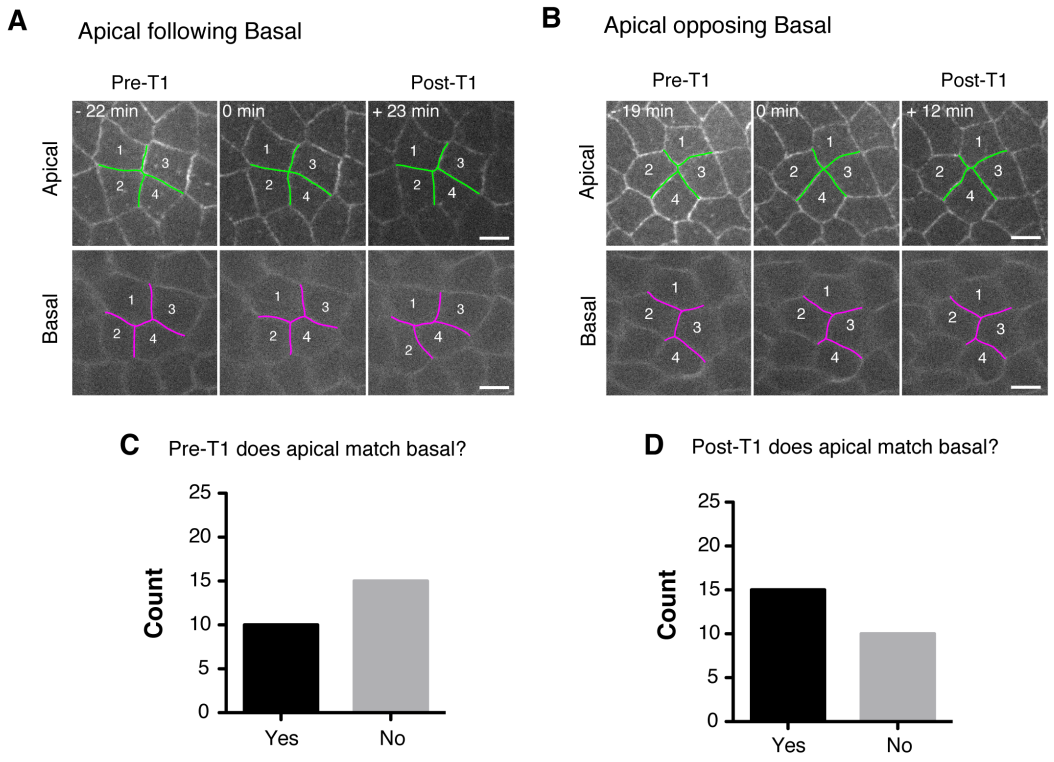


**Figure 6-5: Apical T1 transitions are not driven by basal ordering**

(**A**) Example of an apical T1 transition where junction structure matches basal structure post-transition. (**B**) Example of an apical T1 transition where junction structure matches basal prior to T1 transition. Scale bars = 5µm. (**C**) Bar chart counting whether apical structure matches basal or not prior to neighbour exchange (**D**) Bar chart counting whether apical structure matches basal or not after neighbour exchange. 25 transitions / n = 2 flies.

*If or Cyo / Basigin-YFP; ubi-bazooka-mCh / +*

(Carl Zeiss Axiovert, Larval development at 25$^{o}$C)

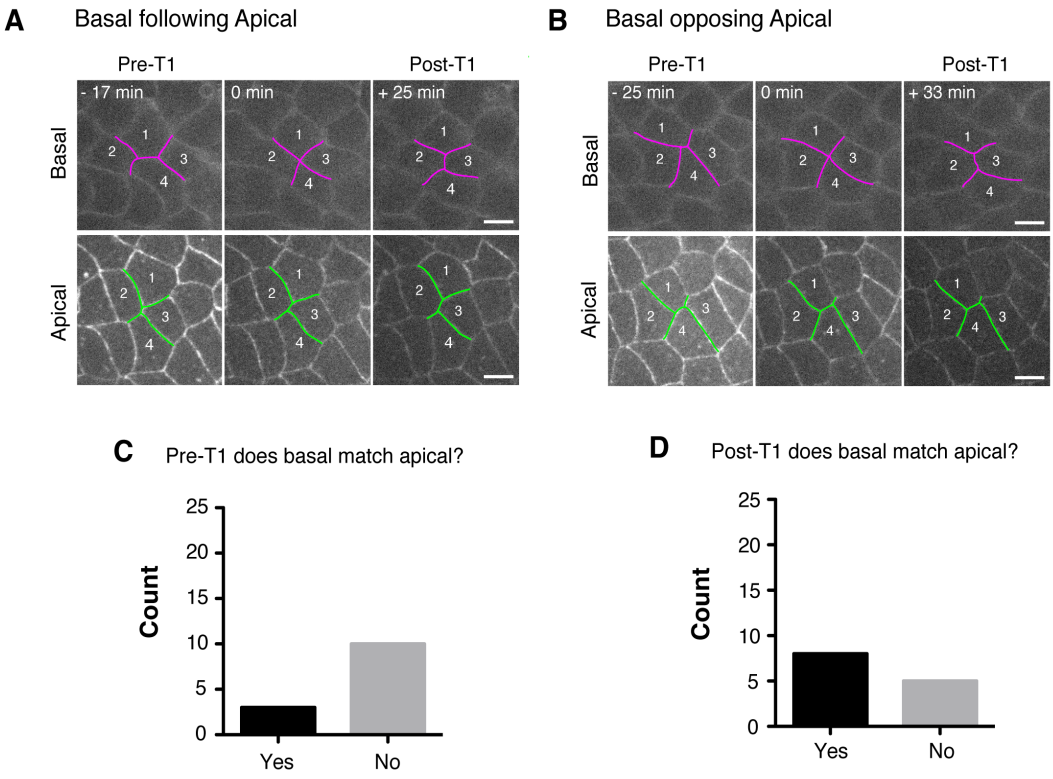


**Figure 6-6: Basal T1 transitions are not driven by apical ordering**

(**A**) Example of a basal T1 transition where junction structure matches apical structure post-transition. (**B**) Example of a basal T1 transition where junction structure matches apical prior to T1 transition. Scale bars = 5µm. (**C**) Bar chart counting whether apical structure matches basal or not prior to neighbour exchange. (**D**) Bar chart counting whether basal structure matches apical or not after neighbour exchange. n = 13 transitions / 2 flies.

*If or Cyo / Basigin-YFP; ubi-bazooka-mCh / +*

(Carl Zeiss Axiovert, Larval development at 25$^{o}$C)

## 6.5 Basal neighbour exchange events do not contribute to local ordering

In Chapter 3, I asked whether apical neighbour exchange was contributing to order for the cells within the four-cell cluster undergoing neighbour exchange. Although differences were slight, neighbour exchange tended to locally increase the proportion of hexagonal packing. Here, I ask whether this is also true for basal neighbour exchange. Again, the cells involved in a basal event were segmented at –20, 0, and +20 mins (Fig. 6.7A). Cells were grouped according to whether they lost a junction (L) or gained a junction (G).

Accordingly, cells that gained a junction by undergoing neighbour exchange tended to gain sides (Fig. 6.7B), whilst cells that lost a junction decreased their mean polygon number (Fig. 6.7E). As for apical cells, basal cells that gained and lost junctions respectively increased and decreased their percentage of hexagons (Fig. 6.7C & F). Unlike for apical neighbour exchange events, cells gaining and losing junctions did not respectively increase or decrease their areas (Fig. 6.7D & G).

When all gain and loss cells were grouped together, no change was observed in the mean polygon number pre- and post- transition (Fig. 6.7H). As described for apical transitions, the only way this could change would be for lots of intercalation events to be occurring on the edge of the four cells involved in the neighbour exchange event.

Basal neighbour exchange also did not increase the proportion of hexagons of the cells involved, as was seen for apical, but actually decreased their proportion locally (Fig. 6.7I). The variance of polygon distributions was not significantly different from before the transition to after (Fig. 6.7J). It can therefore be concluded that, unlike apical neighbour exchange, basal T1s do not contribute to local order. Equally though, basal neighbour exchange is not locally disordering the tissue and so basal transitions appear passive and random.

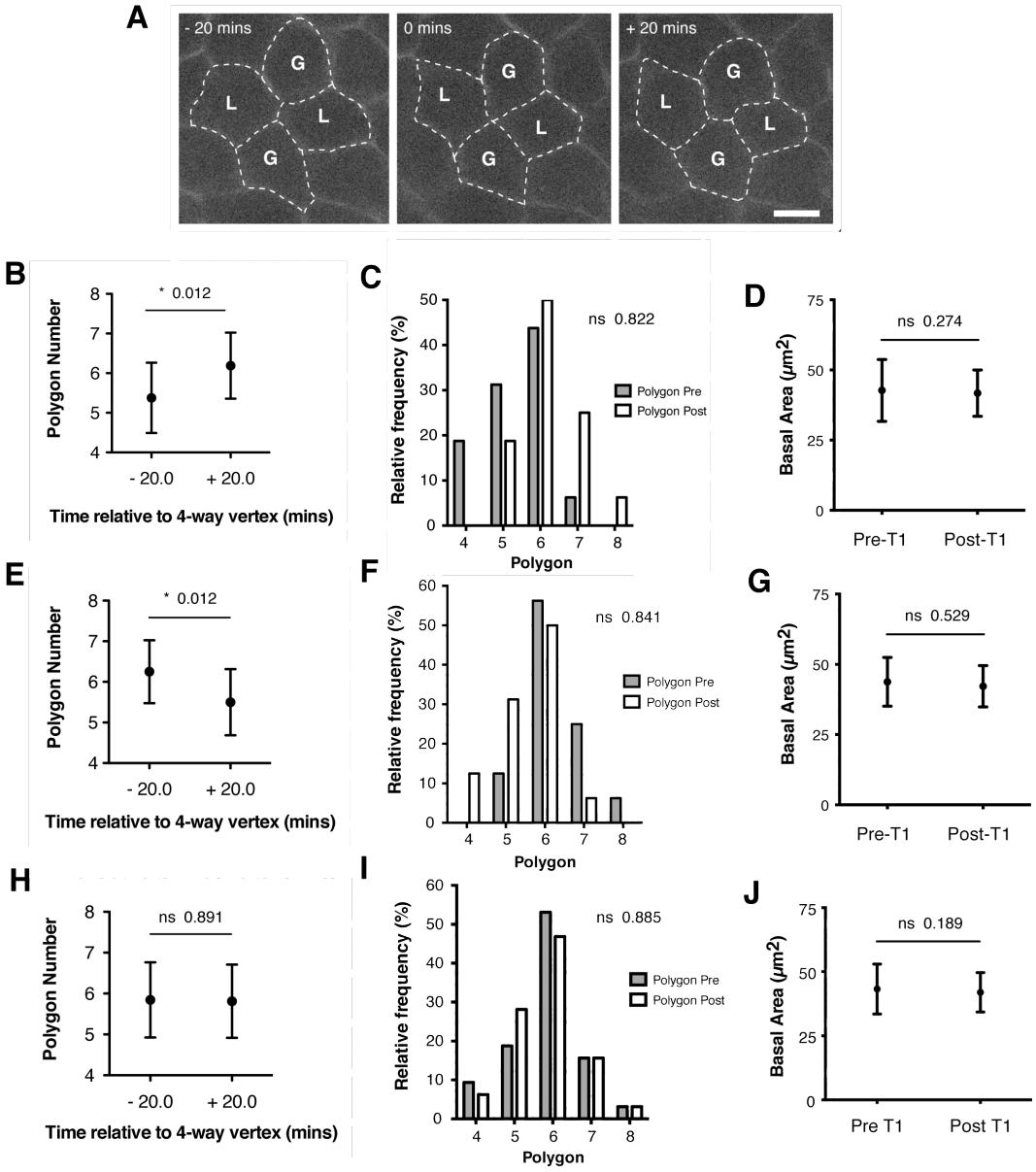


**Figure 6-7: Cell areas remain stable during basal neighbour exchange**

(**A**) Example of a basal neighbour exchange event (imaged with Basigin-YFP). Scale bar = 5μm. (**B**) Mean polygon number 20 mins pre and post the 4-way vertex of a T1 transition for cells gaining a junction, with polygon distribution (**C**) and cell area (**D**). Mean polygon number (**E**), polygon distributions (**F**) and areas (**G**) for cells losing a junction. Mean polygon number (**H**), polygon distributions (**I**) and areas (**J**) for all cells. Graphs for cells gaining and losing junction n = 16 transitions / 2 nota, for graphs of all cells n = 32 transitions / 2 nota. P-values for B, D, E, G, H and J represent results of unpaired t-tests. P-values for C, F and I represent results of F-test to compare variances.

## 6.6 Cell areas redistribute after asymmetric cell division

When nota are imaged with DE-cadherin-GFP for *UAS-Rok*$^{RNAi}$ beyond 13.5 h AP many of the cells in the epithelium fail cell division. Attempts are made to form a new adherens junction contact between the two daughters cells, but these contacts then proceed to break. A population of the cells will however complete division, suggesting that the RNAi is not fully penetrant (Fig. 6.8A). These divisions are highly asymmetric at the apical surface, as measured by the ratio of apical area between the two daughters (Fig. 6.8B). It is unclear how this asymmetry is propagated in 3-dimensions, whether the spindle is tilted during mitosis, or if the two daughters have similar volume. However, when the apical area ratio of the two daughters of an asymmetric cell division is tracked through time we find that the areas of the two daughters become more equal (Fig 6.8C). The larger daughter cell will lose apical area, as the smaller daughter cell gains area suggestive of volume sorting.

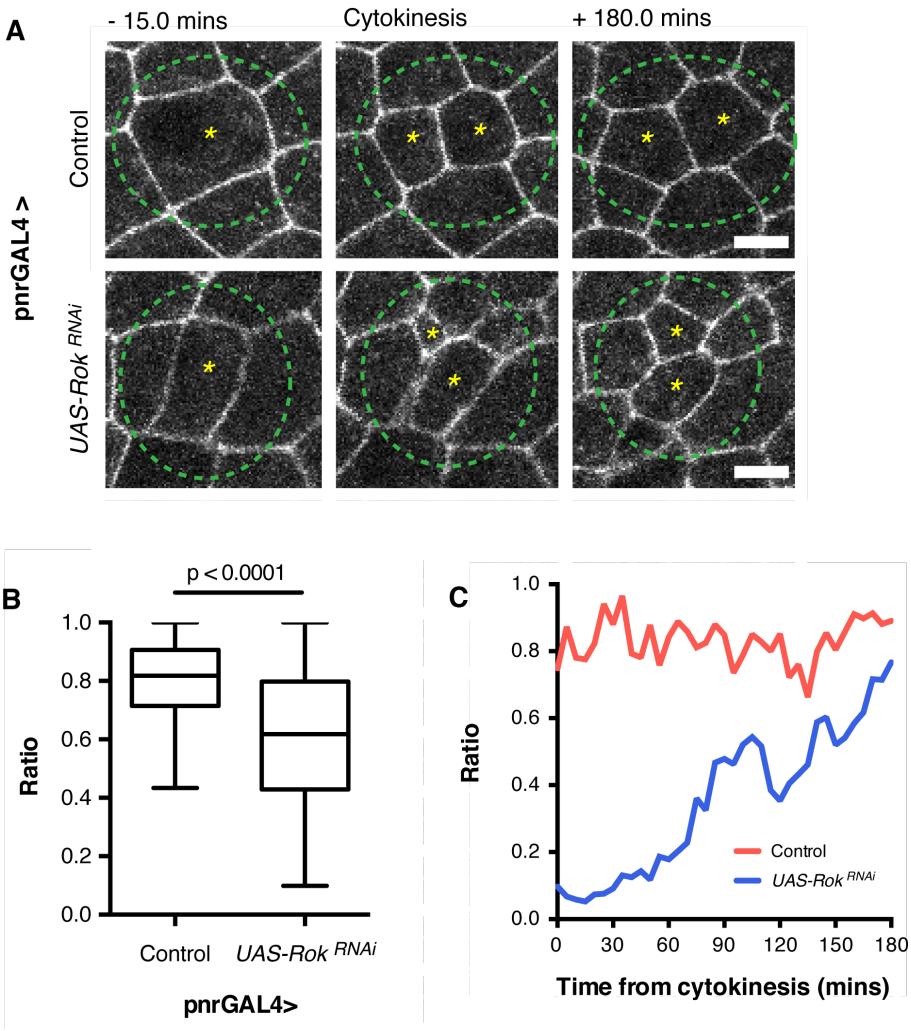


**Figure 6-8: Daughter cells evenly redistribute their areas post-asymmetric division.**

(**A**) Cells labelled with DE-cadherin-GFP prior to division, at cytokinesis, and three hours later for control and *UAS-Rok*$^{RNAi}$. Yellow stars label dividing mother and daughter cells. Scale bar = 5µm. (**B**) Box-and-whisker plot of daughter cells ratios (smaller/bigger) post-division. P-value calculated from Mann-Whitney statistical test. n = 176-185 divisions from 2 flies for each. (**C**) Line graph of daughter cell ratios through time post division for control and a *UAS-Rok*$^{RNAi}$ asymmetric division (cells used in **A**).

*w*$^{1118}$*; DE-cad-GFP(KI) / +; pnrGAL4 / +* (Larval development at 25°C)
*DE-cad-GFP(KI) / UAS-Rok*$^{RNAi}$*; pnrGAL4 / +* (Larval development at 29°C)

(Leica SPE2)

## 6.7 Apical and basal areas are not correlated

Adjustments in apical area, following asymmetric cell division, suggest that volume movements in XZ could drive changes in apical area, facilitated by junction rearrangements. If a volume sorting mechanism were driving apical movements then it could be expected that apical and basal areas of individual cells would be anti-correlated. To test this assumption, as before, apical junctions were visualised and imaged with Bazooka-mCh whilst Basigin-YFP was used to label the basolateral membrane (Fig 6.9A). Spider-GFP was not used as it bleached heavily, had background signal in the nucleus, and cell contacts were too indistinct to isolate basal T1 transitions (not shown). Even with Basigin-YFP, basal cell-cell contacts were indistinguishable at the most basal regions due to overlapping membranes and filopodial protrusions (Cohen et al., 2010; Georgiou and Baum, 2010). Therefore we decided to take basal measurements at 4μm beneath the adherens junction signal, which was just above the nucleus. By matching apical junction structure to cell-cell contacts at this medial plane it was clear that cells in the notum are not perfectly columnar. Thus, cells that share neighbours apically, such as cells labelled 2 and 6 in Fig 6.9A, share an apical cell-cell contact, but are often separated basally. Conversely, cells 3 and 5 do not share an apical contact, but share a contact basally.

Moreover, for most cells there was no correlation between apical and basal area (Fig 6.9B). With a Spearman's rank correlation coefficient, a moderately positive correlation was found between apical and basal area of individual cells. Therefore, at 12 h AP some cells are bigger than others. These data therefore do not support a volume-sorting based hypothesis of apical movement.

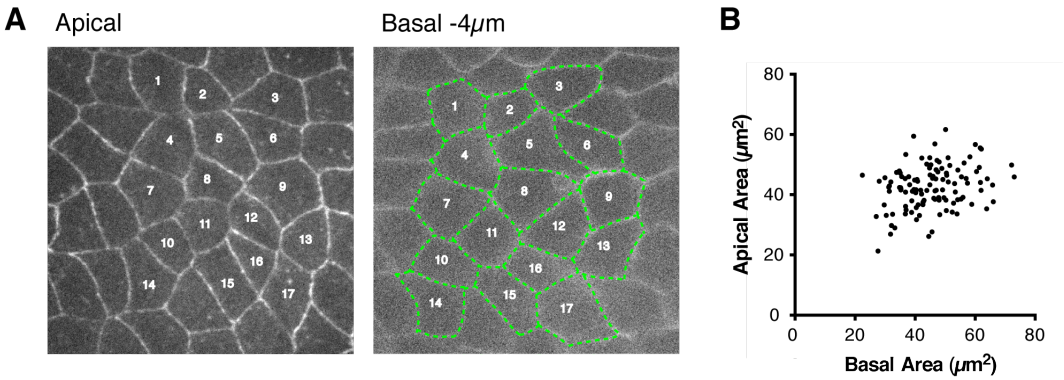


**Figure 6-9: Apical cell area does not correlate with basal area**

(**A**) Apical junctions were visualised with Baz-mCh. Basolateral membranes were labelled with Basigin-YFP. Numbers label cells apically and basally. Basal areas were measured at 4µm beneath the AJ Baz-mCh marker. (**B**) Apical area was plotted against basal area for each individual cell. Spearman's rank = 0.26. n = 117 cells / 2 flies.

*Basigin-YFP / IF or Cyo ; ubi-bazooka-mCh / +*

(Carl Zeiss Axiovert, Larval development at 25$^{o}$C)

## 6.8 Discussion

In previous chapters I have showed that apical actomyosin is not required for neighbour exchange under stable growth conditions, as it is in GBE. Therefore in this chapter I investigated the requirement of adherens junction turnover for cell intercalation. By imaging a temperature sensitive form of Dynamin and blocking endocytosis at restrictive temperatures it was still possible to observe clear neighbour exchange events in the presence of junctional discontinuities with DE-cadherin-GFP. Under these conditions exchange events were less frequent suggesting that turnover was non-essential but was aiding the exchange of apical cell-cell contacts. These data support a sliding model of cell intercalation in which the adherens junction network acts a fluid system to allow lateral movement of vertices.

Are adherens junctions required at all? In testing this, I found that the adherens junction isn't essential as neighbour exchange events were observed in the *UAS-ß-catenin*$^{RNAi}$ expressing *pannier* domain, which had a 30% level of E-cadherin and was positive for active Myosin II. Neighbour exchange events seen in the absence of an AJ further confirm the non-requirement for actomyosin contractility as Myo-II localises to isolated apical ring structures. With higher resolution and non-bleaching membrane-markers it would be interesting to see how AJ-independent neighbour exchange quantitatively compares to control and whether passive movements drive similar changes in apical cell packing. Recent TEM analysis of these tissues (not shown) indicates that in the absence of an adherens junction cells still retain close basolateral junction contacts. Tissues have a basement membrane (Appendix 9.2), are covered by an overlying cuticle layer, and in the absence of an adherens junction retain cell polarity, divide in the epithelial plane and still form an adult tissue.

Movement in the absence of an AJ or apical actomyosin does suggest that basal movement could supply the forces driving apical neighbour exchange. However by our measures, apical movements occur independently of basal neighbour exchange, and apical neighbour exchange events are not propagated basally. Basal events do appear to be more passive that apical events as apical neighbour exchange events tend to order, while basal exchanges do not. This suggests that the apical actomyosin cytoskeleton, present at 12 h AP, may provide enough junction tension to drive

increased order. This is supported by *UAS-Rok*$^{RNAi}$ tissues, which are less ordered than control, even with increased numbers of neighbour exchange events. Under *UAS-Rok*$^{RNAi}$ conditions however, apical movements may be more susceptible to basal movements due to absence of inhibitory apical contractile force.

# 7. Results: Changes in actomyosin localisation during later notum development aid hexagonal tissue packing

## 7.1 Introduction

Thus far, I have concentrated on the dynamics and neighbour exchange events that occur during a small window of pupal development between 12 and 13.5 h. Between 13 and 20 h AP ~30% of midline cells delaminate from the tissue (Marinari et al., 2012). During the same period all cells within the scutum divide once, and a subset of these divide to form evenly spaced sensory organ precursor cells. These divisions disorder the tissue. Late in pupal development tissue packing in the notum becomes much more regular. It is not known how the tissue gets from a disordered state post-division at ~20 h AP to an ordered hexagonally packed tissue between 25 and 30 h. This will be investigated in this chapter, by following the localisation of Myosin II and seeing how developmental changes in localisation correlate with junction tensions and tissue packing.

## 7.2 Developmental Myosin II relocalisation to the junction correlates with an increase in line tension

To track apical Myo II localisation through pupal development Sqh-GFP was imaged with an apical junction marker, Baz-mCh. Single images were collected at set intervals from 12 through to 30 h AP. Myo II localisation at 12 h AP has previously been described (Fig. 4.1). Total Myo II is predominantly at the junction but is also observed in a medioapical meshwork that links to the junctional pool. Between 12 and 20 h AP, all cells in the tissue divide, ~30% of midline cells delaminate, and a subset of cells differentiate to sensory organ precursors. As a consequence of these divisions, by 20 h AP, all of the cells are smaller. However Myo II still localises to both medial and junctional pools (Fig. 7.1). Between 20 and 30 h AP though, Myo II is progressively lost from its medial pool and increases in density at the junction. At 12 and 20 h it is not possible, using conventional confocal microscopy, to determine to which cell the junctional Myo II cables belong to as they form thin structures that overlap with AJ signal. Between 25 and 30 h medial Myo II is removed from the

apical surface. Junctional Myo II is much denser and forms in discrete intracellular cortical rings, linked tissue-wide through AJ contacts (Fig. 7.1).

To determine if a denser junctional Myo II network correlated with an increase in line tension laser ablation cuts were made at 12, 20 and 30 h AP. This was indeed the case (Fig 7.2A). However while displacement was greater at 20 h, mean displacement measured at 10 s after the cut was not significantly different (Fig 7.2A). By 30 h vertex displacement at 30 h was significantly higher than at both 12 and 20 h AP. This shows that increased density of junctional Myo II correlates with increased line tension and is in agreement with previous work from the lab (Marinari et al., 2012).

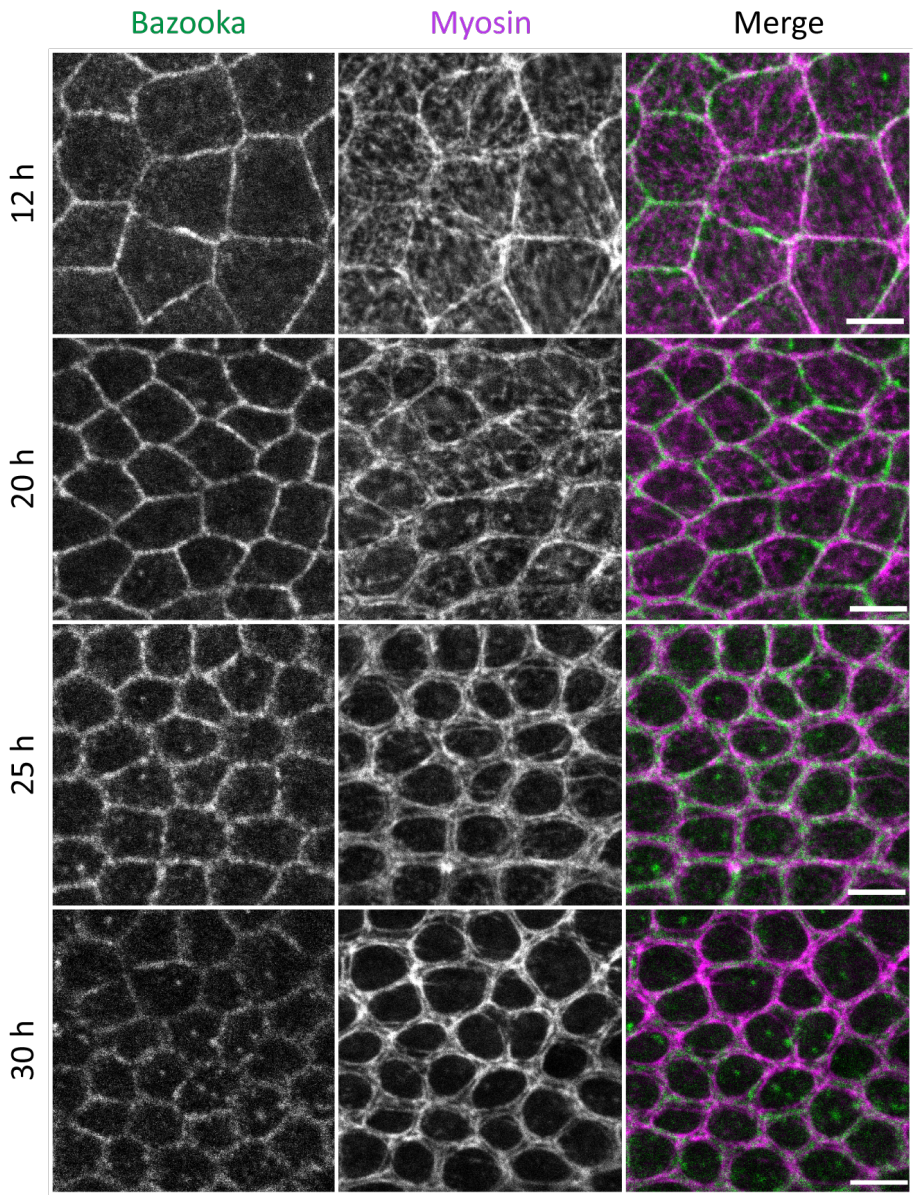


**Figure 7-1: Between 20 and 30 h AP apico- medial Myosin II levels decrease as junctional Myosin II levels increase.**

Nota imaged at 12, 20, 25, and 30 h AP with Bazooka-mCh (apical adherens junction marker) and Myosin-GFP (MRLC). Scale bar = 5µm.

*$sqh^{Ax3}$ / Y or +; sqh-GFP / +; ubi-bazooka-mCh / +*

(Carl Zeiss Axiovert, Larval and pupal development at 25°C)

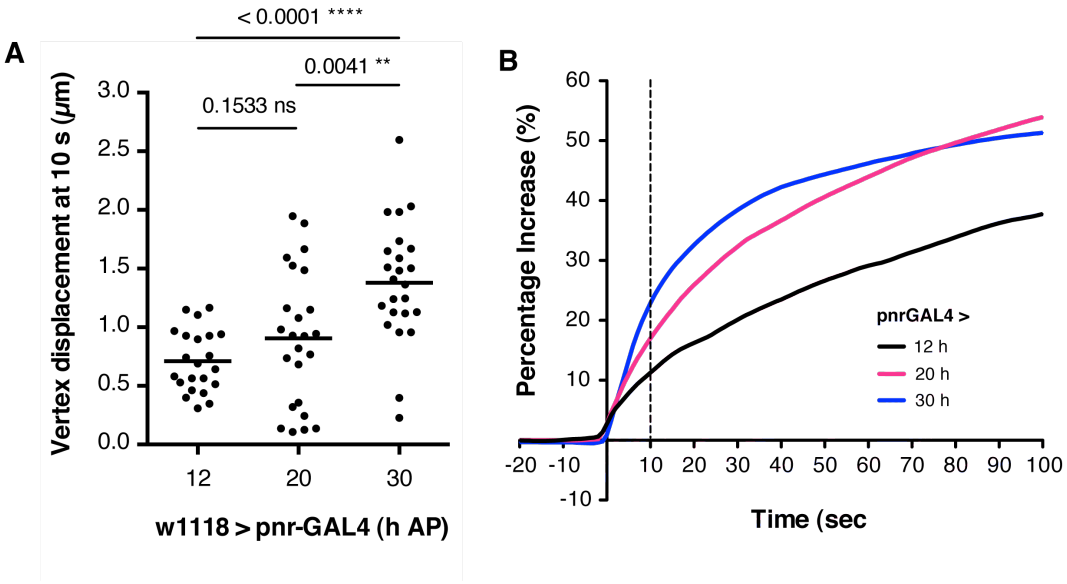


**Figure 7-2: Junction tension increases during tissue development**

(**A**) Aligned scatter plot of total vertex displacement at 10 s after ablation for junctions at 12, 20 and 30 h AP. Line indicates median. P-values from unpaired t-test. n = 22-24 cuts from 5-7 flies. (**B**) Line graph of mean vertex displacement measured as a percentage of pre-ablation median length. SEM not shown.

## 7.3 Increased junctional Myosin II correlates with improved tissue packing and order

In a 2D vertex model increased line tension and contractility tend to drive the system towards a hexagonally packed ground state (Farhadifar et al., 2007). To see how increased levels of junctional Myo II, at these late stages of tissue development, affect tissue packing I undertook measures of cell geometry though time.

Baz-mCh labelled nota were segmented at 12, 20, 25 and 30 h AP (Fig. 7.3A). Although cell divisions increase disorder the proportion of hexagons remained steady from 12 to 20 h AP (Fig. 7.3B). Between 20 and 30 h however, the proportion of hexagons in the tissue dramatically increased from ~50 to ~60%, as the levels of junctional actomyosin increased.

As a second measure of order, I next examined variance in junction lengths. Division complicates this, as it causes the mean junction length to decrease. However, the coefficient of variation still provides a good measure, as it is a standardised measure of dispersion that represents the ratio of the standard deviation to the mean. The lower the percentage variation, the less variable the data. Using this measure, the variance in junction lengths was found to decrease over developmental time, from 12 to 20 h, and again from 20 through to 25-30 h AP (Fig. 7.3C). Again this is suggestive of increased order.

As a final measure of cell packing order, I looked at ellipse elongation to measure variation in cell shape. An ellipse was fit to each cell in the tissue and the ratio of its major / minor axis plotted. Less elliptical, or more circular cells, suggest an increasingly perfect hexagonal lattice. Using this measure ellipse ratios decline beyond 20 h AP (Fig. 7.3D).

During this work I noticed that beyond 25 h, a subset of cells within the epithelia expand in apical area. These are the microchaetes, the mechanosensory bristle structures that form on the thorax of the fly, as a result of the two rounds of asymmetric division performed by each primary sensory organ precursor cell (SOP). Microchaetes comprise two inner cells, the neurone and sheath; and two outer cells,

the socket and the shaft (Fichelson and Gho, 2003; Gho et al., 1999; Roegiers et al., 2001). The area of the socket cells increases rapidly from ~25h AP. These cells therefore contributed to an increase in mean cell area between 25 and 30 h and their presence in the tissue will have affected the mean number of neighbours, junction length variance and ellipse elongation (not shown).

These cells can be seen as a discrete population when plotting polygon number against cell area. In the 1920's F.T. Lewis stated that cell areas increase linearly with the number of sides the cell has (Lewis, 1926, 1928). By plotting the mean area for each polygon class through development we observe that packing of the *Drosophila* notum fits this law perfectly up to 25 h AP (Fig. 7.4). However, this correlation is no longer linear at 30 h, as the SOP cells with increased neighbours (8 and 9 neighbours) have disproportionately large cell areas.

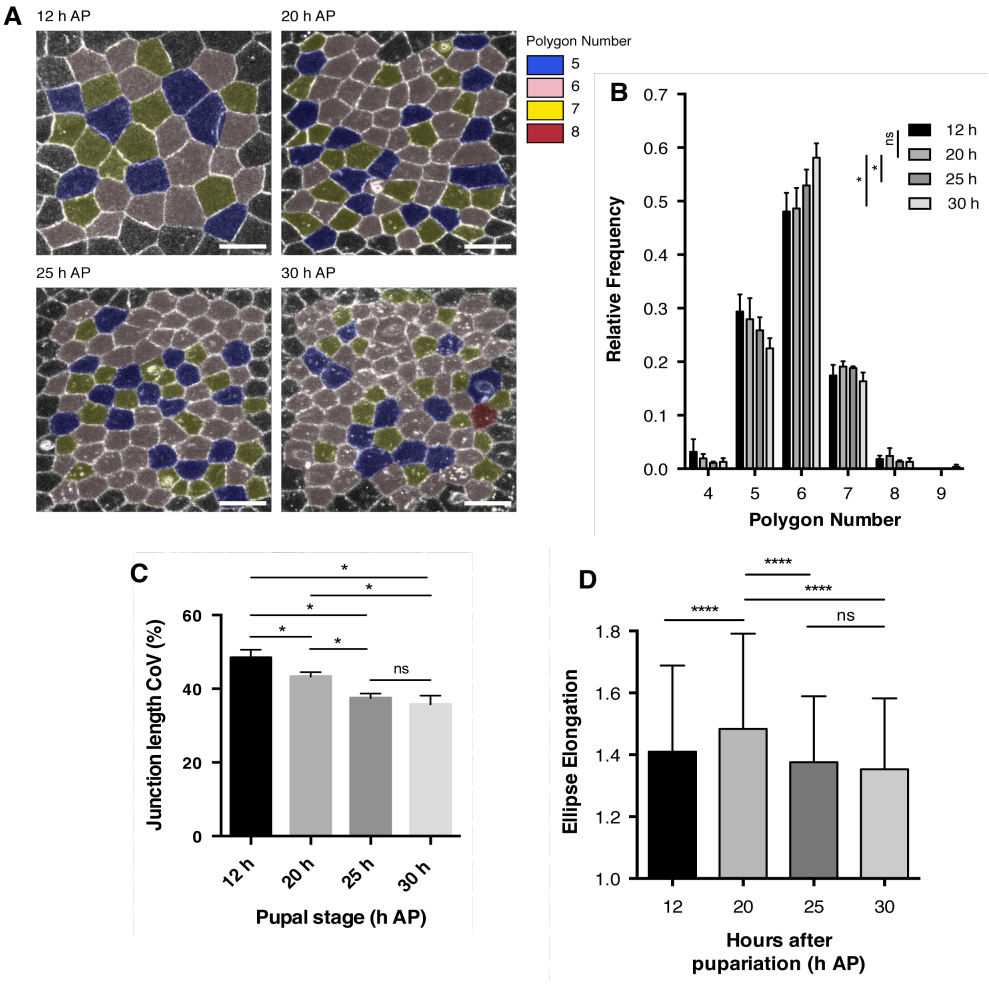


**Figure 7-3: Hexagonal packing increases between 20 and 30 h AP**

(**A**) Cells at several developmental time-points coloured by the number of sides they have. Scale bar = 10 µm. (**B**) Histogram of polygon distribution. n = 695-1023 cells from 3-5 flies. Error bars indicate standard deviation between individuals. P-values for t-test, 12 h v 20 h = 0.0743 (ns), 20 h v 25 h = 0.8165 (ns), 20 h v 30 h = 0.5586 (ns). P-values for F-test to compare variances, 12 h v 20 h = 0.5486 (ns), 20 h v 25 h = 0.0281 (*), 20 h v 30 h = 0.0155 (*). (**C**) Bar chart of coefficient of variation of junction lengths. n = 4 variances calculated from 2302-3376 junctions. (**D**) Bar chart comparing ellipse elongation of cells. n = 695-1023 cells from 4-5 flies. P-values calculated from Mann-Whitney statistical tests.

*$sqh^{Ax3}$ / Y or +; sqh-GFP / + ; ubi-bazooka-mCh / +*

(Carl Zeiss Axiovert, Larval and pupal development at 25°C)

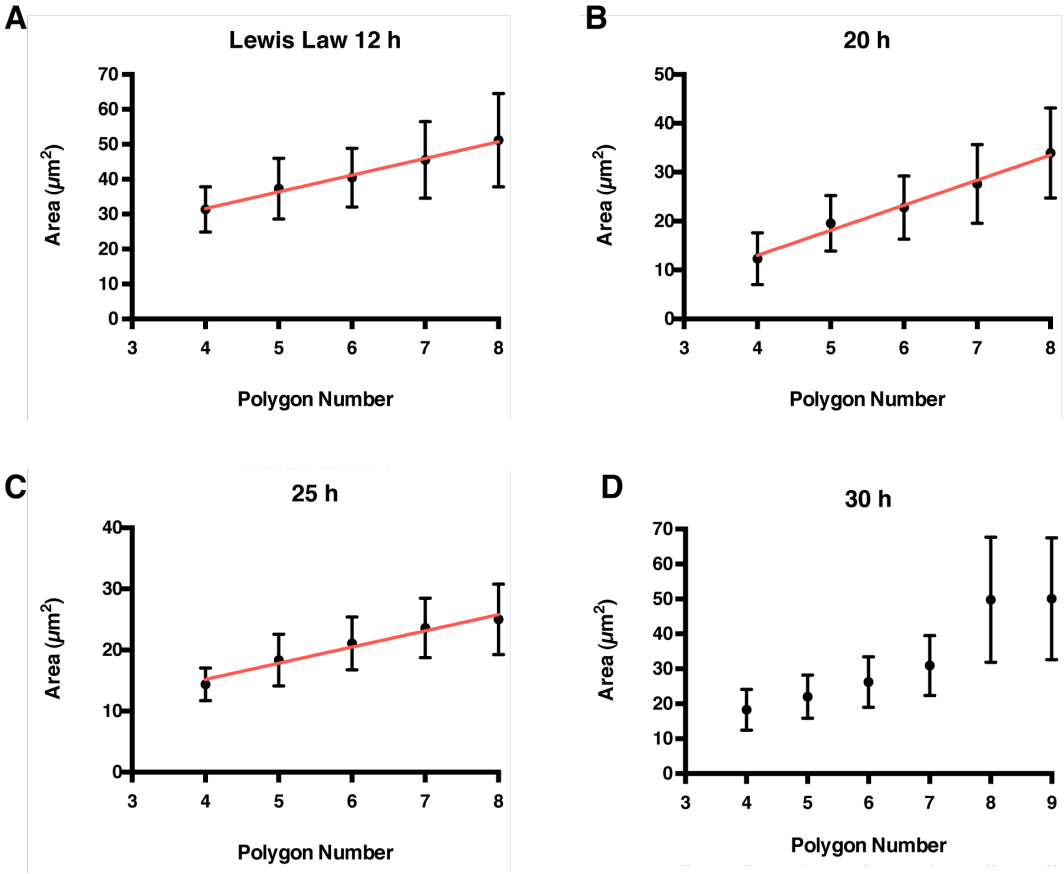


**Figure 7-4. Cell area increases with the number of neighbours consistent with Lewis Law**

The number of neighbours a cell has (polygon number) is plotted against its individual cell area at 12 (**A**), 20 (**B**), 25 (**C**), 30 h AP (**D**). Dots represent mean, tails represent SD. 695-1023 cells from 4-5 flies. **A**, Slope = 4.787, $R^2$ = 0.992; **B**, Slope = 5.13, $R^2$ = 0.986; **C**, Slope = 2.649, $R^2$ = 0.971.

## 7.4 Discussion

The analysis of Myosin II localisation through pupal development revealed a change in localisation at 20 h AP. In early pupal development a predominantly junctional Myo II pool is present alongside a pulsatile medial network. Beyond 20 h, post-division and delamination, the medial pool completely disappears through displacement to the junction. The mechanisms that mediate this movement to the junction are currently unknown; though appear to be regulated by developmental timing.

Increased junctional Myo II density correlates with increased line tension. Initial vertex displacement after laser ablation increased from 12 h through to 30 h AP. Several measures showed that this increased tension was associated with improved tissue packing. The proportion of hexagonal cells increased from 20 to 30 h, whilst junction length variances and ellipse elongations decreased, which is indicative of increasingly regular cell shapes. In the absence of division and delamination neighbour exchange must occur to increase hexagonal packing. The inhibitory role for Myo II suggests that as contractility increases, cell-cell contacts created through ordering neighbour exchange events become locked in place. Thus *UAS-Rok*$^{CAT}$ and *UAS-sds22*$^{RNAi}$, described in previous chapters, may mimic premature tissue development. In the General Discussion I will explore how these results and pupal tissue packing fit with 2D vertex models of epithelial development.

# 8. General Discussion

## 8.1 The notum versus germ band elongation

By investigating junction fluctuations and neighbour exchange events in the *Drosophila* notum I have looked to understand the mechanisms of cell intercalation that occur under conditions of homeostatic growth. As current models of neighbour exchange have been developed based upon studies of tissues undergoing rapid changes in shape my analysis may provide a new model of neighbour exchange that works for non-morphogenetically active epithelia that are ubiquitous across nature.

To study the dynamics of neighbour exchange, fluorescently labelled markers were used to tag discretely localised adherens junction proteins and track adherens junction movements in a 2D plane. Through image segmentation and analysis these movements were compared to hypothetical models of exchange. T1 transitions in the notum were shown to be qualitatively different from those expected under the standard model used to explain GBE. Thus neighbour exchange events were randomly positioned in time, position and orientation. Cumulative events did not lead to tissue morphogenesis, though did contribute to slight increases in tissue order over the period from 12 -13.5 h AP. Unlike GBE, neighbouring junction lengths were anti-correlated with one another indicating a potential sliding mechanism of neighbour exchange; further supported by the fact that junction turnover is not essential for intercalation.

Importantly, cell intercalation was also shown to occur independently of actomyosin contractility. Polarised contractile forces in the scutellum, generated by the atypical Myosin Dachs, show that polarised tension in the notum can be used to drive changes in tissue shape (Bosveld et al., 2012). However in the region of the notum studied here, Myo II played no role even though it drives morphogenesis in the embryonic germ band. This is likely a consequence of polarity. The planar polarised localisation of Myo II in the germ band drives the loss of specific junctions with a defined direction. The role of the adherens junction is to keep contractile Myosin II at the junction so the force it produces can alter the rate of neighbour exchange. In the notum however Myosin II is not polarised. Forces are balanced across the tissue thereby inhibiting junction movement. In this work, T1s in the notum were found to be reversible. Moreover, they were symmetrical in time, i.e. they expand and

contract at the same rate as expected by sliding. By contrast, in GBE the two events are different, though the mechanisms by which junctions expand during intercalation in the germ band are less clear. Work from the pupal wing disc suggests a role for PTEN and PIP3/PIP2 in junctional elongation (Bardet et al., 2013). In this model junction expansion is facilitated by a loss of inhibitory Myo II. However a requirement for Myo II to specifically drive junction loss does not fit with our model. Our data suggests a more general model in which neighbour exchange is driven by fluctuations in junction length that are Myo II independent. So what are the molecular mechanisms that would allow such movement?

## 8.2 Quantitatively measuring junction dynamics to understand mechanisms of neighbour exchange

To establish a link between the role of molecular Myosin II to T1 transitions and then to global tissue behaviour I explored junction fluctuations in collaboration with Charlotte Strandkvist (Baum lab, UCL). I have not included the results from this study in my thesis as the analysis is still in progress, and the results will form the majority of Charlotte's own thesis. However, the data are integral to the future publication of this work and so I will discuss the questions raised and data here.

The key question we looked to answer, was whether neighbour exchange events are a direct consequence of junction fluctuations, i.e. do junctions undergo T1 transitions as a result of general fluctuations in their length? In this scenario, while long junctions change in length, short junctions would occasionally shorten to zero and undergo an exchange event from similar length changes. If this were the case, it could explain the observation that neighbour exchange is independent of actomyosin contractility and AJ turnover.

To ask if fluctuations that drive exchange are identical to those in the general population I segmented time-lapse images from regions outside the midline, as for Fig. 3.1 (50+ cells, 200 + junctions), at 30 s intervals from 12 – 13.5 h AP. This produces a large dataset of all cell and junction descriptions. Charlotte then fitted a smoothing filter to all junction fluctuations to analyse their dynamics. These fluctuations were broken down to sections of expansion and contraction. The length

difference between the beginning and end of each section, the length persistence, was plotted as a histogram. For each junction undergoing a T1, only the lengths immediately preceding and proceeding t=0 were plotted. Comparison of the distributions of junction length persistence for junctions undergoing T1 with those of the global population showed them to be the same. This supports the idea that the two types of fluctuation are identical, as expected if cells undergo neighbour exchange as a result of stochastic length fluctuations.

As already observed, Myo II can affect the number of neighbour exchange events, with increasing levels of active Myo II inhibiting T1 transitions. This implies that junctions should fluctuate less than control under conditions of increased Myo II. To compare length fluctuations with changing Myo II levels, Charlotte used the mean squared displacement (MSD) as a measure. Importantly MSD values were increased for junctions with decreased Myosin activity (*UAS-Rok*$^{RNAi}$ and *UAS-sqh*$^{AA}$). This fits with the key finding of my thesis work that Myo II constrains junction dynamics. The results of increasing Myo II activity were less clear-cut, partly because the analysis was confounded by junction discontinuities causing segmentation errors and by global tissue deformation induced when Myo II was increased.

## 8.3 Hypothetical molecular mechanisms of cell intercalation

When I looked at total junction lengths during a T1 I noted that there was no junctional loss. Moreover endocytosis was not required. These results show that the mechanism of T1 is not a two-step process. Instead they are suggestive of a sliding mechanism, with the three-way vertex acting as a virtual point that can laterally move to extend or decrease the distance of a cell-cell contact. Sliding would be a useful mechanism to facilitate stress dissipation on short time-scales. Moreover this could be seen as an ideal way to make developing epithelia robust to perturbations, such as division, delamination and shear.

How might this work? The cell-cell contact is made up of homophilic E-cadherin interactions. Stable cadherin puncta are held in place at the junction by intracellular increases in the level of apical actomyosin contractility (Cavey et al., 2008). I envisage a ‘zipper’ mechanism by which junctions expand and contract in the

absence of endocytic turnover (Fig 8.1). During junction loss, the movement of the vertex, the 'zipper', mediates the breakage of E-cadherin contacts between two neighbouring cells (Fig. 8.1B). Lateral movement of transmembrane E-cadherin monomers across the vertex, allows new homophilic contacts to made. As a result there is concomitant loss and gain of length as levels of junctional E-cadherin are conserved as a consequence of the lateral movement of E-cadherin molecules across vertices. This preserves E-cadherin densities at cell-cell contacts ensure the maintenance of tissue integrity, with little energy cost. The energy barrier depends on cost of breaking E-cadherin contacts. This will be increased in E-cadherin cluster, with increased Myo II activity, and reduced with lower Myo II levels, through *UAS-Rok*$^{RNAi}$ (Lecuit and Lenne, 2007).

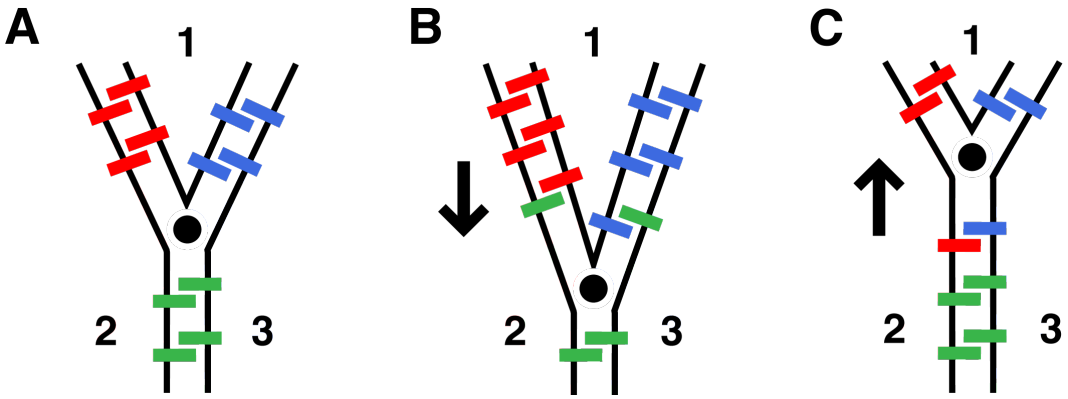


**Figure 8-1: Model of DE-Cadherin zippering**

Hypothetical model of three-way vertex movement facilitated by E-Cadherin zippering and movement of molecules across the vertex. (**A**) Cells labelled 1, 2 and 3. DE-cadherin dimers labelled red between cells 1 and 2, blue between 1 and 3, and green between 2 and 3. (**B**) Movement of cell downwards, to shorten the contact between 2 and 3, breaks E-cadherin dimers between 2 and 3. (**C**) Movement of vertex upwards, extending the contact between 2 and 3, breaks contacts of cell 1.

## 8.4 Visualising potential lateral E-cadherin movement

To determine whether E-cadherin can flow across contacts as envisaged in Fig. 8.1 an ideal experiment to visualise movement would be to use a photo-convertible E-cadherin. We are currently restricted by the constructs available such as EOS and Dendra, as they clump together and bleach too heavily (Appendix 9.5). In a perfect experiment, a region of the junction would be stably photo-labelled during a T1 transition. If driven by endocytosis, the labelled region would be removed as the junction shrinks (Fig. 8.2A). If neighbour exchange occurred, in the absence of junction turnover, there are two possible scenarios. The first scenario is that E-cadherin is stable, and vertices move across the photo-labelled region (Fig 8.2B). The vertex movement in this example though cannot be easily reconciled with the zippering mechanism I previously proposed. Alternatively the lateral diffusion of E-cadherin and the breakage and formation of new dimer contacts, between pre-labelled and photo-labelled monomers could allow for vertex movement across the photo-labelled region. As a further test of the requirement for junction turnover one could undertake the same experiment with *shibire* flies at restrictive temperatures, where the experiment is not confounded by endocytosis.

A simpler method to infer lateral E-cadherin movement during neighbour exchange would be to use FRAP. Junctions can be bleached and kymographs used to observe, with high enough resolution, the mode of E-cadherin recovery. Diffusion would tend to lead to recovery from one or both sides of the bleached region. By contrast, vesicle trafficking would tend to lead to uniform recovery across the whole junction. One could continually bleach a junction and plot the junction intensity of first, second and third neighbours within the same cell (Fig. 8.3). Under restrictive conditions *shibire*$^{ts}$ flies, could be used to block endocytosis. If the junctional intensity of first neighbours decreased faster than those of neighbours further away, this would again be indicative of lateral movement of E-cadherin within cells. Bleached monomers would laterally move into non-bleached regions, thereby reducing the mean intensity of those junctions.

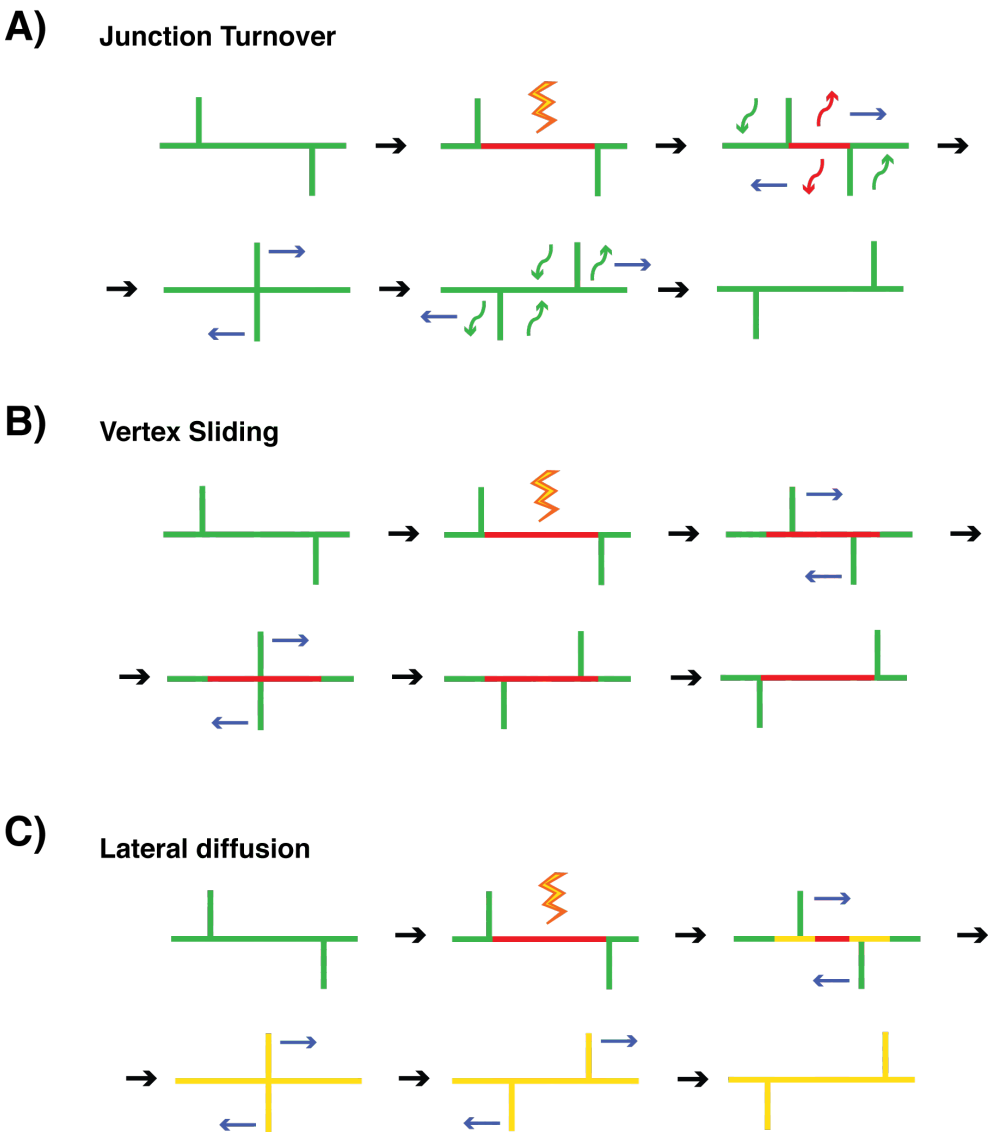


**Figure 8-2: Using photobleaching to follow E-cadherin movement during neighbour exchange**

A hypothetical experiment to visualise the movement of E-cadherin during neighbour exchange. A pre-labelled (green) junction undergoing exchange is stably photo-labelled (red). (**A**) An example where junction turnover drives exchange. The photo-labelled region is lost as the junction contracts. (**B**) Stable positioning of the photo-labelled region in the absence of lateral movement. The vertices of neighbouring junctions move across the photo-labelled region. (**C**) Lateral diffusion of E-cadherin facilitates neighbour exchange. The tissue acts as a fluid network, and photo-labelled monomers form dimers (yellow) in neighbouring cell-cell contacts.

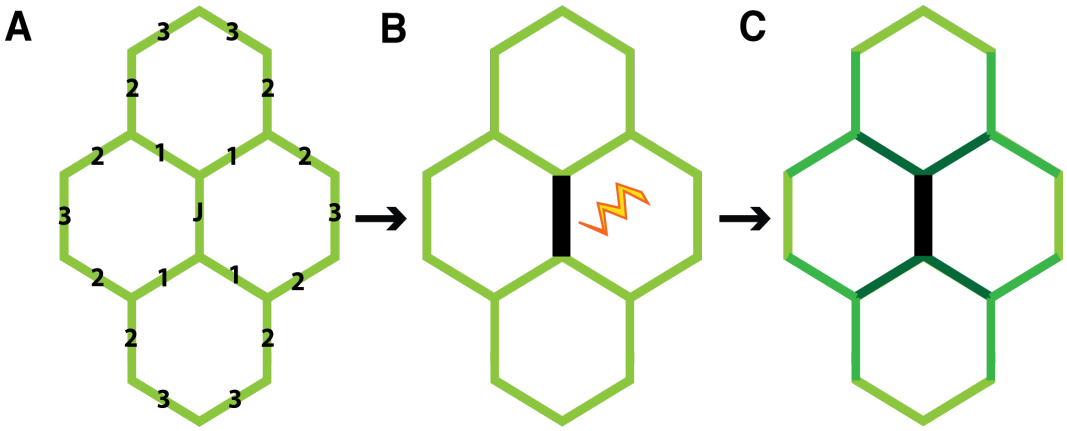


**Figure 8-3: Neighbours will decrease fluoresecence intensity as bleached DE-cadherin-GFP molecules laterally move from a junction being continually bleached**

Diagram of a hypothetical FRAP experiment to test for lateral movement of DE-cadherin within the adherens junction network. (**A**) Four linked cells labelled with DE-cadherin-GFP. J, junction to be bleached. 1, 2, 3, indicate first, second and third neighbours to bleached junction, respectively. (**B**) J is bleached, causing the fluorescence intensity of DE-cadherin molecules within the junction to equal zero. (**C**) J is continually bleached at regular intervals. Lateral movement of bleached molecules from J will move into neighbouring junctions. This will lower the fluorescence intensity of junctions in a gradient that will be dependent on distance from the bleached junction. Shibire flies can be used to block endocytosis so fluorescence intensity is only affected by lateral movement.

## 8.5 How the notum fits with 2D vertex models of epithelial tissue development

Another way to understand how molecules control junctional behaviour and impact on tissue dynamics is to use models. A popular way to do this is to use 2D vertex models. These can be used to simulate the physical properties that generate the packing geometries seen in the notum and how the tissue approaches hexagonal packing through development. Using the framework developed by Farhadifar *et al.,* the resting network can be seen to evolve through time, satisfying mechanical force balances at each step before converging upon two steady states (Farhadifar et al., 2007). Mehonic *et al.* showed that introducing a noise parameter into the model helped the system to reach these equilibrium states faster (Marinari et al., 2012).

Working with Charlotte Strandkvist and Marc de Genne with Guillaume Salbreux (Crick Institute, London) we sought to use these models to understand the role of Myosin II in epithelial tissue packing. At 12 h AP the *Drosophila* notum has a disordered packing geometry with low junction tensions and low contractility. Between 13.5 and 20 h widespread division removes ordered packing, as suggested by the Gibson Markov-Model (Gibson et al., 2006). In the vertex model these stages represent a soft network. Under these conditions, simulations of the soft network will reach a steady state in which packing geometries are irregular but cells have similar areas and perimeters. However, as junctional Myosin II increases gradually from 20 h AP the tissue will tend towards an elastic phase and hexagonal packing.

Thus at early stages, low junctional Myo II levels may facilitate cell movement. This fluidity allows the local dissipation of force imbalances produced by division and delamination events. As junction tensions increase steadily post-division some neighbour exchanges occur so that T1 transition events passively order the tissue. However with increasing levels of junctional Myo II and cortical contractility, the tissue will behave increasingly fixed and elastic. This process is akin to annealing. Using the example of mild steel, forging heats the metal to a high temperature to bring it to a malleable and ductile state. This soft phase is analogous to early pupal development and the presence of fluid junction dynamics. As it slowly cools crystals form locking the system down, as crystal packing orders. Thus at late developmental stages slow increases in actomyosin may tend the tissue towards an ordered

structure. At 30 h AP the high contractility locks the regular hexagonal packing in place. Decreasing Myo II levels is equivalent to keeping the metal at a high temperature, and maintaining a fluid state. Conversely, an early increase in active Myo II is analogous to quenching the metal, as is done with swords (steel), thereby freezing dislocations in the crystal structure.

The global round of division, that induces disorder in the notum, makes it difficult to test how changing levels of junctional contractility correlate with tissue packing (Fig 8.4A). How would the tissue freely develop in the absence of cell division? An experiment to test this question would be to use an RNAi against Cdc25/String, to block cells at the G2/M checkpoint. Then it would be possible to precisely measure how changing tissue packing states correlate with development increases in the levels of junctional Myo II (Fig. 8.4B). It could be predicted that slow increases in junction tension would allow the tissue to pack faster than it would in control (without confounding effects of division). Furthermore, changing gradients of contractility could then be tested in this system. It may be expected that in conditions of low actomyosin contractility, through Rok knockdown, the tissue would remain in a disordered soft phase throughout development (Fig. 8.4C). Conversely, constitutively high levels of active Myo II may drive the tissue rapidly towards a hexagonally packed state faster than control in the absence of division (Fig. 8.4D).

Returning to the control development scenario, expressing altered levels of active Myosin II late, after division at 20h, may also push the tissue out of hexagonal packing. Increased Myo II activity may drive the tissue towards regular hexagonal packing faster, or possibly too quickly as irregular packing dislocations do not have the time to resolve and are locked in place. Expressing RNAi for Rok may reverse the effects of annealing and push the tissue toward a soft-phase with increasingly irregular packing.

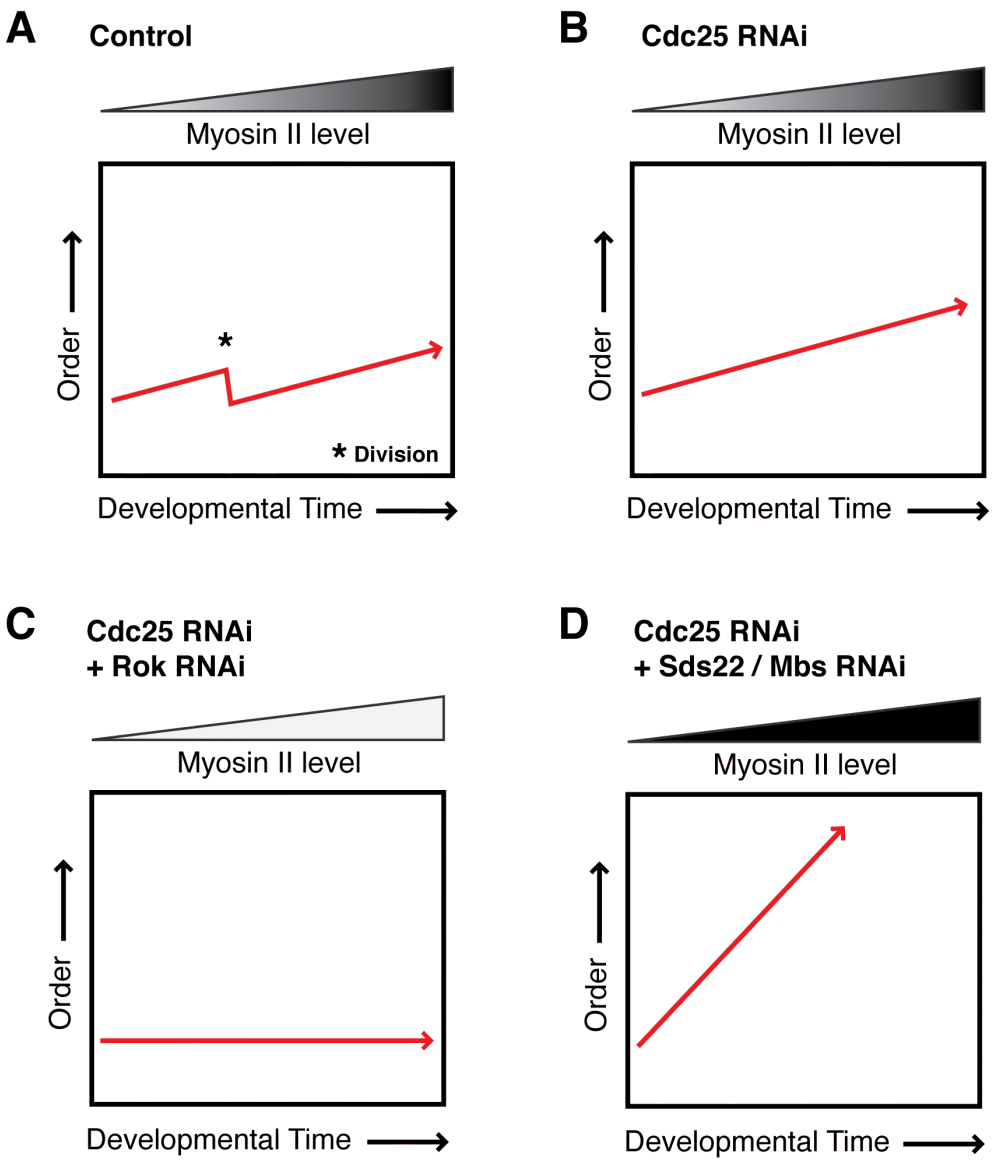


**Figure 8-4: Hypothetical models of tissue packing during notum development**

**(A)** Representation of increasing tissue order through developmental time for control. Developmental increases in Myo II levels push the tissue towards an increasingly ordered state. Disorder is induced through a round of cell division mid-development. **(B)** In the absence of cell division the tissue increases in order as the same rate as control but will reach ordered states faster due to a lack of disorder. **(C)** In the absence of division and with constitutively low Myo II levels the tissue cannot order. **(D)** Early increases in Myo II levels, in the absence of cell division, quickly drive the model towards hexagonal packing.

## 8.6 Where is the force coming from to drive apical movements?

A major question that remains unanswered from this work is that if apical movements are not driven by actomyosin contractility then where are these forces generated? In Chapter 6 I attempted to answer this question by looking to determine where T1s initiate along the apical-basal axis. I found that cells change apical and basal neighbours independently of one another. This is surprising in the context of epithelial morphogenesis where apical contractile forces have been shown to propagate basally and generate 3-dimentional changes in tissue shape. It would be interesting to repeat the same analysis in the absence of apical contractility (e.g., *UAS-Rok*$^{RNAi}$) as apical forces may inhibit the influence of basal movements upon apical dynamics. This again suggests that T1s are not driven by apical actomyosin.

As the tissue develops through time, the apical 2D surface becomes increasingly regular and ordered. The variance between apical and basal areas could become tighter as the tissue potentially becomes more columnar. If this were the case, forces along lateral junctions may drive apical neighbour exchange. A 3D view is therefore required to fully understand the evolution of tissue structure and order Improved light sheet microscopy methods, such as Selective Plain Illumination Microscopy (SPIM), that have recently been used to image stages of embryogenesis (Krzic et al., 2012) could be used to gain a full 3D reconstruction of the notum during pupal development.

## 8.7 Outlook and future perspectives

In this thesis I have attempted to uncover the general mechanisms that are used to drive neighbour exchange under conditions of homeostatic growth. One of the major findings is that, unlike in rapid morphogenetic processes, actomyosin contractility is not required. Moreover endocytosis plays a minor role. Rather, noisy and seemingly stochastic junction fluctuations allow cellular movement to alleviate force imbalances. The dissipation of local tensions and stress may help the system to reach mechanical equilibriums. In contrast to morphogenetic processes such as GBE, where Myo II is polarised, increased isotropic actomyosin contractility in the notum

inhibits movement within the tissue, though a slow increase through developmental time anneals the system towards a regularly packed structure. This work may help to explain the mechanisms by which stresses are relieved in conditions of overgrowth and to understand how epithelia relieve stresses.

# 9. Appendix

**A** 12 h AP

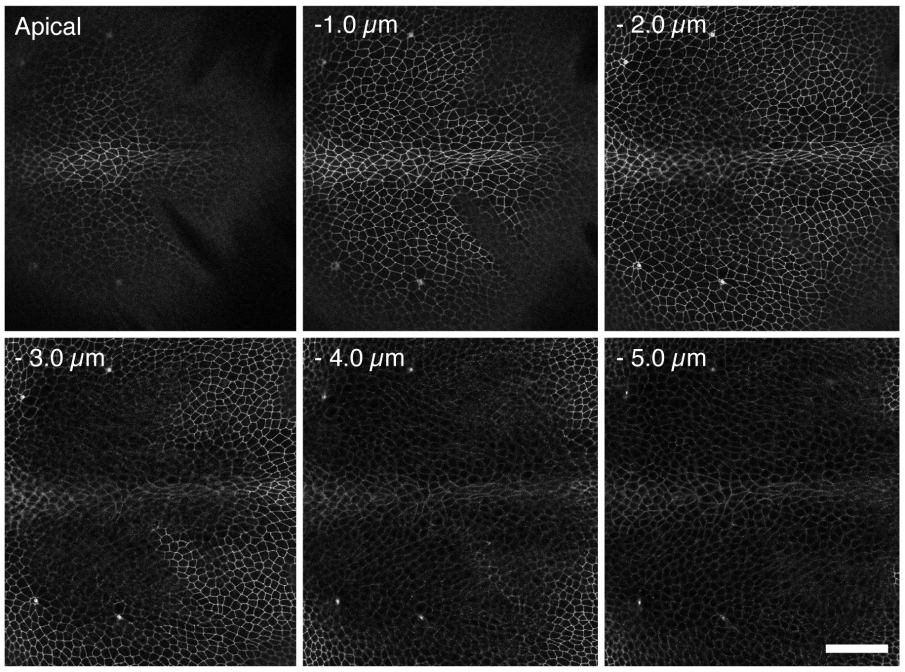


**B** 16 h AP

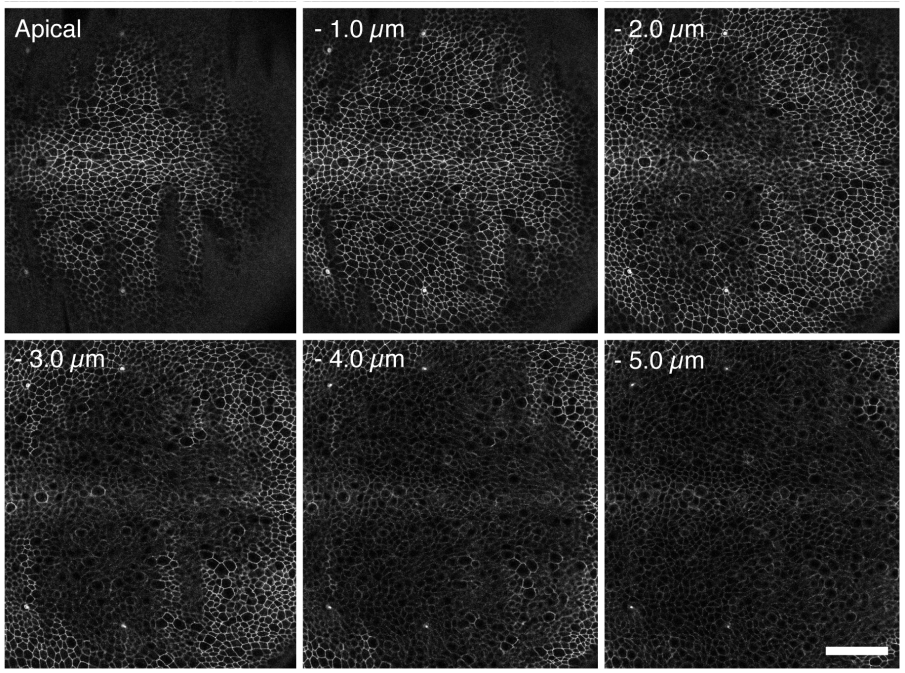

**C** 20 h AP

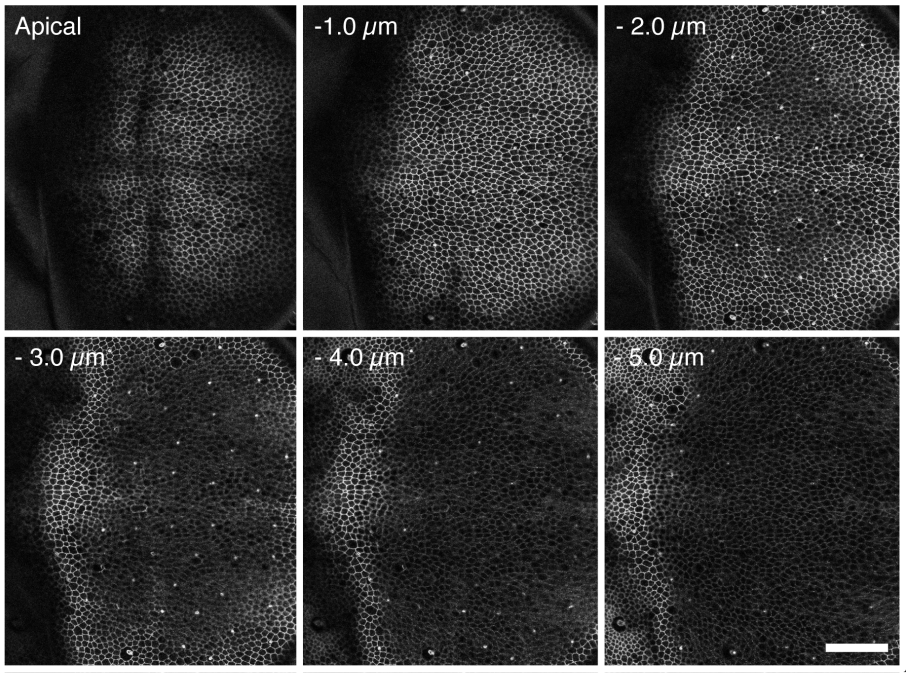


**D** 25 h AP

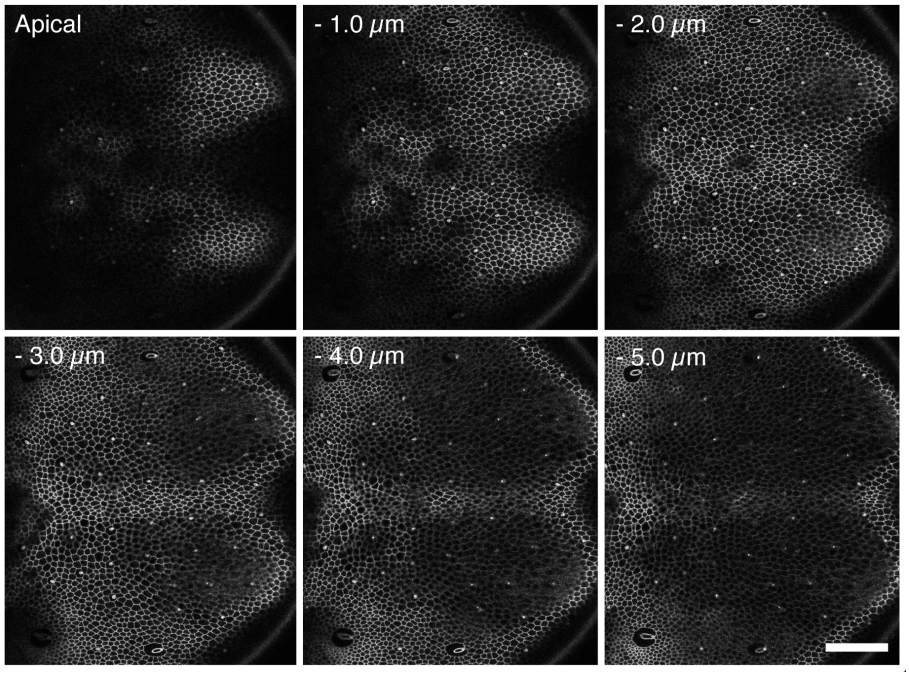

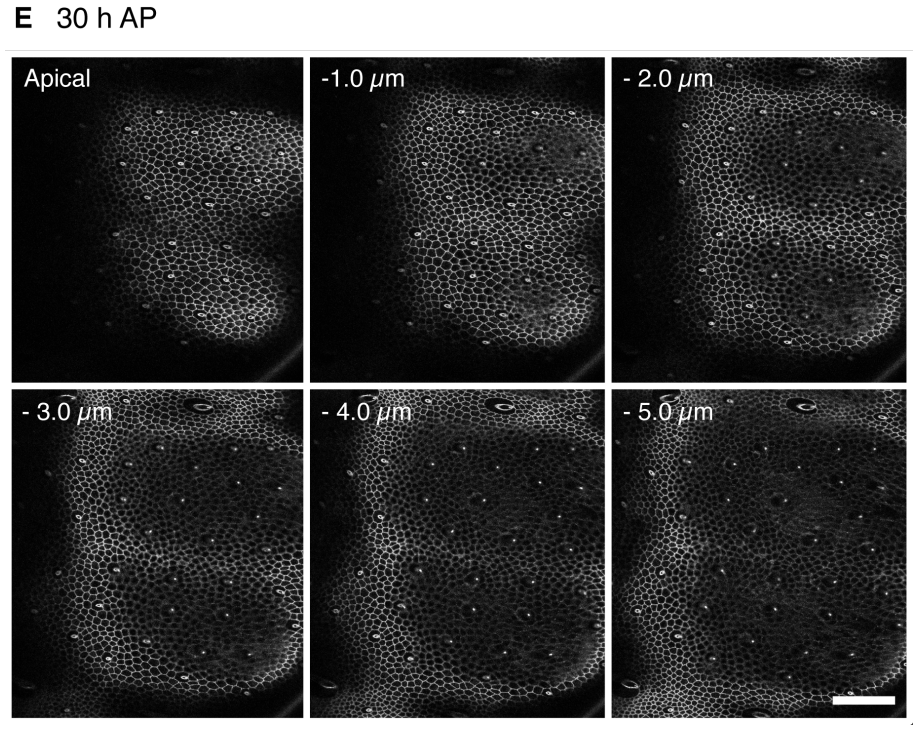


**Figure 9-1: Notum z-projections**

Supplement to **Fig. 1.3**. DE-cadherin-GFP labelled images of the notum at 12 (**A**), 16 (**B**), 20 (**C**), 25 (**D**) and 30 h AP (**E**. Z-slice montages at 1µm intervals. Posterior (left) to anterior (right), with the midline in the centre of each image. Scale bar = 50µm.

*DE-cad-GFP(KI)*

(Leica SPE2, Larval development at 25$^{o}$C)

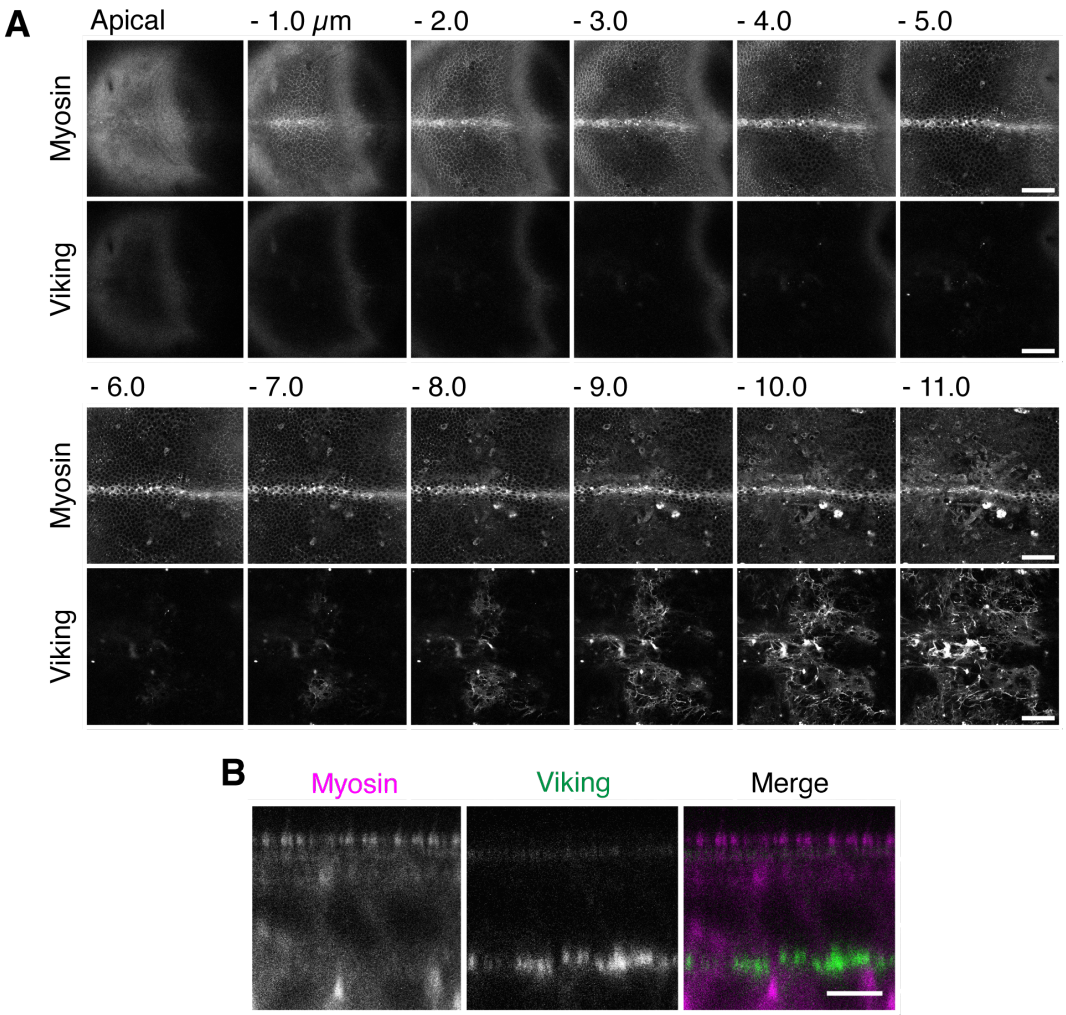


**Figure 9-2: The *Drosophila* notum sits on top of a basement membrane.**

(**A**) MRLC-Cherry (*spg-sqh*) used to label cells apical to basal. Viking-GFP (homolog of Collagen IV) labels basement membrane. 1µm z-slices. Scale bar = 50µm. (**B**) Higher magnification XZ image of epithelium and basement membrane. Scale bar = 5µm.

*viking*$^{G454}$ / + ; *sqh-mCherry* / +

(Leica SPE2, Larval development at 25$^{o}$C)

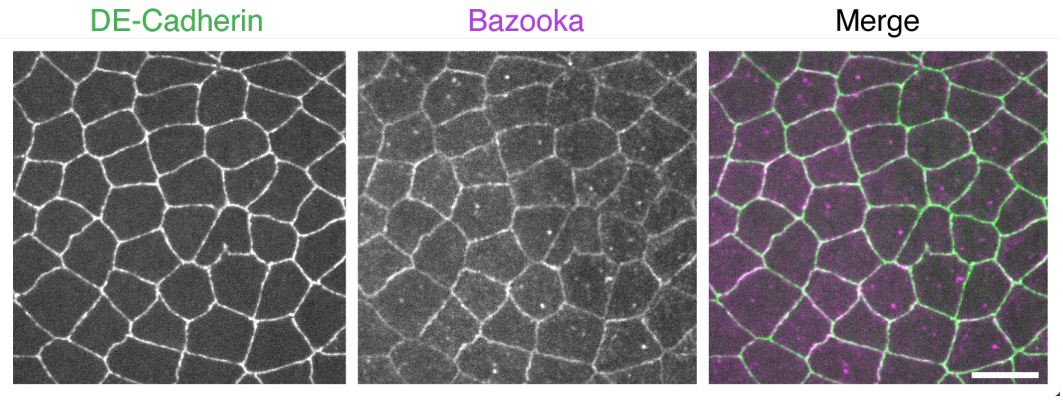


**Figure 9-3: Bazooka localises apically, at the level of the adherens junction, with DE-cadherin**

Supplement to **Fig. 4.1**. Max projection of 2 x 0.5µm slices of a notum imaged with DE-cad-GFP and Baz-mCh. Merge shows co-localisation at the adherens junction. Scale bar = 10µm.

*DE-cad-GFP(KI) / If or Cyo ; ubi-bazooka-mCh / +*

(Leica SPE2, Larval development at 25°C)

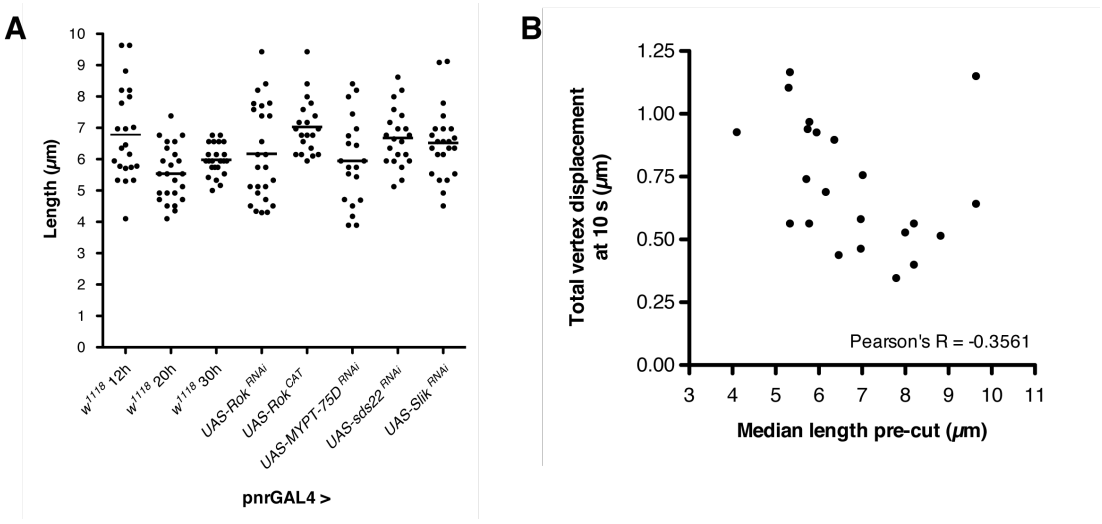


**Figure 9-4: Pre-ablation junction lengths and vertex displacement v length**

Supplement to **Fig. 4.7**, **5.3** and **7.2**. (**A**) Plot of individual junction lengths pre-ablation. Line indicates median. (**B**) Scatter plot of pre-ablation junction length versus total vertex displacement at 10 s after ablation for control ($w^{1118}$). Pearsons R was used to determine level of correlation.

| **Plateau unpaired t-test** | $w^{1118}$ | *UAS- Rok*$^{RNAi}$ | *UAS-Rok*$^{CAT}$ | *UAS-sds22*$^{RNAi}$ |
|---|---|---|---|---|
| Plateau | 0.4465 | 0.4365 | 0.3551 | 0.372 |
| Plateau SD | 0.04508 | 0.01233 | 0.01602 | 0.02279 |
| Variance ($SD^2$) | 0.002032206 | 0.000152029 | 0.00025664 | 0.000519384 |
| n | 30 | 35 | 33 | 32 |
| V / n | 6.77402E-05 | 4.34368E-06 | 7.77698E-06 | 1.62308E-05 |
| Variance difference from $w^{1118}$ mean | N/A | 7.20839E-05 | 7.55172E-05 | 8.3971E-05 |
| SqRt VD | N/A | 0.008490224 | 0.008690063 | 0.009163567 |
| Difference between means (+ve) | N/A | 0.01 | 0.0914 | 0.0745 |
| t test | N/A | 1.177825286 | 10.51776033 | 8.130021552 |
| Degrees of freedom (n1 + n2 - 2) | N/A | 63 | 61 | 60 |
| p value (two tailed) | N/A | 0.2433 | 0.0001 | 0.0001 |
| Signficant? | N/A | ns | **** | **** |

| **K-fast unpaired t-test** | $w^{1118}$ | *UAS- Rok*$^{RNAi}$ | *UAS-Rok*$^{CAT}$ | *UAS-sds22*$^{RNAi}$ |
|---|---|---|---|---|
| K-fast | 0.1489 | 0.3075 | 0.3943 | 0.277 |
| K-fast (SD) | 0.05876 | 0.1083 | 0.2245 | 0.1363 |
| Variance ($SD^2$) | 0.003452738 | 0.01172889 | 0.05040025 | 0.01857769 |
| n | 30 | 35 | 33 | 32 |
| V / n | 0.000115091 | 0.000335111 | 0.00152728 | 0.000580553 |
| Variance difference from $w^{1118}$ mean | N/A | 0.000450202 | 0.001642372 | 0.000695644 |
| SqRt VD | N/A | 0.021217973 | 0.040526184 | 0.026375065 |
| Difference between means (+ve) | N/A | 0.1586 | 0.2454 | 0.1281 |
| t test | N/A | 7.474794922 | 6.055344428 | 4.856860026 |
| Degrees of freedom (n1 + n2 - 2) | N/A | 63 | 61 | 60 |
| p value (two tailed) | N/A | 0.0001 | 0.0001 | 0.0001 |
| Signficant? | N/A | **** | **** | **** |

| **K-slow unpaired t-test** | $w^{1118}$ | *UAS- Rok*$^{RNAi}$ | *UAS-Rok*$^{CAT}$ | *UAS-sds22*$^{RNAi}$ |
|---|---|---|---|---|
| K-slow | 0.007247 | 0.0122 | 0.01185 | 0.00979 |
| K-slow (SD) | 0.001813 | 0.001223 | 0.001828 | 0.001783 |
| Variance ($SD^2$) | 3.28697E-06 | 1.49573E-06 | 3.34158E-06 | 3.17909E-06 |
| n | 30 | 35 | 33 | 32 |
| V / n | 1.09566E-07 | 4.27351E-08 | 1.0126E-07 | 9.93465E-08 |
| Variance difference from $w^{1118}$ mean | N/A | 1.52301E-07 | 2.10826E-07 | 2.08912E-07 |
| SqRt VD | N/A | 0.000390257 | 0.000459158 | 0.000457069 |
| Difference between means (+ve) | N/A | 0.004953 | 0.004603 | 0.002543 |
| t test | N/A | 12.6916273 | 10.02487909 | 5.563710138 |
| Degrees of freedom (n1 + n2 - 2) | N/A | 63 | 61 | 60 |
| p value (two tailed) | N/A | 0.0001 | 0.0001 | 0.0001 |
| Signficant? | N/A | **** | **** | **** |

**Table 9-1: Statistical analyses of FRAP data**

Supplement to **Fig. 4.14**. Data from two-phase association curves of control ($w^{1118}$), *UAS-Rok*$^{RNAi}$, *UAS-Rok*$^{CAT}$ and *UAS-sds22*$^{RNAi}$. p-values represent unpaired t-tests versus control.

| **pnrGAL4 >** | ***w*$^{1118}$** | ***UAS-Rok*$^{RNAi}$** |
|---|---|---|
| **Best-fit values** | | |
| Slope | -0.05463 ± 0.003173 | -0.07338 ± 0.004814 |
| Y-intercept when X=0.0 | 0.3947 ± 0.02802 | 0.1769 ± 0.04305 |
| X-intercept when Y=0.0 | 7.225 | 2.411 |
| 1/slope | -18.31 | -13.63 |
| 95% Confidence Intervals | | |
| Slope | -0.06085 to -0.04841 | -0.08281 to -0.06394 |
| Y-intercept when X=0.0 | 0.3398 to 0.4496 | 0.09255 to 0.2613 |
| X-intercept when Y=0.0 | 5.626 to 9.219 | 1.131 to 4.039 |
| **Goodness of Fit** | | |
| R square | 0.2417 | 0.189 |
| Sy.x | 0.4025 | 0.6331 |
| **Is slope significantly non-zero?** | | |
| F | 296.5 | 232.3 |
| DFn, DFd | 1.000, 930.0 | 1.000, 997.0 |
| P value | < 0.0001 | < 0.0001 |
| Deviation from zero? | Significant | Significant |
| **Are the slopes equal?**<br>F = 10.2613. DFn=1 DFd=1927<br>P=0.001381 | | |

**Table 9-2: Comparison of T1 contractions for control and Rok knockdown transitions**

Supplement to **Fig. 3.6** and **4.12**.

| **pnrGAL4 >** | ***w*$^{1118}$** | ***UAS-Rok*$^{RNAi}$** |
|---|---|---|
| **Best-fit values** | | |
| Slope | 0.05714 ± 0.002711 | 0.06086 ± 0.003373 |
| Y-intercept when X=0.0 | 0.3981 ± 0.02412 | 0.2583 ± 0.03011 |
| X-intercept when Y=0.0 | -6.967 | -4.245 |
| 1/slope | 17.5 | 16.43 |
| **95% Confidence Intervals** | | |
| Slope | 0.05183 to 0.06245 | 0.05425 to 0.06747 |
| Y-intercept when X=0.0 | 0.3508 to 0.4454 | 0.1993 to 0.3174 |
| X-intercept when Y=0.0 | -8.541 to -5.652 | -5.800 to -2.980 |
| Goodness of Fit | | |
| R square | 0.3186 | 0.2486 |
| Sy.x | 0.3479 | 0.4417 |
| **Is slope significantly non-zero?** | | |
| F | 444.2 | 325.5 |
| DFn, DFd | 1.000, 950.0 | 1.000, 984.0 |
| P value | < 0.0001 | < 0.0001 |
| Deviation from zero? | Significant | Significant |
| **Are the slopes equal?**<br>F = 0.731489. DFn=1 DFd=1934<br>P=0.3925 | | |

**Table 9-3: Comparison of T1 expansions for control and Rok knockdown transitions**

Supplement to **Fig. 3.6** and **4.12**.

| pnrGAL4 > | $w^{1118}$ | *UAS-Rok*$^{RNAi}$ |
|---|---|---|
| **Best-fit values** | | |
| Slope | 0.05810 ± 0.007632 | 0.07345 ± 0.01011 |
| Y-intercept when X=0.0 | -0.4067 ± 0.06740 | -0.05464 ± 0.09043 |
| X-intercept when Y=0.0 | 6.999 | 0.7439 |
| 1/slope | 17.21 | 13.61 |
| **95% Confidence Intervals** | | |
| Slope | 0.04315 to 0.07306 | 0.05363 to 0.09327 |
| Y-intercept when X=0.0 | -0.5388 to -0.2746 | -0.2319 to 0.1226 |
| X-intercept when Y=0.0 | 3.823 to 12.27 | -1.353 to 4.201 |
| **Goodness of Fit** | | |
| R square | 0.05867 | 0.05026 |
| Sy.x | 0.9681 | 1.33 |
| **Is slope significantly non-zero?** | | |
| F | 57.97 | 52.76 |
| DFn, DFd | 1.000, 930.0 | 1.000, 997.0 |
| P value | < 0.0001 | < 0.0001 |
| Deviation from zero? | Significant | Significant |
| **Are the slopes equal?**<br>F = 1.43578. DFn=1 DFd=1927<br>P=0.231 | | |

**Table 9-4: Comparison of four first neighbours during T1 contractions for control and Rok knockdown transitions**

Supplement to **Fig. 3.6** and **4.12**.

| pnrGAL4 > | $w^{1118}$ | *UAS-Rok*$^{RNAi}$ |
|---|---|---|
| **Best-fit values** | | |
| Slope | -0.07215 ± 0.005923 | -0.07355 ± 0.006766 |
| Y-intercept when X=0.0 | -0.4370 ± 0.05270 | -0.03300 ± 0.06040 |
| X-intercept when Y=0.0 | -6.057 | -0.4486 |
| 1/slope | -13.86 | -13.6 |
| **95% Confidence Intervals** | | |
| Slope | -0.08376 to -0.06054 | -0.08681 to -0.06029 |
| Y-intercept when X=0.0 | -0.5403 to -0.3337 | -0.1514 to 0.08538 |
| X-intercept when Y=0.0 | -8.825 to -4.030 | -2.461 to 1.003 |
| **Goodness of Fit** | | |
| R square | 0.1351 | 0.1072 |
| Sy.x | 0.7601 | 0.8859 |
| **Is slope significantly non-zero?** | | |
| F | 148.4 | 118.2 |
| DFn, DFd | 1.000, 950.0 | 1.000, 984.0 |
| P value | < 0.0001 | < 0.0001 |
| Deviation from zero? | Significant | Significant |
| **Are the slopes equal?**<br>F = 0.0241247. DFn=1 DFd=1934<br>P=0.8766 | | |

**Table 9-5: Comparison of four first neighbours during T1 expansion for control and Rok knockdown transitions**

Supplement to **Fig. 3.6** and **4.12**.

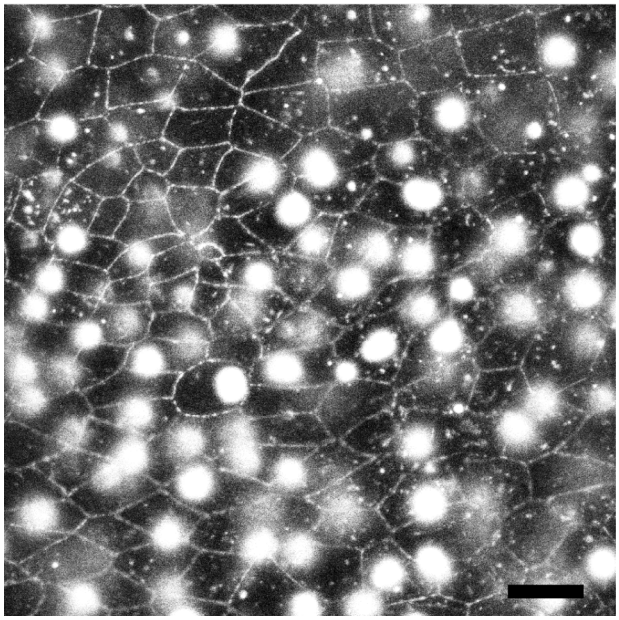

**Figure 9-5: Eos-cadherin notum expression**

Supplement to **Fig. 6.1**. An image of E-cadherin-EOS expression in the notum before activation. Scale bar = 10 µm.

*UAS- E-cad::EosFP / If ; pnrGAL4 / +*

(Leica SP2, Larval development at 25$^{o}$C)

# Bibliography


Abe, K., and Takeichi, M. (2008). EPLIN mediates linkage of the cadherin catenin complex to F-actin and stabilizes the circumferential actin belt. Proceedings of the National Academy of Sciences of the United States of America *105*, 13-19.

Aberle, H., Schwartz, H., and Kemler, R. (1996). Cadherin-catenin complex: protein interactions and their implications for cadherin function. Journal of cellular biochemistry *61*, 514-523.

Aigouy, B., Farhadifar, R., Staple, D.B., Sagner, A., Roper, J.C., Julicher, F., and Eaton, S. (2010). Cell flow reorients the axis of planar polarity in the wing epithelium of Drosophila. Cell *142*, 773-786.

Alessi, D., MacDougall, L.K., Sola, M.M., Ikebe, M., and Cohen, P. (1992). The control of protein phosphatase-1 by targetting subunits. The major myosin phosphatase in avian smooth muscle is a novel form of protein phosphatase-1. European journal of biochemistry / FEBS *210*, 1023-1035.

Andrianantoandro, E., and Pollard, T.D. (2006). Mechanism of actin filament turnover by severing and nucleation at different concentrations of ADF/cofilin. Molecular cell *24*, 13-23.

Arber, S., Barbayannis, F.A., Hanser, H., Schneider, C., Stanyon, C.A., Bernard, O., and Caroni, P. (1998). Regulation of actin dynamics through phosphorylation of cofilin by LIM-kinase. Nature *393*, 805-809.

Ashburner, M. (1989). Drosophila: A laboratory model (Cold Spring Harbor Laboratory Press, Cold Spring Harbor, NY).

Aspenstrom, P., Lindberg, U., and Hall, A. (1996). Two GTPases, Cdc42 and Rac, bind directly to a protein implicated in the immunodeficiency disorder Wiskott-Aldrich syndrome. Current biology : CB *6*, 70-75.

Bardet, P.L., Guirao, B., Paoletti, C., Serman, F., Leopold, V., Bosveld, F., Goya, Y., Mirouse, V., Graner, F., and Bellaiche, Y. (2013). PTEN controls junction lengthening and stability during cell rearrangement in epithelial tissue. Dev Cell *25*, 534-546.

Baum, B., and Georgiou, M. (2011). Dynamics of adherens junctions in epithelial establishment, maintenance, and remodeling. The Journal of cell biology *192*, 907-917.

Baum, B., Li, W., and Perrimon, N. (2000). A cyclase-associated protein regulates actin and cell polarity during Drosophila oogenesis and in yeast. Current biology : CB *10*, 964-973.

Baumgartner, S., Littleton, J.T., Broadie, K., Bhat, M.A., Harbecke, R., Lengyel, J.A., ChiquetEhrismann, R., Prokop, A., and Bellen, H.J. (1996). A Drosophila neurexin is required for septate junction and blood-nerve barrier formation and function. Cell *87*, 1059-1068.

Bellaiche, Y., and Schweisguth, F. (2001). Lineage diversity in the Drosophila nervous system. Current opinion in genetics & development *11*, 418-423.

Beloussov, L.V., Louchinskaia, N.N., and Stein, A.A. (2000). Tension-dependent collective cell movements in the early gastrula ectoderm of Xenopus laevis embryos. Development genes and evolution *210*, 92-104.

Ben-Aissa, K., Patino-Lopez, G., Belkina, N.V., Maniti, O., Rosales, T., Hao, J.J., Kruhlak, M.J., Knutson, J.R., Picart, C., and Shaw, S. (2012). Activation of moesin, a protein that links actin cytoskeleton to the plasma membrane, occurs by phosphatidylinositol 4,5-bisphosphate (PIP2)

binding sequentially to two sites and releasing an autoinhibitory linker. The Journal of biological chemistry *287*, 16311-16323.

Berryman, M., Franck, Z., and Bretscher, A. (1993). Ezrin is concentrated in the apical microvilli of a wide variety of epithelial cells whereas moesin is found primarily in endothelial cells. Journal of cell science *105 ( Pt 4)*, 1025-1043.

Bertet, C., Rauzi, M., and Lecuit, T. (2009). Repression of Wasp by JAK/STAT signalling inhibits medial actomyosin network assembly and apical cell constriction in intercalating epithelial cells. Development *136*, 4199-4212.

Bertet, C., Sulak, L., and Lecuit, T. (2004). Myosin-dependent junction remodelling controls planar cell intercalation and axis elongation. Nature *429*, 667-671.

Bilder, D., Li, M., and Perrimon, N. (2000). Cooperative regulation of cell polarity and growth by Drosophila tumor suppressors. Science *289*, 113-116.

Blanchoin, L., Amann, K.J., Higgs, H.N., Marchand, J.B., Kaiser, D.A., and Pollard, T.D. (2000). Direct observation of dendritic actin filament networks nucleated by Arp2/3 complex and WASP/Scar proteins. Nature *404*, 1007-1011.

Blankenship, J.T., Backovic, S.T., Sanny, J.S., Weitz, O., and Zallen, J.A. (2006). Multicellular rosette formation links planar cell polarity to tissue morphogenesis. Dev Cell *11*, 459-470.

Bosveld, F., Bonnet, I., Guirao, B., Tlili, S., Wang, Z., Petitalot, A., Marchand, R., Bardet, P.L., Marcq, P., Graner, F.*, et al.* (2012). Mechanical control of morphogenesis by Fat/Dachsous/Four-jointed planar cell polarity pathway. Science *336*, 724-727.

Brand, A.H., and Perrimon, N. (1993). Targeted gene expression as a means of altering cell fates and generating dominant phenotypes. Development *118*, 401-415.

Brasch, J., Harrison, O.J., Honig, B., and Shapiro, L. (2012). Thinking outside the cell: how cadherins drive adhesion. Trends in cell biology *22*, 299-310.

Bretscher, A., Edwards, K., and Fehon, R.G. (2002). ERM proteins and merlin: integrators at the cell cortex. Nat Rev Mol Cell Biol *3*, 586-599.

Brittle, A.L., Repiso, A., Casal, J., Lawrence, P.A., and Strutt, D. (2010). Four-jointed modulates growth and planar polarity by reducing the affinity of dachsous for fat. Current biology : CB *20*, 803-810.

Britton, J.S., Lockwood, W.K., Li, L., Cohen, S.M., and Edgar, B.A. (2002). Drosophila's insulin/PI3-kinase pathway coordinates cellular metabolism with nutritional conditions. Dev Cell *2*, 239-249.

Busson, D., and Pret, A.M. (2007). GAL4/UAS targeted gene expression for studying Drosophila Hedgehog signaling. Methods in molecular biology *397*, 161-201.

Butler, L.C., Blanchard, G.B., Kabla, A.J., Lawrence, N.J., Welchman, D.P., Mahadevan, L., Adams, R.J., and Sanson, B. (2009). Cell shape changes indicate a role for extrinsic tensile forces in Drosophila germ-band extension. Nature cell biology *11*, 859-864.

Calleja, M., Herranz, H., Estella, C., Casal, J., Lawrence, P., Simpson, P., and Morata, G. (2000). Generation of medial and lateral dorsal body domains by the pannier gene of Drosophila. Development *127*, 3971-3980.

Campos-Ortega, J.A., and Hartenstein, V. (1985). The Embryonic development of Drosophila melanogaster (Berlin: Springer-Verlag).

Carreno, S., Kouranti, I., Glusman, E.S., Fuller, M.T., Echard, A., and Payre, F. (2008). Moesin and its activating kinase Slik are required for cortical stability and microtubule organization in mitotic cells. The Journal of cell biology *180*, 739-746.

Caussinus, E., Colombelli, J., and Affolter, M. (2008). Tip-cell migration controls stalk-cell intercalation during Drosophila tracheal tube elongation. Current biology : CB *18*, 1727-1734.

Cavey, M., Rauzi, M., Lenne, P.F., and Lecuit, T. (2008). A two-tiered mechanism for stabilization and immobilization of E-cadherin. Nature *453*, 751-756.

Cereijido, M., Contreras, R.G., and Shoshani, L. (2004). Cell adhesion, polarity, and epithelia in the dawn of metazoans. Physiological reviews *84*, 1229-1262.

Chang, H., and Wang, L.A. (2010). A simple proof of Thue's Theorem on Circle Packing. arXiv10094322v1 [mathMG].

Chen, M.S., Obar, R.A., Schroeder, C.C., Austin, T.W., Poodry, C.A., Wadsworth, S.C., and Vallee, R.B. (1991). Multiple forms of dynamin are encoded by shibire, a Drosophila gene involved in endocytosis. Nature *351*, 583-586.

Clark, H.F., Brentrup, D., Schneitz, K., Bieber, A., Goodman, C., and Noll, M. (1995). Dachsous encodes a member of the cadherin superfamily that controls imaginal disc morphogenesis in Drosophila. Genes & development *9*, 1530-1542.

Classen, A.K., Anderson, K.I., Marois, E., and Eaton, S. (2005). Hexagonal packing of Drosophila wing epithelial cells by the planar cell polarity pathway. Dev Cell *9*, 805-817.

Cocucci, E., Gaudin, R., and Kirchhausen, T. (2014). Dynamin recruitment and membrane scission at the neck of a clathrin-coated pit. Molecular biology of the cell *25*, 3595-3609.

Cohen, M., Georgiou, M., Stevenson, N.L., Miodownik, M., and Baum, B. (2010). Dynamic filopodia transmit intermittent Delta-Notch signaling to drive pattern refinement during lateral inhibition. Dev Cell *19*, 78-89.

Costa, M., Wilson, E.T., and Wieschaus, E. (1994). A putative cell signal encoded by the folded gastrulation gene coordinates cell shape changes during Drosophila gastrulation. Cell *76*, 1075-1089.

Cox, R.T., Kirkpatrick, C., and Peifer, M. (1996). Armadillo is required for adherens junction assembly, cell polarity, and morphogenesis during Drosophila embryogenesis. The Journal of cell biology *134*, 133-148.

Craig, R., Smith, R., and Kendrick-Jones, J. (1983). Light-chain phosphorylation controls the conformation of vertebrate non-muscle and smooth muscle myosin molecules. Nature *302*, 436-439.

da Silva, S.M., and Vincent, J.P. (2007). Oriented cell divisions in the extending germband of Drosophila. Development *134*, 3049-3054.

Damke, H., Baba, T., Warnock, D.E., and Schmid, S.L. (1994). Induction of mutant dynamin specifically blocks endocytic coated vesicle formation. The Journal of cell biology *127*, 915-934.

Dang, I., Gorelik, R., Sousa-Blin, C., Derivery, E., Guerin, C., Linkner, J., Nemethova, M., Dumortier, J.G., Giger, F.A., Chipysheva, T.A*., et al.* (2013). Inhibitory signalling to the Arp2/3 complex steers cell migration. Nature *503*, 281-284.

Dawes-Hoang, R.E., Parmar, K.M., Christiansen, A.E., Phelps, C.B., Brand, A.H., and Wieschaus, E.F. (2005). folded gastrulation, cell shape change and the control of myosin localization. Development *132*, 4165-4178.

Dayel, M.J., Holleran, E.A., and Mullins, R.D. (2001). Arp2/3 complex requires hydrolyzable ATP for nucleation of new actin filaments. Proceedings of the National Academy of Sciences of the United States of America *98*, 14871-14876.

Dayel, M.J., and Mullins, R.D. (2004). Activation of Arp2/3 complex: addition of the first subunit of the new filament by a WASP protein triggers rapid ATP hydrolysis on Arp2. PLoS biology *2*, E91.

Desai, R., Sarpal, R., Ishiyama, N., Pellikka, M., Ikura, M., and Tepass, U. (2013). Monomeric alpha-catenin links cadherin to the actin cytoskeleton. Nature cell biology *15*, 261-273.

Dietzl, G., Chen, D., Schnorrer, F., Su, K.C., Barinova, Y., Fellner, M., Gasser, B., Kinsey, K., Oppel, S., Scheiblauer, S*., et al.* (2007). A genome-wide transgenic RNAi library for conditional gene inactivation in Drosophila. Nature *448*, 151-156.

Dorsten, J.N., Kolodziej, P.A., and VanBerkum, M.F. (2007). Frazzled regulation of myosin II activity in the Drosophila embryonic CNS. Developmental biology *308*, 120-132.

Eisenhoffer, G.T., Loftus, P.D., Yoshigi, M., Otsuna, H., Chien, C.B., Morcos, P.A., and Rosenblatt, J. (2012). Crowding induces live cell extrusion to maintain homeostatic cell numbers in epithelia. Nature *484*, 546-549.

Eisenhoffer, G.T., and Rosenblatt, J. (2013). Bringing balance by force: live cell extrusion controls epithelial cell numbers. Trends in cell biology *23*, 185-192.

Etienne-Manneville, S., and Hall, A. (2002). Rho GTPases in cell biology. Nature *420*, 629-635.

Farhadifar, R., Roper, J.C., Aigouy, B., Eaton, S., and Julicher, F. (2007). The influence of cell mechanics, cell-cell interactions, and proliferation on epithelial packing. Current biology : CB *17*, 2095-2104.

Fernandez-Gonzalez, R., Simoes Sde, M., Roper, J.C., Eaton, S., and Zallen, J.A. (2009). Myosin II dynamics are regulated by tension in intercalating cells. Dev Cell *17*, 736-743.

Fichelson, P., and Gho, M. (2003). The glial cell undergoes apoptosis in the microchaete lineage of Drosophila. Development *130*, 123-133.

Fire, A., Xu, S., Montgomery, M.K., Kostas, S.A., Driver, S.E., and Mello, C.C. (1998). Potent and specific genetic interference by double-stranded RNA in Caenorhabditis elegans. Nature *391*, 806-811.

Founounou, N., Loyer, N., and Le Borgne, R. (2013). Septins regulate the contractility of the actomyosin ring to enable adherens junction remodeling during cytokinesis of epithelial cells. Dev Cell *24*, 242-255.

Frank, M., and Kemler, R. (2002). Protocadherins. Current opinion in cell biology *14*, 557-562.

Franke, J.D., Montague, R.A., and Kiehart, D.P. (2005). Nonmuscle myosin II generates forces that transmit tension and drive contraction in multiple tissues during dorsal closure. Current biology : CB *15*, 2208-2221.

Fristrom, D. (1988). The cellular basis of epithelial morphogenesis. A review. Tissue & cell *20*, 645-690.

Fristrom, D., and Liebrich, W. (1986). The hormonal coordination of cuticulin deposition and morphogenesis in Drosophila imaginal discs in vivo and in vitro. Developmental biology *114*, 1-11.

Fristrom, D.K., and Fristrom, J.W. (1993). The metamorhpic development of the adult epidermis. In The Development of Drosophila melanogaster, C. Bate, and A. Martinez Arias, eds. (Cold Spring Harbor Laboratory Press, Cold Sping Harbor, NY.), pp. 843-897.

Fukami, K., Furuhashi, K., Inagaki, M., Endo, T., Hatano, S., and Takenawa, T. (1992). Requirement of phosphatidylinositol 4,5-bisphosphate for alpha-actinin function. Nature *359*, 150-152.

Gary, R., and Bretscher, A. (1995). Ezrin self-association involves binding of an N-terminal domain to a normally masked C-terminal domain that includes the F-actin binding site. Molecular biology of the cell *6*, 1061-1075.

Geim, A.K., and Novoselov, K.S. (2007). The rise of graphene. Nature materials *6*, 183-191.

Georgiou, M., and Baum, B. (2010). Polarity proteins and Rho GTPases cooperate to spatially organise epithelial actin-based protrusions. Journal of cell science *123*, 1089-1098.

Georgiou, M., Marinari, E., Burden, J., and Baum, B. (2008). Cdc42, Par6, and aPKC regulate Arp2/3-mediated endocytosis to control local adherens junction stability. Current biology : CB *18*, 1631-1638.

Gerlitz, O., Nellen, D., Ottiger, M., and Basler, K. (2002). A screen for genes expressed in Drosophila imaginal discs. The International journal of developmental biology *46*, 173-176.

Gho, M., Bellaiche, Y., and Schweisguth, F. (1999). Revisiting the Drosophila microchaete lineage: a novel intrinsically asymmetric cell division generates a glial cell. Development *126*, 3573-3584.

Gho, M., and Schweisguth, F. (1998). Frizzled signalling controls orientation of asymmetric sense organ precursor cell divisions in Drosophila. Nature *393*, 178-181.

Gibson, M.C., Patel, A.B., Nagpal, R., and Perrimon, N. (2006). The emergence of geometric order in proliferating metazoan epithelia. Nature *442*, 1038-1041.

Gibson, M.C., and Perrimon, N. (2003). Apicobasal polarization: epithelial form and function. Current opinion in cell biology *15*, 747-752.

Gibson, W.T., Veldhuis, J.H., Rubinstein, B., Cartwright, H.N., Perrimon, N., Brodland, G.W., Nagpal, R., and Gibson, M.C. (2011). Control of the mitotic cleavage plane by local epithelial topology. Cell *144*, 427-438.

Goldschmidt-Clermont, P.J., Machesky, L.M., Baldassare, J.J., and Pollard, T.D. (1990). The actin-binding protein profilin binds to PIP2 and inhibits its hydrolysis by phospholipase C. Science *247*, 1575-1578.

Gomez, G.A., McLachlan, R.W., and Yap, A.S. (2011). Productive tension: force-sensing and homeostasis of cell-cell junctions. Trends in cell biology *21*, 499-505.

Goode, B.L., and Eck, M.J. (2007). Mechanism and function of formins in the control of actin assembly. Annual review of biochemistry *76*, 593-627.

Grusche, F.A., Hidalgo, C., Fletcher, G., Sung, H.H., Sahai, E., and Thompson, B.J. (2009). Sds22, a PP1 phosphatase regulatory subunit, regulates epithelial cell polarity and shape [Sds22 in epithelial morphology]. BMC developmental biology *9*, 14.

Guillot, C., and Lecuit, T. (2013a). Adhesion disengagement uncouples intrinsic and extrinsic forces to drive cytokinesis in epithelial tissues. Dev Cell *24*, 227-241.

Guillot, C., and Lecuit, T. (2013b). Mechanics of epithelial tissue homeostasis and morphogenesis. Science *340*, 1185-1189.

Guo, M., Jan, L.Y., and Jan, Y.N. (1996). Control of daughter cell fates during asymmetric division: interaction of Numb and Notch. Neuron *17*, 27-41.

Hacker, U., and Perrimon, N. (1998). DRhoGEF2 encodes a member of the Dbl family of oncogenes and controls cell shape changes during gastrulation in Drosophila. Genes & development *12*, 274-284.

Hall, A. (1998). Rho GTPases and the actin cytoskeleton. Science *279*, 509-514.

Hao, J.J., Liu, Y., Kruhlak, M., Debell, K.E., Rellahan, B.L., and Shaw, S. (2009). Phospholipase C-mediated hydrolysis of PIP2 releases ERM proteins from lymphocyte membrane. The Journal of cell biology *184*, 451-462.

Harris, T.J. (2012). Adherens junction assembly and function in the Drosophila embryo. International review of cell and molecular biology *293*, 45-83.

Hartenstein, V., and Campos-Ortega, J.A. (1985). Fate-mapping in wild-type Drosophila melanogaster. 1.The spatio-temporal pattern of embryonic cell divisions. Roux's Archives of Developmental Biology *194*, 181-195.

Hartenstein, V., and Posakony, J.W. (1989). Development of adult sensilla on the wing and notum of Drosophila melanogaster. Development *107*, 389-405.

Hartenstein, V., and Posakony, J.W. (1990). A dual function of the Notch gene in Drosophila sensillum development. Developmental biology *142*, 13-30.

Hartshorne, D.J. (1998). Myosin phosphatase: subunits and interactions. Acta physiologica Scandinavica *164*, 483-493.

Heisenberg, C.P., and Bellaiche, Y. (2013). Forces in tissue morphogenesis and patterning. Cell *153*, 948-962.

Heitzler, P., and Simpson, P. (1991). The choice of cell fate in the epidermis of Drosophila. Cell *64*, 1083-1092.

Herszterg, S., Leibfried, A., Bosveld, F., Martin, C., and Bellaiche, Y. (2013). Interplay between the dividing cell and its neighbors regulates adherens junction formation during cytokinesis in epithelial tissue. Dev Cell *24*, 256-270.

Higgs, H.N. (2005). Formin proteins: a domain-based approach. Trends in biochemical sciences *30*, 342-353.

Hipfner, D.R., Keller, N., and Cohen, S.M. (2004). Slik Sterile-20 kinase regulates Moesin activity to promote epithelial integrity during tissue growth. Genes & development *18*, 2243-2248.

Homem, C.C., and Peifer, M. (2008). Diaphanous regulates myosin and adherens junctions to control cell contractility and protrusive behavior during morphogenesis. Development *135*, 1005-1018.

Huang, J., Zhou, W., Dong, W., Watson, A.M., and Hong, Y. (2009). From the Cover: Directed, efficient, and versatile modifications of the Drosophila genome by genomic engineering. Proceedings of the National Academy of Sciences of the United States of America *106*, 8284-8289.

Huang, T.Y., DerMardirossian, C., and Bokoch, G.M. (2006). Cofilin phosphatases and regulation of actin dynamics. Current opinion in cell biology *18*, 26-31.

Huber, A.H., and Weis, W.I. (2001). The structure of the beta-catenin/E-cadherin complex and the molecular basis of diverse ligand recognition by beta-catenin. Cell *105*, 391-402.

Hughes, S.C., and Fehon, R.G. (2006). Phosphorylation and activity of the tumor suppressor Merlin and the ERM protein Moesin are coordinately regulated by the Slik kinase. The Journal of cell biology *175*, 305-313.

Hutson, M.S., Tokutake, Y., Chang, M.S., Bloor, J.W., Venakides, S., Kiehart, D.P., and Edwards, G.S. (2003). Forces for morphogenesis investigated with laser microsurgery and quantitative modeling. Science *300*, 145-149.

Irvine, K.D., and Wieschaus, E. (1994). Cell intercalation during Drosophila germband extension and its regulation by pair-rule segmentation genes. Development *120*, 827-841.

Jacinto, A., Wood, W., Balayo, T., Turmaine, M., Martinez-Arias, A., and Martin, P. (2000). Dynamic actin-based epithelial adhesion and cell matching during Drosophila dorsal closure. Current biology : CB *10*, 1420-1426.

Jacinto, A., Wood, W., Woolner, S., Hiley, C., Turner, L., Wilson, C., Martinez-Arias, A., and Martin, P. (2002). Dynamic analysis of actin cable function during Drosophila dorsal closure. Current biology : CB *12*, 1245-1250.

Jacobson, A.G., Oster, G.F., Odell, G.M., and Cheng, L.Y. (1986). Neurulation and the cortical tractor model for epithelial folding. Journal of embryology and experimental morphology *96*, 19-49.

Janson, L.W., Sellers, J.R., and Taylor, D.L. (1992). Actin-binding proteins regulate the work performed by myosin II motors on single actin filaments. Cell motility and the cytoskeleton *22*, 274-280.

Johnson, H.E., King, S.J., Asokan, S.B., Rotty, J.D., Bear, J.E., and Haugh, J.M. (2015). F-actin bundles direct the initiation and orientation of lamellipodia through adhesion-based signaling. The Journal of cell biology *208*, 443-455.

Jordan, P., and Karess, R. (1997). Myosin light chain-activating phosphorylation sites are required for oogenesis in Drosophila. The Journal of cell biology *139*, 1805-1819.

Jung, H.S., Komatsu, S., Ikebe, M., and Craig, R. (2008). Head-head and head-tail interaction: a general mechanism for switching off myosin II activity in cells. Molecular biology of the cell *19*, 3234-3242.

Kasza, K.E., Farrell, D.L., and Zallen, J.A. (2014). Spatiotemporal control of epithelial remodeling by regulated myosin phosphorylation. Proceedings of the National Academy of Sciences of the United States of America *111*, 11732-11737.

Kiehart, D.P., Galbraith, C.G., Edwards, K.A., Rickoll, W.L., and Montague, R.A. (2000). Multiple forces contribute to cell sheet morphogenesis for dorsal closure in Drosophila. The Journal of cell biology *149*, 471-490.

Kimura, K., Ito, M., Amano, M., Chihara, K., Fukata, Y., Nakafuku, M., Yamamori, B., Feng, J., Nakano, T., Okawa, K.*, et al.* (1996). Regulation of myosin phosphatase by Rho and Rho-associated kinase (Rho-kinase). Science *273*, 245-248.

Knowles-Barley, S., Longair, M., and Armstrong, J.D. (2010). BrainTrap: a database of 3D protein expression patterns in the Drosophila brain. Database : the journal of biological databases and curation *2010*, baq005.

Knust, E., and Bossinger, O. (2002). Composition and formation of intercellular junctions in epithelial cells. Science *298*, 1955-1959.

Kojima, S., Mishima, M., Mabuchi, I., and Hotta, Y. (1996). A single Drosophila melanogaster myosin light chain kinase gene produces multiple isoforms whose activities are differently regulated. Genes to cells : devoted to molecular & cellular mechanisms *1*, 855-871.

Kolsch, V., Seher, T., Fernandez-Ballester, G.J., Serrano, L., and Leptin, M. (2007). Control of Drosophila gastrulation by apical localization of adherens junctions and RhoGEF2. Science *315*, 384-386.

Kovar, D.R. (2006). Molecular details of formin-mediated actin assembly. Current opinion in cell biology *18*, 11-17.

Krzic, U., Gunther, S., Saunders, T.E., Streichan, S.J., and Hufnagel, L. (2012). Multiview light-sheet microscope for rapid in toto imaging. Nature methods *9*, 730-733.

Kunda, P., Pelling, A.E., Liu, T., and Baum, B. (2008). Moesin controls cortical rigidity, cell rounding, and spindle morphogenesis during mitosis. Current biology : CB *18*, 91-101.

Kunda, P., Rodrigues, N.T., Moeendarbary, E., Liu, T., Ivetic, A., Charras, G., and Baum, B. (2012). PP1-mediated moesin dephosphorylation couples polar relaxation to mitotic exit. Current biology : CB *22*, 231-236.

Landsberg, K.P., Farhadifar, R., Ranft, J., Umetsu, D., Widmann, T.J., Bittig, T., Said, A., Julicher, F., and Dahmann, C. (2009). Increased cell bond tension governs cell sorting at the Drosophila anteroposterior compartment boundary. Current biology : CB *19*, 1950-1955.

Lane, N.J., and Swales, L.S. (1982). Stages in the assembly of pleated and smooth septate junctions in developing insect embryos. Journal of cell science *56*, 245-262.

Langevin, J., Morgan, M.J., Sibarita, J.B., Aresta, S., Murthy, M., Schwarz, T., Camonis, J., and Bellaiche, Y. (2005). Drosophila exocyst components Sec5, Sec6, and Sec15 regulate DE-Cadherin trafficking from recycling endosomes to the plasma membrane. Dev Cell *9*, 365-376.

Lassing, I., and Lindberg, U. (1985). Specific interaction between phosphatidylinositol 4,5-bisphosphate and profilactin. Nature *314*, 472-474.

le Duc, Q., Shi, Q., Blonk, I., Sonnenberg, A., Wang, N., Leckband, D., and de Rooij, J. (2010). Vinculin potentiates E-cadherin mechanosensing and is recruited to actin-anchored sites within adherens junctions in a myosin II-dependent manner. The Journal of cell biology *189*, 1107-1115.

Lecuit, T., and Lenne, P.F. (2007). Cell surface mechanics and the control of cell shape, tissue patterns and morphogenesis. Nat Rev Mol Cell Biol *8*, 633-644.

Leevers, S.J., Weinkove, D., MacDougall, L.K., Hafen, E., and Waterfield, M.D. (1996). The Drosophila phosphoinositide 3-kinase Dp110 promotes cell growth. The EMBO journal *15*, 6584-6594.

Levayer, R., Pelissier-Monier, A., and Lecuit, T. (2011). Spatial regulation of Dia and Myosin-II by RhoGEF2 controls initiation of E-cadherin endocytosis during epithelial morphogenesis. Nature cell biology *13*, 529-540.

Lewis, F.T. (1926). The effect of cell division on the shape and size of hexagonal cells. Anatomical Records *33*, 331-335.

Lewis, F.T. (1928). The correlation between cell division and the shapes and size of prismatic cell in the epidermis of cucumis. Anatomical Records *38*, 341-376.

Li, F., and Higgs, H.N. (2003). The mouse Formin mDia1 is a potent actin nucleation factor regulated by autoinhibition. Current biology : CB *13*, 1335-1340.

Li, Z., Dong, X., Wang, Z., Liu, W., Deng, N., Ding, Y., Tang, L., Hla, T., Zeng, R., Li, L., *et al.* (2005). Regulation of PTEN by Rho small GTPases. Nature cell biology *7*, 399-404.

Lickert, H., Bauer, A., Kemler, R., and Stappert, J. (2000). Casein kinase II phosphorylation of E-cadherin increases E-cadherin/beta-catenin interaction and strengthens cell-cell adhesion. The Journal of biological chemistry *275*, 5090-5095.

Lock, J.G., and Stow, J.L. (2005). Rab11 in recycling endosomes regulates the sorting and basolateral transport of E-cadherin. Molecular biology of the cell *16*, 1744-1755.

Lye, C.M., and Sanson, B. (2011). Tension and epithelial morphogenesis in Drosophila early embryos. Current topics in developmental biology *95*, 145-187.

Mahoney, P.A., Weber, U., Onofrechuk, P., Biessmann, H., Bryant, P.J., and Goodman, C.S. (1991). The fat tumor suppressor gene in Drosophila encodes a novel member of the cadherin gene superfamily. Cell *67*, 853-868.

Maiden, S.L., and Hardin, J. (2011). The secret life of alpha-catenin: moonlighting in morphogenesis. The Journal of cell biology *195*, 543-552.

Mandaron, P., and Sengel, P. (1973). Effect of cytochalasin B on the evagination in vitro of leg imaginal discs. Developmental biology *32*, 201-207.

Manning, A.J., Peters, K.A., Peifer, M., and Rogers, S.L. (2013). Regulation of epithelial morphogenesis by the G protein-coupled receptor mist and its ligand fog. Sci Signal *6*, ra98.

Manning, A.J., and Rogers, S.L. (2014). The Fog signaling pathway: insights into signaling in morphogenesis. Developmental biology *394*, 6-14.

Mao, Y., Rauskolb, C., Cho, E., Hu, W.L., Hayter, H., Minihan, G., Katz, F.N., and Irvine, K.D. (2006). Dachs: an unconventional myosin that functions downstream of Fat to regulate growth, affinity and gene expression in Drosophila. Development *133*, 2539-2551.

Mao, Y., Tournier, A.L., Hoppe, A., Kester, L., Thompson, B.J., and Tapon, N. (2013). Differential proliferation rates generate patterns of mechanical tension that orient tissue growth. The EMBO journal *32*, 2790-2803.

Marinari, E., Mehonic, A., Curran, S., Gale, J., Duke, T., and Baum, B. (2012). Live-cell delamination counterbalances epithelial growth to limit tissue overcrowding. Nature *484*, 542-545.

Martin, A.C., Kaschube, M., and Wieschaus, E.F. (2009). Pulsed contractions of an actin-myosin network drive apical constriction. Nature *457*, 495-499.

Martin-Blanco, E., Pastor-Pareja, J.C., and Garcia-Bellido, A. (2000). JNK and decapentaplegic signaling control adhesiveness and cytoskeleton dynamics during thorax closure in Drosophila. Proceedings of the National Academy of Sciences of the United States of America *97*, 7888-7893.

Martinez-Arias, A. (1993). Development and patterning of the larval epidermis. In The development of Drosophila melanogaster, A. Martinez Arias, and M. Bate, eds. (Cold Spring Harbor, NY: Cold Spring Harbor Laboratory Press), pp. 517-607.

Mason, F.M., Tworoger, M., and Martin, A.C. (2013). Apical domain polarization localizes actin-myosin activity to drive ratchet-like apical constriction. Nature cell biology *15*, 926-936.

Matakatsu, H., and Blair, S.S. (2008). The DHHC palmitoyltransferase approximated regulates Fat signaling and Dachs localization and activity. Current biology : CB *18*, 1390-1395.

Matsudaira, P. (1991). Modular organization of actin crosslinking proteins. Trends in biochemical sciences *16*, 87-92.

Matsumoto, K., Toh-e, A., and Oshima, Y. (1978). Genetic control of galactokinase synthesis in Saccharomyces cerevisiae: evidence for constitutive expression of the positive regulatory gene gal4. Journal of bacteriology *134*, 446-457.

Matsumura, F. (2005). Regulation of myosin II during cytokinesis in higher eukaryotes. Trends in cell biology *15*, 371-377.

McGuire, S.E., Le, P.T., Osborn, A.J., Matsumoto, K., and Davis, R.L. (2003). Spatiotemporal rescue of memory dysfunction in Drosophila. Science *302*, 1765-1768.

McGuire, S.E., Mao, Z., and Davis, R.L. (2004). Spatiotemporal gene expression targeting with the TARGET and gene-switch systems in Drosophila. Science's STKE : signal transduction knowledge environment *2004*, pl6.

Means, A.R., Bagchi, I.C., VanBerkum, M.F., and Kemp, B.E. (1991). Regulation of smooth muscle myosin light chain kinase by calmodulin. Advances in experimental medicine and biology *304*, 11-24.

Miki, H., Suetsugu, S., and Takenawa, T. (1998). WAVE, a novel WASP-family protein involved in actin reorganization induced by Rac. The EMBO journal *17*, 6932-6941.

Miranda, K.C., Khromykh, T., Christy, P., Le, T.L., Gottardi, C.J., Yap, A.S., Stow, J.L., and Teasdale, R.D. (2001). A dileucine motif targets E-cadherin to the basolateral cell surface in Madin-Darby canine kidney and LLC-PK1 epithelial cells. The Journal of biological chemistry *276*, 22565-22572.

Morais-de-Sa, E., Mirouse, V., and St Johnston, D. (2010). aPKC phosphorylation of Bazooka defines the apical/lateral border in Drosophila epithelial cells. Cell *141*, 509-523.

Morin, X., Daneman, R., Zavortink, M., and Chia, W. (2001). A protein trap strategy to detect GFP-tagged proteins expressed from their endogenous loci in Drosophila. Proceedings of the National Academy of Sciences of the United States of America *98*, 15050-15055.

Mullins, R.D. (2000). How WASP-family proteins and the Arp2/3 complex convert intracellular signals into cytoskeletal structures. Current opinion in cell biology *12*, 91-96.

Mullins, R.D., Heuser, J.A., and Pollard, T.D. (1998). The interaction of Arp2/3 complex with actin: nucleation, high affinity pointed end capping, and formation of branching networks of filaments. Proceedings of the National Academy of Sciences of the United States of America *95*, 6181-6186.

Munjal, A., and Lecuit, T. (2014). Actomyosin networks and tissue morphogenesis. Development *141*, 1789-1793.

Nakamura, F., Amieva, M.R., and Furthmayr, H. (1995). Phosphorylation of threonine 558 in the carboxyl-terminal actin-binding domain of moesin by thrombin activation of human platelets. The Journal of biological chemistry *270*, 31377-31385.

Neumann, M., and Affolter, M. (2006). Remodelling epithelial tubes through cell rearrangements: from cells to molecules. EMBO reports *7*, 36-40.

Nezami, A.G., Poy, F., and Eck, M.J. (2006). Structure of the autoinhibitory switch in formin mDia1. Structure *14*, 257-263.

Niggli, V., and Rossy, J. (2008). Ezrin/radixin/moesin: versatile controllers of signaling molecules and of the cortical cytoskeleton. The international journal of biochemistry & cell biology *40*, 344-349.

Niwa, R., Nagata-Ohashi, K., Takeichi, M., Mizuno, K., and Uemura, T. (2002). Control of actin reorganization by Slingshot, a family of phosphatases that dephosphorylate ADF/cofilin. Cell *108*, 233-246.

Nobes, C.D., and Hall, A. (1995). Rho, rac, and cdc42 GTPases regulate the assembly of multimolecular focal complexes associated with actin stress fibers, lamellipodia, and filopodia. Cell *81*, 53-62.

Novoselov, K.S., Geim, A.K., Morozov, S.V., Jiang, D., Zhang, Y., Dubonos, S.V., Grigorieva, I.V., and Firsov, A.A. (2004). Electric field effect in atomically thin carbon films. Science *306*, 666-669.

Nusslein-Volhard, C., Frohnhofer, H.G., and Lehmann, R. (1987). Determination of anteroposterior polarity in Drosophila. Science *238*, 1675-1681.

Oda, H., and Tsukita, S. (2001). Real-time imaging of cell-cell adherens junctions reveals that Drosophila mesoderm invagination begins with two phases of apical constriction of cells. Journal of cell science *114*, 493-501.

Ohashi, K., Nagata, K., Maekawa, M., Ishizaki, T., Narumiya, S., and Mizuno, K. (2000). Rho-associated kinase ROCK activates LIM-kinase 1 by phosphorylation at threonine 508 within the activation loop. The Journal of biological chemistry *275*, 3577-3582.

Oshima, K., and Fehon, R.G. (2011). Analysis of protein dynamics within the septate junction reveals a highly stable core protein complex that does not include the basolateral polarity protein Discs large. Journal of cell science *124*, 2861-2871.

Pare, A.C., Vichas, A., Fincher, C.T., Mirman, Z., Farrell, D.L., Mainieri, A., and Zallen, J.A. (2014). A positional Toll receptor code directs convergent extension in Drosophila. Nature *515*, 523-527.

Parks, A.L., and Muskavitch, M.A. (1993). Delta function is required for bristle organ determination and morphogenesis in Drosophila. Developmental biology *157*, 484-496.

Parks, S., and Wieschaus, E. (1991). The Drosophila gastrulation gene concertina encodes a G alpha-like protein. Cell *64*, 447-458.

Patel, A.B., Gibson, W.T., Gibson, M.C., and Nagpal, R. (2009). Modeling and inferring cleavage patterns in proliferating epithelia. PLoS computational biology *5*, e1000412.

Paul, A.S., and Pollard, T.D. (2008). The role of the FH1 domain and profilin in formin-mediated actin-filament elongation and nucleation. Current biology : CB *18*, 9-19.

Pearce, P. (1978). Structure in nature is a strategy for design (Cambridge: MIT Press).

Perez, T.D., Tamada, M., Sheetz, M.P., and Nelson, W.J. (2008). Immediate-early signaling induced by E-cadherin engagement and adhesion. The Journal of biological chemistry *283*, 5014-5022.

Pollard, T.D., and Mooseker, M.S. (1981). Direct measurement of actin polymerization rate constants by electron microscopy of actin filaments nucleated by isolated microvillus cores. The Journal of cell biology *88*, 654-659.

Pollitt, A.Y., and Insall, R.H. (2009). WASP and SCAR/WAVE proteins: the drivers of actin assembly. Journal of cell science *122*, 2575-2578.

Qin, J., Xie, Y., Wang, B., Hoshino, M., Wolff, D.W., Zhao, J., Scofield, M.A., Dowd, F.J., Lin, M.F., and Tu, Y. (2009). Upregulation of PIP3-dependent Rac exchanger 1 (P-Rex1) promotes prostate cancer metastasis. Oncogene *28*, 1853-1863.

Raftopoulou, M., and Hall, A. (2004). Cell migration: Rho GTPases lead the way. Developmental biology *265*, 23-32.

Rapsomaniki, M.A., Kotsantis, P., Symeonidou, I.E., Giakoumakis, N.N., Taraviras, S., and Lygerou, Z. (2012). easyFRAP: an interactive, easy-to-use tool for qualitative and quantitative analysis of FRAP data. Bioinformatics *28*, 1800-1801.

Rauzi, M., Lenne, P.F., and Lecuit, T. (2010). Planar polarized actomyosin contractile flows control epithelial junction remodelling. Nature *468*, 1110-1114.

Renaud, O., and Simpson, P. (2002). Movement of bristle precursors contributes to the spacing pattern in Drosophila. Mechanisms of development *119*, 201-211.

Rhyu, M.S., Jan, L.Y., and Jan, Y.N. (1994). Asymmetric distribution of numb protein during division of the sensory organ precursor cell confers distinct fates to daughter cells. Cell *76*, 477-491.

Ridley, A.J. (2001). Rho GTPases and cell migration. Journal of cell science *114*, 2713-2722.

Riento, K., and Ridley, A.J. (2003). Rocks: multifunctional kinases in cell behaviour. Nat Rev Mol Cell Biol *4*, 446-456.

Rivard, N. (2009). Phosphatidylinositol 3-kinase: a key regulator in adherens junction formation and function. Front Biosci (Landmark Ed) *14*, 510-522.

Rodriguez-Boulan, E., and Macara, I.G. (2014). Organization and execution of the epithelial polarity programme. Nat Rev Mol Cell Biol *15*, 225-242.

Roegiers, F., Younger-Shepherd, S., Jan, L.Y., and Jan, Y.N. (2001). Two types of asymmetric divisions in the Drosophila sensory organ precursor cell lineage. Nature cell biology *3*, 58-67.

Roeth, J.F., Sawyer, J.K., Wilner, D.A., and Peifer, M. (2009). Rab11 helps maintain apical crumbs and adherens junctions in the Drosophila embryonic ectoderm. PloS one *4*, e7634.

Rohatgi, R., Ho, H.Y., and Kirschner, M.W. (2000). Mechanism of N-WASP activation by CDC42 and phosphatidylinositol 4, 5-bisphosphate. The Journal of cell biology *150*, 1299-1310.

Roper, K. (2015). Integration of cell-cell adhesion and contractile actomyosin activity during morphogenesis. Current topics in developmental biology *112*, 103-127.

Roubinet, C., Decelle, B., Chicanne, G., Dorn, J.F., Payrastre, B., Payre, F., and Carreno, S. (2011). Molecular networks linked by Moesin drive remodeling of the cell cortex during mitosis. Journal of Cell Biology *195*, 99-112.

Royou, A., Field, C., Sisson, J.C., Sullivan, W., and Karess, R. (2004). Reassessing the role and dynamics of nonmuscle myosin II during furrow formation in early Drosophila embryos. Molecular biology of the cell *15*, 838-850.

Rubin, G.M., Yandell, M.D., Wortman, J.R., Gabor Miklos, G.L., Nelson, C.R., Hariharan, I.K., Fortini, M.E., Li, P.W., Apweiler, R., Fleischmann, W.*, et al.* (2000). Comparative genomics of the eukaryotes. Science *287*, 2204-2215.

Ruderman, N.B., Kapeller, R., White, M.F., and Cantley, L.C. (1990). Activation of phosphatidylinositol 3-kinase by insulin. Proceedings of the National Academy of Sciences of the United States of America *87*, 1411-1415.

Ruysch, F. (1703). Thesaurus Anatomicus III [Atomist thesaurus III], Vol 3 (Amsterdam: Janssonion-Waesbergios).

Salbreux, G., Charras, G., and Paluch, E. (2012). Actin cortex mechanics and cellular morphogenesis. Trends in cell biology *22*, 536-545.

Samakovlis, C., Hacohen, N., Manning, G., Sutherland, D.C., Guillemin, K., and Krasnow, M.A. (1996). Development of the Drosophila tracheal system occurs by a series of morphologically distinct but genetically coupled branching events. Development *122*, 1395-1407.

Sano, K., Tanihara, H., Heimark, R.L., Obata, S., Davidson, M., St John, T., Taketani, S., and Suzuki, S. (1993). Protocadherins: a large family of cadherin-related molecules in central nervous system. The EMBO journal *12*, 2249-2256.

Sarpal, R., Pellikka, M., Patel, R.R., Hui, F.Y., Godt, D., and Tepass, U. (2012). Mutational analysis supports a core role for Drosophila alpha-catenin in adherens junction function. Journal of cell science *125*, 233-245.

Sato, N., Funayama, N., Nagafuchi, A., Yonemura, S., Tsukita, S., and Tsukita, S. (1992). A gene family consisting of ezrin, radixin and moesin. Its specific localization at actin filament/plasma membrane association sites. Journal of cell science *103 ( Pt 1)*, 131-143.

Schmidt, A., Heid, H.W., Schafer, S., Nuber, U.A., Zimbelmann, R., and Franke, W.W. (1994). Desmosomes and cytoskeletal architecture in epithelial differentiation: cell type-specific plaque components and intermediate filament anchorage. European journal of cell biology *65*, 229-245.

Schneeberger, E.E., and Lynch, R.D. (2004). The tight junction: a multifunctional complex. American journal of physiology Cell physiology *286*, C1213-1228.

Schupbach, T., and Wieschaus, E. (1986). Germline autonomy of maternal-effect mutations altering the embryonic body pattern of Drosophila. Developmental biology *113*, 443-448.

Sellers, J.R. (2000). Myosins: a diverse superfamily. Biochimica et biophysica acta *1496*, 3-22.

Sept, D., and McCammon, J.A. (2001). Thermodynamics and kinetics of actin filament nucleation. Biophysical journal *81*, 667-674.

Shih, J., and Keller, R. (1992). Cell motility driving mediolateral intercalation in explants of Xenopus laevis. Development *116*, 901-914.

Simoes Sde, M., Blankenship, J.T., Weitz, O., Farrell, D.L., Tamada, M., Fernandez-Gonzalez, R., and Zallen, J.A. (2010). Rho-kinase directs Bazooka/Par-3 planar polarity during Drosophila axis elongation. Dev Cell *19*, 377-388.

Simoes Sde, M., Mainieri, A., and Zallen, J.A. (2014). Rho GTPase and Shroom direct planar polarized actomyosin contractility during convergent extension. The Journal of cell biology *204*, 575-589.

Simon, M.A., Xu, A., Ishikawa, H.O., and Irvine, K.D. (2010). Modulation of fat:dachsous binding by the cadherin domain kinase four-jointed. Current biology : CB *20*, 811-817.

Simpson, P., Woehl, R., and Usui, K. (1999). The development and evolution of bristle patterns in Diptera. Development *126*, 1349-1364.

Solon, J., Kaya-Copur, A., Colombelli, J., and Brunner, D. (2009). Pulsed forces timed by a ratchet-like mechanism drive directed tissue movement during dorsal closure. Cell *137*, 1331-1342.

Sonnenblick, B.P. (1950). The early embryo of Drosophila melanogaster. In Biology of Drosophila, M. Demerec, ed. (New York: John Wiley), pp. 62-167.

Soosairajah, J., Maiti, S., Wiggan, O., Sarmiere, P., Moussi, N., Sarcevic, B., Sampath, R., Bamburg, J.R., and Bernard, O. (2005). Interplay between components of a novel LIM kinase-slingshot phosphatase complex regulates cofilin. The EMBO journal *24*, 473-486.

Speck, O., Hughes, S.C., Noren, N.K., Kulikauskas, R.M., and Fehon, R.G. (2003). Moesin functions antagonistically to the Rho pathway to maintain epithelial integrity. Nature *421*, 83-87.

Spiering, D., and Hodgson, L. (2011). Dynamics of the Rho-family small GTPases in actin regulation and motility. Cell adhesion & migration *5*, 170-180.

St Johnston, D., and Nusslein-Volhard, C. (1992). The origin of pattern and polarity in the Drosophila embryo. Cell *68*, 201-219.

Suster, M.L., Seugnet, L., Bate, M., and Sokolowski, M.B. (2004). Refining GAL4-driven transgene expression in Drosophila with a GAL80 enhancer-trap. Genesis *39*, 240-245.

Sutherland, D., Samakovlis, C., and Krasnow, M.A. (1996). branchless encodes a Drosophila FGF homolog that controls tracheal cell migration and the pattern of branching. Cell *87*, 1091-1101.

Sweeton, D., Parks, S., Costa, M., and Wieschaus, E. (1991). Gastrulation in Drosophila: the formation of the ventral furrow and posterior midgut invaginations. Development *112*, 775-789.

Takeichi, M. (1995). Morphogenetic roles of classic cadherins. Current opinion in cell biology *7*, 619-627.

Takeichi, M. (2014). Dynamic contacts: rearranging adherens junctions to drive epithelial remodelling. Nat Rev Mol Cell Biol *15*, 397-410.

Tamada, M., Farrell, D.L., and Zallen, J.A. (2012). Abl regulates planar polarized junctional dynamics through beta-catenin tyrosine phosphorylation. Dev Cell *22*, 309-319.

Tapon, N., and Hall, A. (1997). Rho, Rac and Cdc42 GTPases regulate the organization of the actin cytoskeleton. Current opinion in cell biology *9*, 86-92.

Tardieu, A. (1988). Eye lens proteins and transparency: from light transmission theory to solution X-ray structural analysis. Annual review of biophysics and biophysical chemistry *17*, 47-70.

Tepass, U., Gruszynski-DeFeo, E., Haag, T.A., Omatyar, L., Torok, T., and Hartenstein, V. (1996). shotgun encodes Drosophila E-cadherin and is preferentially required during cell rearrangement in the neurectoderm and other morphogenetically active epithelia. Genes & development *10*, 672-685.

Tepass, U., Tanentzapf, G., Ward, R., and Fehon, R. (2001). Epithelial cell polarity and cell junctions in Drosophila. Annual review of genetics *35*, 747-784.

Thompson, D.A.W. (1917). On Growth and Form (Cambridge: Cambridge University Press).

Tóth, L.F. (1964). What the bees know and what they do not know. Bulletin of the American Mathematical Society *70*, 468-481.

Traub, L.M. (2003). Sorting it out: AP-2 and alternate clathrin adaptors in endocytic cargo selection. The Journal of cell biology *163*, 203-208.

Tsukita, S., and Furuse, M. (2002). Claudin-based barrier in simple and stratified cellular sheets. Current opinion in cell biology *14*, 531-536.

Tsukita, S., Furuse, M., and Itoh, M. (2001). Multifunctional strands in tight junctions. Nat Rev Mol Cell Biol *2*, 285-293.

Tyler, S. (2003). Epithelium--the primary building block for metazoan complexity. Integrative and comparative biology *43*, 55-63.

Usui, K., and Kimura, K. (1993). Sequential emergence of the evenly spaced microchaetes on the notum of Drosophila. Development, Genes and Evolution *203*, 151-158.

Usui, K., and Simpson, P. (2000). Cellular basis of the dynamic behavior of the imaginal thoracic discs during Drosophila metamorphosis. Developmental biology *225*, 13-25.

van der Bliek, A.M., and Meyerowitz, E.M. (1991). Dynamin-like protein encoded by the Drosophila shibire gene associated with vesicular traffic. Nature *351*, 411-414.

Van Lierop, J.E., Wilson, D.P., Davis, J.P., Tikunova, S., Sutherland, C., Walsh, M.P., and Johnson, J.D. (2002). Activation of smooth muscle myosin light chain kinase by calmodulin. Role of LYS(30) and GLY(40). The Journal of biological chemistry *277*, 6550-6558.

Vanhaesebroeck, B., Stephens, L., and Hawkins, P. (2012). PI3K signalling: the path to discovery and understanding. Nat Rev Mol Cell Biol *13*, 195-203.

Verdier, V., Guang Chao, C., and Settleman, J. (2006). Rho-kinase regulates tissue morphogenesis via non-muscle myosin and LIM-kinase during Drosophila development. BMC developmental biology *6*, 38.

Vereshchagina, N., Bennett, D., Szoor, B., Kirchner, J., Gross, S., Vissi, E., White-Cooper, H., and Alphey, L. (2004). The essential role of PP1beta in Drosophila is to regulate nonmuscle myosin. Molecular biology of the cell *15*, 4395-4405.

Vicente-Manzanares, M., Ma, X., Adelstein, R.S., and Horwitz, A.R. (2009). Non-muscle myosin II takes centre stage in cell adhesion and migration. Nat Rev Mol Cell Biol *10*, 778-790.

Wegner, A. (1976). Head to tail polymerization of actin. Journal of molecular biology *108*, 139-150.

Whyte, J.R., and Munro, S. (2002). Vesicle tethering complexes in membrane traffic. Journal of cell science *115*, 2627-2637.

Wigglesworth, V.B. (1940). Local and general factors in the development of 'pattern' in Rhodnius prolixus. Journal of Experimental Biology *17*, 180-200.

Winter, C.G., Wang, B., Ballew, A., Royou, A., Karess, R., Axelrod, J.D., and Luo, L. (2001). Drosophila Rho-associated kinase (Drok) links Frizzled-mediated planar cell polarity signaling to the actin cytoskeleton. Cell *105*, 81-91.

Wootton, R.J. (1992). Functional morphology of insect wings. Annual Review of Entomology *37*, 113-140.

Wyatt, T.P., Harris, A.R., Lam, M., Cheng, Q., Bellis, J., Dimitracopoulos, A., Kabla, A.J., Charras, G.T., and Baum, B. (2015). Emergence of homeostatic epithelial packing and stress dissipation through divisions oriented along the long cell axis. Proceedings of the National Academy of Sciences of the United States of America *112*, 5726-5731.

Yap, A.S., Niessen, C.M., and Gumbiner, B.M. (1998). The juxtamembrane region of the cadherin cytoplasmic tail supports lateral clustering, adhesive strengthening, and interaction with p120ctn. The Journal of cell biology *141*, 779-789.

Yonemura, S., Wada, Y., Watanabe, T., Nagafuchi, A., and Shibata, M. (2010). alpha-Catenin as a tension transducer that induces adherens junction development. Nature cell biology *12*, 533-542.

Young, P.E., Richman, A.M., Ketchum, A.S., and Kiehart, D.P. (1993). Morphogenesis in Drosophila requires nonmuscle myosin heavy chain function. Genes & development *7*, 29-41.

Zallen, J.A., and Wieschaus, E. (2004). Patterned gene expression directs bipolar planar polarity in Drosophila. Dev Cell *6*, 343-355.

Zeitlinger, J., and Bohmann, D. (1999). Thorax closure in Drosophila: involvement of Fos and the JNK pathway. Development *126*, 3947-3956.

Zhang, Y., Sivasankar, S., Nelson, W.J., and Chu, S. (2009). Resolving cadherin interactions and binding cooperativity at the single-molecule level. Proceedings of the National Academy of Sciences of the United States of America *106*, 109-114.

Zigmond, S.H., Evangelista, M., Boone, C., Yang, C., Dar, A.C., Sicheri, F., Forkey, J., and Pring, M. (2003). Formin leaky cap allows elongation in the presence of tight capping proteins. Current biology : CB *13*, 1820-1823.

Zitserman, D., and Roegiers, F. (2011). Live-cell imaging of sensory organ precursor cells in intact Drosophila pupae. Journal of visualized experiments : JoVE.